Towards a Quantum Leap in Oceanic Oxygen Observation

From Oxygen Optode Characterization to Autonomous Observation of Gas Exchange and Net Community Production

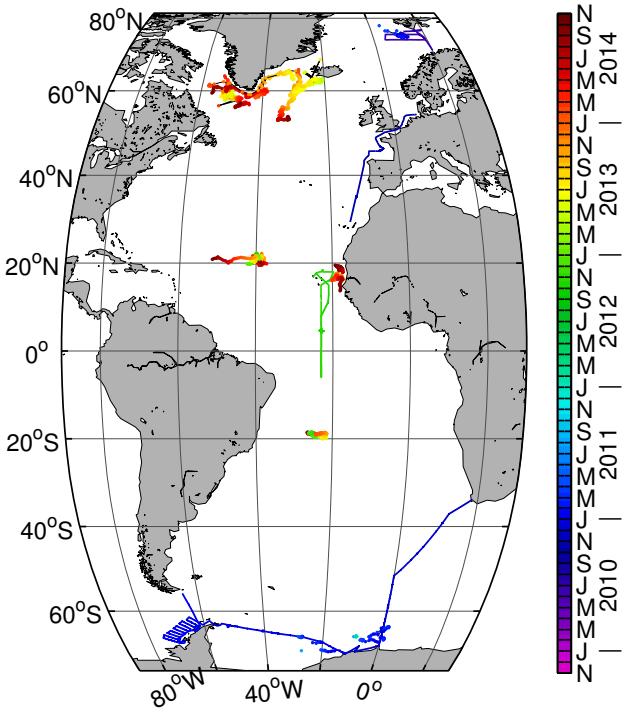

Dissertation zur Erlangung des Doktorgrades der Mathematisch-Naturwissenschaftlichen Fakultät der Christian-Albrechts-Universität zu Kiel

vorgelegt von

Henry Bittig

Kiel, 2014

Cover figure: Positions of all Argo-O_2 floats I have been involved with during this PhD thesis and tracks of all oceanic research cruises I participated in this time.

Erstgutachter	Prof. Arne Körtzinger
Zweitgutachterin	Prof. Christa A. Marandino
Tag der mündlichen Prüfung	8. Dezember 2014
Zum Druck genehmigt	8. Dezember 2014
gez.	Prof. Wolfgang J. Duschl, Dekan

Und meine Reisen in China haben wahrhaftig
wenig Bedeutung verglichen mit den tastenden
Schritten im Dunkeln vom Bett zur Küche,
auf der Suche nach einem Glas Wasser.

Ennio Flaiano, *Nächtliches Tagebuch*

Abstract

This thesis presents ways to use autonomous oxygen observations to quantitatively estimate biological productivity and gas exchange. For this purpose, high quality oxygen sensor data are essential and the metrological prerequisites are established through dedicated experiments and procedures.

Oxygen optodes promise to be long term stable due to their optical detection principle. Thus they seem predestined for autonomous deployments. However, their response to oxygen is non-linear and they require a most accurate calibration. A new calibration setup is described which is based on electrochemical oxygen generation. It can be used to multipoint calibrate oxygen optodes with an accuracy of 1 µmol kg^{-1}.

This setup also helped in the identification of optode sensor drift which is stronger at high oxygen levels than at low oxygen. Such a drift severely compromises the field deployability of optodes as well as the current routine of optode factory or laboratory calibration, sensor shipment, and subsequent deployment with an associated delay of a week to a year. Drift rates of up to −3.5 % in 2 months strongly impair the potential to reach a targeted field accuracy of 1 µmol/kg (Gruber et al., 2010). An in-situ referencing method is thus crucial to detect and quantify an optode drift. Based on near-surface and in-air measurements, a method to accurately reference optodes on Argo floats is described. This referencing method is available throughout the entire instrument's lifetime and thus also capable to correct not only pre-deployment drift but also any further drift during deployment.

Profiling applications rely on a fast time response to adequately resolve gradients. Optodes, however, do have a slow response compared to electrochemical oxygen sensors. The time response of oxygen optodes is extensively characterized in laboratory and field experiments and the impact of the response time on sensor data is quantified. Response times can be drastically reduced when optodes are pumped and a framework is presented to predict the response time based on temperature and the flow conditions of the deployment platform.

This metrological work lays the foundation for a new quality of autonomous oxygen observations. Concurrent underway measurements of oxygen together with nitrogen and carbon dioxide in Southern Ocean surface waters are presented, revealing the different level of physical or biological control. A mixed layer gas exchange model is applied and adequately reproduces the spatial and temporal distribution of physical super- and undersaturation. It is used to improve oxygen-based net community production (NCP) estimates by removing physical contributions, e.g., due to entrainment.

Finally, biogeochemical and biooptical data from five floats in the North and South Atlantic subtropical gyres are discussed and analyzed. In both gyres, there are three depth layers with a distinct biogeochemical characteristic. First, a net productive layer (layer I) is found between the surface and the node of apparent oxygen utilization ($AOU = 0$) around 110 m where nitrate is completely depleted and there still is a net oxygen production. This layer encompasses a shallow oxygen maximum at ca. 60 – 70 m that forms below the mixed layer in spring, summer, and

autumn. Second, there is a net heterotrophic layer (layer II) below until approx. 200 m characterized by a stoichiometric nitrate deficit compared to the oxygen consumption. This layer is split into two subdomains, one where nitrate is in deficit and no measurable nitrate is present above the nitracline (layer IIa), and one where there is measurable nitrate present but it is still in deficit (layer IIb). Third, waters below are net heterotrophic and oxygen and nitrate are stoichiometrically balanced (layer III). The boundary between layer IIb and III is determined by the advective supply of surface nutrients through subtropical mode water.
From the 2 years of float data, quantitative estimates of NCP are derived by using a 1D abiotic model with a dedicated gas exchange module that successfully separates physical and biological effects on oxygen. Production and respiration as well as the stoichiometric imbalance (oxygen excess in the surface and nitrate deficit below) follow the above depth horizons. A mean annual NCP of 1.2 ± 1.1 mol C m^{-2} yr^{-1} and 1.6 ± 0.8 mol C m^{-2} yr^{-1} is obtained for the North and South Atlantic gyre. Optodes drifted during the deployment and a conservative in-situ correction was necessary. The NCP estimates therefore likely represent a lower bound. At the same time, this echoes the need to implement a proper in-situ reference approach as described in this work.

Zusammenfassung

Diese Arbeit beschäftigt sich mit der Nutzung von autonomen Sauerstoffmessungen zur quantitativen Bestimmung biologischer Produktion und des Gasaustauschs. Dies erfordert qualitativ hochwertige Daten von Sauerstoffsensoren. Die messtechnischen Voraussetzungen werden hier durch geeignete Experimente und Methoden erarbeitet.

Sauerstoffoptoden versprechen aufgrund ihres optischen Detektionsprinzips Langzeitstabilität und erscheinen dadurch prädestiniert für den autonomen Feldeinsatz. Ihre Sauerstoffabhängigkeit ist allerdings nicht linear, was daher eine hochgenaue Kalibrierung erfordert. Ein neuer Kalibrieraufbau basierend auf einer elektrochemischen Sauerstofferzeugung wird in dieser Arbeit beschrieben. Er kann für die Mehrpunkt-Kalibrierung von Sauerstoffoptoden mit einer Genauigkeit von 1 µmol kg^{-1} verwendet werden.

Dieser Aufbau hilft außerdem bei der Identifizierung einer Drift bei Sauerstoffoptoden, die bei hohem Sauerstoffgehalt stärker ausgeprägt ist als bei niedrigem. Solch eine Drift kompromittiert die Eignung von Optoden für den Feldeinsatz sowie den zur Zeit üblichen Ablauf von Fabrik- oder Laborkalibration, Sensor-Transport und anschließendem Auslegen mit einem Zeitversatz von einer Woche bis einem Jahr. Driftraten von bis zu −3.5 % in 2 Monaten beeinträchtigen in hohem Maß das Potential, eine angestrebte Feldgenauigkeit von 1 µmol kg^{-1} (Gruber et al., 2010) zu erreichen. Eine in-situ Referenzierung ist daher essentiell für die Identifizierung und Quantifizierung einer Optodendrift. Eine auf oberflächennahen und Luftmessungen basierende Methode zur genauen Referenzierung von Optoden auf Argo-Floats wird in dieser Arbeit beschrieben. Diese Art der Referenzierung ist für die gesamte Dauer des Feldeinsatzes realisierbar und kann daher nicht nur eine Drift bis zur Auslegung sondern auch während des Einsatzes korrigieren.

Profilierende Anwendungen sind auf eine schnelle Sensorantwort angewiesen, um Gradienten angemessen auflösen zu können. Im Vergleich zu elektrochemischen Sauerstoffsensoren haben Optoden allerdings ein langsames Antwortverhalten. Dieses wird ausführlich in Labor und Feld charakterisiert und der Einfluss des Antwortverhaltens auf Sensordaten quantifiziert. Die Zeitkonstante kann durch Pumpen der Optoden drastisch reduziert werden. Ein Modell zur Vorhersage der Zeitkonstante in Abhängigkeit der Temperatur und Umströmung der Feldplattform wird beschrieben.

Diese methodischen Arbeiten legen die Grundlage für eine neue Qualität von autonomen Sauerstoffbeobachtungen. Simultane underway-Messungen von Sauerstoff, Stickstoff und Kohlendioxid im Oberflächenwasser des Südlichen Ozeans werden vorgestellt und machen den unterschiedlichen Grad an physikalischer und biologischer Kontrolle dieser Gase deutlich. Die Anwendung eines Deckschichtmodells einschließlich Gasaustausch reproduziert die räumliche und zeitliche Verteilung der Gase in angemessenem Maße. Es wird entsprechend zur Verbesserung von Abschätzungen der sauerstoffbasierten Nettoproduktion (NCP) verwendet, indem es physikalische Einflüsse z.B. aufgrund von Entrainment entfernt.

Abschließend werden die biogeochemischen und biooptischen Daten von fünf Floats im nord- und südatlantischen Subtropenwirbel diskutiert und analysiert. In beiden Wirbeln existieren drei Tiefenschichten mit jeweils charakteristischer biogeochemischer Signatur. Zuoberst gibt es eine netto-produktive Schicht (layer I) zwischen der Oberfläche und dem Null-Knoten der scheinbaren Sauerstoffzehrung ($AOU = 0$) bei etwa 110 m, in der Nitrat vollständig verbraucht ist und trotzdem eine Netto-Sauerstoffproduktion stattfindet. Diese Schicht schließt das flache Sauerstoffmaximum bei 60 – 70 m ein, das sich unterhalb der Deckschicht im Frühjahr, Sommer und Herbst bildet. Darunter folgt eine netto-heterotrophe Schicht (layer II) bis ungefähr 200 m Tiefe, die durch ein stöchiometrisches Nitrat-Defizit im Vergleich zum Sauerstoffverbrauch charakterisiert ist. Diese Schicht lässt sich in zwei Bereiche teilen: Einer oberhalb der Nitrakline, in dem Nitrat sowohl im Unterschuss als auch nicht im Wasser bestimmbar ist (layer IIa), und einer unterhalb, in dem Nitrat weiterhin im Unterschuss, aber im Wasser messbar vorhanden ist (layer IIb). Als drittes folgt eine netto-heterotrophe Schicht, in der Sauerstoff und Nitrat stöchiometrisch ausgeglichen sind (layer III). Die Grenze zwischen den Schichten IIb und III wird durch den advektiven Zustrom von Oberflächennährstoffen mittels subtropischen Zwischenwassers bestimmt.
Die Nettoproduktion wird basierend auf Floatmessungen der letzten 2 Jahre quantitativ abgeschätzt. Dies erfolgt mit Hilfe eines abiotischen 1D Modells, das zusätzlich ein Gasaustauschmodul aufweist und erfolgreich physikalische und biologische Faktoren auf den Sauerstoffgehalt separiert. Produktion, Zehrung sowie das stöchiometrische Ungleichgewicht (Sauerstoffüberschuss in der Oberfläche und Nitratdefizit darunter) folgen den obigen Tiefenhorizonten. Für den nord- und südatlantischen Subtropenwirbel wird eine durchschnittliche Jahresproduktion von 1.2 ± 1.1 mol C m^{-2} yr^{-1} bzw. 1.6 ± 0.8 mol C m^{-2} yr^{-1} bestimmt. Die Optoden sind während des Einsatzes gedriftet, weswegen eine konservative in-situ Korrektur nötig war. Die NCP-Abschätzung liefert daher eher eine untere Grenze. Gleichzeitig spiegelt dies die Notwendigkeit wider, einen geeigneten in-situ Referenzierungsansatz – wie in dieser Arbeit beschrieben – zu implementieren.

Graphical Abstract

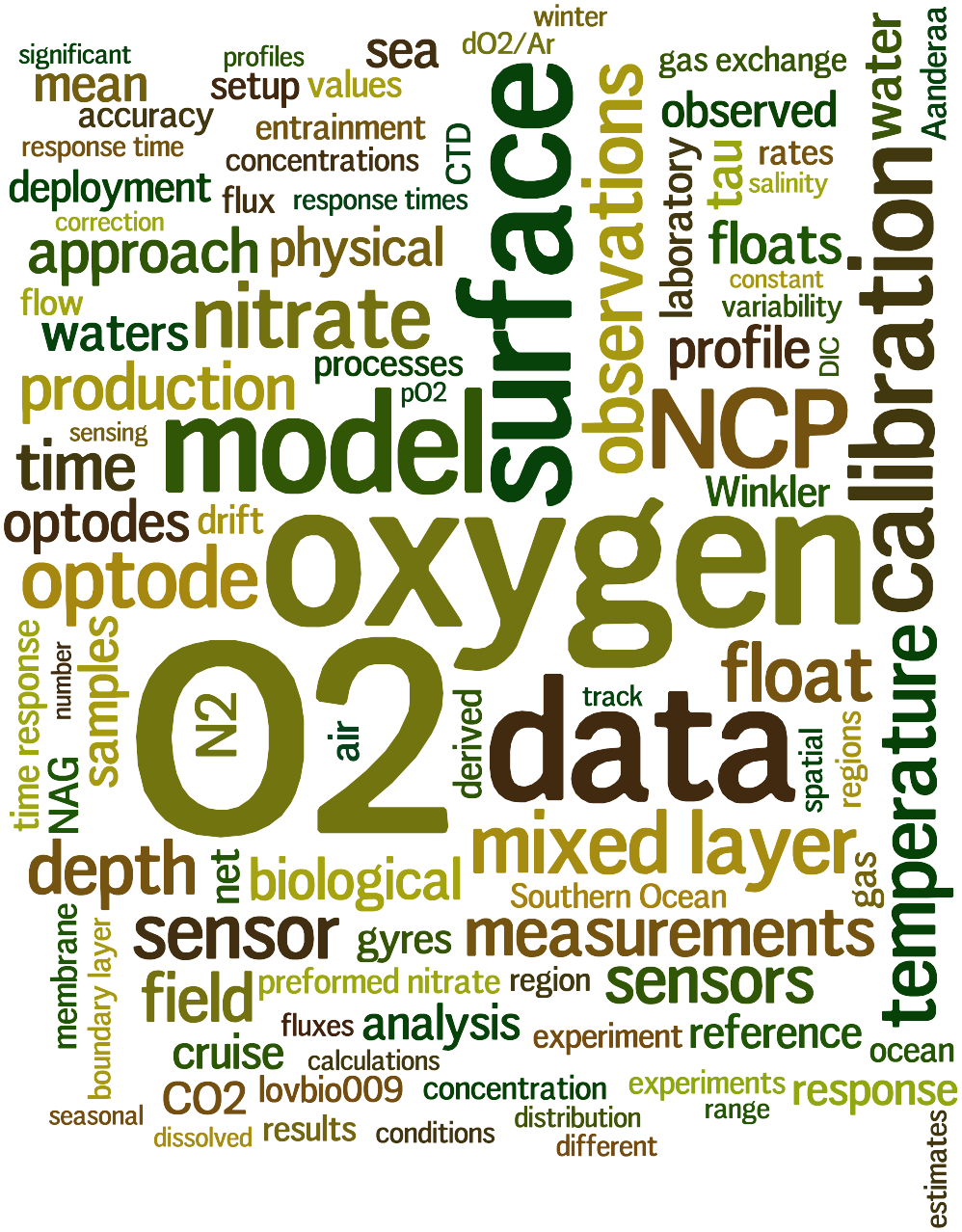

Contents

Introduction

This thesis deals with autonomous oxygen measurements and the sensor technology to do unattended, long-term deployments. It is structured in two parts:

Part I addresses the metrology to accurately measure dissolved oxygen using optodes. A newly developed multipoint calibration setup for oxygen sensors is presented in chapter 2. It also discusses details of optode drift identified by repeated calibrations with this setup. Chapter 3 shows a new method on how in-air measurements of oxygen optodes deployed on floats can be used to provide a much-needed reference in-situ and over the course of a field deployment. The metrology part is concluded by the characterization of the time response of oxygen optodes (chapter 4). In addition, that chapter provides a framework to predict response times and their effect on data based on information about the deployment platform.

Part II addresses the biogeochemistry of dissolved oxygen in the surface and sub-surface ocean. Based on 10 weeks of underway measurements in the Southern Ocean, biological and physical controls on N_2, O_2 and CO_2 in surface waters are discussed in chapter 6. The remaining two chapters focus on the subtropical North and South Atlantic. Five Bio-Argo floats have been deployed in the subtropical gyres and their data are used to infer a qualitative picture of biogeochemistry in chapter 7. Three distinct biogeochemical layers are observed and a concept about their linkage is established. Chapter 8 in turn provides quantitative estimates of net community production by separating the biological contribution from physical effects with the aid of an abiotic 1D model.

Part I

Metrology

1 Oxygen Measurements

Today, there are three main methods to measure the concentration of dissolved oxygen in seawater. The first is a wet-chemical titration developed by Winkler (1888), while the other two are sensor-based: One uses electrodes and a polarographic approach and the other applies optodes and a luminescence quenching approach. The latter will be the main focus of the following chapters.

1.1 Wet-Chemical Approach: Winkler Titration

Principle

This chemical determination is based on Winkler (1888) and uses the oxidation potential of oxygen as well as the electrochemical properties of the pickling reagents added during sampling.

Water is sampled by filling known-volume, glas-stoppered flasks bottom-up with a Tygon tubing extending to the flasks' bottom and letting the sample overflow to minimize contamination by air. With addition of the pickling reagents (concentrated $MnCl_2$ and NaOH/NaI solution, equation 1.1) before inserting the stopper, the oxidation equivalents of the O_2 contained in the sample are quantitatively converted into higher manganese hydroxides/oxides which precipitate (equation 1.2).

$$Mn^{2+} + 2\ OH^- \longrightarrow Mn(OH)_2 \tag{1.1}$$

$$2\ \underset{\text{white}}{\overset{+2}{Mn}(OH)_2} + \overset{\pm 0}{O_2} \longrightarrow 2\ \underset{\text{brown}}{\overset{+4\ -2}{MnO}(OH)_2}\downarrow \tag{1.2}$$

For analysis, the solution is acidified which leads to the oxidation of an equivalent amount of iodide (added with the pickling reagents) to iodine (equation 1.3) due to a pH-dependent shift in the reduction potentials. Sodium thiosulfate is then used to titrate the produced amount of iodine (equation 1.4).

$$2\ \underset{\text{brown}}{\overset{+4}{MnO}(OH)_2} + 4\ \overset{-1}{I^-} + 8\ H^+ \longrightarrow 2\ \overset{+2}{Mn^{2+}} + 2\ \underset{\text{yellow}}{\overset{\pm 0}{I_2}} + 6\ H_2O \tag{1.3}$$

$$2\ \underset{\text{yellow}}{\overset{\pm 0}{I_2}} + 4\ \overset{+2.5}{S_2O_3^{2-}} \longrightarrow 4\ \overset{-1}{I^-} + 2\ \overset{+2}{S_4O_6^{2-}} \tag{1.4}$$

Starch can be used as extremely sensitive indicator to determine the endpoint of this iodometric titration. Alternatively, amperometric or photometric endpoint detections are possible.

All reactions are quantitative and the Winkler titration allows very accurate and precise measurements, provided that care was taken during sampling and analysis. Until today it remains the reference method for dissolved oxygen measurements in marine waters.

Implementation

Given its long history, this approach has been improved several times (e.g., Carpenter, 1965) and is highly standardized today (Dickson, 1994). Commonly, automatic piston burettes, magnetic stirrers, and precise dispensers for the pickling reagents are used. Setups differ mostly in the way the endpoint of the titration is determined. Automated amperometric or photometric detection (Langdon, 2010; Culberson et al., 1991) as well as the use of starch as indicator for iodine and visual endpoint detection are the most common.

Issues

Given the volatility of iodine, the iodometric titration should be done quickly, which favours the visual endpoint detection. The automated ones, however, are less dependent on operator skills and experience.

The risk of air contamination is amplified at very low O_2 concentrations and extreme care must be taken during sampling.

While it is the most accurate way to measure dissolved oxygen, this approach is limited to discrete samples. Moreover, it needs trained personnel to take uncontaminated samples and to perform the analysis, which limits its range of use.

1.2 Polarographic Approach: Electrochemical Sensors

Principle

In 1897, Heinrich Danneel and Walther Nernst first reported the electrochemical reduction of dissolved oxygen (Danneel, 1897; see Severinghaus and Astrup, 1986). The same reaction is used today in electrochemical oxygen sensors which are based on the design of a polarographic probe by Clark et al. (1953).

Dissolved oxygen is reduced to hydrogen peroxide and subsequently to hydroxide according to equation 1.5.

$$\overset{\pm 0}{O_2} + 2\,H_2O \xrightarrow{2\,e^-} \overset{-1}{H_2O_2} + 2\,OH^- \xrightarrow{2\,e^-} 4\,\overset{-2}{OH^-} \tag{1.5}$$

The cathode (Pt or Au), place of the reduction, and the reference anode (Ag|AgCl) are both in the same electrolyte and separated from the environment by a membrane, permeable for oxygen but not for the electrolyte or ionic seawater constituents.

The rate of O_2 reduction at the cathode, which is proportional to the electrical current between both electrodes, solely depends on the known diffusion geometry of the sensor and the number of oxygen molecules diffusing through the membrane per time interval. As the sensor consumes oxygen, an adequate flow of sample water past the membrane is necessary to avoid depletion in front of the membrane, i.e., electrochemical sensors need to be pumped.

Because of the continuous consumption, a concentration-dependent steady state is reached when diffusive supply balances the loss by electrochemical reduction, i.e., a steady-state O_2 gradient is established inside the sensor. This is typically a fast process and response times τ of such sensors are small.

Implementation

One of the most common electrochemical sensors is the Sea-Bird SBE43, the standard sensor on many CTDs. It uses a gold cathode, Teflon membrane, and has an internal temperature measurement to compensate the sensor output. Sophisticated algorithms for response time and pressure hysteresis corrections are available (Edwards et al., 2010).

Issues

While this type of sensors is well characterized, the electrochemical approach suffers a few major drawbacks, e.g., sensors need to be pumped and they tend to drift on timescales of weeks and months. The sensor's sensitivity is reduced with time mostly due to permeability changes (changes of the membrane and contamination through surfactants or fouling) and frequent recalibrations and monitoring of the sensor's performance is required (Sea-Bird Electronics, 2010).

The permeability of the membrane is temperature and hydrostatic pressure dependent which affects the amount of oxygen that reaches the cathode even if ambient O_2 levels are stable. This is compensated for by the calculation protocols.

Still, such sensors can be very accurate and they typically have a fast time response. Earlier versions with silver cathodes suffered poisoning of the electrodes in hydrogen sulfide environments, but this issue has been solved by using gold as cathode material (Sea-Bird Electronics, 2010).

1.3 Luminescence Quenching Approach: Optical Sensors

Principle

One of the first descriptions of luminescence quenching by oxygen has been given by Kautsky (1939) and almost all luminophores are quenched by molecular oxygen (Lakowicz, 2006, chap. 8).

When the luminophore is excited with a short pulse of light of the correct wavelength, it may relax to its ground state by non-radiative processes and light emission, i.e., luminescence, with associated rate constants k_{nr} and k_f, respectively. Since this is a rate controlled process, the luminescence intensity I_0 decays exponentially with

the luminescence lifetime $\Lambda_0 = 1/(k_f + k_{nr})$ (figure 1.1a), where the index 0 denotes the absence of oxygen.

Oxygen may quench the luminescence of the excited state L^* by collision with the luminophore which is called *dynamic quenching*:

$$L^* + O_2 \longrightarrow L + O_2^* \tag{1.6}$$

This way of radiationless relaxation reduces both the luminescence intensity I and lifetime Λ (figure 1.1b). The amount of quenching can be related to the Stern-Volmer equation

$$\frac{I_0}{I} = \frac{\Lambda_0}{\Lambda} = 1 + K'_{SV} \cdot c^M_{O_2} = 1 + k_q \cdot \Lambda_0 \cdot c^M_{O_2} \,, \tag{1.7}$$

where $K'_{SV} = k_q \cdot \Lambda_0$ is the Stern-Volmer constant, k_q the bimolecular quenching constant, and $c^M_{O_2}$ the oxygen concentration inside the sensing foil (^{M}). Since the equilibrium between sensing foil and ambient seawater is established via equal partial pressures pO_2 (see background below) and the O_2 solubility $\alpha^M_{O_2}$ inside the sensing foil generally is unknown, the latter can be included in $K_{SV} = K'_{SV} \cdot \alpha^M_{O_2}$ and equation 1.7 altered to

$$\frac{I_0}{I} = \frac{\Lambda_0}{\Lambda} = 1 + K_{SV} \cdot pO_2 = 1 + k_q \cdot \Lambda_0 \cdot \alpha^M_{O_2} \cdot pO_2 \,. \tag{1.8}$$

The bimolecular quenching constant k_q is proportional to the diffusivity of oxygen (Smoluchowski equation, see, e.g., Lakowicz, 2006, chap. 8), i.e., dynamic quenching is diffusion controlled.

Quenching does not consume any oxygen and optodes therefore do not need to be pumped to reach a stable (and correct) signal. A steady-state is reached if partial pressures are equal throughout the system. Molecular transport to reach that equilibrium requires some time and response times τ are typically longer than for electrochemical sensors (see, e.g., Linek et al., 2009).

Implementation

Luminescence intensity measurements are easily biased by changes in the excitation light source intensity, ambient scattering, and other matrix effects and thus, are prone to enhanced drift. Therefore, all optical oxygen sensors used in marine science measure the luminescence lifetime Λ rather than its intensity I, using a single-frequency phase shift technique.

Instead of using a short pulse, the excitation is intensity-modulated (figure 1.1c – h). The emission is modulated with the same frequency but, due to the finite lifetime Λ of the excited state, phase shifted relative to the excitation. For exponential luminescence decays, the lifetime Λ is proportional to the tangent of the phase shift φ with f being the modulation frequency (see equation 1.9, derivation given in Lakowicz (2006), chap. 5). The Stern-Volmer equation is therefore not valid for phase shifts φ but only for their tangent!

$$\tan\varphi = 2\pi \cdot f \cdot \Lambda \tag{1.9}$$

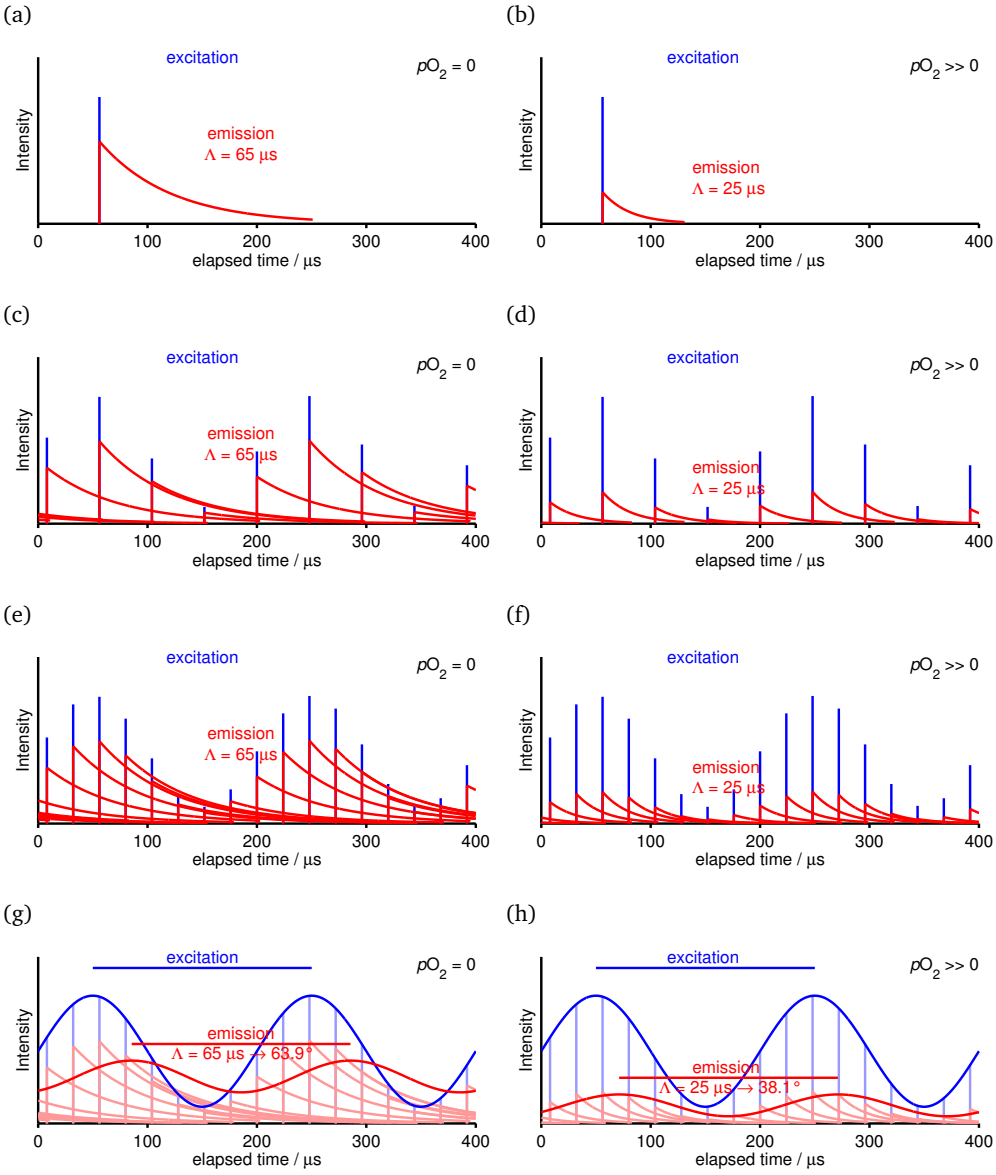

Figure 1.1: Illustration of luminescence decay, quenching, and phase shift lifetime measurement under absence of O_2 (left column) and presence of O_2 (right column), respectively. A single, short impulse excitation of the luminophore and its associated luminescence decay is shown in a & b. Addition of more and more, intensity-modulated excitation pulses (c & d, e & f) and superposition of the luminescence decays leads to an intensity-modulated and phase shifted emission in the continuous case (g & h). The phase shift φ depends on the lifetime Λ according to equation 1.9.

The luminophores are immobilized in a gas-permeable matrix or coated onto a solid support to avoid leaching. In the sensing foil of both Aanderaa optodes and Sea-Bird optodes (PSt3 membrane, PreSens, Regensburg, Germany), a luminescent platinum porphyrine complex is embedded into a silicone matrix. The optodes differ, however, in their modulation frequencies f (5000 Hz for Aanderaa and 3840 Hz for Sea-Bird), which does affect the measured phase shift but not the lifetime of the luminophore. Modulation frequencies f are chosen to match the lifetime Λ and give well-measureable phase shift φ (equation 1.9).

Because of the equilibration between sensing membrane and ambient liquid, oxygen optodes are pO_2 sensors by principle (see equation 1.21 below)!

While they do not consume oxygen, their transient time response is still flow-dependent since flow affects the molecular transfer in the vicinity the sensing membrane – water boundary.

The optical window of the Aanderaa optodes is freely accessible to the ambient medium, while it is contained inside a flow-through plenum for the Sea-Bird SBE63 optode (figure 1.2a and b, respectively). The former thus can be used unpumped causing application-dependent flow conditions while the latter is designed for a pumped mode of operation with well-defined flow.

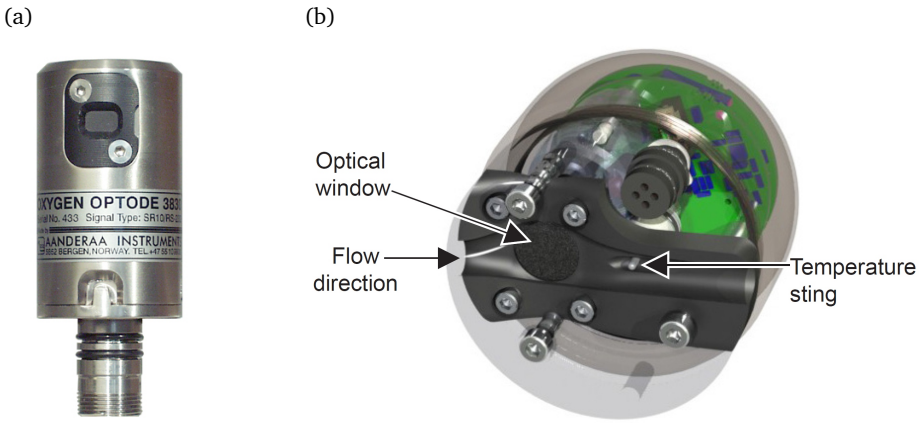

Figure 1.2: Position and accessibility of the optical window for (a) an Aanderaa optode (model 3830) and (b) a Sea-Bird SBE63 optode.

Issues

The sensor O_2 response generally deviates from the linear Stern-Volmer behaviour implied by equation 1.8 and shows a downward curvature (with increasing pO_2). In solution, however, the luminophore shows a linear Stern-Volmer plot (Huber, 2010). The reason is that in low-viscosity solutions, temporal fluctuations of the environmental influences are much faster than the timescale of luminescence and interactions with the environment and thus decay kinetics are uniform. This is different in condensed media such as the sensing foil and the kinetics get more complex (Draxler and Lippitsch, 1996). The observed downward curvature of Stern-Volmer plots is

mostly attributed to such heterogeneity of interactions, e.g., multiple sites or a continuous distribution (e.g., Demas et al., 1995; Hartmann et al., 1995). A two-site model is generally adequate to describe such non-linear Stern-Volmer behaviour,

$$\frac{I_0}{I} = \left(\frac{f_1}{1 + K_{SV1} \cdot pO_2} + \frac{1 - f_1}{1 + K_{SV2} \cdot pO_2} \right)^{-1} , \tag{1.10}$$

with f_1 being the intensity fraction of the first component under unquenched conditions (Carraway et al., 1991). However, a good fit of the model to data does not imply physical significance of the extracted parameters (James and Ware, 1985; Demas et al., 1995, 1999).

However, even the matrix itself may lead to quenching of the luminescence, yielding a non-exponential luminescence decay and explaining the non-linear Stern-Volmer behaviour with only a single O_2-quenching parameter (Draxler and Lippitsch, 1996).

Due to its non-linear behaviour, proper calibration of oxygen optodes both in oxygen and temperature is necessary but poses some challenge, which will be addressed in chapter 2. But also calibration functions used for marine sensors are an issue. Initially, high-order polynomials were used to relate the phase shift φ to the oxygen concentration. More recently, a Stern-Volmer inspired parametric approach has been established following

$$\frac{\varphi_0(T)}{\varphi} = 1 + K_{SV}(T) \cdot c_{O_2} . \tag{1.11}$$

This was suggested by Uchida et al. (2008) and is being used most frequently, either in its original form or with some modifications (Uchida et al., 2010; Bittig et al., 2012, see chapter 2, equations 2.6–2.9; Bittig, 2011, unpublished; Sea-Bird Electronics, 2012). However, these calculations apply the phase shift directly and have no physical justification (see equation 1.9 above).

Recently, McNeil and D'Asaro (2014) proposed another calibration equation "based on physical properties of the sensing foil", lending from the two-site model (Carraway et al., 1991) according to equation 1.10 by simply replacing intensities with lifetimes. However, equation 1.10 is based on the additivity of light intensities I_1 and I_2 of two luminophore sites according to

$$I = I_1 + I_2 = \frac{f_1 \cdot I_0}{1 + K_{SV1}} + \frac{f_2 \cdot I_0}{1 + K_{SV2}} \text{ and} \tag{1.12}$$

$$f_1 + f_2 = 1 , \tag{1.13}$$

whereas for a single frequency phase shift technique lifetimes Λ_1 and Λ_2 need to be weighted in a more complex way (Lakowicz, 2006, chap. 5):

$$\Lambda = \frac{\frac{\alpha_1 \cdot \Lambda_1^2}{1 + (2\pi \cdot f)^2 \cdot \Lambda_1^2} + \frac{\alpha_2 \cdot \Lambda_2^2}{1 + (2\pi \cdot f)^2 \cdot \Lambda_2^2}}{\frac{\alpha_1 \cdot \Lambda_1}{1 + (2\pi \cdot f)^2 \cdot \Lambda_1^2} + \frac{\alpha_2 \cdot \Lambda_2}{1 + (2\pi \cdot f)^2 \cdot \Lambda_2^2}} \quad \text{, with} \tag{1.14}$$

$$\alpha_i = f_i \quad \text{since } f_1 = \frac{\alpha_1 \cdot \Lambda_{0,1}}{\alpha_1 \cdot \Lambda_{0,1} + \alpha_2 \cdot \Lambda_{0,2}} \text{ and } \Lambda_{0,1} = \Lambda_{0,2} = \Lambda_0 . \tag{1.15}$$

The approach of McNeil and D'Asaro (2014) and the Uchida variants yield comparable misfits to calibration data in the order of 1 $\mu mol\,kg^{-1}$.

Another unresolved question is the reliable long term stability of optodes. During storage or transport, a drift of the optodes' response has been observed for most optodes (Bittig et al., 2012; D'Asaro and McNeil, 2013; Takeshita et al., 2013). This is in contrast to field data where they seem to be stable for years (e.g., Körtzinger et al., 2005; Hahn, 2013). The reason for these contrasting observations is yet unresolved. It may be linked to changes in the matrix or diffusion of the luminophore inside the matrix (and thus to temperature), or to the number of excited states & molecules generated and the energy deposition into the sensing foil (and thus to the number of measurement cycles).

A method to track optode long term stability is described in chapter 3, where in-air measurements are used to detect a sensor drift on Argo-O_2 floats.

Some concern exists to use optodes for profiling applications due to their long response times τ compared to electrochemical sensors. The time response of five commercial optodes, its dependence on temperature and flow, as well as its effect on data is dealt with in detail in chapter 4.

Finally, the hydrostatic pressure effect of optodes is relatively weakly characterized. Basically, there are two studies for Aanderaa optodes, one giving a linear pressure correction of +4.0 % / 1000 dbar (Tengberg et al., 2006) and the other giving a number of +3.2 % / 1000 dbar (Uchida et al., 2008). Temperature-controlled pressure vessel experiments have been performed with Aanderaa and Sea-Bird SBE63 optodes during this PhD project, however, results will be described in a later publication.

Background

(Photo-) Luminescence is the emission of light as a result of the absorption of photons and covers both fluorescence, i.e., spin-allowed singlet-singlet transitions with a typical lifetime of nanoseconds, and phosphorescence, i.e., spin-forbidden triplet-singlet transitions with typical lifetimes from milliseconds to hours. Lifetimes for the systems discussed here are between 20 µs and 70 µs and arise from a transition between a metal-ligand charge transfer excited state with triplet character ^{3}MLCT and the singlet ground state $^1S_0$ (Lakowicz, 2006; Okura and Kamachi, 2011).

A schematic of the energy diagram is shown in figure 1.3 (after Quaranta et al., 2012). It depicts fluorescence and phosphorescence of a luminophore as well as the quenching by molecular oxygen.

Absorption of blue or green light (in the case of the PreSens GmbH PSt3 membranes with a platinum porphyrine as luminophore) excites the luminophore from the singlet ground state $^1S_0$ to the excited singlet state ^{1}MLCT involving the promotion of an electron from a metal *d* orbit to a ligand π^* orbit in a metal-to-ligand charge transfer (MLCT) transition. With a vibrational energy level of the excited triplet state ^{3}MLCT close to the vibrational ground level of the excited singlet state ^{1}MLCT and enhanced by the heavy-atom effect of Pt ("spin-orbit coupling"), the system quickly undergoes intersystem crossing (ISC) to ^{3}MLCT. The state ^{3}MLCT

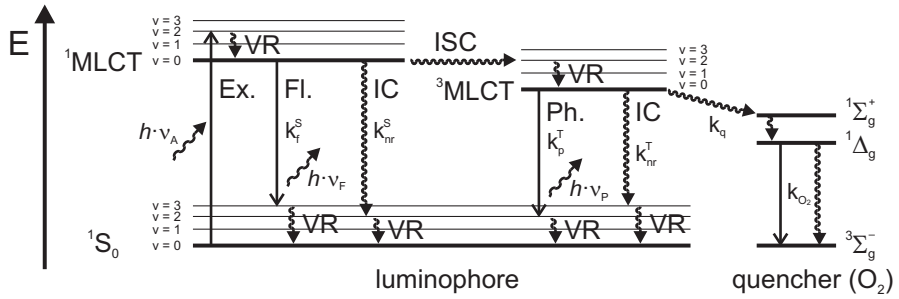

Figure 1.3: Energy diagram for a luminophore and O_2 as quencher with associated processes: Excitation (Ex.), fluorescence (Fl.), phosphorescence (Ph.), and collisional quenching by molecular O_2. Molecular term symbols are given for the O_2 triplet ground state ($^3\Sigma_g^-$) and the O_2 singlet excited states ($^1\Sigma_g^+$ with unpaired and $^1\Delta_g$ with paired electrons in the π^* orbit) (after Quaranta et al., 2012).

may be de-excited by phosphorescence or internal conversion (i.e., non-radiative). However, the transition ^{3}MLCT $\rightarrow$ $^1S_0$ is classically spin-forbidden (i.e., small rate constant, long lifetime) due to the change in spin multiplicity. However, spin-orbit coupling with the Pt somewhat enhances this process (Quaranta et al., 2012; Lakowicz, 2006, chap. 20).

If molecular oxygen interacts with the excited state (by collision), it may absorb the excess energy by exciting one of its own electrons to give singlet oxygen ($^1\Sigma_g^+$ and eventually $^1\Delta_g$), or by getting reduced to superoxide. Thus the luminescence intensity I and lifetime Λ of the excited state gets reduced (figure 1.1b) due to the *collisional* or *dynamic quenching*. In contrast, with *static quenching* the luminophore's excitation would be inhibited in the first place, e.g., by forming a non-luminescent complex.

Oxygen optodes rely on an equilibrium between their sensing membrane (^{M}) and the ambient liquid (^{L}). With multiple phases, equilibrium is determined by equal chemical potential μ, i.e., the chemical potential of oxygen inside the sensing foil $\mu_{O_2}^M$ must equal the chemical potential of oxygen in the ambient water $\mu_{O_2}^L$:

$$\mu_{O_2}^M \stackrel{!}{=} \mu_{O_2}^L \tag{1.16}$$

The chemical potential of oxygen μ_{O_2} (dissolved in a porous membrane or solution) is defined using the standard chemical potential $\mu_{O_2}^+$ and its activity a_{O_2} (equation 1.17, see, e.g., Wedler, 1985).

$$\mu_{O_2} = \mu_{O_2}^+(T,p) + \mathrm{R}\cdot T\cdot \ln\frac{a_{O_2}}{1\ \mathrm{mol\,L^{-1}}} \tag{1.17}$$

The standard chemical potential $\mu_{O_2}^+(T,p)$ refers to an imaginary state at temperature T and hydrostatic pressure p with dissolved oxygen being present as only, pure component and behaving as if infinitely diluted (e.g., being in the liquid state at room temperature). In addition, this standard state is also specific to the medium, i.e., $\mu_{O_2}^{+,M} \neq \mu_{O_2}^{+,L}$.

A simpler and more penetrable description is possible if all chemical potentials are referenced to a common standard chemical potential, that of the pure gas $\mu^{\circ}_{O_2}(T,p)$ with $f\,O_2$ being the fugacity.

$$\mu_{O_2} = \mu^{\circ}_{O_2}(T,p) + R{\cdot}T{\cdot}\ln\frac{f\,O_2}{1\ \text{bar}} \tag{1.18}$$

By addition of a gaseous phase in equilibrium (as a thought experiment) and using the definition of the Henry constant K_H / bar L mol^{-1},

$$K_H = \frac{f\,O_2}{a_{O_2}} = \frac{1}{\alpha_{O_2}}\ , \tag{1.19}$$

the standard chemical potentials can be easily converted:

$$\mu^{\circ}_{O_2}(T,p) = \mu^{+,M}_{O_2}(T,p) - R{\cdot}T{\cdot}\ln K^M_H = \mu^{+,L}_{O_2}(T,p) - R{\cdot}T{\cdot}\ln K^L_H \tag{1.20}$$

Thus, the equilibrium condition (equation 1.16) can be restated as

$$\mu^M_{O_2} = \mu^{\circ}_{O_2}(T,p) + R{\cdot}T{\cdot}\ln\frac{f^M}{1\ \text{bar}} \stackrel{!}{=} \mu^{\circ}_{O_2}(T,p) + R{\cdot}T{\cdot}\ln\frac{f^L}{1\ \text{bar}} = \mu^L_{O_2}\ . \tag{1.21}$$

There are alternative definitions with the standard chemical potential only depending on temperature and not on hydrostatic pressure, but this has unreasonable implications for the activity coefficient at high pressures (see Ludwig and Macdonald, 2005).

1.4 Measurement Platforms

Ship-based Observations

Traditionally, oceanographic observations are based on dedicated research ships and cruises. Such cruises cover a large area within a short time and that way provide a “quasi-synoptical” view of a region. One of the first examples is probably the R/V Meteor cruise 1925 – 1927, crossing the South Atlantic on 13 transects with a total of 310 stations (see figure 1.4, from Wattenberg, 1939).

Ship surveys are typically manned with a multidisciplinary team of scientists and other specially-trained personnel and yield highly-accurate, simultaneous measurements of a plethora of physical, chemical, and biological parameters. Various deployment modes with distinct spatial and temporal resolutions are possible – from underway measurements to hydrocast vertical profiles to anchored moorings, for which such ships are required for deployment and recovery. On the downside, such endeavours are quite expensive because of the costs for ship time, skilled labor, and equipment.

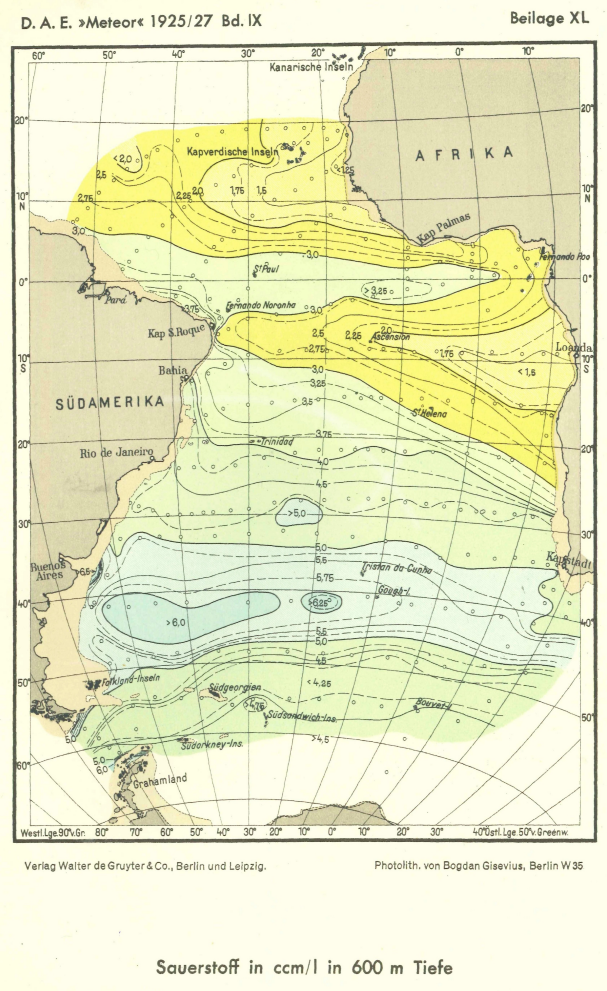

Figure 1.4: Dissolved oxygen distribution (in ml L^{-1}) at 600 m depth in the South Atlantic based on the R/V Meteor cruise 1925 – 1927 (from Wattenberg, 1939).

Autonomous Observations

More recently, autonomously operating instruments and vehicles became popular. These platforms are unmanned and equipped with multi-parameter sensors, follow a well-defined, automated measurement program, and may be (partially) remote controllable. However, such platforms do rely on accurate and reliable sensors.

A good example is the Argo-Program, initiated at the end of the '90s to measure temperature and salinity in the upper 2000 m of the oceans to determine heat and freshwater budgets (Argo Science Team, 1998; Gould et al., 2004). They are based on then-mature CTD probes and a float platform (Davis et al., 1992) as depicted in figure 1.5a.

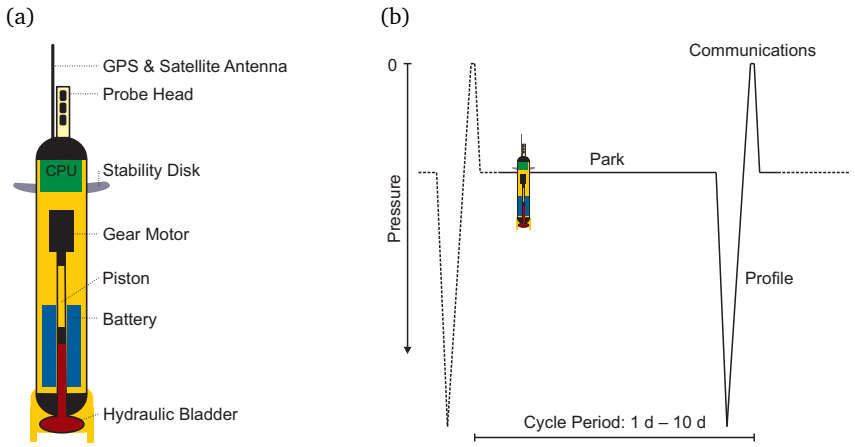

Figure 1.5: Schematic of an Argo float (a, after http://commons.wikimedia.org/wiki/File:BrnBld_ArgoFloat.svg) and the standard park & profile operation cycle (b).

The float is based on a buoyancy engine which allows for changing the outer volume of the instrument while keeping its mass and thus through generating positive or negative buoyancy to ascend or descend in the water column. For this, oil is pumped into the hydraulic bladder or back into the pressure housing's reservoir by a piston pump. A typical float cycle is shown in figure 1.5b: After a park period of typically ten days, the float descends to its maximum depth to initiate a measurement profile to the surface. At the surface, it transmits the data via satellite and may receive updated cycle parameters. The float then descends to its parking depth until the next cycle is initiated.

While the platforms themselve work autonomously until their battery capacity is exhausted, they do require additional, shore-based resources (e.g., data acquisition centers) and rely on satellite communication.

With currently about 3000 floats at a nominal spacing of $3^\circ \times 3^\circ$ between 60 S and 60 N, the Argo program became a global observation array with its data being freely available to the public and the scientific community. Still, re-seeding of new floats is necessary due to their finite lifetime of 4 – 5 years.

Other autonomous platforms are similar by concept, i.e., both ice-tethered profilers (ITPs) as well as gliders use a buoyancy engine, while they differ in their mobility. The former is moored, while the latter may navigate freely. Another class of autonomous observations are sea surface measurements by voluntary observing ships (VOS) or wavegliders, a mode of operation especially popular for near-surface work, e.g., dissolved gases.

Common to these observations is the need for accurate, stable, robust, and energy-efficient sensors. Without proper technology, a specific parameter can not be measured adequately. Recent advances made multidisciplinary multi-sensor deployments feasible, e.g., combining biogeochemical (oxygen, nitrate) and biooptical sensors (chlorophyll *a* fluorescence, CDOM fluorescence, particle backscatter, photosynthetic available radiation) on the same float, thus building a multidisciplinary research platform alike to ships.

While it took R/V Meteor more than two years to cover the South Atlantic (and about a decade to publish the data), a similar amount of data can be obtained today by Argo, Argo-O_2, and Bio-Argo floats in less than a month, albeit the floats' set of parameters is still more limited. However, the acquisition of more and more data means more and more data to be quality controlled, which is an increasingly demanding task.

2 Oxygen Optode Calibration and Stability Assessment

published as:
Bittig, H. C., Fiedler, B., Steinhoff, T., and Körtzinger, A. 2012. A novel electrochemical calibration setup for oxygen sensors and its use for the stability assessment of Aanderaa optodes. Limnol. Oceanogr.: Methods **10**: 921–933. [doi:10.4319/lom.2012.10.921].

Abstract

We present a laboratory calibration setup for the individual multi-point calibration of oxygen sensors. It is based on the electrochemical generation of oxygen in an electrolytic carrier solution. Under thorough control of the conditions, i. e. temperature, carrier solution flow rate, and electrolytic current, the amount of oxygen is strictly given by Faradays laws and can be controlled to within ±0.5 μmol L^{-1} (2 SD). While Winkler samples can be taken for referencing with a reproducibility between triplicates of 0.8 μmol L^{-1} (2 SD), the calibration setup can provide a Winkler-free way of referencing with an accuracy of ±1.2 μmol L^{-1} (2 SD). Thus calibrated oxygen optodes have been deployed in the Southern Ocean and the Eastern Tropical Atlantic both in profiling and underway mode and confirm the validity of the laboratory calibrations to within few μmol L^{-1}. In two cases, the optodes drifted between deployments which was easily identified using the calibration setup. The electrochemical calibration setup may thus facilitate accurate oxygen measurements on a large scale, and its small size makes it possible to configure as a mobile, sea-going, Winkler-free system for oxygen sensor calibrations.

Keywords: oxygen, optode, ocean observation, calibration, ocean deoxygenation

Acknowledgements

The authors want to thank the captains, crew and scientists of R/V Polarstern ANT-XXVII/1 and ANT-XXVII/2 as well as R/V Maria S. Merian MSM 18/3. Many thanks go to Carolina Dufour (LEGI/CNRS, Université de Grenoble, Grenoble/France) for her patience with and dedication to the Winkler samples of ANT-XXVII/2, Andreas Pinck (GEOMAR, Kiel/Germany) for the design of the improved current source, Martina Lohmann (GEOMAR, Kiel/Germany) for measuring the Winkler samples of MSM 18/3, Jostein Hovdenes (AADI, Bergen/Norway) for support with the optodes, Andreas Schmuhl and Detlef Foge (AMT GmbH, Rostock/Germany) for helpful advice on their O_2 generator, and Sebastian Fessler (GEOMAR, Kiel/Germany) for assistance in the early stages of the project. Financial support by the following projects is gratefully acknowledged: OCEANET of the WGL Leibniz Association, O2-Floats (KO 1717/3-1) and the SFB754 of the German Science Foundation (DFG), and the project SOPRAN (03F0611A and 03F0462A) of the German Research Ministry (BMBF).

2.1 Introduction

Dissolved oxygen for long has been and still is one of the most common and most widely measured parameters of oceanography. Its observation has an unmatched history of more than a century. Stressing this, the laboratory principle for discrete samples remained essentially unchanged since Winkler (1888) and still is, with some improvements, the method of choice for reference measurements (Dickson, 1994).

Besides, dissolved oxygen has been termed the "oceanographer's canary bird" as it is influenced by major biogeochemical and physical processes (primary production, remineralization, air-sea gas exchange, and water mass ventilation) and thus represents a most sensitive key parameter in marine global change research (Körtzinger et al., 2004; Keeling et al., 2010). In addition, the broad interest in dissolved oxygen measurements is illustrated by the plethora of its measurement platforms: long time series moorings (Karl and Lukas, 1996; Steinberg et al., 2001), repeat hydrography cruises (e. g. Stendardo et al., 2009) or underway measurements (Juranek et al., 2010), autonomous instruments (Körtzinger et al., 2005; Gruber et al., 2010), or during incubations and mesocosm studies (Robinson and Williams, 2005).

While there are sensors available to assist in such studies, they have to fulfill certain requirements of reliability, long-term stability, dynamic response, precision, and accuracy. Especially the latter is a critical issue. For example, the main uncertainty of a net community production estimate from in situ oxygen and nitrogen gas measurements stems from the oxygen sensor calibration (Emerson et al., 2008). Their estimate of a surface mixed layer biological oxygen production of 4.8 ± 2.7 mol m^{-2} yr^{-1} at the Hawaii Ocean time series station is prone to a ± 2.5 mol m^{-2} yr^{-1} uncertainty due to an 0.5 % (approx. 1.2 μmol L^{-1}) error in the dissolved oxygen data input.

For the application on Argo floats, an accuracy threshold of 5 μmol kg^{-1} has been defined for the data to be of useful quality to address scientific objectives, while the accuracy target for the desired data quality has been set to 1 μmol kg^{-1} (Gruber et al., 2010).

On the other hand, long-term stability of different sensor designs remains a critical issue. For optical oxygen sensors such as the Aanderaa optode, there is no evidence of drift during a deployment period (Tengberg et al., 2006). Between deployments, however, there are several observations that processes yet unidentified lead to a change in the sensor response, e. g. between factory calibration and in situ data (Takeshita et al., 2010; Neill, 2011, pers. comm.; this study). While this is more a sensor issue, a dedicated calibration facility could improve the data quality through regular and accurate recalibrations. This emphasizes the need for a simple calibration setup.

The most common calibration approach is an in situ calibration against Winkler samples of a colocated CTD cast. This can be done with high accuracy (Uchida et al., 2008), but is tedious for a larger number of sensors and logistically not always feasible. The main disadvantage is, that the reference points for calibration are limited to the set of field conditions (oxygen content and temperature) encountered during the sampling time. Furthermore, they are superimposed by additional ambient effects like a pressure dependence. All data outside the parameter range provided by the field conditions during calibration are accessible only through extrapolation and thus less reliable. This is less of an issue for ship cruises with reference measurements throughout the entire cruise. It becomes more important for moored deployments with calibration opportunities typically only at the beginning and at the end of the deployment periods, or even worse for Argo-O_2 floats with a single deployment profile only.

The less popular approach is a multi-point laboratory calibration in which a set of reference points under controlled conditions are used for calibration. These should be so widely distributed as to cover all expected field conditions and the field measurements are essentially interpolations between these reference points, which gives more confidence with regard to data quality. In order to adjust the temperature and the oxygen content, these variables have to be forced in a controlled manner. The former can be done by submerging the sensors in a thoroughly mixed, thermostated bath, while the latter can be accomplished by usage of gas cylinders of N_2 and O_2/N_2 mixtures and bubbling stones, which is done in all such setups known to the authors. As reference for the absolute oxygen content, Winkler samples or previously Winkler-calibrated sensors are used. This is crucial because a complete equilibration with the gas mixture requires both extended equilibration times and constant ambient pressure. Accuracies as high as 0.5 μmol L^{-1} can be achieved by such calibration setups (Neill, 2011, pers. comm.). Here we present a different way to force the oxygen content by using electrochemistry instead of gas mixtures. This reduces the size of the setup significantly and enhances both the portability and ease of use.

The electrochemical approach is based on the electrolysis of aqueous solutions, where at the anode molecular oxygen is produced (equation 2.1).

$$\text{Anode} \qquad \overset{\pm 0}{\mathrm{O_2}} + 2\,\mathrm{H_2O} + 4\,e^- \rightleftharpoons 4\,\overset{-\mathrm{II}}{\mathrm{OH^-}} \qquad E_0 = +0.401\,\mathrm{V} \tag{2.1}$$

$$\text{Cathode} \qquad 2\,\overset{+\mathrm{I}}{\mathrm{H_2O}} + 2\,e^- \rightleftharpoons \overset{\pm 0}{\mathrm{H_2}} + 2\,\mathrm{OH^-} \qquad E_0 = -0.828\,\mathrm{V} \tag{2.2}$$

If the flow rate (V/t) through the electrolytic cell and the electrolytic current (Q/t) is set, the oxygen concentration of the electrolytic carrier solution is strictly given by Faradays laws (equation 2.3, 2.4), where n is the number of moles, z the number of electrons transferred, F the Faraday constant (96485 C mol^{-1}), I the electrolytic current, t the time, and c the volumetric concentration, respectively.

$$n \cdot z \cdot \mathrm{F} = I \cdot t \tag{2.3}$$

$$\rightarrow \qquad c = \frac{n}{V} = \frac{1}{z \cdot \mathrm{F}} \cdot \frac{I}{\frac{V}{t}} \tag{2.4}$$

$$c \,/\, \mu\mathrm{mol\ L^{-1}} = 155.5 \cdot \frac{I \,/\, \mathrm{mA}}{\frac{V}{t} \,/\, \mathrm{mL\ min^{-1}}}$$

For repeatability, the carrier solution has to be degassed, i. e. stripped of oxygen, before the electrolysis to ensure a common background between different runs. Thus, the carrier solution obtaines a defined concentration of dissolved oxygen that can be used in a flow system-based calibration setup.

2.2 Materials and Procedures

Materials

The calibration setup is based on the degassing of an electrolyte or carrier solution and the subsequent electrochemical in situ production of dissolved oxygen. That solution is then adjusted in temperature and passed to the sensors for calibration.

The setup, shown schematically in figure 2.1, is designed as a flow system with an electrochemical oxygen generator (G200, AMT Analysenmesstechnik GmbH, Rostock/Germany) as the central element. A flow meter, a cryostat, a section to tap Winkler samples and a pressure gauge were added as auxiliaries.

From the reservoir, the carrier solution, a 0.02 M sodium hydroxide solution, is transported through the flow system by means of a peristaltic pump (ISM829 Reglo Analog, Ismatec, Glattbrugg/Switzerland) provided by AMT. Downstream, the AMT generator contains a built-in degassing unit for the carrier solution and an electrolytic cell. Two separate circuits are used for the cathodic and anodic side. The degassing is based on maintaining a vacuum outside gas-permeable tubing through which the anodic carrier solution is passed and thus stripped of all dissolved gases. To ensure a stable electrolysis, the flow rate through the anode is controlled and the pump regulated by a high precision flow meter (miniCori-Flow M13, Bronkhorst Mättig GmbH, Kamen/Germany), installed between the pump and the generator. Moreover, triplicate Winkler samples can be taken as references between the generator and custom-made flow-through cells for the oxygen sensors. Several flow-through cells and sensors can be assembled in a row and calibrated simultaneously.

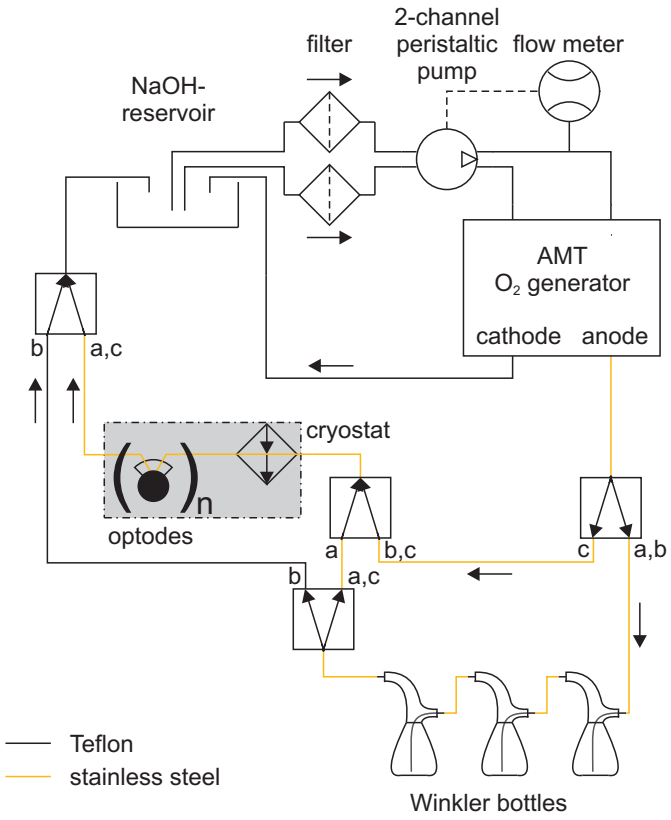

Figure 2.1: Schematic of the calibration setup. The dash-dot encircled shaded grey area indicates the thermostated bath.

They are completely submerged in a thermostated bath, in which the carrier solution has been brought to the same temperature. All the other parts of the system, including the generator itself, the carrier solution reservoir and the Winkler bottles, are at room temperature. The tubing for the carrier solution downstream of the electrolytic cell is made of stainless steel, to exclude any air contamination. Valves can be used to bypass the oxygen sensors (option b in figure 2.1) or the Winkler bottles (option c in figure 2.1), respectively. A pressure sensor was added at the generator's degassing unit, to monitor the residual vacuum pressure.

The flow rate through the generator is restricted to 10 mL min^{-1} – 12 mL min^{-1}, to maintain both a homogeneous solution and complete dissolution of oxygen at the electrode. With an electrolysis current of 0 mA to 20 mA, oxygen concentrations between 0 µmol L^{-1} and 311 µmol L^{-1} (120 % oxygen saturation at 25 °C) can be achieved without limitations on distinct saturation levels. The temperature can be chosen freely within 1 °C – 36 °C.

Procedures

A typical parameter set at constant generator settings (16 mA) is shown in figure 2.2. The strong dependence of the optodes phase signal on temperature is clearly visible. All oxygen data are based on these two raw parameters and depend both on an adequate functional model of sensor response and an adequate set of calibration coefficients (see figure 2.3).

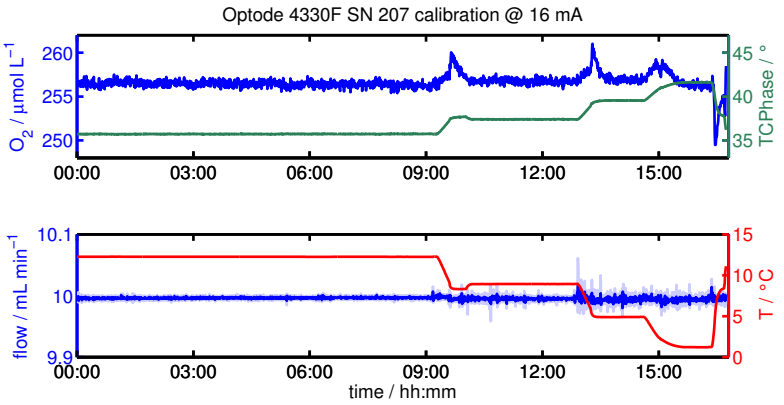

Figure 2.2: Plot of optode and calibration setup parameters at constant generator settings and different thermostated bath temperatures. Upper panel: Oxygen concentration and optode phase signal. Lower panel: Carrier solution flow rate and temperature.

For an eligible calibration reading, an arbitrary stability criterion of the drift in the oxygen concentration, smaller than 0.02 µmol L^{-1} min^{-1} over a period of 15 min, has to be fulfilled. Under these conditions, only negligible gradients exist between generator exit, Winkler bottles and sensor flow-through cells.

Standard procedures for Winkler samples require the bottles to be overflown by three times their volume before fixation (Dickson, 1994). However, this is not

feasible in a flow system with only 10 mL min^{-1} flow rate. Consequently, it has been adopted by flushing the bottles from bottom to top within the closed system using glass-made flow caps for the Winkler bottles (see schematic in figure 2.1). At sampling after the stability criterion has been reached, the solution in the bottle neck possibly contaminated by atmospheric oxygen is then replaced by the solution from the Winkler flow cap above and thus contamination is minimized. At analysis, the pickled sample is acidified by twice the amount of sulphuric acid to account for the high pH of the carrier solution. If Winkler samples are taken at each calibration point, about 3 to 4 points can be done per working day.

The obtained data of temperature, sensor phase and Winkler oxygen can then be fitted to any desired model of sensor oxygen response, an example of the Aanderaa optode oxygen response shown in figure 2.3. It is based on the Uchida et al. (2008) model. Unlike the original publication, the oxygen concentration is not used directly but is converted to partial pressure pO_2 and then used as fit parameter in the model.

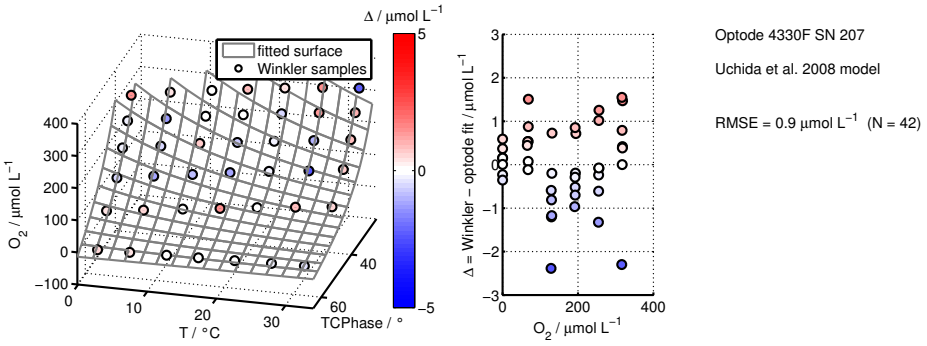

Figure 2.3: Calibration response of an Aanderaa optode. The oxygen concentration is plotted against temperature and phase as independent variables (left panel). The Uchida calibration model fits the sensor's functional behaviour by a Stern-Volmer-inspired, non-linear approach. The colour code and the middle panel give the absolute difference Δ between Winkler samples and fitted surface. Statistical figures for the model are also given in the right panel.

The functional model (equation 2.6) is inspired by the Stern-Volmer equation (equation 2.5) substituting the lifetimes Λ in the presence of oxygen and Λ_0 in the absence of oxygen with the phase signals φ and φ_0, respectively. Additional polynomials are introduced to account for the temperature dependence of the Stern Volmer constant K_{SV} and zero phase signal (equations 2.7 and 2.8) as well as to scale the phase signal again (equation 2.9).

$$\frac{\Lambda_0}{\Lambda} = 1 + K_{SV} \cdot c_{O_2} \tag{2.5}$$

$$\frac{\varphi_0}{\varphi'} = 1 + K_{SV} \cdot pO_2 \tag{2.6}$$

$$K_{SV} = c_0 + c_1 \cdot T + c_2 \cdot T^2 \tag{2.7}$$

$$\varphi_0 = c_3 + c_4 \cdot T \tag{2.8}$$

$$\varphi' = c_5 + c_6 \cdot \varphi \tag{2.9}$$

$$pO_2 = \frac{c_{O_2}}{\alpha_{O_2}} \tag{2.10}$$

Strictly, the Stern-Volmer equation is derived from molecular quenching kinetics that require the O_2 concentration inside the sensor membrane to be used (equation 2.5). Due to different solubilities, however, this is not the concentration of the ambient medium, i. e. sea water. Instead, the equilibrium between sensor membrane and environment is characterized by equal partial pressures pO_2, which is used for all calculations (equation 2.6).

The sensor membrane oxygen solubility as proportionality factor between partial pressure and concentration is thus included in the Stern Volmer constant K_{SV} by this approach. On the other hand, the Henry's law solubility constant α_{O_2} / µmol L^{-1} Pa^{-1} is used to convert the ambient sea water concentration to partial pressure (equation 2.10). The non-linear response of the optode is clearly visible from the obtained data (figure 2.3).

The 0.02 M NaOH carrier solution may be considered as being nearly freshwater. For highest accuracy, a salinity correction should be applied to the partial pressure calculation, as saturation levels are affected by ionic interactions with the medium. However, sea water solubility (Garcia and Gordon, 1992) is not per se applicable to a 0.02 M NaOH carrier solution with considerable different chemical composition. Oxygen solubility in different salt solutions was analyzed by Clegg and Brimblecombe (1990). Their parametrization gives a salinity correction factor for 0.02 M NaOH of 0.99158(6) between 1 °C and 36 °C, by which the (freshwater) solubility α_{O_2} in equation 2.10 should be scaled. The factor relates to an effective sea water salinity of 1.25 psu − 1.60 psu.

2.3 Performance Assessment

Laboratory Evaluation

The resolutions of the environmental variables, i. e. temperature, carrier solution flow rate, and electrolytic current, are 0.01 °C, 0.001 mL min^{-1}, and 0.001 mA, respectively. They can be constrained (2 SD) to within 0.007 °C, 0.01 mL min^{-1} and 0.01 mA, respectively, and the stability of the system is illustrated in figure 2.4. The variability in the environmental variables amounts to a theoretical uncertainty in the O_2 concentration of ±0.5 µmol L^{-1} (2 SD). This is confirmed by the oxygen

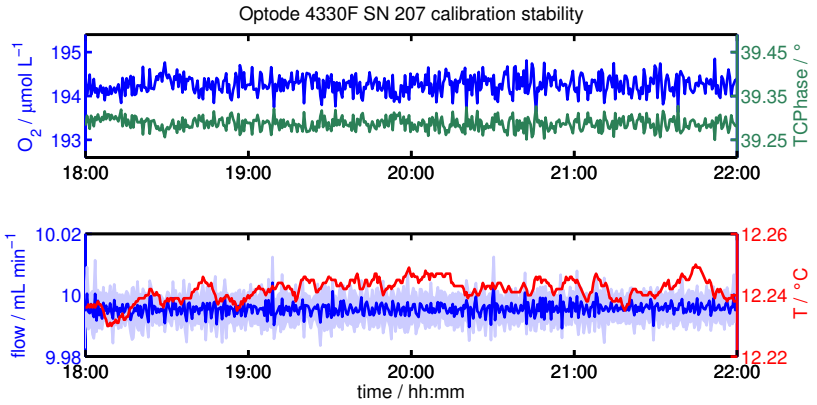

Figure 2.4: Sample plot of a stable state of the calibration system. Upper panel: Oxygen concentration and phase signal as sensor data. Lower panel: Carrier solution flow rate and temperature as environmental conditions. Dark blue shows the flow rate averaged over the optode's sampling interval (30 s), while light blue includes the flow rate standard deviation within that interval.

concentration observed by the sensors, which is stable to within the same range and mainly affected by fluctuations in the flow rate with a time lag of approx. 15 min.

The generator may be used to generate different oxygen concentrations only, while the Winkler samples provide absolute numbers for the sensor calibration. However, the comparison of the Winkler samples with the theoretical value from the generator settings (equation 2.4) indicates an alternative way of referencing.

The best fit between Winkler samples and generator settings is illustrated in figure 2.5. It can be seen that the slope is close enough to 1 to take 100 % electrolysis efficiency as granted. In addition, their difference is shown in figure 2.6. This directly gives the accuracy and precision of the calibration setup without Winkler referencing, +4.7 µmol L^{-1} and ±1.2 µmol L^{-1}, respectively. At the same time, the offset observed is independent of the oxygen concentration and the temperature.

Assuming an incomplete degassing step, which is independent of the electrolytic current or thermostated bath temperature, the background for the electrolytic oxygen addition would increase uniformly. Therefore, a pressure sensor was installed temporarily at the degassing unit and a total residual pressure of 25 ± 2 mbar was observed. Starting from first principles, i. e. equilibrium with the atmosphere and the O_2 mole fraction in air, the degassing pressure equals a residual oxygen concentration of 6.6 ± 0.5 µmol L^{-1}. Without the pressure sensor installed there is a reduced number of possible leaks. In consequence, the degassing pressure is presumable slightly lower and the 6.6 µmol L^{-1} should be considered as an upper bound for the first principles approach to explain the offset. The accuracy of the calibration setup without Winkler referencing is thus characterized by the repeatability of the degassing step and the level to which the residual oxygen content can be constrained.

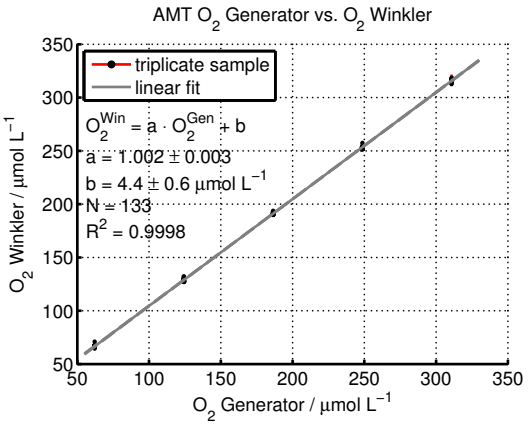

Figure 2.5: Nominal generator oxygen concentration after eq. 2.4 vs. triplicate Winkler samples with standard deviation of the triplicates as red bars. The linear least-squares fit is indicated in grey.

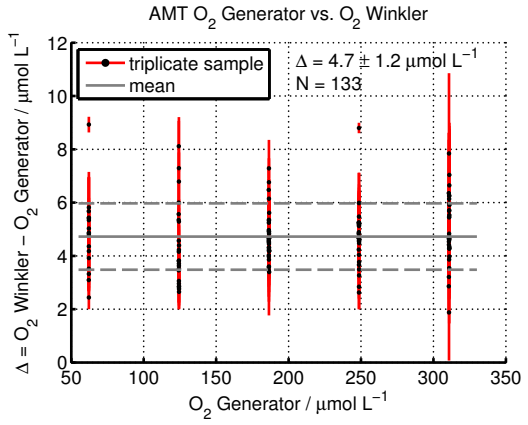

Figure 2.6: Difference between triplicate Winkler samples and nominal generator oxygen concentration after eq. 2.4 vs. oxygen concentration. The mean of the residual Δ is marked in grey and the standard deviation of the triplicates is indicated as red bars.

Field Evaluation

(a) R/V Polarstern cruise ANT-XXVII/1 (b) R/V Polarstern cruise ANT-XXVII/2

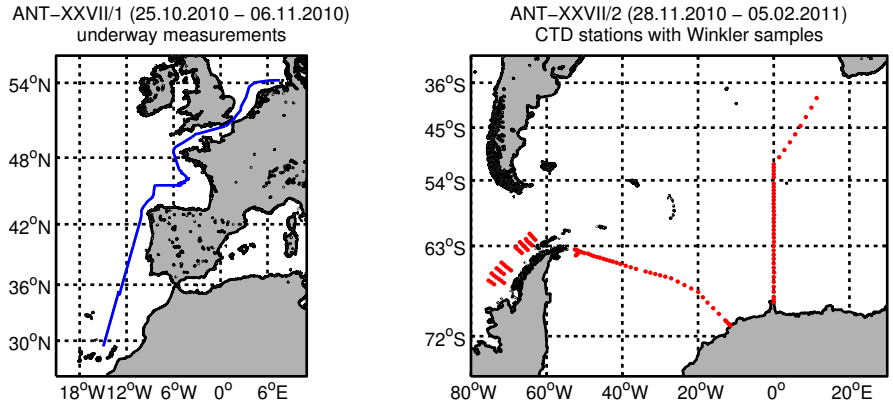

(c) R/V Maria S. Merian cruise MSM 18/3

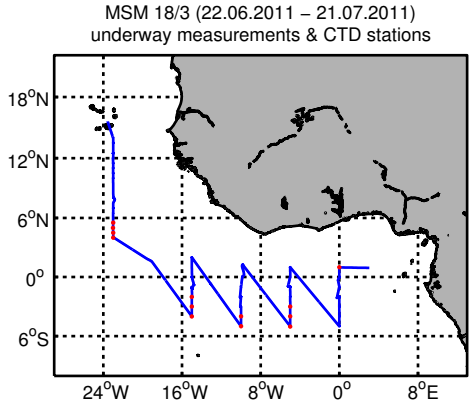

Figure 2.7: Cruise plots of all cruises used for the field evaluation. Underway measurements are marked in blue and positions of CTD stations with Winkler bottle data are denoted as red dots.

The calibration setup was assessed indirectly by the performance of oxygen optodes during the course of different field deployments. A first set of optodes was deployed in underway mode between Bremerhaven and Las Palmas and attached to the CTD in the Southern Ocean (locations given in figure 2.7a and b), while a second set of optodes was used in the Eastern Tropical Atlantic both in underway and CTD mode (figure 2.7c). In all cases, an individual multi-point calibration was performed before and after the cruises using the laboratory setup. Besides, sodium sulfite was used for the calibration of the zero oxygen level. The field data are based on Winkler bottle data sampled and analyzed according to standard procedures (Dickson, 1994). While there is practically no published evidence of drift of optical sensors during deployments (Tengberg et al., 2006), the stability between deployments or between calibration and deployment is not granted (Takeshita et al., 2010; Neill, 2011, pers. comm.; this study), for which the pre- and post-cruise laboratory calibrations should give sufficient indication.

At this point, a clear distinction must be done regarding accuracy statements for the oxygen sensors and the calibration setup. Any field evaluation relies on an adequate functional model of the sensor's oxygen response, e. g. the Uchida et al. (2008) model. Consequently, all field samples are compared to the combined performance of the calibration reference points and the functional model (e. g. figure 2.3).

Essentially, all sensor data depend on the proper conversion of the engineering raw data, i. e. phase shift and temperature, to the variables of interest, i. e. oxygen concentration. If the sensor data are excellent but the functional model or calibration parameters do not grasp the sensor's behaviour, the derived data will be inaccurate. The same is true for the reverse extreme with an excellent functional model but blurred reference or raw data. Both effects are hard to distinguish and commonly merged under the term "sensor accuracy". On the other hand, the accuracy of the calibration setup itself, i. e. the quality of the calibration reference points, is independent of the sensor and thus independent of the sensor's functional model.

Thus, when using the setup to generate different conditions only, its accuracy is essentially the Winkler accuracy (0.8 μmol L^{-1} from triplicate Winkler samples (2 SD)), while for the Winkler-free mode of operation, the accuracy is represented by the degree to which the incomplete degassing of the carrier solution can be characterized, i. e. $\pm$1.2 μmol L^{-1} from comparison to 133 triplicate Winkler samples.

Still, any field application of (calibrated) oxygen sensors relies on the combination of both the calibration reference points and the functional model. The mean difference between sensor and Winkler reference data and its standard deviation gives a clear indication of their combined performance in the field and the sensor accuracy of interest. On the other hand, the root-mean-square error (RMSE) between laboratory Winkler samples and sensor data can be interpreted as the misfit between calibration reference points and sensor functional model, i. e. the accuracy of the laboratory calibration. The RMSE lies in the range of 0.9 μmol L^{-1} to 1.9 μmol L^{-1} for the optode calibrations discussed in the following paragraphs.

The first set of field data was obtained on R/V Polarstern during the cruises ANT-XXVII/1 and ANT-XXVII/2. Two Aanderaa oxygen optodes, a standard model 3830 and a fast response model 4330F, were calibrated before the cruises in October 2010 and recalibrated afterwards in July 2011. Whereas the initial calibration consisted of 29 points between 50 μmol L^{-1} and 315 μmol L^{-1} and between 1 °C and 18 °C, respectively, the post-cruise calibration was more extensive and contained 42 points between 0 μmol L^{-1} and 315 μmol L^{-1} and between 2 °C and 32 °C, respectively.

The comparison of both sets of laboratory data for both optodes is shown in figure 2.8a and 2.8b. The left panels show the shape of the fitted optode response function (Uchida et al., 2008) in grey and the 29 individual points (black circle) on which the initial calibration is based. The 42 points of the post-cruise calibration are distinguished on wether they fall within the calibrated range (yellow circle) or lie outside the initial calibration (purple circle). The statistics in the right panels are given for the points inside the calibrated range only. The colour shading and the middle panels show the difference between initial calibration and Winkler data of the post-cruise calibration.

(a) Optode 3830 SN 529

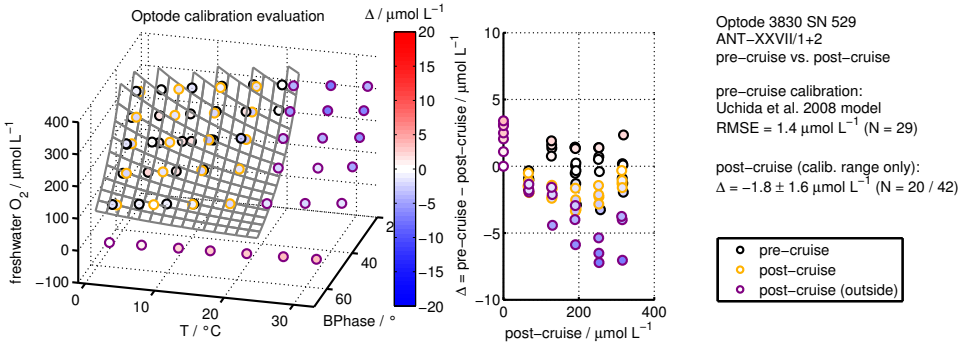

(b) Optode 4330F SN 207

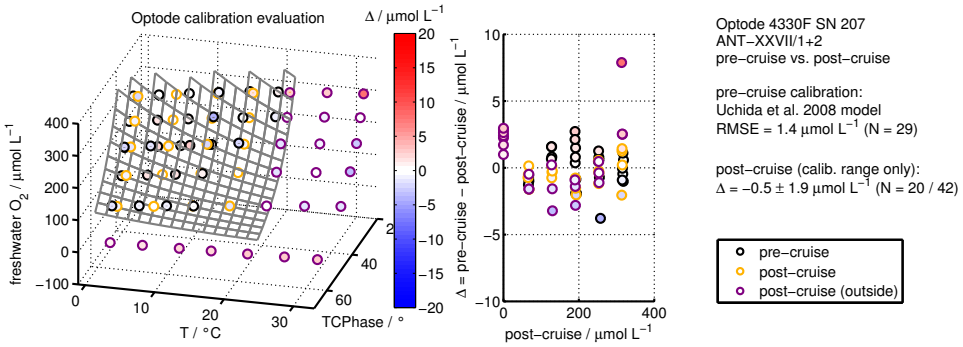

Figure 2.8: Repeated calibration of optodes before and after the R/V Polarstern cruises ANT-XXVII/1 and ANT-XXVII/2. Left panel: Initial calibration points (black circle) and fitted optode response function (grey) with repeated calibration samples inside (yellow circle) and outside (purple circle) the calibrated range. Middle panel: Difference between pre-cruise calibrated optode reading and post-cruise Winkler samples. The colour axis shows the same difference in both panels. Right panel: Statistical figures for both the initial and repeated calibration with 95 % confidence interval.

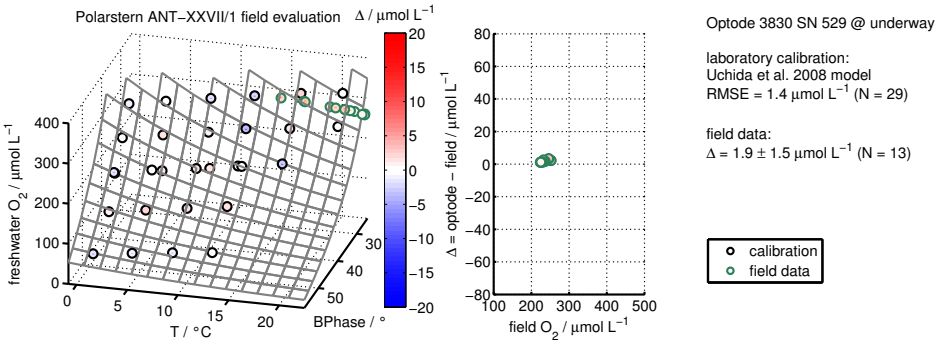

Figure 2.9: Underway field evaluation of optode 3830 SN 529 during cruise ANT-XXVII/1. Left panel: Calibration points (black) and optode response as function of phase and temperature (grey) with field samples (green) mapped into the same, freshwater sample space of the calibration. Middle panel: Difference between optode reading and Winkler field samples. The colour axis shows the same difference in both panels. Right panel: Statistical figures for both the calibration and the field samples.

Good agreement was obtained between both data sets: The offset was found to be at the edge of the 95 % confidence interval (2 SD) for the 3830 optode or non-distinguishable for the 4330F optode, respectively. At the same time, it is obvious that the calibration becomes mediocre if predictions are made outside its range (e. g. between 20 °C – 32 °C), even if it may perform well in distinct regions of the sample space (e. g. 50 µmol L^{-1} – 200 µmol L^{-1}).

The first deployment was made in underway mode directly after the initial calibration between 25. October 2010 and 6. November 2010 on R/V Polarstern (ANT-XXVII/1). Only the 3830 model was used and 13 Winkler samples were taken between Bremerhaven and Las Palmas. Their results are shown in figure 2.9. The left panel gives the initial calibration (grey) with the 29 individual points (black circle) on which it is based. The underway Winkler samples are denoted by green circles and the difference between calibrated optode reading and field Winkler samples is given both as colour shading and in the middle panel. The optode's initial calibration is found to be at slightly higher oxygen concentrations than the Winkler samples. However, the offset of 1.9 ± 1.5 µmol L^{-1} is at the edge of significance and the laboratory calibration matches well to the field data.

A second, far more extensive evaluation was performed during the following cruise leg (R/V Polarstern, ANT-XXVII/2, 25. November 2010 – 5. February 2011, see figure 2.7b) with the sensors attached to the CTD. The CTD was stopped at each bottle stop such that the sensor readings of temperature and salinity but not of oxygen were allowed to settle, before the Niskin bottle was closed. Following this procedure, a total of 2296 Winkler samples were taken at 122 stations and the results are shown in figure 2.10 for both sensors.

Again, the colour shading gives the difference between the initial laboratory calibration and the Winkler field data. In contrast to previous figures, a distinction

(a) Optode 3830 SN 529

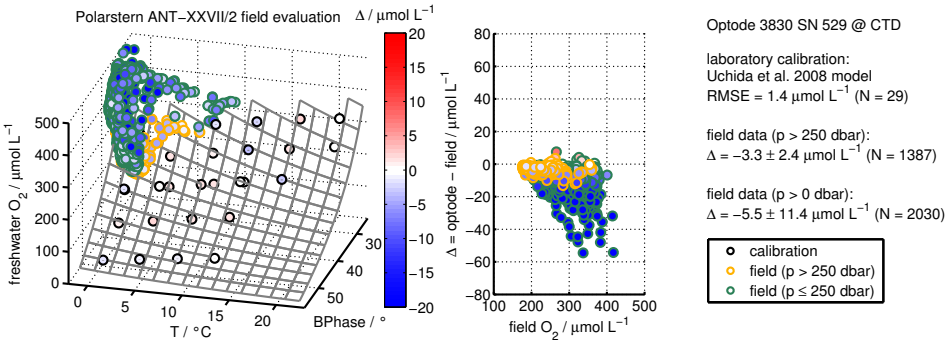

(b) Optode 4330F SN 207

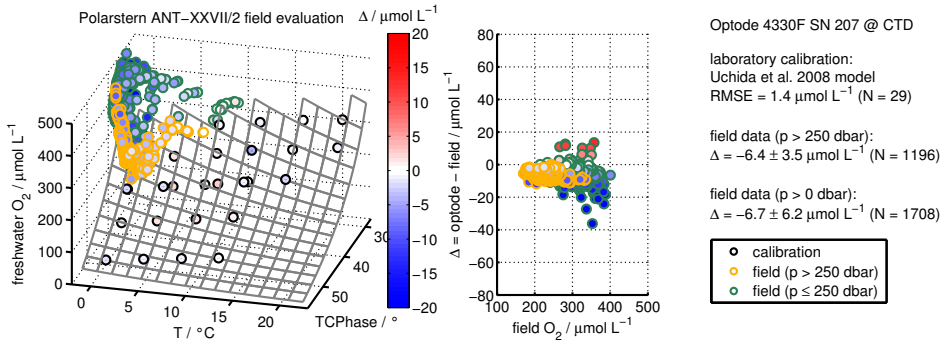

Figure 2.10: CTD field evaluation during cruise ANT-XXVII/2. Left panel: Calibration points (black) and optode response as function of phase and temperature (grey) with field samples below the thermocline (yellow) and above the thermocline (green) mapped into the same freshwater sample space of the calibration. Middle panel: Difference between optode calibration and Winkler field samples for samples below the thermocline (yellow) and above the thermocline (green). The colour axis shows the same difference in both panels. Right panel: Statistical figures for both the calibration and the field samples.

is made between surface samples above and close to the thermocline ($p \leq 250$ dbar), marked with green circles, and samples below the thermocline ($p > 250$ dbar), marked with yellow circles.

The data obtained fall within a very narrow temperature range ($0.5 \pm 3.0\,^{\circ}C$ for all Winkler samples), so that the temperature slope of the calibration can not be validated by this data set. On the other hand, the maximum oxygen concentration during the laboratory calibration is limited by the maximum electrolysis current allowed by the generator. The issue becomes evident in the left panels of figure 2.10, where most deep samples are just at the edge of the calibrated range, while most surface samples are beyond. However, considering their location close to the limits of the calibrated range or slightly beyond, the initial calibration appears to be well suited for the field samples, as the offset Δ between sensor data and Winkler samples is only slightly exceeding its confidence limit (2 SD) and, more importantly, there is no trend in the calibration bias visible (middle panel).

Due to issues with the dynamic response of the optodes, as well as increased variability, the scatter is enhanced in the surface region. Moreover, a pronounced response time effect is observed for the 3830 model with an approx. threefold response time compared to the 4330F model. Because the bottle stops are made during the upcast, the sensors lag behind the rising oxygen concentration towards the surface, which leads to a dynamically induced underestimation by the optodes, compared to the Winkler samples. This is clearly visible for the 3830 model as a negative bias in the green-circled samples in figure 2.10a, middle panel, and less of an issue for the fast response model 4330F (figure 2.10b). The latter is confirmed by the same offset Δ for the 4330F sensor for both the deep samples and all samples, including the surface gradient region, indicative of a fast enough sensor for that region.

A second set of field data was acquired on the R/V Maria S. Merian cruise MSM 18/3 (21. June 2011 – 21. July 2011) to the Eastern Tropical Atlantic. Two Aanderaa optodes, both a standard model 4330, were calibrated before the cruise in April 2011 and recalibrated afterwards in December 2011. One was used for underway measurements while the other was attached to the CTD.

The initial calibration consisted of an extensive, 42 point calibration between 0 μmol L^{-1} and 315 μmol L^{-1} and 2 °C and 32 °C, respectively. In contrast, the post-cruise calibration was done with an improved setup as described in the last section, which features a electrolytic current source of up to 30 mA, and is thus capable of generating oxygen levels above 315 μmol L^{-1}. It consists of 42 points ranging from 0 % to 130 % oxygen saturation and 2 °C to 32 °C, respectively.

As illustrated in figure 2.11, there is a clear drift of the sensor's response between pre-cruise and post-cruise calibration. While the pre-cruise calibration RMSE is as low as 1.9 μmol L^{-1}, the observed difference between pre-cruise calibrated sensor readings and post-cruise calibration Winkler samples may be an order of magnitude higher. Moreover, both sensors possess a common deployment history (newly purchased and exposed to 2000 dbar several times) and show a comparable drift with a significant change in the sensor response. A similar drift behaviour has been observed for other optodes (Neill, 2011, pers. comm.). Because the match between

(a) Optode 4330 SN 563

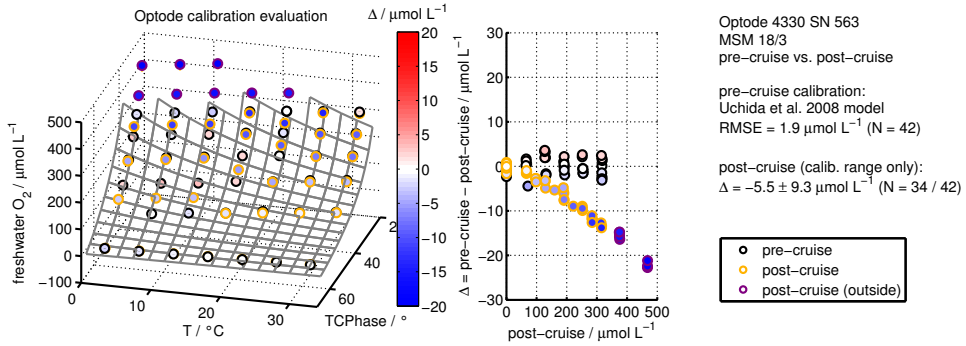

(b) Optode 4330 SN 564

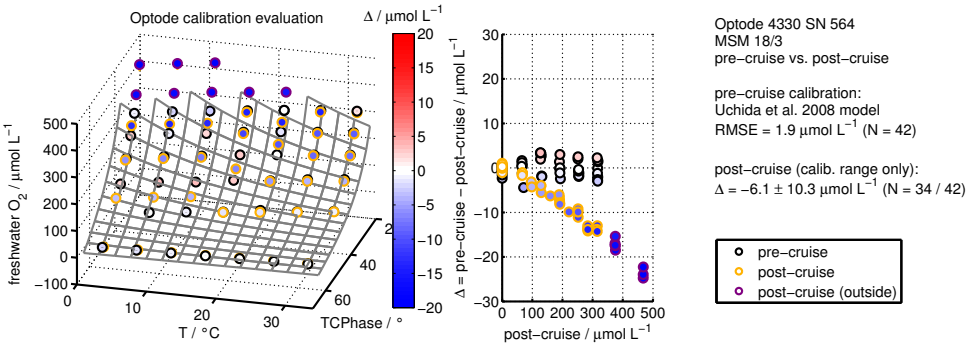

Figure 2.11: Repeated calibration of optodes before and after the R/V Maria S. Merian cruise MSM 18/3. Left panel: Initial calibration points (black circle) and fitted optode response function (grey) with repeated calibration samples inside (yellow circle) and outside (purple circle) the calibrated range. Middle panel: Difference between pre-cruise calibrated optode reading and post-cruise Winkler samples. The colour axis shows the same difference in both panels. Right panel: Statistical figures for both the initial and repeated calibration with 95 % confidence interval.

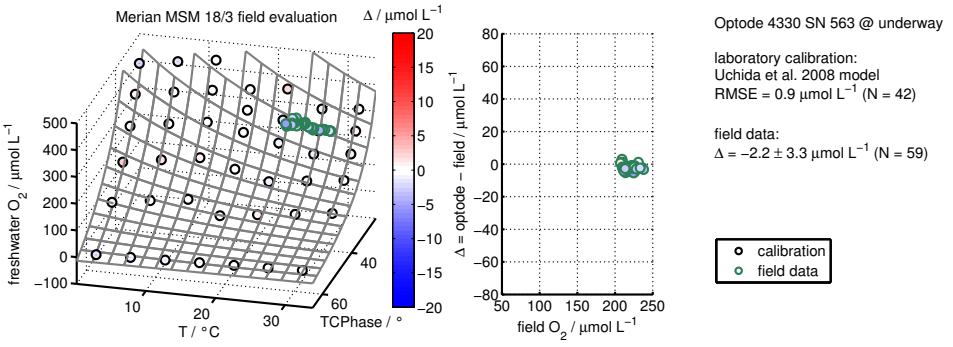

Figure 2.12: Underway field evaluation of optode 4330 SN 563 during cruise MSM 18/3 with post-cruise calibration. Left panel: Calibration points (black) and optode response as function of phase and temperature (grey) with field samples (green) mapped into the same, freshwater sample space of the calibration. Middle panel: Difference between optode calibration and Winkler field samples. The colour axis shows the same difference in both panels. Right panel: Statistical figures for both the calibration and the field samples.

field data and sensor data is better using the post-cruise calibration (not shown), the latter is chosen for the field evaluation of the calibration setup to decouple it from the unresolved sensor drift issue.

The optode in underway mode was evaluated against 59 Winkler samples during 26 days of continuous measurements (see figure 2.12). While there is a bias for the initial calibration in the order of 10 µmol L^{-1} (not shown), the post-cruise calibration gives a good match of -2.2 ± 3.3 µmol L^{-1}.

During the cruise, the second optode was attached to the CTD at 13 stations with 282 Winkler samples available as reference. However, no separate bottle stops were performed during these casts and the Niskin bottles were fired in drive-by mode. The results are shown in figure 2.13 and the data distinguished between surface samples above or close to the thermocline (green circles) and deeper samples below 100 dbar (yellow circles) in analogy to the R/V Polarstern cruise. In contrast to the R/V Polarstern cruise, the field data are spread both on a broad temperature and oxygen range and fall well within the calibration range of both the pre-cruise (not shown) and post-cruise calibration (left panel). However, there is a significantly higher scatter of the residuals (middle panel) which can be attributed to both the larger oxygen gradient and the sensor's dynamic response, the effect of which are amplified by the drive-by bottle fires. The calibration bias of -0.8 µmol L^{-1} for the deep samples and -3.2 µmol L^{-1} for all samples, respectively, is within or only slightly exceeds the laboratory calibration accuracy of 1.0 µmol L^{-1} and is well inside the field uncertainty. Additionally, there is no visible trend in the difference between optode reading and Winkler field samples, i. e. both the non-linear temperature and oxygen behaviour of the optode has been grasped by the laboratory calibration.

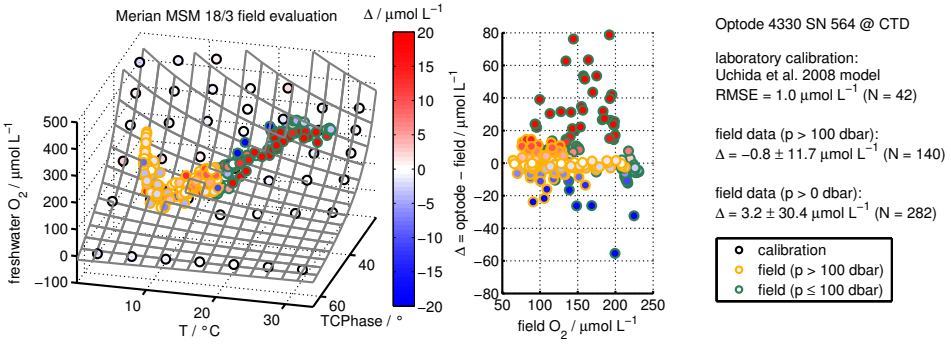

Figure 2.13: CTD field evaluation of optode 4330 SN 564 during cruise MSM 18/3 with post-cruise calibration. Left panel: Calibration points (black) and optode response as function of phase and temperature (grey) with field samples below the thermocline (yellow) and above the thermocline (green) mapped into the same, freshwater sample space of the calibration. Middle panel: Difference between optode calibration and Winkler field samples for samples below the thermocline (yellow) and above the thermocline (green). The colour axis shows the same difference in both panels. Right panel: Statistical figures for both the calibration and the field samples.

2.4 Discussion and Summary

The flow-system based calibration setup with electrochemical O_2 generation proves to be well-suited for the individual multi-point calibration of oxygen sensors. While the O_2 generator forces the oxygen content of the carrier solution, its flow rate needs to be constrained thightly in order to provide stable O_2 concentrations. By these means, different oxygen concentrations up to 315 µmol L^{-1} can be obtained at a high stability of within ±0.5 µmol L^{-1} (2 SD). On the other hand, the temperatures of both the carrier solution and the sensors are thoroughly controlled as a prerequisite for reliable reference points for the sensor calibration.

While triplicate Winkler samples with a typical reproducibility of 0.8 µmol L^{-1} (2 SD) can be taken for external reference, the system may provide a Winkler-free way to calibrate oxygen sensors. As the environmental conditions can be controlled very accurately, the electrolytic current and carrier solution flow rate define the oxygen concentration to within an accuracy of ±1.2 µmol L^{-1}. This illustrates the high repeatability of the system, albeit an incomplete degassing that causes a remaining offset of 4.7 µmol L^{-1} has to be taken into account. These figures have been obtained from the direct comparison of triplicate Winkler samples with the generator settings and are valid for the entire operation range, i. e. 1 °C – 36 °C and 0 µmol L^{-1} – 315 µmol L^{-1}, respectively.

However, the proper and accurate calibration of oxygen sensors is the main purpose. A good agreement has been found between the individual multi-point laboratory calibration of Aanderaa oxygen optodes and Winkler samples under various field conditions, both polar and tropical, and deployment modes, both profiling and

underway. While the polar deployments suffered from an imperfect match between the parameter range in calibration and field measurements for temperature and oxygen, the mismatch did not exceed -6.4 μmol L^{-1} for samples below the thermocline. Moreover, it is a constant offset to the otherwise well-grasped sensor's oxygen response, as indicated by the low scatter of ≤ 3.5 μmol L^{-1} (2 SD), and points towards issues in the fitting equations for the optode response at low temperatures. For the tropical deployments, all field samples are within the calibrated range. There is a calibration bias of only -0.8 μmol L^{-1} for samples below the thermocline and both the temperature and the oxygen behaviour of the optode are properly characterized by the laboratory calibration. However, a drift of the optodes between the pre- and post-cruise calibration has been observed for the tropical deployment, and only the post-cruise calibration has been used for the evaluation.

The laboratory calibrations showed RMSE values as measure of accuracy between 0.9 μmol L^{-1} and 1.9 μmol L^{-1} when combined with the Uchida et al. (2008) functional model of the optode's oxygen response. At the same time, the repeated calibrations with varying calibrated ranges indicate a good parametrization of the oxygen slope in the Uchida et al. (2008) model when being extrapolated (figure 2.11), while the temperature slope parametrization might have room for improvement (figure 2.8 and polar deployments mismatch).

During the course of the R/V Maria S. Merian field evaluation, the appeal of simple means for a repeated calibration has become obvious. From the pre- and post-cruise calibration the otherwise elusive sensor drift is clearly identified. Thus, the interpretation of the field data can be based unambiguously on the more adequate calibration parameters.

While the observed sensor drift discredits the overall long-term stability of optical sensors, the two 4330 optodes changed their oxygen response in a very similar and distinct manner. Moreover, the post-cruise calibration fits well to the field data with several months in between. In fact, the time between deployment and post-cruise calibration is twice as long as the time between pre-cruise calibration and deployment, where most of the response change appeared. In consequence, optodes still represent the most stable oxygen sensors with a possibly non-continuous drift related to its usage. In any case, the drift is not erratic and may be detected and corrected for.

The calibration setup presented here has the potential to make oxygen sensor calibrations less time and skill demanding and, more important, regular recalibrations feasible. Frequent snapshots of a sensor's oxygen response will be a crucial step towards an understanding of sensor drift between deployments and conditions that enhance or reduce this drift.

It should be noted that the laboratory calibration can not be done in pure freshwater as the electrolytic medium by necessity contains ions, but its low salinity effect can be compensated for (Clegg and Brimblecombe, 1990). The high pH, however, may not be a suitable environment for every kind of sensor and sensing material. Still, the calibration setup is not specific for a special sensor type but any model that is compatible with high pH conditions can be used with a custom flow-through cell. The systems size does not exceed common bench-top instrumentation and, more

importantly, it does not need separate gas cylinders or similar, difficult to handle equipment or consumables. The oxygen content is solely dependent on the conditions given by the setup and is independent of ambient humidity or atmospheric pressure, which are easily influenced by air conditioning in laboratories.

In addition, the calibration setup does not necessarily depend on external referencing, but offers a Winkler-free mode of operation. It is small and robust enough as to build a mobile, sea-going, and Winkler-free calibration setup for oxygen sensors. Moreover, the calibrations obtained by this laboratory setup proved to be valid under various field conditions and underline the versatility of the calibration setup. It thus represents a system capable to facilitate high accuracy automated dissolved oxygen measurements on a large scale by providing reliable and easy access to accurate individual multi-point sensor calibrations.

2.5 Comments and Recommendations

The maximum electrolytic current of 20 mA provided by the oxygen generator proved to be insufficient as freshwater and saltwater (35 psu) oxygen saturation levels can not be reached below 15 °C and 5 °C, respectively. Thus, a separate current source providing up to 30 mA was developed. This equals a concentration of 465 µmol L^{-1} or 105 % and 133 % saturation at 1 °C in fresh- and saltwater, respectively, and should be adequate for most oceanographic purposes. Furthermore, the valves shown in figure 2.1 were replaced by electric isolation valves (100T3, Bio-Chem Fluidics Inc, Boonton, USA), while the temperature, electrolytic current and flow rate regulation was integrated into the same LabVIEW routine as the sensor data logging. All this was done in order to eliminate sources of variability and to further improve the repeatability. These improvements were already in place for the R/V Maria S. Merian MSM 18/3 post-cruise calibration.

For the calibration setup described here, the total equipment costs amount to ca. 22000 Euro, while the running costs are basically the trained staff and consumables to measure the Winkler samples if desired.

2.6 Nomenclature

E_0	standard reduction potential / V
V	volume / ml
t	time / s
Q	charge / C
n	amount of substance / mol
z	number of electrons transferred, stochiometric factor
F	Faraday constant: 96485 C mol^{-1}
I	electric current / mA
c_{O_2}	concentration of oxygen / µmol L^{-1}
pO_2	partial pressure of oxygen / Pa
α_{O_2}	Henry's law oxygen solubility constant, Bunsen coefficient / µmol L^{-1} Pa^{-1}

Λ	fluorophore excited state lifetime in the presence of O_2 / s
Λ_0	fluorophore excited state lifetime in the absence of O_2 / s
φ	phase signal in the presence of O_2 / °
φ_0	phase signal in the absence of O_2 (zero phase signal) / °
K_{SV}	Stern-Volmer constant of the fluorophore
$c_0 \ldots c_6$	calibration coefficients of the Uchida et al. (2008) model

AMT	AMT Analysenmesstechnik GmbH, Rostock/Germany
SD	standard deviation
RMSE	root-mean-square error

3 In-situ Referencing using in-air Measurements

submitted as:
Bittig, H. C. and Körtzinger, A. 2014. Near-surface and in-air oxygen optode measurements on a float provide an accurate in-situ calibration reference. J. Atmos. Oceanic Techn.

Abstract

A yet unexplained drift of (some) oxygen optodes during storage/transport and thus significant deviations from factory/laboratory calibrations has been a major handicap for autonomous oxygen observations as it makes a reliable in-situ reference essential. Traditionally, this called for a ship-based reference cast which poses some challenge for opportunistic float deployments. Here, we present an easily-implemented alternative using near-surface/in-air measurements of an Aanderaa optode on a 10 cm stalk and compare it to the more traditional approaches (factory, laboratory, and in-situ deployment calibration). In-air samples show a systematic bias depending on the water saturation, which is likely caused by occasional submersions of the standard-height stalk optode. Linear regression of measured in-air supersaturation against in-water supersaturation (using ancillary meteorological data to define the saturation level) robustly removes this bias and thus provides a precise (0.2 %) and accurate (<1 %) in-situ correction, which is available throughout the entire instrument's lifetime.

Acknowledgements

The authors want to thank Sea-Bird for their efforts with float and firmware customization, Patrice Brehmer (IRD, Dakar, Senegal) for invaluable logistical help as well as the captain and crew of M/V Samba Laobe Fall. Optode 4330 SN 564 data on lovbio059c were thankfully acquired by Raphalle Sauzede and Antoine Poteau (OAO-LOV, Villefranche, France). Financial support by the following projects is gratefully acknowledged: E-AIMS (EU FP7 project no. 312642) for float WMO ID 6900890 and remOcean (EU ERC grant agreement 246777) for float WMO ID 6901646 as well as O2-Floats (KO 1717/3-1) and the SFB754 of the German Science Foundation (DFG).

3.1 Introduction

The use of optode in-air measurements as a potential reference has been suggested with the advent of optical oxygen sensors on floats (Körtzinger et al., 2005). This, however, received little further attention due to the optical technology's promise to be long-term stable. Despite proven in-situ stability (e.g., Tengberg et al., 2006; Takeshita et al., 2013), it became evident in recent years that a drift occurs frequently, mostly during periods when sensors were not deployed in the field (Bittig et al., 2012; Takeshita et al., 2013; D'Asaro and McNeil, 2013), and in-situ calibration has become a crucial part.

In-situ calibration can be done using Winkler-type oxygen titration of discrete samples from a hydrocast taken at the time and place of the float deployment (requires adequate ship capabilities and gives only information at the beginning; see section 3.2), through comparison to an oxygen climatology (relying on a smoothed, potentially coarse set of historical data; see Takeshita et al., 2013), or by comparing in-air optode measurements with an atmospheric pO_2 (continuous throughout deployment albeit only at one O_2 level).

In-air referencing thus appeared on the agenda again and Fiedler et al. (2013) demonstrated the principle's feasibility, while Emerson and Bushinsky (2014) and Bushinsky et al. (2014) show that such measurements can be accurate to 0.5 %. Here we show that the achievable precision can be as low as 0.3 mbar (2σ) under ideal field conditions (figure 3.1). An Aanderaa optode model 4330 SN 564 (AADI, Bergen, Norway), shown to be prone to drift (Bittig et al., 2012), was mounted on a Bio-Argo float (lovbio059c, PROVOR CTS4, nke Instrumentation, Hennebont, France; WMO ID 6901646) and set to sample in air (50 s interval) on deck (shaded, windward, wetted optode foil) of R/V Pourquois-pas? just before deployment in the Irminger Sea. While temperature and phase shift vary somewhat, optode pO_2 (based on a laboratory calibration performed 4 month prior) is highly stable. Moreover, the difference to an atmospheric pO_2 based on ship-board meteorological observations (equ. 3.4) is as low as +0.3 mbar.

In this paper, we show a new approach to use near-surface and in-air O_2 measurements as a reference and compare it to other calibration methods. At the same

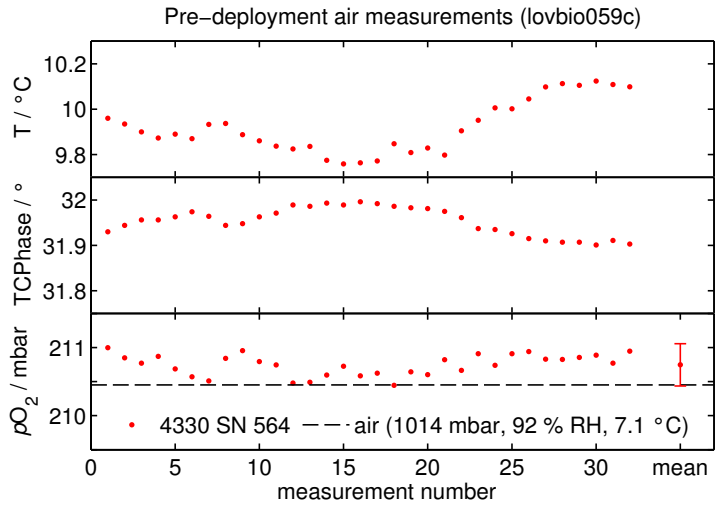

Figure 3.1: Optode 4330 SN 564 in-air measurements (50 s interval) onboard R/V Pourquois-pas? before deployment of float lovbio059c (WMO ID 6901646). From top to bottom: Optode temperature, phase shift, and pO_2 (with mean±2σ). Air pO_2 ($pO_{2,air}$) calculated using equ. 3.4 with ship-board meteorological observations is shown as dashed line for reference.

time, we want to illustrate the utility of and caveats associated with optode in-air measurements.

3.2 Methods

Navis Dual-O_2 Float and Near-Surface Measurement Sequence

A Navis float (Sea-Bird, Inc., Bellevue, USA; SN F0272; WMO ID 6900890) was equipped with two oxygen optodes, a Sea-Bird SBE63 integrated into the CTD's pumped path and an Aanderaa model 4330 SN 1280 (AADI, Bergen, Norway) attached on a short stalk (10 cm) on the float's top cap, thereby reaching about mid-height of the CTD cage.

In normal float applications, the CTD pump is switched off at 6 dbar (to avoid contamination of the conductivity cell) which is therefore the shallowest SBE63 optode observation.

A special near-surface sequence for the Aanderaa optode was implemented in the Navis float's firmware: At the end of its profile, 5 samples (20 s interval) are taken with the air bladder deflated, i.e., just below the water-air interface (approx. 0.3 dbar). After that, the air bladder is inflated and 10 samples (30 s interval) are taken with the optode extending into the air. All data presented here stem from the Aanderaa optode.

A typical example of this near-surface sequence is shown in figure 3.2. Spikes in pressure during inflated sampling indicate that the optode is occasionally submerged/wetted during these "in-air" measurements.

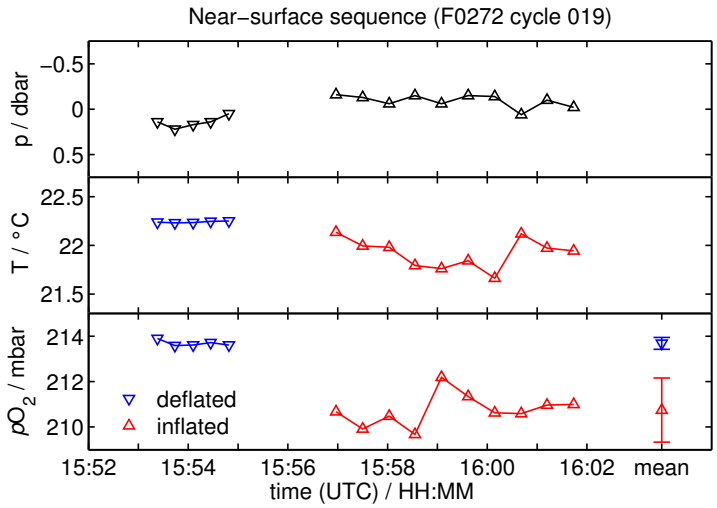

Figure 3.2: Near-surface samples of hydrostatic pressure (top), optode temperature (middle), and optode pO_2 (bottom) with deflated air bladder (downward triangles; in-water) and inflated air bladder (upward triangles; in-air), respectively, for float F0272 (WMO ID 6900890). Surface waters are supersaturated for cycle 019 and mean deflated and inflated pO_2 are given with $\pm 2\sigma$ errorbars.

The float was deployed on Sept. 27, 2013, near 16° N 17.6° W in the Eastern tropical North Atlantic oxygen minimum zone and stayed about 50 – 200 nm offshore the West African coast. It was set to a 5 d cycle interval and surfaced in the afternoon until cycle 44, when the cycle interval was reduced to 4.75 d to have it surface at different times of the day.

Pre-Deployment Optode Calibrations

The Aanderaa optode 4330 SN 1280 was multipoint factory calibrated (accuracy 2 µmol L^{-1} or 1.5 %, Tengberg and Hovdenes, 2014) just 1.5 month prior to the deployment and laboratory multipoint calibrated (RMSE 1.2 µmol L^{-1} to triplicate Winkler samples) 2 month prior to the deployment using a method described by Bittig et al. (2012).

CTD-O_2 Deployment Cast and Match to Float Profile

A light-weight sensor package consisting of a SBE37-IMP Microcat (Sea-Bird, Inc., Bellevue, USA) and an Aanderaa fast-response optode model 4330F SN 135 (AADI, Bergen, Norway) attached to a custom logger was lowered down to 409 dbar (ca. +0.5/−0.15 dbar s^{-1} average descent/ascent velocity, 6 s logging interval) to obtain a reference CTD-O_2 profile just before the float launch and 18 h before completion of the first float profile.

Extensive multipoint laboratory calibrations (following Bittig et al., 2012) of the 4330F optode 2 weeks before as well as 3.5 and 8.5 months after the deployment

have a mean bias of +0.1 μmol L^{-1} (mean RMSE 1.5 μmol L^{-1}), indicating that this optode was indeed stable. We therefore have high confidence in the reference profile even in the absence of discrete Winkler samples.

The reference and float profile were matched on a mixed axis x of potential density σ_θ and pressure p as follows:

$$x = \sigma_\theta + \delta_p \text{ , where} \tag{3.1}$$

$$\delta_p = (\Sigma - \sigma_\theta(p=0)) \cdot \frac{\text{MLD} - p}{\text{MLD}} \qquad , p \leq \text{MLD} \tag{3.2}$$

$$\delta_p = 0 \text{ kg m}^{-3} \qquad , p > \text{MLD} \tag{3.3}$$

with δ_p being a pressure-based distortion to σ_θ and MLD being the pressure of the mixed layer depth. The paramater Σ determines $x(p=0)$ and was (arbitrarily) set to 10 kg m^{-3}, so that δ_p dominates over σ_θ variations within the mixed layer.

While this mixed axis match is isopycnal below the mixed layer, it accounts for the dominance of depth (e.g., impact of irradiance on surface density and diel biogeochemical cycles) within the mixed layer.

In addition, mixed layer samples ($\delta_p < 0$ kg m^{-3}) were given a 5-fold weight in the regression against the reference to account for the float's bias in the number of surface samples against deeper samples.

Air pO_2 Calculations

Near-surface float pO_2 was calculated using optode temperature and phase shift and the Uchida et al. (2008) model as described in Bittig et al. (2012).

NCEP/NCAR reanalysis data (provided by the NOAA/OAR/ESRL PSD, Boulder, USA, at ftp://ftp.cdc.noaa.gov/Datasets/ncep.reanalysis/) of atmospheric pressure p_{air}, relative humidity φ, and air temperature T_{air} provided an independent atmospheric $pO_{2,\text{air}}$ reference according to

$$pO_{2,\text{air}} = \chi O_2 \cdot (p_{\text{air}} - \varphi \cdot pH_2O(T_{\text{air}})) \tag{3.4}$$

where $\chi O_2 = 0.20946$ is the mixing ratio of O_2 in dry air (Glueckauf, 1951) and $pH_2O(T)$ the water vapor pressure (Weiss and Price, 1980).

Optode Drift Correction

Optode drift appears to follow an exponential time behaviour under constant storage conditions (D'Asaro and McNeil, 2013) and be approximately linear with oxygen (Bittig et al., 2012). However, a small offset may be present at zero oxygen (see figure 11 in Bittig et al., 2012), so that we applied a slope and offset correction on pO_2 when our O_2 range was wide enough (deployment cast) and limited the correction to a slope on pO_2 otherwise (air pO_2).

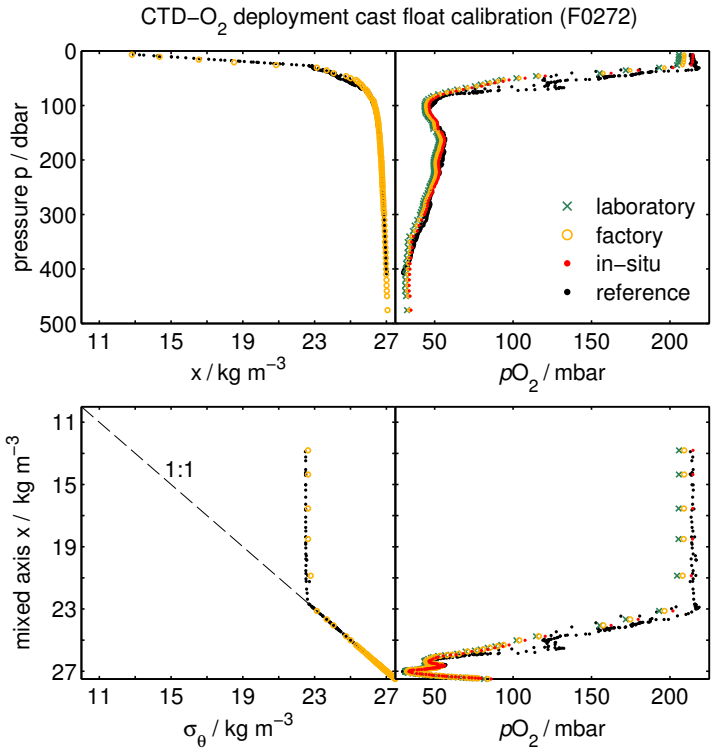

Figure 3.3: CTD-O_2 reference cast (black dots) and first F0272 (WMO ID 6900890) float profile (18 h later) of x and σ_θ (left) and pO_2 (right) against pressure (upper panel) and the mixed axis x (lower panel). Below the mixed layer (≈30 dbar), x and σ_θ follow the 1:1 line (dashed), i.e., $\delta_p = 0$. pO_2 is based on the laboratory (green crosses), factory (yellow circles), and an in-situ deployment cast calibration (red dots).

3.3 Results and Discussion

CTD-O_2 Deployment Cast

Figure 3.3 shows the first float profile together with the deployment cast. Float pO_2 was calculated using the laboratory calibration (green crosses), factory calibration (yellow circles), and a slope & offset corrected laboratory calibration (red dots) with the deployment cast as reference (slope 1.037, offset +1.4 mbar, RMSE to deployment cast 6.3 µmol kg^{-1} incl. oxycline, mixed layer bias +0.2 µmol kg^{-1}).

Both the laboratory and factory calibration suggest an accuracy of 1.2−3 µmol kg^{-1}. This is exceeded, however, by offsets in the mixed layer of −8.3 µmol kg^{-1} and −5.1 µmol kg^{-1}, respectively, which follows the previously observed pattern (e.g., Bittig et al., 2012) of optodes drifting towards too low sensor readings. However, a drift of approx. −3.5 % in 2 months exceeds the rates previously reported (≈ −1 % / 2 months, D'Asaro and McNeil, 2013) and may be caused by tropical temperatures or the sensor shipment.

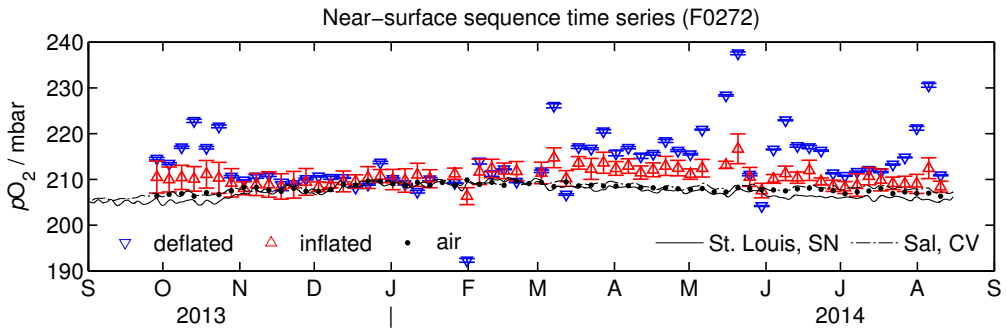

Figure 3.4: Time series of near-surface measurements for float F0272 (WMO ID 6900890) using the deployment calibration showing deflated (downward triangles) and inflated (upward triangles) float pO_2 (mean±2σ). Air pO_2 (dots) as comparison is based on interpolated NCEP/NCAR meteorological data (equ. 3.4). Black lines give calculated air pO_2 at WMO stations in St. Louis, Senegal (continuous line; station ID 69600; 100 nm eastward) and on Sal, Cape Verde (dash-dot line; station ID 08594; 250 nm westward).

Near-Surface Measurements

Near-surface float measurements of pO_2 together with NCEP/NCAR-based air pO_2 are shown in figure 3.4 up to cycle 065. In-water (deflated) measurements agree well with mixed layer data (not shown). However, in-air (inflated) measurements are offset to the air reference depending on the in-water pO_2.

While the optode 4330 extends into the air during (most) inflated measurements, the standard-height stalk seems to be too short to remove the effect of occasional wave-caused submersions, causing a marked carry-over effect. However, the carry-over effect is linear with (water) supersaturation and does not seem to depend on daytime (figure 3.5).

Providing the optode works the same in air and water, there should be no carry-over at true 100 % O_2 saturation, i.e.,

$$pO_{2,\mathrm{sat}}^{\mathrm{infl}} = pO_{2,\mathrm{sat}}^{\mathrm{defl}} = pO_{2,\mathrm{air}} \; . \tag{3.5}$$

The linear carry-over between inflated (in-air) and deflated (in-water) observations may thus be parameterized as a linear function of (water) supersaturation,

$$pO_2^{\mathrm{infl}} - pO_{2,\mathrm{air}} = c \cdot \left(pO_2^{\mathrm{defl}} - pO_{2,\mathrm{air}} \right) \; , \tag{3.6}$$

where c is the observed slope (figure 3.5, left). Here, $pO_{2,\mathrm{air}}$ is not constant but scales with local atmospheric pressure and humidity (equ. 3.4; see also figure 3.4).

Correcting the observed oxygen with a slope m ($pO_2 = m \cdot pO_{2,\mathrm{obs}}$) or offset a ($pO_2 = pO_{2,\mathrm{obs}} + a$), respectively, affects both sides and equation 3.6 becomes

$$m \cdot pO_{2,\mathrm{obs}}^{\mathrm{infl}} - pO_{2,\mathrm{air}} = c \cdot \left(m \cdot pO_{2,\mathrm{obs}}^{\mathrm{defl}} - pO_{2,\mathrm{air}} \right) \text{ and} \tag{3.7}$$

$$pO_{2,\mathrm{obs}}^{\mathrm{infl}} + a - pO_{2,\mathrm{air}} = c \cdot \left(pO_{2,\mathrm{obs}}^{\mathrm{defl}} + a - pO_{2,\mathrm{air}} \right) \; . \tag{3.8}$$

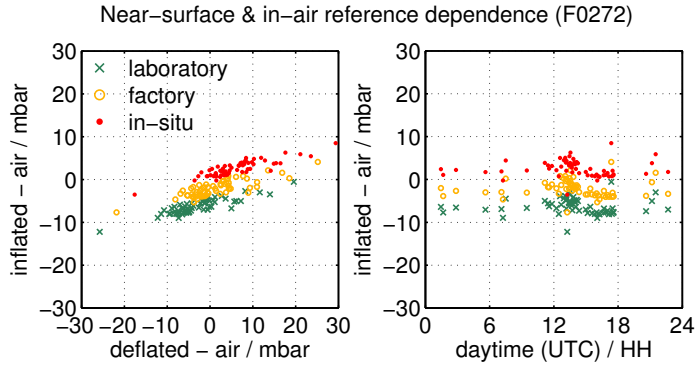

Figure 3.5: Plot of float-observed in-air supersaturation (inflated–air) against in-water supersaturation (deflated–air; left) and daytime (right) using the laboratory (green crosses), factory (yellow circles), and in-situ calibration (red dots). Errorbars are omitted for clarity. (Float F0272; WMO ID 6900890)

Rearrangement yields

$$pO_{2,\mathrm{obs}}^{\mathrm{infl}} = c \cdot pO_{2,\mathrm{obs}}^{\mathrm{defl}} + \frac{1-c}{m} \cdot pO_{2,\mathrm{air}} \quad \text{and} \tag{3.9}$$

$$pO_{2,\mathrm{obs}}^{\mathrm{infl}} = c \cdot pO_{2,\mathrm{obs}}^{\mathrm{defl}} + (1-c) \cdot \left(pO_{2,\mathrm{air}} - a\right) , \tag{3.10}$$

which can be used for a linear regression.

Using NCEP/NCAR reanalysis meteorological data, the slopes m and offsets a as given in table 3.1 were obtained from equ. 3.9 & 3.10. The slope/offset differences between calibrations are consistent with direct regressions/comparisons between calibrations, indicating that the calculations are robust.

The uncertainty for p_{air} in reanalysis models is on the order of 2 mbar (Smith et al., 2001) or better (van den Besselaar et al., 2011; Clissold, 2008). This translates to a relatively small absolute error of 0.2 % in m or 0.4 mbar in a.

The example shown here takes advantage of large surface super- and undersaturations in a coastal upwelling system. Artificially limiting the data to $[-1\ \%; +3\ \%]$

Table 3.1: Correction parameters and fit RMSE of the in-air reference approach for float F0272 (WMO ID 6900890) using a slope (upper part, equ. 3.9) or offset (lower part, equ. 3.10) correction (confidence intervals at 95 % level).

calibration	c	$m-1$ / %	a / mbar	RMSE / mbar
laboratory	0.23 ± 0.03	$+3.6 \pm 0.2$		0.9
factory	0.23 ± 0.04	$+1.5 \pm 0.2$		1.1
in-situ	0.23 ± 0.03	-0.7 ± 0.2		0.9
laboratory	0.23 ± 0.03		$+7.3 \pm 0.4$	0.9
factory	0.23 ± 0.04		$+3.2 \pm 0.4$	1.1
in-situ	0.23 ± 0.03		-1.5 ± 0.4	0.9

in saturation anomaly to mimic an oligotropic, open ocean system, the carry-over slope c becomes less constrained but slopes m and offsets a remain unaffected (within confidence intervals).

3.4 Summary

Today's oxygen optodes can not be used "out-of-the-box" to obtain highly-accurate seawater O_2 data, so that some kind of in-situ reference is required.

An in-situ reference profile has the highest yield of information (variety of temperature, oxygen, pressure) though it is limited to the location's hydrography and time of the profile. Moreover, obtaining a profile is complicated if not impossible for opportunistic deployments of autonomous instruments.

In-air measurements as an alternative are accurate, easily implemented, and available for the entire lifetime of the instrument, but they rely on the air pO_2, i.e., a single O_2 level only.

Nearby meteorological observations (see, e.g., Fiedler et al., 2013), though not likely to be available on many occasions, would be favourable as an atmospheric reference. NCEP/NCAR reanalysis, however, provides global coverage and uncertainty of the model contributes only little to the uncertainty of our analysis. With more recent reanalysis models (e.g., ERA-Interim, Dee et al. (2011), or MERRA, Rienecker et al. (2011)) and future improvements, this uncertainty will diminish further.

Despite the systematic carry-over effect causing a bias in float-observed "in-air" pO_2, our approach yields well determined (0.4 mbar 95 % CI) and consistent results (similar offsets between different calibrations as from a direct comparison). Noise in the data as well as the magnitude of the carry-over effect (i.e., the slope c) are likely reduced with a higher optode attachment (longer stalk) which would improve the analysis.

Both approaches (in-situ and in-air) match within 1 %, much better than the typical accuracy obtained today (Takeshita et al., 2013). It appears that the in-situ deployment calibration of float F0272 is slightly too high (table 3.1), but this may just illustrate the accuracy achievable with these methods.

Our in-air correction approach requires the oxygen optode to be capable of in-air measurements and integration of the near-surface sequence both into the float's firmware and data transmission. Since a reference $pO_{2,\mathrm{air}}$ can be derived globally using reanalysis models, this correction is not limited in space or time. Therefore, it might be implemented as a standard quality control routine for the entire Argo-O_2 array (Gruber et al., 2010), significantly improving its data accuracy and coherence.

In conclusion, in-air and near-surface optode measurements have the potential to overcome major limitations of current autonomous O_2 observations: they are technically and logistically feasible (often in contrast to a reference profile), accurate to better than 1 %, available for the entire deployment period, and could be applied universally to the entire O_2 float array.

4 Time Response of Oxygen Optodes

published as:
Bittig, H. C., Fiedler, B., Scholz, R., Krahmann, G., and Körtzinger, A. 2014. Time response of oxygen optodes on profiling platforms and its dependence on flow speed and temperature. Limnol. Oceanogr.: Methods **12**: 617–636. [doi:10.4319/lom.2014.12.617].

Abstract

The time response behaviour of Aanderaa optodes model 3830, 4330, and 4330F as well as a Sea-Bird SBE63 optode and a JFE Alec Co. Rinko dissolved oxygen sensor was analyzed both in the laboratory and in the field. The main factor for the time response is the dynamic regime, i. e., the water flow around the sensor, that influences the boundary layer's dynamics. Response times can be drastically reduced if the sensors are pumped. Laboratory experiments under different dynamic conditions showed a close to linear relation between response time and temperature. Application of a diffusion model including a stagnant boundary layer revealed that molecular diffusion determines the temperature behaviour, and that the boundary layer thickness was temperature independent. Moreover, field experiments matched the laboratory findings, with the profiling speed and mode of attachment being of prime importance. The time response was characterized for typical deployments on shipboard CTDs, gliders, and floats and tools are presented to predict the response time as well as to quantify the effect on the data for a given water mass profile. Finally, the problem of inverse filtering optode data to recover some of the information lost by their time response is addressed.

Keywords: response time, oxygen sensor, boundary layer, dynamic error, autonomous platforms

Acknowledgements

The authors want to thank the captains, crew and scientists of R/V Polarstern ANT-XXVII/2, R/V Maria S. Merian MSM 18/3 and MSM 22 as well as of R/V Oceania AREX10 and R/V Islândia. Special thanks go to Sascha Heitkam (TU Dresden, Dresden/Germany) for fruitful discussions and comments on boundary layers and fluid mechanics. Support by Gerd Rohardt (AWI, Bremerhaven/Germany) and Sebastian Milinski (GEOMAR, Kiel/Germany) with the CTD data processing of the R/V Polarstern and R/V Islândia cruises is gratefully acknowledged. Many thanks go to Jostein Hovdenes (AADI, Bergen/Norway) for valuable feedback on their sensors and Norge Larson (Sea-Bird, Bellevue/USA) for early access to and feedback on their sensor, as well as to an anonymous reviewer for valuable comments on signal processing. Financial support by the following projects is gratefully acknowledged: O2-Floats (KO 1717/3-1) and the SFB754 of the German Science Foundation (DFG) as well as the projects SOPRAN (03F0611A and 03F0462A) and HGF-CV-Station (03F0649A) of the German Research Ministry (BMBF).

4.1 Introduction

Dissolved oxygen has an unmatched history in ocean observation among all chemical ocean parameters. It belongs to the most commonly measured chemical quantities and the most mature chemical sensors are available for dissolved oxygen (Johnson et al., 2007). Traditionally, these were Clark-type electrochemical sensors, one of the most mature versions of which is the widely used Sea-Bird SBE43 electrode. They feature a fast time response, which make them suitable for profiling applications like ship-based CTD surveys. However, their major drawback is the need for recalibrations or in situ reference samples on timescales of weeks to months since they lack long-term stability.

More recently (as early as the late '90s), optical oxygen sensors for marine applications emerged as an alternative (Klimant et al., 1995; Demas et al., 1999). Unlike electrodes, these optodes do not consume oxygen so their absolute response is not flow sensitive (Tengberg et al., 2006). However, their response rate to a changing O_2 level definitely is flow sensitive.

Optodes have been shown to be stable during deployments of several years (e. g., Körtzinger et al., 2005) but calibrations may change between laboratory characterization and deployment (e. g., Bittig et al., 2012). While recalibrations are in principle feasible during ship-based CTD surveys, they pose a significant challenge for newer and more innovative, profiling observation platforms such as floats and gliders. Especially these autonomous and unattended platforms call for cost-effective, energy-efficient, long-term-stable, accurate, robust, and reliable sensors. While none of today's commercial optodes meet all requirements, they fulfill many criteria and belong to the standard configuration of many instruments, e. g., Argo-O_2 floats (Gruber et al., 2010).

However, a major concern with the application of optodes on profiling platforms is the comparatively slow response attributed to these sensors. Little is known about

the actual in situ time response and the specific effects on the data. We aim to fill this gap with a systematic study of five commercially available optical oxygen sensors.

The main goal is the quantification of the time response and its effect under field conditions. The two factors influencing the time response are the flow speed in front of the sensor and the temperature. Two sets of laboratory experiments were performed to separate them: First, the flow speed dependence was investigated at constant temperature, and second, the temperature dependence was analyzed under constant flow regime. The findings from these experiments were then validated against field deployments on today's major oceanographic platforms: shipboard CTDs, gliders, and floats. The flow speed turned out to be of prime importance and response times τ well below 10 s are easily obtained if the sensors are pumped.

4.2 Materials and Procedures

Optode Descriptions

The sensing principle of optical oxygen sensors is based on the dynamic or collisional quenching of luminescence by oxygen. After a luminophore has been excited with short-wavelength light, it may return to its ground state either through radiationless de-excitation or through luminescence, i. e., emission of light with longer wavelength. If oxygen is present, O_2 can collide with the luminophore and absorb the excess energy of the excited state thereby quenching luminescence. Both the luminescence intensity I and the excited state lifetime Λ are reduced by collisional quenching and their behaviour is described by the Stern-Volmer equation (equation 4.1)

$$\frac{I_0}{I} = \frac{\Lambda_0}{\Lambda} = 1 + K_{SV} \cdot pO_2 \tag{4.1}$$

where pO_2 is the partial pressure of O_2, K_{SV} is the Stern-Volmer constant, and I_0 and Λ_0 are the intensity and lifetime in absence of oxygen, respectively.

Using an intensity-modulated excitation light source, the luminescence emission is modulated, too, but phase shifted due to the finite lifetime of the excited state according to equation 4.2

$$\tan\varphi = 2\pi \cdot f \cdot \Lambda \tag{4.2}$$

with f being the modulation frequency and φ the phase shift. The calibration coefficients relate the phase shift φ (and temperature T) as measured quantity to the oxygen partial pressure pO_2 as quantity of interest. (Commonly, temperature-dependent parameterizations for $\Lambda_0(T)$ and $K_{SV}(T)$ (see equation 4.1) are applied.)

All sensors used in this study have been thoroughly calibrated using Winkler-based multi-point laboratory (Bittig et al., 2012) or in situ calibrations (details can be found in the appendix). The partial pressure pO_2 is the quantity determining equilibrium between different media, i. e., the sensing membrane and the bulk environment, and will be used for most of the discussions. However, the oxygen concentration c_{O_2} is used for all field applications. Both parameters essentially carry

optode manufacturer	optode model	flow regime	luminophore matrix	response time τ / s
Aanderaa	3830 / 4330	diffusive	PreSens PSt3	25 s
Aanderaa	4330F	diffusive	PreSens PSt3*	8 s
Sea-Bird	SBE63	pumped	PreSens PSt3	6 s
JFE Alec Co.	Rinko	diffusive	PMMA coating	(0.4 s)**

Table 4.1: Optode properties and manufacturer specifications. (*) The 4330F model uses a thinner version of the PSt3 membrane without optical isolation. (**) The manufacturer states a gas phase response time only.

the same information and can be converted using the Henry's law solubility constant α_{O_2} / μmol kg^{-1} Pa^{-1}.

The oxygen optode models 3830, 4330, and 4330F (Aanderaa Data Instruments AS, Bergen/Norway) as well as the SBE63 optode (Sea-Bird Electronics Inc., Bellevue/USA) are based on a luminescent platinum porphyrine complex immersed in a silicone membrane (PSt3 membrane, PreSens GmbH, Regensburg/Germany). The membrane is mounted on an optical window. While the membrane is exposed directly to the ambient medium for the Aanderaa optodes, the SBE63 is designed for use in a CTD's pumped flow path. Therefore, the optical window is contained within a plenum, i. e., a flow-through mount, and is not exposed to the ambient medium without it being pumped through the plenum.

The Rinko optical oxygen sensor (JFE Alec Co. Ltd., Kobe/Japan) uses the same dynamic quenching principles but different materials. Its luminophore is coated onto the optical window (transparent acrylic resin PMMA) which is open to the ambient medium.

Time Response Quantification

For quantification of the time response, two measures are used. The first one is a response time τ which is the standard way of characterization (Tengberg et al., 2006; Sea-Bird Electronics, 2012). It corresponds to the time constant of an exponential step response. The second is based on a diffusional model of the optode – water interface. It consists of two stationary layers, one for the sensing membrane and one for the aqueous boundary layer in front of the membrane.

Since oxygen diffusivity D in water is about three orders of magnitude smaller than the kinematic viscosity ν (Schmidt number $\mathrm{Sc} = \nu/D \approx 500$), oxygen diffusion occurs entirely within the inner 10 % of the velocity boundary layer where the flow is considerably decelerated by friction. Advection can thus be neglected inside the diffusive boundary layer and the layer can be treated as stagnant.

The model is based on Fickian diffusion and uses temperature-dependent parameterizations for the diffusivity $D(T)$ and solubility $S(T)$ in both layers. The sensing membrane thickness l_M is prescribed while the stagnant, diffusive boundary layer thickness l_L is adjusted to match the observation.

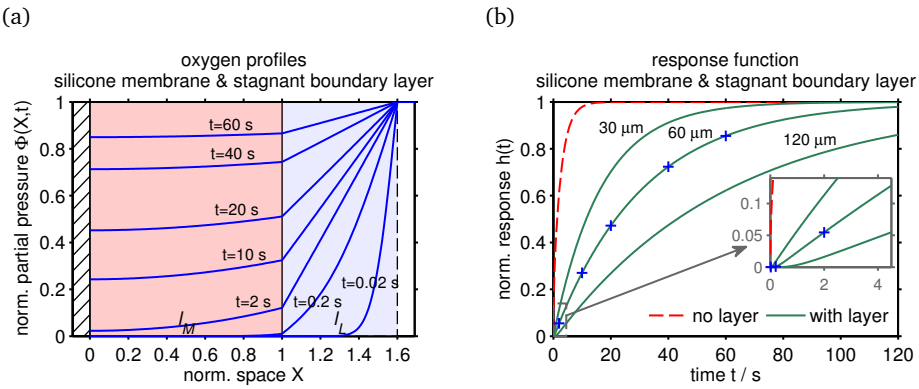

Figure 4.1: Two-layer diffusional optode model consisting of a silicone membrane ($0 \leq X \leq 1$, $l_M = 100$ µm, Aanderaa optode standard foil) with impermeable boundary (hatched, optical window) on one side and a stagnant boundary layer ($1 \leq X \leq \frac{l_M+l_L}{l_M}$, $l_L = 60$ µm, slow CTD cast) on the other side ($T = 25$ °C). (a) Oxygen profiles inside the two layers after an ambient step change in normalized partial pressure $\Phi(X > \frac{l_M+l_L}{l_M}, t = 0)$ from 0 to 1. O_2 only reaches the membrane after permeating the boundary layer and the O_2 supply is limited by the O_2 diffusion along the boundary layer gradient. (b) Step response function $h(t)$ for different boundary layer thicknesses l_L (green) and for a gas phase time response ($l_L = 0$ µm, dashed red).

The model is illustrated in figure 4.1a and step response curves $h(t)$ for different l_L values are shown in figure 4.1b. The smaller the boundary layer, the steeper the gradient between ambient medium and sensing membrane and thus the stronger the O_2 supply to the sensor. In consequence, the sensor's time response becomes faster. Details of the diffusional model can be found in the appendix.

Laboratory Experiments

Laboratory experiments were designed as isothermal step response experiments. An aquarium pump and a N_2 gas cylinder were used to adjust the oxygen content of two water reservoirs, one close to air saturation and one strongly depleted in O_2. These two reservoirs were at the same temperature and the sensors were switched between them (ca. 10 times in both directions). With this design, both falling (air → N_2) and rising (N_2 → air) steps can be observed.

To investigate the flow speed and temperature influence on the sensor's time response separately, two types of laboratory experiments were done: One where the flow rate was varied while the temperature was kept constant at 25 °C (experiment **1**), and three where the mixing was kept constant while data were obtained at different temperatures (experiments **2** – **4**). Table 4.2 gives a summary of both the laboratory and field experiments (explained below) and the sensors used for each setup.

exp. no.	experiment type	experiment label	sensor model / serial number 3830	4330	4330F	SBE63	Rinko
1	lab (s)	flow speed		1225	135	392	
2	lab (T)	pumped		1225	135	115	
3	lab (T)	lab standard	1260	183	207		
4	lab (T)	"slow-platform"		845	207	115*	54
5	field	ANT-XXVII/2	529		207		10
6	field	MSM 18/3		564			
7	field	glider	1059				
8	field	polar floats	8 units				
9	field	CO_2 float	1 unit				

Table 4.2: Summary of both flow speed (s) and temperature (T) laboratory and field experiments with associated sensor serial numbers if the sensor model was present. (*) The SBE63 was used unpumped with bare optical window for experiment **4**.

For the flow speed experiment **1**, a pumped setup was used in combination with the SBE63's plenum or a custom flow cell for the Aanderaa optodes, and a three way valve to switch the two reservoirs. The flow rate was adjusted using an Ismatec Ecoline VC-380 peristaltic pump (Ismatec GmbH, Wertheim/Germany) (100 – 2500 mL min^{-1}) or a SBE 5P/5T pump (7000 mL min^{-1}), respectively. The manufacturer's plenum for the SBE63 has a small inner volume of 3.5 mL, whereas our plenum for the Aanderaa optodes has 23.5 mL.

For the temperature experiments, three different flow regimes were chosen: For the pumped experiment **2**, the same setup as above was used with the highest flow rate but the temperature of the reservoirs and sensors varied between 2 °C and 32 °C. Experiment **3** resembled the most common laboratory setup to determine response times (Tengberg et al., 2006; Uchida, 2010), using two thoroughly stirred beakers as reservoirs and moving the sensors quickly between both. Finally, experiment **4** imitated slowly-moving platforms such as gliders and floats. As gently-stirred reservoirs, the internal bowls of two identical cryostats (F25, Julabo GmbH, Seelbach/ Germany) were used. Again, sensors were switched by moving them quickly between both reservoirs. For this experiment, the plenum of the SBE63 was removed and all sensors used with bare optical windows. It needs to be stressed that using the SBE63 unpumped is not intended by the manufacturer.

For quantification, all step response curves $h(t)$ were fitted individually and outliers detected and removed using a generalized extreme Studentized deviate (ESD) test (Rosner, 1983). Figure 4.2 shows an example of the (normalized) step response curves for optode 3830 SN 1260 at 16 °C during experiment **3**. The fit equation for the exponential response time τ is given in equation 4.3

$$h(t) = A \cdot \left(1 - e^{-\frac{t-t_0}{\tau}}\right) \tag{4.3}$$

where A is an amplitude to match the height of the step and t_0 is a time offset to precisely match the start of the step within the time discrete sensor samples.

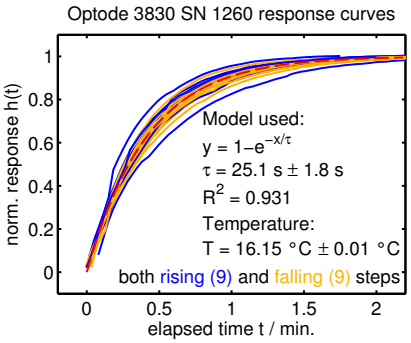

Figure 4.2: Normalized step response curves $h(t)$ for optode 3830 SN 1260 at 16 °C (experiment **3**) with exponential fit (red dashed line).

The boundary layer thickness l_L was obtained analogously from the step response curves $h(t)$. Since the results from rising and falling steps are indistinguishable (see figure 4.2), they are merged for clarity in all subsequent plots.

Field Experiments

The field experiments feature the major profiling platforms commonly equipped with oxygen sensors: Hydrocasts with a CTD (experiments **5** & **6**) and profiles by autonomous gliders and floats (experiments **7** – **9**).

Table 4.3 gives a summary of the technical data for the field deployments, i. e., the number of profiles for each sensor, the duration of the acquired record together with the sampling rate as well as the velocity and temperature regime of the deployment. The sensors used in each experiment are given in table 4.2.

In these field applications, the optode essentially measures a delayed, filtered version of the true oxygen profile.

The in situ model below (equations 4.4 – 4.6) mimics the optode by applying a single-pole low-pass filter on the "true" oxygen profile, i. e., by convoluting the optode time response with the "true" oxygen profile. Its purpose is to obtain an in situ response time τ. The "true" in situ oxygen profile originates from a fast respond-

exp. no.	experiment label	sensor model	no. of profiles	duration of profiles	sample interval	vel. range / dbar s^{-1}	T range / °C
5	ANT-XXVII/2	3830	149	322 h	5 s	0.5 – 1.2	−1.1 – 2.5
5	ANT-XXVII/2	4330F	175	324 h	5 s	0.5 – 1.2	−1.1 – 2.5
5	ANT-XXVII/2	Rinko	168	332 h	24 Hz	0.5 – 1.2	−1.1 – 2.5
6	MSM 18/3	4330	13	11 h	5 s	0.2 – 1.0	4.7 – 26.4
7	glider	3830	65	108 h	2 s	ca. 0.3	5.6 – 28.5
8	polar floats	3830	8	52 h	50 – 600 s	0.09	−1.4 – 3.9
9	CO_2 float	3835	1	2 h	ca. 150 s	0.03	14.1 – 27.1

Table 4.3: Specifications of the CTD, glider, and float field experiments.

ing reference sensor (e. g., a SBE43 clark-type electrode, equation 4.6) on the same platform or from a co-located reference profile through an isopycnal match. The bilinear Z-transform (equation 4.4, see appendix) of the time-continuous response (equation 4.3) is used for the time-discrete data.

$$c_{i+1}^{\text{filt}} = a \cdot c_i^{\text{filt}} + b \cdot \left(c_{i+1}^{\text{in situ}} + c_i^{\text{in situ}}\right), \qquad a = 1 - 2\,b\,, \quad b = \left(1 + 2\,\frac{\tau}{t_{i+1} - t_i}\right)^{-1} \tag{4.4}$$

$$c_{i=0}^{\text{in situ}} - c_{i=0}^{\text{filt}} = f_0 \tag{4.5}$$

$$c_i^{\text{in situ}} = c_i^{\text{SBE43}} + r \tag{4.6}$$

The filter was applied to a short interval of the "true" in situ oxygen profile $c^{\text{in situ}}$ following the recursive equation 4.4 with the initial condition equation 4.5 and the calibration offset r (equation 4.6). The latter allows to compensate for a possible calibration mismatch between optode and SBE43 that would otherwise bias the model fit.

Figure 4.3 illustrates the in situ model, which foremost approximates the shape of the profile. In the example, the quasi-continuous SBE43 record c^{SBE43} provides the reference O_2 profile shape. Within a short time window, the profile data is filtered with a response time τ to simulate the effect of the optode response (c^{filt}). The response time τ is then iteratively refined (as well as f_0 and r) until the filtered profile c^{filt} matches the discrete optode record c^{optode}.

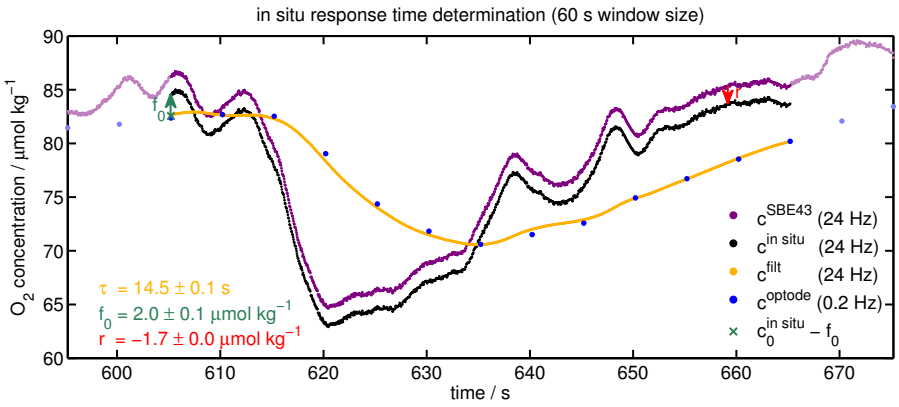

Figure 4.3: Illustration of the in situ model. The optode observations (blue dots) are approximated within a 60 s time window (i. e., $605 - 665$ s of the cast) by c^{filt} (yellow dots), which is the in situ O_2 (black dots) filtered with the time constant τ. The in situ O_2 is based on the SBE43 observations (purple dots) allowing for a calibration offset r (red arrow) within the fit routine. The initial forcing f_0 (green arrow) defines the start member (green cross) of the filter. The parameters and initial condition are given with their 95 % confidence bounds. (During this 60 s time window, the temperature was 9.0±0.4 °C and the CTD descended from 394 dbar to 456 dbar.)

By letting the time window float through the entire profile record, an in situ response time τ is thus obtained for each optode observation. Strictly speaking, it is rather a response time difference to the reference sensor, but the standard processing (e. g., for the SBE43, see Edwards et al., 2010) is assumed to produce a reference profile with zero lag. Due to the short duration of the time window, changes in velocity s and temperature T were small (90th percentile of $\sigma(s)$ and $\sigma(T)$ at 0.2 dbar s^{-1} and 0.5 °C for **6**) and therefore a mean value was used to characterize each time window.

The response times follow an inverse Gaussian distribution. Therefore, all plots of field data in the assessment section show only the respective distribution's mode (i. e., most frequent) value, the distribution's width, and its mean value. Further technical and quality control aspects of this approach are detailed in the appendix.

4.3 Assessment

The assessment starts with the laboratory experiments **1** – **4**, i. e., the flow speed and temperature dependence of the time response. It continues with a discussion of the CTD field deployments (**5** & **6**). Subsequently, the time response impact on data and a possible reconstruction of an original O_2 profile are illustrated with these data. At the end, the assessment proceeds with the glider and float field deployments (**7** – **9**).

Flow Speed Dependence

All sensors show the same behaviour: Both the response time τ and the boundary layer thickness l_L are inversely proportional to the flow speed (figure 4.4). However, the sensors are not fully comparable since the geometry of the custom Aanderaa optode's flow cell and the SBE63 plenum differed somewhat: The flow hit the optical window of the Aanderaa optodes in a 45° angle while it passed it tangentially in the SBE63 plenum. Moreover, the dead volume of the plenums were different (23.5 mL vs. 3.5 mL), affecting the mixing time inside the plenum. The data presented here are not corrected for any such geometry effect.

Given the large spread of flow rates during experiment **1**, response times τ vary between a few seconds and close to a hundred seconds at 100 mL min^{-1} (data not shown). Compared to that, differences between sensors are small, e. g., an Aanderaa optode model 4330 with standard foil can achieve the same response time as a model 4330F with fast response foil if the flow rate is doubled. At the same time, all sensors can yield response times τ below 10 s if they are used in pumped mode (experiment **2**).

For the diffusional model (figure 4.4b), a sensing membrane thickness l_M of 100 µm was used for the Aanderaa standard foil (model 4330), while 30 µm was used for the fast response foil (model 4330F) (PSt3 membranes, Huber, 2010). The Sea-Bird SBE63 optode was treated in the same way as the PSt3 standard foil.

When extrapolated to infinite flow rates, the boundary layer should vanish completely ($l_L^\infty \to 0$ µm) and only the sensing foil time response should remain. This

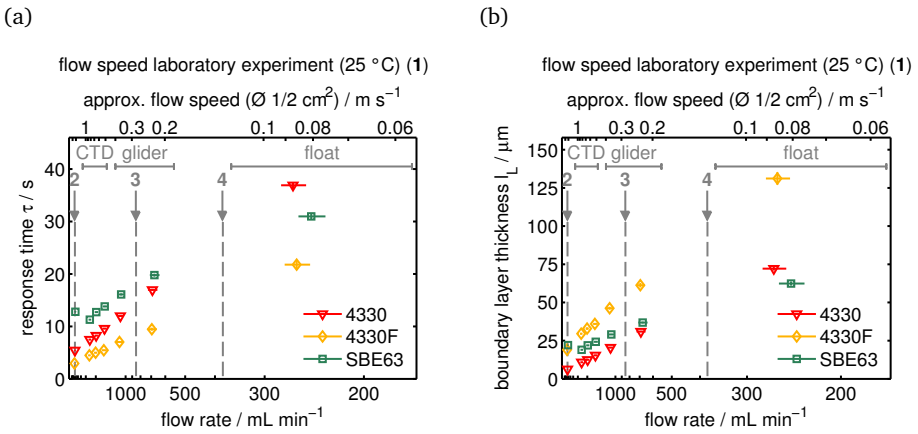

Figure 4.4: Flow rate dependence of the time response at 25 °C (experiment **1**). Data are plotted vs. the reciprocal flow rate for both methods, the exponential approach (a) and the two-layer diffusional model (b). Flow rates were converted to an estimate of the flow speed using a plenum cross section of $\frac{1}{2}$ cm^2. Grey arrows denote approximate flow regimes used for the temperature dependent experiments **2** – **4** (figure 4.5). Approximate regimes for field platforms are indicated by grey bars.

is indeed found for the standard foil model 4330 ($l_L^\infty = 4 \pm 4$ µm, $\pm 1\,\sigma$). The fast response model 4330F and the SBE63 optode, however, have a significant non-zero intercept ($l_L^\infty = 18 \pm 4$ µm and $l_L^\infty = 14 \pm 3$ µm, respectively). This indicates that part of the sensing membrane time response gets falsely attributed to the boundary layer.

To obtain consistency within the diffusional model, l_M was adjusted to 50 µm for the fast response foil and to 130 µm for the SBE63 optode hereafter. In fact, all three sensors then follow the same l_L – flow rate dependence (not shown), indicating that the diffusional model is suitable to characterize the boundary layer processes in front of the sensor membrane for all sensors.

Based on boundary layer theory (Schlichting and Gersten, 1997), the thickness of the velocity boundary layer is inversely proportional to the square-root of the Reynolds number and thus flow speed. l_L scales accordingly which leads to the faster response at high flow rates.

Temperature Dependence

From the spread of flow rates of experiment **1**, three distinct regimes were chosen to analyze the temperature influence: experiment **2** with pumped sensors at the high end (figure 4.5a & 4.5b), experiment **3** with thoroughly-stirred beakers (figure 4.5c & 4.5d) to provide results comparable to other lab studies, and experiment **4** at the low end (figure 4.5e & 4.5f) to imitate comparatively slow, buoyancy-driven platforms such as floats and gliders.

At low temperatures, solubilities $S(T)$ increase so that more O_2 molecules have to diffuse into the sensing membrane to obtain the same pO_2, i. e., the same re-

sponse. At the same time, diffusivities $D(T)$ decrease so that this diffusion takes longer. Both effects lead to markedly increased response times τ at low temperatures. Over the temperature range 2 °C – 34 °C, response times τ vary by approximately ± 25 % around the mean value.

The boundary layer thickness l_L, however, is rather constant for a given experiment, indicating that molecular diffusion is the dominant process for the temperature dependence.

Experiment **2** yields a number of useful results:

(a) The sensor time response can be accelerated when used in a pumped setup, an approach that has been realized for the SBE63.

(b) A pumped setup yields a highly reproducible time response (95 % confidence intervals are hardly visible in figure 4.5a).

(c) With a boundary layer of only ca. 5 µm, response times τ in experiment **2** are close to their lower limits (i. e., the gas phase response).

The SBE63 optode appears to use a thicker sensing foil than the Aanderaa standard foil model 4330, or the geometry effect of the plenum is of considerable importance (see also experiment **1**).

In a pumped setup, sensors can be even faster than claimed by the manufacturer, see, e. g., the Aanderaa optode specifications in table 4.1. Moreover, boundary layer thicknesses l_L vary only marginally (4 µm − 6 µm), show no temperature dependence, and are the same for all sensors.

The standard laboratory time response setup with stirred beakers (experiment **3**) gives results similar to the ones reported in the literature (see table 4.1, Aanderaa Data Instruments AS (2012), and Tengberg et al. (2006)), with response times τ for the standard foil models 3830 and 4330 around 25 s and around 8 s for the fast response foil model 4330F. Again, the boundary layer thickness for both the 4330 and the 4330F optode are comparable ($l_L \approx 29 \pm 5$ µm), supporting the validity of the diffusional model. The somewhat higher values for the 3830 optode might be an effect of the different geometry of that model compared to the 4330 optode.

Finally, experiment **4** imitates the least-turbulent deployment platforms and provides the following findings:

(a) The Aanderaa optode model 4330 appears to use a slightly thinner membrane than the SBE63 optode and is therefore, in principle, faster.

(b) The JFE Alec Co. Rinko sensor is the fastest of all optodes, although its response time τ is an order of magnitude higher than claimed by the manufacturer (see table 4.1, JFE Alec Co. (2009)).

(c) Even with slow response times τ, their temperature dependence is explained by solubility $S(T)$ and diffusivity $D(T)$ variations (i. e., $l_L(T)$ is approximately constant).

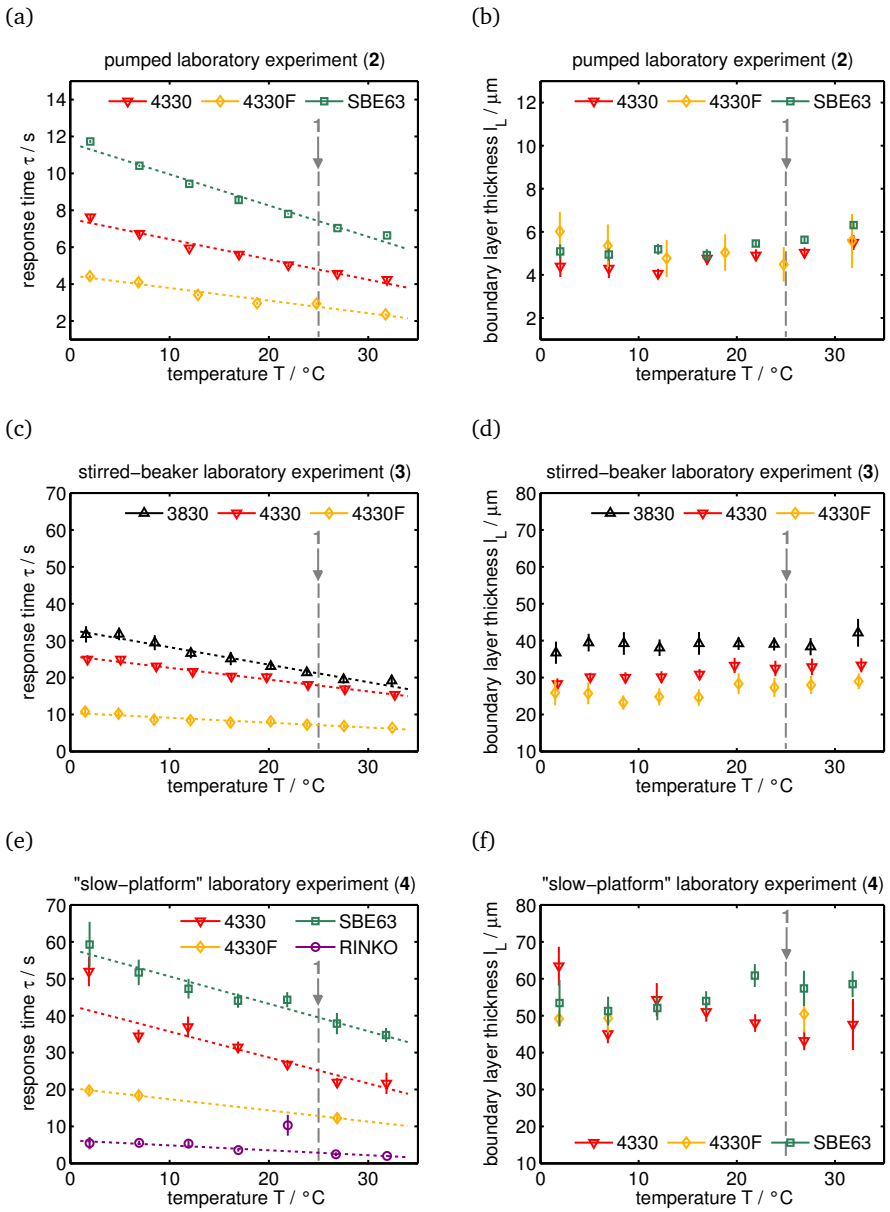

Figure 4.5: Temperature dependence of the time response at three flow regimes. Experiments (from top to bottom) are: a pumped setup **2** (a & b), a stirred-beaker standard setup **3** (c & d), and a "slow-platform"-imitating setup **4** (e & f). Results are shown for both an exponential approach (left column) and a two-layer diffusional model (right column). The grey arrow denotes the temperature of the flow speed experiment **1** (figure 4.4).

No sensing membrane thickness l_M was available for the JFE Alec Co. Rinko. If it were zero, the liquid boundary layer l_L would have to be around 133±32 µm for the observed time response (figure 4.5e). This is unrealistically high compared to the other three sensors of experiment **4** (figure 4.5f). Rather, the sensor's coating itself possesses a response delay (i. e., it needs to be "filled" with O_2), which is falsely attributed to the boundary layer.

CTD Field Experiments

CTD-mounted optodes were investigated on two cruises: the R/V Polarstern cruise ANT-XXVII/2 (Rohardt et al., 2011) to the Southern Ocean (experiment **5**) and the R/V Maria S. Merian cruise MSM 18/3 (Krahmann and Fischer, 2012) to the Eastern Tropical North Atlantic (experiment **6**). On both cruises, a calibrated SBE43 sensor served as reference to derive the optode's in situ response times τ. The results of both experiments are presented in figure 4.6. The left panels show photographs of the sensors' attachments to the CTD frame, while the middle and right panels show the binned in situ response time distributions vs. vertical velocity and temperature, respectively.

The flow speed was the dominant factor in the laboratory experiments **1**– **4**. In fact, a flow speed dependence can be seen with the field data of the JFE Alec Co. Rinko in experiment **5** (figure 4.6b) and much more obvious with the Aanderaa optode in experiment **6** (figure 4.6c). In both settings, the optical window pointed downward and the sensors were attached without obstacles to the flow nearby. The optodes' time response is fastest during downcast and slowest when the CTD was near-stationary or hoisted slowly, with a factor of 2 in between the bins' response times τ.

In contrast, the Aanderaa optodes in experiment **5**, attached in horizontal direction close to a bar of the CTD frame, show no sign of a speed dependence (figure 4.6a). In fact, the frame seems to create a regime of constant local turbulence, even at low speeds.

The mode of attachment and orientation of a sensor is therefore a crucial part of the setup design.

Both experiments **5** & **6** support the temperature dependence found in the laboratory (experiments **2** – **4**), being slower at low temperatures (figure 4.6, right panels). Still, the spread of the field data (and the limited temperature range of **5**) would have made it difficult to derive a temperature relation without the laboratory evidence.

The average response times τ of 35±15 s and 14±10 s for the Aanderaa optodes model 3830 and model 4330F in **5** translate to a boundary layer thickness l_L of 41 ± 21 µm for the standard foil and 39 ± 32 µm for the fast response foil ($\pm 1\,\sigma$). Regarding the Rinko sensor, the field analysis yields an average response time of 4.7±2.6 s, compared to the processed SBE43 reference (Edwards et al., 2010). This appears to be a more suitable estimate of the Rinko response time τ under real conditions than the gas phase response time given by the manufacturer (table 4.1).

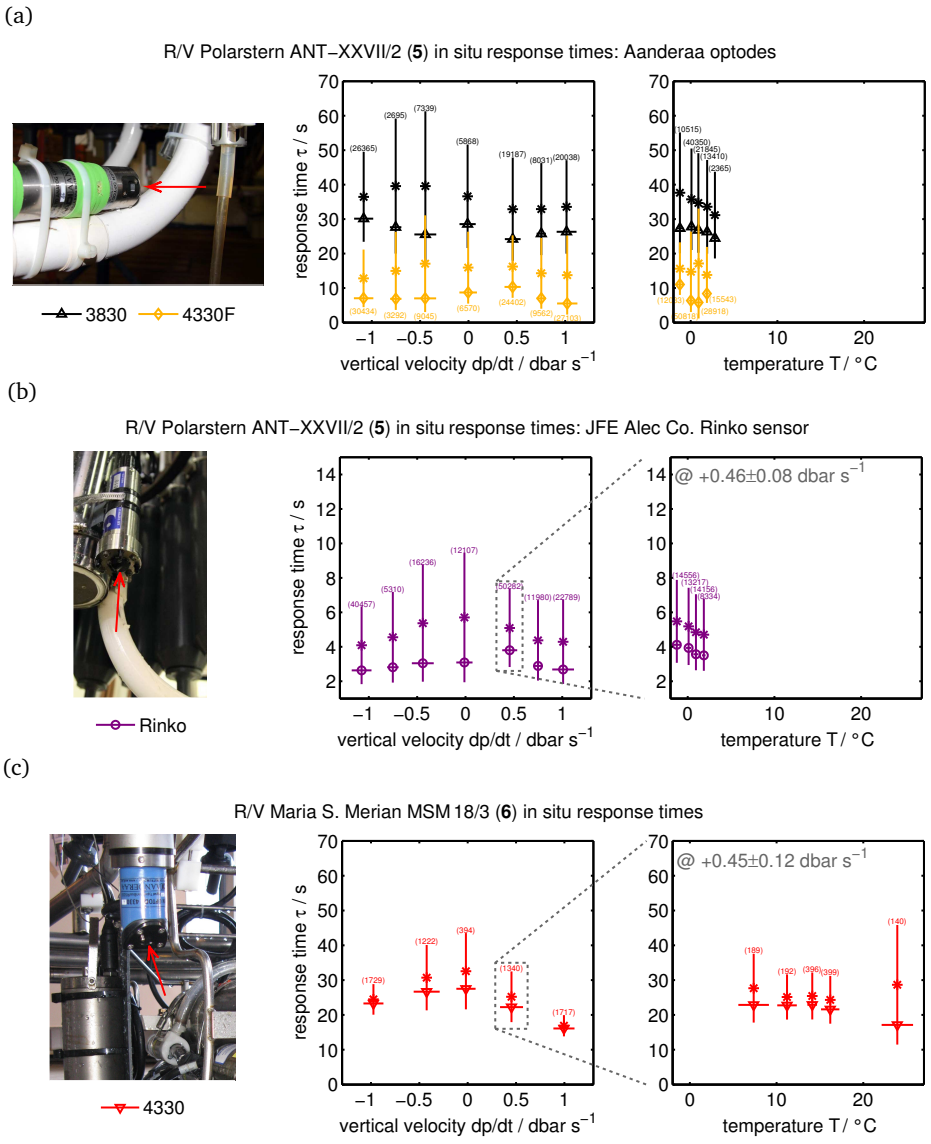

Figure 4.6: In situ response times for CTD experiments **5** and **6**. Left panels: Sensor attachment and orientation at the CTD frame. The red arrow points at the optical window. During R/V Polarstern ANT-XXVII/2 (**5**), both Aanderaa optodes were attached adjacent to a horizontal bar with the optical window facing out horizontally (a). In contrast, the JFE Alec Co. Rinko sensor (**5**) (b) and the optode during R/V Maria S. Merian MSM 18/3 (**6**) (c) were attached without obstacles nearby and with the optical window facing downward. Middle panels: In situ response time τ against CTD vertical velocity with mode value (marker), distribution width (bar, mean $\pm\,\sigma$), and mean value (asterisk). The number of observations in each bin is given in parentheses. Right Panels: In situ response time τ against temperature. For the JFE Alec Co. Rinko data of **5** and for **6**, only one distinct velocity bin (grey dotted box) was used due to the flow speed dependence.

For the standard foil model 4330 in **6**, however, the l_L varies between 19±4 µm when the sensing foil is hit directly (+1.0 dbar s^{-1} bin) and 48±18 µm when it is effectively shaded by the CTD body and Niskin bottles (0.0 dbar s^{-1} & −0.5 dbar s^{-1} bins).

Time Response Impact and Oxygen Data Reconstruction

The effect of the time response on data acquired in the field is discussed below. As an example, a CTD station from experiment **6** at 4.5° N 23° W located in the oxygen minimum zone off Northwest Africa is used. Besides substantial O_2 gradients throughout the profile, both temperature and vertical velocity vary during this CTD cast, so their combined effect can be illustrated.

For a given O_2 profile, the optode measures a filtered analogue (see equation 4.4). This filter has two effects:

- Fine scale structure of the original O_2 profile is lost.
- The sensor responds with a delay to every gradient.

The effects are cumulative, i. e., a gradient or forcing a moment ago still has an influence on the current measurement. So every past fluctuation or gradient (weighted with the scale of the response time) has, in principle, an influence on the measurement error β_i^{filt} between true profile $c_i^{\text{in situ}}$ and filtered measurement c_i^{filt}.

$$\beta_i^{\text{filt}} = c_i^{\text{filt}} - c_i^{\text{in situ}} \tag{4.7}$$

However, since the fine scale structure shows both positive and negative fluctuations, these tend to cancel out. In contrast, water mass gradients tend to persist longer than the timescale of the time response. They are in fact the main cause for the observed measurement error β.

The error β depends on the local forcing δ, defined as

$$\delta = -g \cdot s \cdot \tau(T) = -\frac{\mathrm{d}c}{\mathrm{d}p} \cdot \frac{\mathrm{d}p}{\mathrm{d}t} \cdot \tau(T) \tag{4.8}$$

with $g = \mathrm{d}c/\mathrm{d}p$ being the O_2 gradient and $s = \mathrm{d}p/\mathrm{d}t$ the vertical velocity. β is essentially the filtered version of δ.

Figure 4.7 shows both the downcast and upcast of the above mentioned CTD station, with the O_2 profile on the left and the measurement error β on the right. Apart from the reference profile (black) and the optode measurements (blue), it contains a simulation of the optode time response (yellow) based on the reference and a reconstruction of the original profile (red) based on the optode (details below).

The fine scale fluctuations of the reference profile (black) between 500 dbar and 600 dbar are not grasped by the optode measurements (blue), but do not cause a strong error either. The surface oxycline around 100 dbar, however, causes a significant error since it represents a strong peak in the local forcing δ due to its extreme gradient. For the upcast, the measurement error β then declines exponentially as there are no further gradients (i. e., δ=0) in the surface mixed layer.

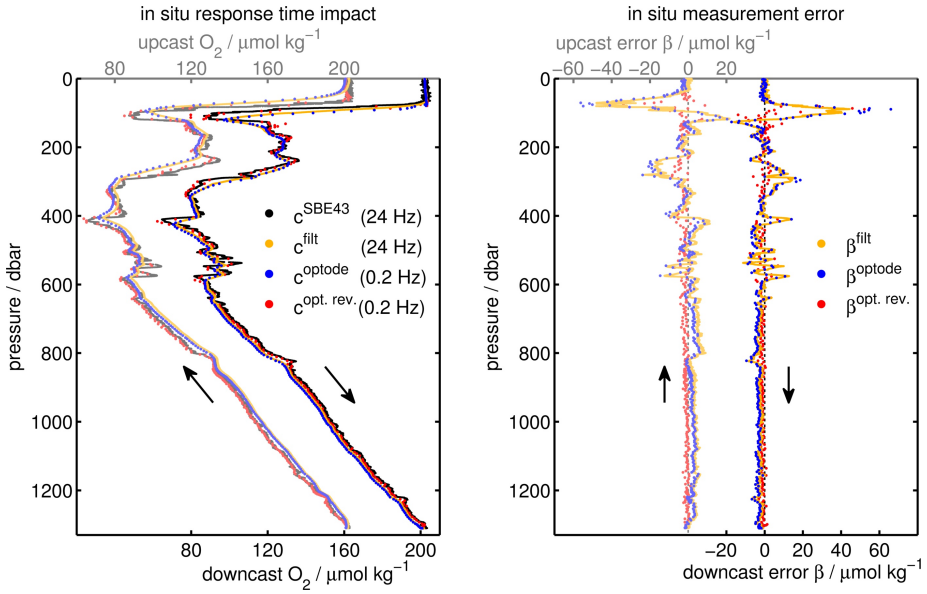

Figure 4.7: Downcast and upcast (brighter coloured and offset by -40 µmol kg^{-1}) O_2 profile (left) and measurement error β (right) as acquired at the R/V Maria S. Merian MSM 18/3 CTD station at 4.5° N 23° W (experiment **6**). The quasi-continuous and fast SBE43 reference data are given in black. The simulated optode-like time response is shown in yellow and the actual optode observations (model 4330) are given in blue. The different contributions to the measurement error are illustrated in figure 4.8. The red dots show the reconstruction of the original O_2 profile from the optode observations.

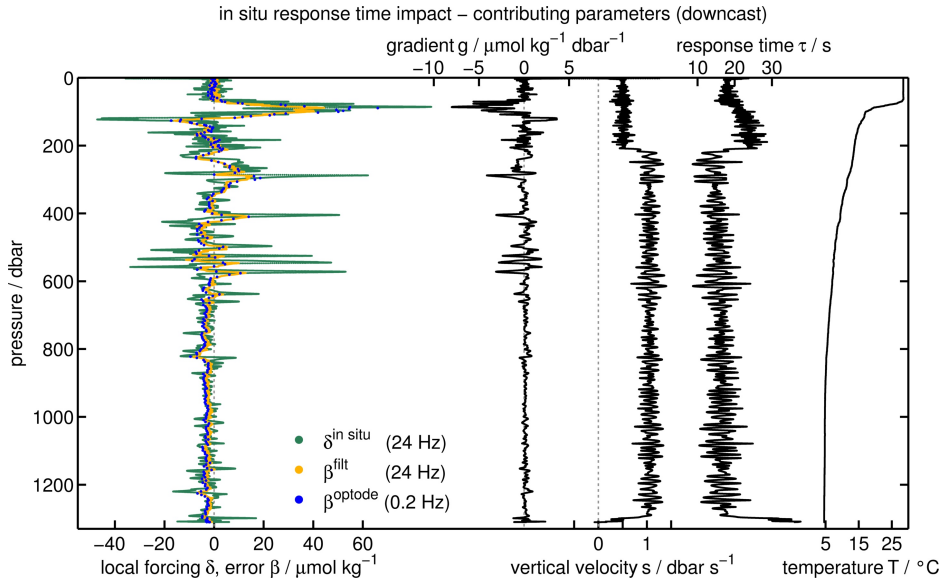

Figure 4.8: Modelled and observed measurement error β and its influence factors for the downcast at R/V Maria S. Merian MSM 18/3 CTD station at 4.5° N 23° W (experiment **6**). The local forcing δ is the product of O_2 gradient g, vertical velocity s, and response time τ. Applying the filter to the local forcing δ directly gives the measurement error β. The temperature effect on the response time τ is pronounced near the surface where velocities are small.

The different factors affecting the optode time response are separated in figure 4.8 for the downcast section of the same profile.

The low velocities in the upper 200 dbar cause a thicker boundary layer than for the remainder of the downcast, but high surface temperatures lead to relatively small response times. At greater depths, high velocities lead to a considerably thinner boundary layer but low temperatures increase response times. The resulting response time τ is therefore only $5-10$ s higher in the surface than at depth. Still, gradients are highest near the surface and thus is the local forcing δ as well as the (accumulated) measurement error β.

For the simulation of the optode time response (yellow in both figures 4.7 & 4.8), response times τ were derived using the boundary layer l_L – vertical velocity s relation from experiment **6** and then converting l_L to response times τ at in situ temperatures.

The reverse operation to simulating the optode time response, i. e., the reconstruction (or deconvolution) of the original profile from time-lagged measurements, is of great importance for practical applications. However, this approach has some major caveats:

(a) The reconstruction or deconvolution severely amplifies noise in the data.

(b) The data sample interval should be about an order of magnitude shorter than the response time.

Dedicated algorithms have been developed for the noise issue in order to minimize processing artifacts (e. g., Miloshevich et al., 2004). These have been applied both to atmospheric data (e. g., radiosonde humidity measurements, Miloshevich et al., 2004) and oceanic data (e. g., float pCO_2 measurements, Fiedler et al., 2013) and are used in this work as well (see appendix).

The reconstruction is shown in red in figure 4.7. Despite the fact that the sample interval condition given above is poorly met (5 s sample interval vs. ca. 20 s response time), the deconvolution still gives a reasonable result (root-mean-square error of 4.8 $\mu mol\,kg^{-1}$ compared to 9.7 $\mu mol\,kg^{-1}$ for the original sensor data). Moreover, realistic finescale features are restored but artifacts occur at strong gradients, e. g., the subsurface oxycline. A higher temporal resolution might have improved the reconstruction in these parts of the profile.

Glider Field Experiment

A Slocum glider (Teledyne Webb Research, Falmouth, MA, USA) was used for experiment **7** with an Aanderaa optode model 3830 attached close to the glider's tail. It was deployed during R/V Maria S. Merian cruise MSM 22 near 5° N 23° W and circled around a mooring at that location. The glider cycled the upper 900 m of the water column, regularly crossing the thermocline. For comparison, a total of 6 CTD casts were performed during the glider's 3-week deployment period within a distance of 10 nm. Only glider dives with a time difference below 8 hours were considered and results are given in figure 4.9.

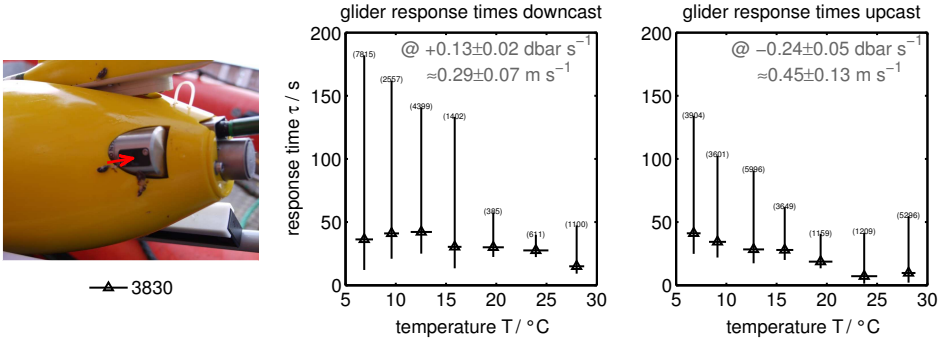

Figure 4.9: Results of the field deployment on a Slocum glider during R/V Maria S. Merian MSM 22 (**7**). Left panel: Sensor attachment and orientation of the optode at the glider's tail. The red arrow points at the optical window. Middle and right panel: In situ response time distribution for the downward and upward dives against temperature with mode value (marker), distribution width (bar, mean ± σ), and mean value (asterisk). The number of observations per bin is given in parentheses.

The glider's speed was derived from the vertical velocity, the pitch angle, and an assumed angle of attack of 3°. It is relatively constant for this buoyancy-driven platform. However, the upcasts in experiment **7** are slightly faster as are the upcast response times τ, reflecting the flow speed influence. More dominantly, however, a strong temperature effect can be seen in the response times τ for both the down-

cast (middle panel) and the upcast (right panel). The diffusional model is able to explain the temperature dependence of the mode value of the response time distribution. However, there is a significant fraction of very high response times τ, which considerably broaden the width of the distribution.

Given the broad and asymmetric distribution, a mean response time τ seems of little value. Translated to a boundary layer thickness l_L, the downcast ranges at an average of 110±86 µm whereas the upcast yields 71±60 µm (±1 σ).

Argo-Float Field Experiments

For the polar float experiment **8**, a total of 8 floats (each with an Aanderaa optode model 3830) were deployed in polar seas: 6 during R/V Polarstern cruise ANT-XXVII/2 (see experiment **5**) in the Weddell Sea and 2 during R/V Oceania cruise AREX10 along 75° N in the West Spitsbergen Current. The floats had a typical ascent velocity of -0.087 ± 0.002 dbar s^{-1} and they did log the time stamp for each float observation. This allowed the comparison to CTD profiles measured nearby.

For the cold waters, the floats gave response times τ around 190±230 s and an average l_L of 210±230 µm, much larger than anticipated from the laboratory experiments alone. However, their results are badly constrained as they measured their first profile only 10 days after deployment, which adversely affects the match between float and CTD-based reference profile.

A slightly different float was used for the CO_2 float experiment **9**. It was equipped with an Aanderaa optode model 3835, a shallow water version of the model 3830, and a pCO_2 sensor (see Fiedler et al., 2013). The float was deployed in the vicinity of the Cape Verde Ocean Observatory (CVOO, 17.6° N 24.3° W, http://cvoo.geomar.de), located in the Eastern Tropical North Atlantic oxygen minimum zone. In contrast to standard Argo floats, it performed a test profile just after its deployment. This allowed a more direct comparison to a CTD profile measured by R/V Islândia directly after completion of the first profile on-site. Both profiles are shown in figure 4.10, together with a simulation of the optode time response.

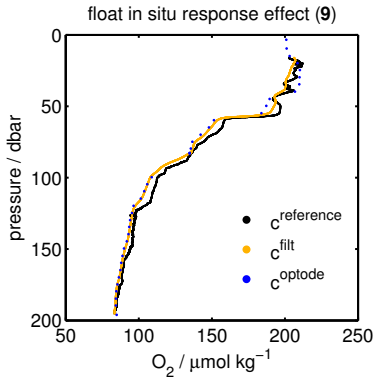

Figure 4.10: Oxygen profile of an experimental Argo-O_2/pCO_2 float (blue) with co-located reference profile from R/V Islândia (black) and simulated sensor time response (yellow) (experiment **9**).

A boundary layer thickness l_L around 440±80 µm was found to match the observations of experiment **9** best. This equals response times τ around 280±50 s, even higher than for the polar floats (experiment **8**) despite the warmer temperatures. However, this experimental float showed an average ascent speed of only -0.026 ± 0.012 dbar s^{-1} for the 200 m profile, which is very slow even for a float. The extremely low velocity environment thus causes the high response times.

Still, even with such high response times τ, the measurement error during experiment **9** is as low as 4 µmol kg^{-1} on average and does not exceed a maximum of 16 µmol kg^{-1}. This is due to the float's slow progression through the water column including gradient regions, which counterbalances the high response times τ (see equation 4.8).

4.4 Summary

Oxygen optode response times τ vary over a large range depending on the flow speed and temperature regime of the application. They can be as short as a few seconds in pumped setups (see experiments **1** & **2**) or well above 100 s on slowly profiling gliders (**7**) or floats (**8** & **9**). Even on the same platform, they are dependent on the optode's orientation (**5**).

However, we showed that, despite their (potentially) slow time response, optodes can be successfully deployed on profiling platforms to produce meaningful data. The impact of the time response on the oxygen data can be quantified and the "true" oxygen profile can be reconstructed under suitable conditions.

In principle, we found no difference between the results from laboratory experiments (**1 – 4**) and field applications (**5 – 9**) and findings are transferable between artificial step response experiments and small and continuous in situ gradients.

The main influence factor on the time response is the flow around the sensor spot, followed by temperature.

In the laboratory (**1**), an indirect proportionality was found for the time response and the flow rate (figure 4.4). In the field, however, no strict functional behaviour was discernible, but the inverse relation is clear (see, e. g., figure 4.6c).

For the temperatures found in the ocean, a close to linear temperature effect on the response time τ was found at set flow conditions (experiments **2 – 4**; figure 4.5, left column). This is caused by the temperature dependence of molecular diffusion, i. e., variations in oxygen diffusivity $D(T)$ and solubility $S(T)$ both in the aqueous boundary layer and in the sensing material.

In fact, boundary layer effects are a significant portion of the sensor's time response in water and must not be neglected. The manufacturers' specifications (table 4.1) could be confirmed for the Aanderaa optodes using a thoroughly-stirred setup (**3**) and for the Sea-Bird SBE63 optode using a pumped setup (**2**). For the JFE Alec Co., Inc. Rinko, however, response times τ were an order of magnitude higher than given by the manufacturer ($\tau = 0.4$ s in the gas phase, JFE Alec Co., 2009) in all of our experiments due to boundary layer effects always present in water.

Using a two-layer diffusional model made up of a sensing membrane layer and a stagnant, immobile liquid boundary layer on top (figure 4.1), combined with pa-

rameterizations for $D(T)$, $S(T)$, and Fickian diffusion (see appendix), the temperature dependence of the sensor time response vanishes (figure 4.5, right column). Instead, the liquid boundary layer thickness l_L is independent of temperature and can thus be used to characterize the flow regime.

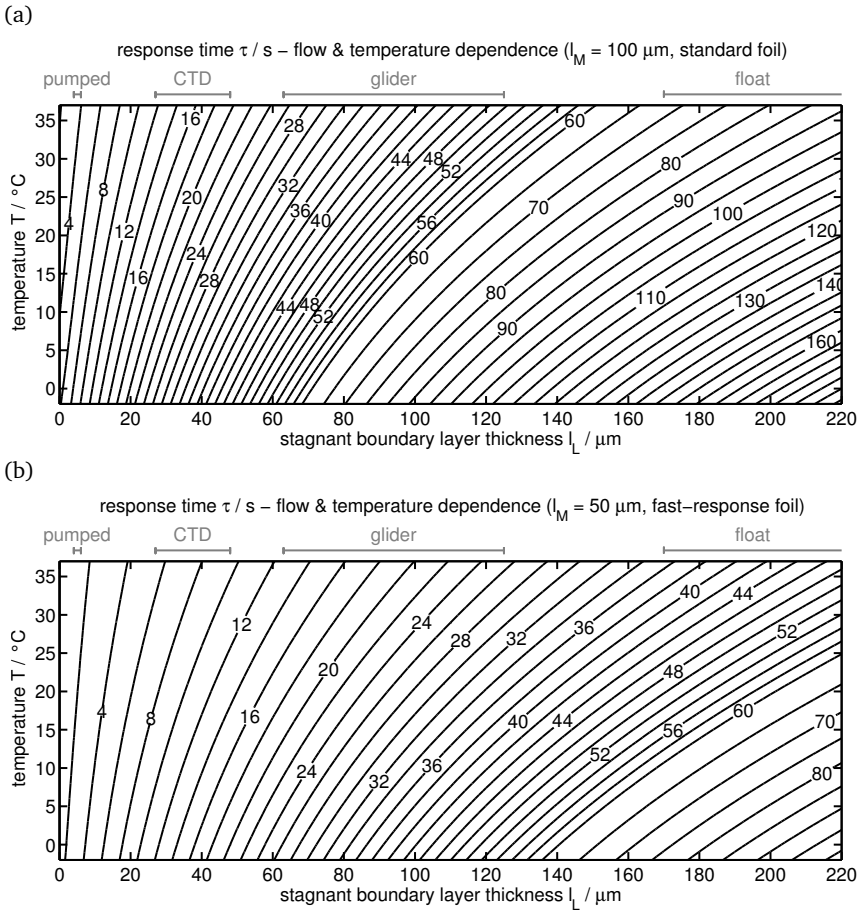

Figure 4.11: Response time τ as a function of stagnant boundary layer thickness l_L and temperature T for a silicone sensing membrane with thickness $l_M = 100$ µm (a) and $l_M = 50$ µm (b). These thicknesses relate to model l_M typical for an Aanderaa optode standard foil and a fast response foil, respectively. Grey bars denote the approximate regime for different field deployments. (For clarity, the spacing of the contour lines changes from 2 s to 5 s at $\tau = 60$ s.)

Figure 4.11 gives the relation between boundary layer thickness l_L, temperature T, and response time τ for both a silicone sensing membrane with 100 µm thickness (a) and one with 50 µm thickness (b). They represent the model membrane thicknesses l_M typical for an Aanderaa optode standard and fast response foil, respectively.

No such chart could be produced for the Rinko dissolved oxygen sensor due to lack of information about the sensing material thickness. Since the intended use of the Sea-Bird SBE63 is a pumped mode with set flow rate, no chart for $l_M = 130$ µm is given but readers are referred to experiment **2** (figure 4.5a).

The look up charts of figure 4.11 can be used in two ways:

(a) to characterize the flow regime (l_L) if a response time τ measurement exists

(b) to predict the response time τ if the flow regime (l_L) is known

It therefore provides a tool to predict the time response for a given application. With knowledge of the sensor's response behaviour, its impact on data accuracy and quality can be quantified as well as the original O_2 profile reconstructed (e. g., figure 4.7).

The results can be used by the community to refine thresholds for response times τ to be achieved by manufacturers, with the aim to yield scientifically usable data (see Gruber et al., 2010)

We found typical l_L regimes for CTDs to be between $20-50$ µm, depending on the CTD velocity (e. g., +1 dbar s^{-1} downcast vs. near-stationary or slow upcast) and sensor attachment (experiments **5** & **6**).

Similarly, a boundary layer thickness l_L around 90 µm was observed on a glider (**7**), and around a few hundred µm on floats (**8** & **9**). The latter two estimates are based on few observations only and need to be confirmed by further work. However, they indicate the magnitude to be expected on these important new platforms.

In addition, figure 4.11 mirrors the interplay between turbulent and molecular transport. Since the two-layer diffusional model considers only molecular diffusion, l_L can be seen as a parameter of turbulent transport: exclusively turbulent transport at $l_L \to 0$ and only molecular transport at $l_L \to \infty$. Moreover, the temperature effect on τ is solely due to molecular transport, i. e., $D(T)$ and $S(T)$ variations, while l_L proved to be temperature-independent (experiments **1** – **4**).

In consequence, temperature becomes an important factor for τ at high l_L conditions (right part of figure 4.11) such as during the float experiments **8** & **9**.

Concluding this work, the time response of optical oxygen sensors has been thoroughly investigated and characterized, both in laboratory and field experiments. While the two-layer diffusional model is not a completely accurate model of the hydrodynamics around the optical sensing membrane, it provides a comprehensive and coherent picture of the main processes as well as a useful, quantitative description of the time response.

Our results can be used to assess and predict the effect on observational data even before a deployment, as well as to reconstruct an unbiased profile from field data and thus recover some of the information lost by the time response as illustrated in figure 4.7. A precondition is to know the in situ response time τ, which can be found in this work (see figure 4.5a & 4.11) for typical deployment regimes. We hope this will contribute to improvements in O_2 data quality, especially from new ocean observatories as the Argo-O_2 program (Gruber et al., 2010).

4.5 Recommendations

Based on our work, the following aspects should be considered for field applications.

- Whenever possible, optodes should be used in a pumped mode to achieve the smallest possible response times τ.

Having a small response time τ in the first place reduces the time response impact on the data (equation 4.8) and thus the need to reconstruct an original oxygen series. At the same time, the pumped mode represents the most reproducible mode of operation, thus minimizing uncertainties on τ for such a reconstruction. However, constraints of the deployment platform (especially battery capacity) may prevent the use of a pumped system.

- The sample interval should be significantly shorter than the response time τ in order to resolve gradient regions and to be able to reconstruct the true oxygen profile.

Especially for irregularly spaced data, e. g., on floats, the aspect of a sufficient sample interval – response time ratio should be considered: By increasing the sample frequency in gradient regions, i. e., the oxycline, a reconstruction of an unbiased and accurate field record may be feasible even with high response times.

- Strong gradients or high response times τ may be counterbalanced by small cast velocities (equation 4.8).

The time response impact depends on the platform's progression through water mass gradients. So even with high response times τ, the measurement error may still be acceptable if the velocities are small (e. g., experiment **9**). This might be an interesting option for, e. g., moored profilers.

4.6 Appendix

Sensor Calibrations

The Aanderaa optodes and the Sea-Bird SBE63 used for the laboratory experiments **1** – **4** were individually multi-point calibrated in the laboratory according to Bittig et al. (2012). The JFE Alec Co. Rinko (**4**) used the factory calibration which was validated against the other sensors. For the CTD experiments **5** & **6** and the polar float experiment **8**, the Aanderaa optodes were as well multi-point calibrated in the laboratory (Bittig et al., 2012) and their data validated against in situ Winkler samples. The Rinko sensor of **5** used the factory calibration coefficients and was calibrated in situ against Winkler samples. The same applies to the Aanderaa optode of experiment **9**. The Aanderaa optode of experiment **7** was in situ calibrated before being mounted on the glider. For this, the optode was attached to the CTD frame for a calibration cast. Bottle stops were about 120 s long and Winkler samples as well as data from a Winkler-calibrated SBE43 were used to calibrate the optode (see Hahn, 2013).

Two-Layer Diffusional Model

The model applied to our data is inspired by Linek et al. (2009). They extended a one-layer model of Cox and Dunn (1986) to include a stagnant boundary layer.

Cox and Dunn (1986) used a planar geometry of a luminophore-doped silicone membrane to derive oxygen diffusion coefficients. Their diffusional model is based on Fickian diffusion (equations 4.9 & 4.10), an impermeable boundary at the optical window-side of the sensing membrane (equation 4.11), and a bulk environment assumed to be sufficiently large and well mixed to be considered as infinite, unaffected reservoir (equation 4.12). It uses equation 4.13 as initial condition and considers only one layer, the silicone membrane with thickness l_M. The materials are assumed to be homogenous (uniform D and S) and normalized space ($X = x/l_M$) and partial pressure ($\Phi = pO_2/pO_{2,\infty}$) coordinates are used. In addition, temporal temperature variations are assumed to be small enough to neglect the temperature dependence of D and S.

$$J = -D\,\frac{\partial \Phi(x,t)}{\partial x} \tag{4.9}$$

$$\frac{\partial \Phi(x,t)}{\partial t} = D\,\frac{\partial^2 \Phi(x,t)}{\partial x^2} \tag{4.10}$$

$$\frac{\partial \Phi(x,t)}{\partial x} = 0 \qquad x = 0,\ t \geq 0 \tag{4.11}$$

$$\Phi(x,t) = 1 \qquad x = \text{bulk},\ t \geq 0 \tag{4.12}$$

$$\Phi(x,t) = 0 \qquad t = 0 \tag{4.13}$$

Analogous differential equations have been solved for the conduction of heat decades ago (Carslaw and Jaeger, 1976) and the solution from Crank (1975) is given in equation 4.14.

$$\Phi(X,t) = 1 - \frac{4}{\pi}\sum_{n=0}^{\infty}\left[\frac{(-1)^n}{2n+1}\cdot e^{-\frac{(2n+1)^2}{4}\pi^2\frac{D_M}{l_M^2}\cdot t}\cdot\cos\left(\frac{2n+1}{2}\,\pi\cdot X\right)\right] \tag{4.14}$$

It determines the O_2 profile or partial pressure distribution inside the sensing membrane as illustrated in figure 4.12a.

The time response of the sensor $h(t)$ is assumed to be the integral of the entire sensing membrane ($0 \leq x \leq l_M$) according to equation 4.15.

$$h(t) = \overline{\Phi_M} = \int_0^1 \Phi(X,t)\,\mathrm{d}X = \int_0^{l_M} \Phi(x,t)\,\mathrm{d}x \tag{4.15}$$

The thus obtained step response for the one-layer model of Cox and Dunn (1986) is given in equation 4.16 and shown in figure 4.12b.

$$h(t) = 1 - 8\sum_{n=0}^{\infty}\left[\frac{1}{(2n+1)^2\,\pi^2}\cdot e^{-\frac{(2n+1)^2}{4}\pi^2\frac{D_M}{l_M^2}\cdot t}\right] \tag{4.16}$$

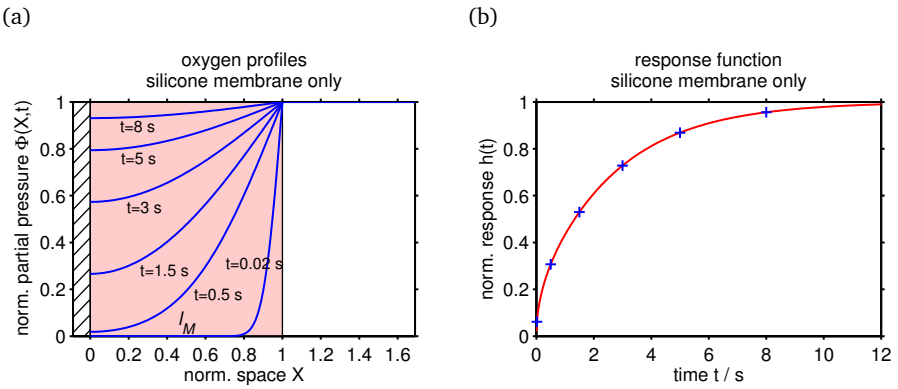

Figure 4.12: One-layer diffusional optode model consisting of a silicone membrane ($0 \leq X \leq 1$) with impermeable boundary (hatched, optical window) after Cox and Dunn (1986). (a) Oxygen profiles inside the membrane after an ambient step change in normalized partial pressure $\Phi(X > \frac{l_M+l_L}{l_M}, t = 0)$ from 0 to 1. (b) Step response $h(t)$ of the optode. A membrane thickness of l_M=100 µm (Aanderaa optode standard foil) and material properties according to table 4.4 were used.

The one-layer model has its representation, e. g., as a gas phase step response experiment (N_2 gas $\leftrightarrow$ air) (see JFE Alec Co., 2009).

The two-layer model of Linek et al. (2009) contains a silicone membrane (thickness l_M) as before. They added an immobile, stagnant liquid boundary layer (thickness l_L) with additional boundary conditions at the layers' interface (continuity of Φ and J: equations 4.17 & 4.18) and adjusting equation 4.10 according to the regime of the layer (equations 4.19 & 4.20).

$$\Big(\Phi(x,t)\Big)_{x\to l_{M-}} = \Big(\Phi(x,t)\Big)_{x\to l_{M+}} \qquad t \geq 0 \qquad (4.17)$$

$$\Big(J(x,t)\Big)_{x\to l_{M-}} = \Big(J(x,t)\Big)_{x\to l_{M+}} \qquad t \geq 0$$

$$D_M \left(\frac{S_M \cdot \partial\Phi(x,t)}{\partial x}\right)_{x\to l_{M-}} = D_L \left(\frac{S_L \cdot \partial\Phi(x,t)}{\partial x}\right)_{x\to l_{M+}} \qquad t \geq 0 \qquad (4.18)$$

$$\frac{\partial\Phi(x,t)}{\partial t} = D_M \frac{\partial^2\Phi(x,t)}{\partial x^2} \qquad 0 \leq x \leq l_M \qquad (4.19)$$

$$\frac{\partial\Phi(x,t)}{\partial t} = D_L \frac{\partial^2\Phi(x,t)}{\partial x^2} \qquad l_M \leq x \leq l_L \qquad (4.20)$$

For the normalized partial pressure Φ, the authors give equation 4.21 as solution to the system of differential equations.

$$\Phi(X,t) = 1 - \sum_{n=0}^{\infty} Q_n \cdot \nu_n(X) \cdot e^{-\lambda_n \frac{D_M}{l_M^2} \cdot t} \qquad 0 \leq X \leq \frac{l_M + l_L}{l_M} \qquad (4.21)$$

It makes use of

$$\nu_n(X) = \cos(\lambda_n X) \qquad 0 \le X \le 1 \tag{4.22}$$

$$\nu_n(X) = \frac{\cos\lambda_n}{\sin(A_L\,\lambda_n)} \sin\left(\sqrt{\frac{D_M}{D_L}}\lambda_n\left(\frac{l_L - l_M}{l_M} - X\right)\right) \qquad 1 \le X \le \frac{l_M + l_L}{l_M} \tag{4.23}$$

and

$$Q_n = \frac{2}{\lambda_n} \frac{\cos(\lambda_n)\,\sin(A_L\,\lambda_n)}{K_L \sin^2(A_L\,\lambda_n) + A_L \cos^2(\lambda_n)} \tag{4.24}$$

where λ_n denotes the n-th positive root of the eigenvalue equation

$$K_L \sin(\lambda_n)\,\sin(A_L\,\lambda_n) - \cos(\lambda_n)\,\cos(A_L\,\lambda_n) = 0 \tag{4.25}$$

governed by the dimensionless parameters A_L, K_L and L_L:

$$A_L = \frac{l_L\,\sqrt{D_M}}{l_M\,\sqrt{D_L}} \tag{4.26}$$

$$L_L = \frac{l_L\,D_M\,S_M}{l_M\,D_L\,S_L} \tag{4.27}$$

$$K_L = \frac{\sqrt{D_M}\,S_M}{\sqrt{D_L}\,S_L} = \frac{L_L}{A_L}\,. \tag{4.28}$$

The step response of the sensor membrane is given by equation 4.29 for the two-layer model (Linek et al., 2009).

$$h(t) = 1 - \sum_{n=0}^{\infty} \frac{Q_n}{\lambda_n} \sin(\lambda_n)\, e^{-\lambda_n^2 \frac{D_M}{l_M^2}\cdot t} \tag{4.29}$$

Again, equation 4.21 determines the O_2 profiles or partial pressure distribution, respectively. It is illustrated for a 100 µm thick silicone membrane (standard foil) and a 60 µm stagnant boundary layer in figure 4.1a. The sensor's step response $h(t)$ (equation 4.29) is shown in figure 4.1b for different stagnant boundary layer thicknesses.

Equation 4.29 has been used to quantify the laboratory results (**1 – 4**), using the boundary layer thickness l_L, an amplitude A, and a time offset t_0 as fit parameters (analogous to the exponential approach, see equation 4.3).

In fact, the exponential approach is a (strong) simplification of the diffusional model: The scale factor in both equation 4.16 and 4.29, $1/(2n+1)^2$ and $Q_n/\lambda_n \sin(\lambda_n)$, respectively, decreases rapidly with increasing index n. At the same time, the factor in the exponential grows proportional to n^2. That causes the leading term ($n=0$) to dominate $h(t)$ except right at the start ($t \to 0$).

Model parameters and material properties are summarized in table 4.4. An Arrhenius-type relation was used for the silicone membrane's diffusivity $D(T)$ and solubility $S(T)$ while empirical equations were applied for the liquid layer (Holmén and Liss, 1984; Garcia and Gordon, 1992).

property	value	source
D_M (25 °C) / $m^2\,s^{-1}$	$1.48{\cdot}10^{-9}$	Robb (1968)
E_D / $kJ\,mol^{-1}$	20.0	Cox and Dunn (1986)
S_M (25 °C) / $mol\,m^{-3}\,Pa^{-1}$	$13.15{\cdot}10^{-5}$	Robb (1968)
E_S / $kJ\,mol^{-1}$	−12.6	Cox and Dunn (1986)
D_L (25 °C) / $m^2\,s^{-1}$	$2.31{\cdot}10^{-9}$	Holmén and Liss (1984)
S_L (25 °C) / $mol\,m^{-3}\,Pa^{-1}$	$1.22{\cdot}10^{-5}$	Garcia and Gordon (1992)
l_M (3830 & 4330) / µm	100	Huber (2010)
l_M (4330F) / µm	50	l_L^∞ extrapolation (**1**)
l_M (SBE63) / µm	130	l_L^∞ extrapolation (**1**)

Table 4.4: Material properties and membrane thickness l_M used for the two-layer diffusional model.

In reality, fluid dynamics differ to some considerable extent with sensor shape (flow field close to the sensing membrane) and deployment mode (flow field around the sensor) and a full description would require the simulation of flows and mass transfer for each case. This includes different shapes and builds of the same sensor model, e. g., the Aanderaa optode model 3830. The stagnant boundary layer model thus has its limitations, but serves as a useful and comprehensive tool to characterize the time response behaviour apart from a phenomenological response time τ.

Filter Discretization

The exponential step response $h(t)$ given by equation 4.3 with a single time constant yields the impulse response $\dot{h}(t)$

$$\dot{h}(t) = \frac{\mathrm{d}}{\mathrm{d}t}\,h(t) = \frac{1}{\tau}\cdot e^{-\frac{t}{\tau}}\ . \tag{4.30}$$

Its LaPlace transform

$$H(\mathrm{s}) = \frac{1}{1+\mathrm{s}\cdot\tau} \tag{4.31}$$

is a single-pole low-pass filter with $\mathrm{s} = j\,2\pi\mathrm{f}$ being the LaPlace variable and f the frequency. The LaPlace transformation translates the continuous time-domain response, $\dot{h}(t)$, to the frequency-domain transfer function, $H(\mathrm{s})$, of the filter.

The bilinear transformation can be used to approximate the continuous filter in the discrete-time domain. It equates integration in the continuous domain with integration by the trapezoidal rule in the discrete domain. The relationship between continuous-time $H(\mathrm{s})$ and discrete-time transfer function $H(z)$ is given by

$$\mathrm{s} = \frac{2}{\Delta t}\cdot\frac{z-1}{z+1}\ , \tag{4.32}$$

where $z = \exp(j\,2\pi f \Delta t)$ and Δt is the sample interval. Substituting equation 4.32 into the LaPlace transform (equation 4.31) gives

$$H(z) = \frac{b \cdot (1 + z^{-1})}{1 - a \cdot z^{-1}} \tag{4.33}$$

with

$$b = \left(1 + 2\,\frac{\tau}{\Delta t}\right)^{-1}, \quad a = 1 - 2\,b\ . \tag{4.34}$$

The discrete realization of the Z-transform $H(z)$ is

$$c_{i+1}^{\text{filt}} = a \cdot c_i^{\text{filt}} + b \cdot \left(c_{i+1}^{\text{in situ}} + c_i^{\text{in situ}}\right), \tag{4.35}$$

which is equal to equation 4.4.

Compared to "simpler" discrete realizations like, e. g.,

$$c_{i+1}^{\text{filt}} = c_i^{\text{filt}} + \left(c_i^{\text{in situ}} - c_i^{\text{filt}}\right) \cdot \left(1 - e^{-\frac{\Delta t}{\tau}}\right), \tag{4.36}$$

the bilinear transformation has the advantage that its phase is independent of the $\Delta t/\tau$ ratio, which is not true for equation 4.36.

Field Data Analysis

The 95 % confidence intervals of the fit parameters τ and r were used as quality control: Only when the response time τ was determined to better than ±5 s and the calibration offset r to better than ±2 µmol kg^{-1} the fit was considered appropriate and rejected otherwise. This ensures that only those observations are retained, where both the optode and the reference showed a time response (i. e., observations near gradients).

The results of the field experiments **5** – **7** were interpreted statistically by using an inverse Gaussian distribution. For experiments **8** & **9**, however, only simple statistics are presented as the number of observations is too limited.

The inverse Gaussian describes the time distribution for Brownian diffusion along a gradient for a set distance and is skewed towards high values. The frequency distribution of the Aanderaa optode in situ response times for experiment **5** is shown in figure 4.13 and proved to be appropriately described by this kind of distribution.

For interpretation, the in situ data were binned into both CTD vertical velocity and temperature bins and the bins fitted individually. For clarity, only the mode value, width (mean ± σ),and mean value of the fitted distribution are given in the figures. In addition, only bins with at least 2 % of the total sample size are shown to ensure statistical robustness. For the same reason, the mean values and standard deviations are based on the fitted distribution in order to reduce the impact of high τ/l_L outliers.

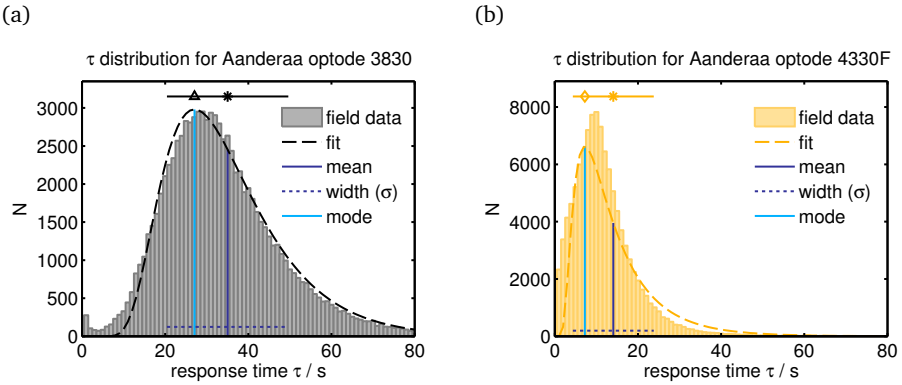

Figure 4.13: Distribution of response times τ obtained from in situ data for the entire R/V Polarstern cruise ANT-XXVII/2 (**5**) for Aanderaa optode model 3830 (a) and model 4330F (b). The coloured histogram shows the field data and the dashed line the fitted inverse Gaussian distribution. The distribution's mean value (blue line), width (mean $\pm\,\sigma$, dotted blue line), and mode value (cyan line) are given. These three parameters are used to describe the skewed distribution in the other figures using the shorthand (asterisk, bar, and marker) depicted at the top.

Reconstruction Algorithm

The main concern of inverse filtering is the amplification of noise in the data. This is an issue especially close to strong gradients, where spurious spikes are introduced easily.

The algorithm after Miloshevich et al. (2004) works both with regularly spaced data (e. g., CTD, glider) as well as with irregularly spaced data (e. g., float) and assumes the true profile to be inherently smooth. We applied a two step procedure, first smoothing the measurements with a ± 0.2 µmol kg^{-1} tolerance and then applying the time-lag correction.

The smoothing algorithm is derivative-based and tries to reduce changes in curvature by displacing the data points within the given tolerance, thus creating a locally-smooth data series. Their time-lag correction inverts equation 4.36 which requires Δt to be an order of magnitude smaller than τ to give the correct phase.

The direct inversion of the bilinear transform (equation 4.35) would be more suitable, but is prone to strong oscillations in the reconstructed profile even with small measurement errors and would require an additional averaging step. However, rearranging equation 4.35 to

$$\frac{c_{i+1}^{\text{in situ}} + c_i^{\text{in situ}}}{2} = \frac{1}{2\,b} \cdot \left(c_{i+1}^{\text{filt}} - a \cdot c_i^{\text{filt}}\right) \tag{4.37}$$

shows that the mean of consecutive data points of the "true" profile $c^{\text{in situ}}$ is directly accessible from the measurements c^{filt}, since the bilinear transformation equates integration between t_i and t_{i+1} with the trapezoidal rule. This profile of consecutive means can be interpolated to the original measurement times and, in fact, gives a

result similar to the Miloshevich et al. (2004) approach but with correct phase (root-mean-square error of 3.6 μmol kg^{-1} for the CTD profile of figure 4.7).

Nomenclature

I	luminescence intensity in the presence of O_2
I_0	luminescence intensity in the absence of O_2
Λ	luminophore excited state lifetime in the presence of O_2 / s
Λ_0	luminophore excited state lifetime in the absence of O_2 / s
K_{SV}	Stern-Volmer constant of the luminophore / Pa^{-1}
pO_2	partial pressure of oxygen / Pa
c_{O_2}	concentration of oxygen / μmol kg^{-1}
α_{O_2}	Henry's law oxygen solubility constant / μmol kg^{-1} Pa^{-1}
φ	phase shift of the sensor / °
f	modulation frequency of the sensor, frequency / s^{-1}
T	temperature / °C
t	(elapsed) time / s
τ	response time / s
$D_i(T)$	diffusivity in layer i / m^2 s^{-1}
ν	kinematic viscosity of water / m^2 s^{-1}
Sc	Schmidt number Sc$=\nu/D$, dimensionless
$S_i(T)$	solubility in layer i / mol m^{-3} Pa^{-1}
l_i	thickness of layer i / m
$h(t)$	normalized step response function, dimensionless
x	space coordinate, location / m
X	normalized space coordinate $X=x/l_M$, dimensionless
$\Phi(x,t)$	normalized partial pressure $\Phi=pO_2/pO_{2,\infty}$, dimensionless
A	step height amplitude for exponential model (eq. 4.3) / μmol kg^{-1}
t_0	time offset for exponential model (eq. 4.3) / s
a	parameter of the bilinear Z-transform (eq. 4.4), dimensionless
b	parameter of the bilinear Z-transform (eq. 4.4), dimensionless
f_0	initial forcing / initial condition for the filter (eq. 4.5) / μmol kg^{-1}
r	calibration offset between $c^{\text{in situ}}$ and c^{SBE43} (eq. 4.6) / μmol kg^{-1}
σ	standard deviation
β_i	measurement error due to time response $h(t)$ at t_i / μmol kg^{-1}
δ_i	local forcing, impulse on β at t_i / μmol kg^{-1}
p	hydrostatic pressure / dbar
s	flow speed, vertical velocity $s=\mathrm{d}p/\mathrm{d}t$ / dbar s^{-1}
g	oxygen gradient $g=\mathrm{d}c/\mathrm{d}p$ / μmol kg^{-1} dbar^{-1}
$J(x,t)$	particle flux / mol m^{-2} s^{-1}
ν_n, Q_n, λ_n	expressions after eq. 4.22 – 4.25, dimensionless
$A_L, L_L K_L$	parameter after eq. 4.26 – 4.28, dimensionless
E_D	activation energy of diffusion of O_2 in silicone / kJ mol^{-1}
E_S	solution enthalpy of O_2 in silicone / kJ mol^{-1}
$\dot{h}(t)$	impulse response function / s^{-1}

H	filter transfer function, dimensionless
s	LaPlace variable / s^{-1}
z	(complex) variable of the Z-transform $z = e^{s\,\Delta t}$, dimensionless
in situ	in situ value
SBE43	SBE43 measured value
filt	filtered / response time influenced value
optode	optode measured value
M	index to sensing membrane
L	index to boundary layer

Part II

Dissolved Oxygen Dynamics

5 Physics and Biology of Oxygen

5.1 Properties of Oxygen

Molecular oxygen, O_2, is a colourless gas at standard conditions. It is a nonpolar but reactive molecule, the second largest constituent of the earth's atmosphere with a mole fraction of 0.20946 in dry air (Glueckauf, 1951), and a crucial element of life on earth. Oxygen is weakly soluble in water and its air and ocean inventories are about $3.7 \cdot 10^{19}$ mol and $3.1 \cdot 10^{17}$ mol, respectively (Duursma and Boisson, 1994). This is in contrast to CO_2 where the oceanic reservoir is about 50 times larger than the atmospheric reservoir. The solubility of O_2 decreases with temperature (Garcia and Gordon, 1992). Therefore, warming of a saturated water parcel causes supersaturation while cooling causes undersaturation.

5.2 Physical Processes

Air Sea Gas Exchange

A general review of air sea gas exchange is given in Jähne and Haußecker (1998) and Wanninkhof et al. (2009) and the aspects relevant to dissolved oxygen are here presented. The air sea gas exchange flux F_{as} of a weakly soluble gas like O_2 is dominated by the transfer resistance in the liquid boundary layer. The air sea flux can be defined as product of a gas transfer velocity k and the concentration difference between bulk water concentration c_{w} and concentration at the interface c_0,

$$F_{\text{as}} = k \cdot (c_{\text{w}} - c_0) = k \cdot \Delta c \ . \tag{5.1}$$

The gas transfer velocity relates to the kinetic forcing and the concentration difference to the thermodynamic forcing of gas exchange. Assuming equilibrium at the interface, c_0 is commonly expressed using an air-side property like the partial pressure pO_2 at the interface (i.e., at 100 % humidity),

$$F_{\text{as}} = k \cdot (c_{\text{w}} - \alpha \cdot pO_2) \ , \tag{5.2}$$

where α is the solubility. Boundary layer dynamics are governing the gas transfer velocity. A number of conceptual models (e.g., rigid wall model, surface renewal

model) predict a relation of k with molecular diffusion and water boundary layer hydrodynamics. The relation can be expressed as

$$k \propto D^n \cdot h(s, l, \nu) \,, \tag{5.3}$$

where D is the molecular diffusivity, and h a model-dependent function of the hydrodynamics depending on a velocity scale (s), a length scale (l), and the kinematic viscosity of water (ν). Depending on the model assumptions, an exponent of $\frac{1}{2} \leq n \leq \frac{2}{3}$ is predicted for the proportionality. This proportionality can also be expressed using the Schmidt number (Sc) which is defined as the ratio between kinematic viscosity and diffusivity, i.e., the ratio between diffusive momentum and mass transport.

Several techniques have been used to determine the gas transfer velocity. They include direct flux techniques which use measurements of F_{as} and Δc to derive k (e.g., eddy correlation and profile method). Another approach are bulk concentration techniques that rely on the time evolution of c^w and c^0 to derive F_{as} and thus a relation to k. They include mass balance measurements using natural tracers (O_2, ^{222}Rn) and pertubation experiments with artificial tracers (e.g., SF_6 and ^{3}He). All these approaches yield a k dependence for a limited time period (hours to weeks) and upscaling of results from field studies needs to be done by bulk parameterizations, e.g., using the wind speed u. There are many factors affecting surface turbulence and thus the gas transfer velocity, e.g., the wave field or surfactants, but wind speed has a dominant effect.

A number of $k - u$ parameterizations based on different experiments, constraints, and assumptions are found in the literature. They vary in their mathematical formulation, from piecewise-linear (Liss and Merlivat, 1986) through quadratic (Wanninkhof, 1992; Ho et al., 2006) to mixed (Nightingale et al., 2000), with zero intercept at no wind (all previous) or with a positive offset (Wanninkhof et al., 2009). At low wind speeds, they agree fairly well though their underlying principles may differ (see Wanninkhof et al., 2009). Discrepancies arise only at high wind speeds where data coverage is sparse.

Diffusive gas exchange governed by Δc as thermodynamic forcing (equation 5.1) is not the only component of the air sea flux: A large enhancement of gas fluxes has been observed at strong winds that is attributed to breaking waves and bubble entrainment. While bubbles exhibit a spectrum of sizes and transfer through bubbles is complex, it can be conceptualized into two endmember processes, bubble injection and bubble exchange (see Emerson and Hedges (2008); figure 5.1a). If bubbles are submerged under water, their gas pressure increases due to surface tension and the hydrostatic pressure. Thus, the tendency for gases to invade the aqueous phase rises. If small bubbles are submerged, they can dissolve completely which is called bubble injection. With bubble injection, all gases contained in the small bubble are transfered to the water at their atmospheric mixing ratio. Larger bubbles, however, may resurface after submersion without complete dissolution. The diffusive gas transfer across the bubble water interface depends both on the Schmidt number and the solubility and this process is called bubble exchange. Bubble injection and exchange fluxes, F_{inj} and F_{ex}, lead to an asymmetry between invasion and evasion (figure 5.1a) and weakly soluble gases (e.g., N_2, O_2,

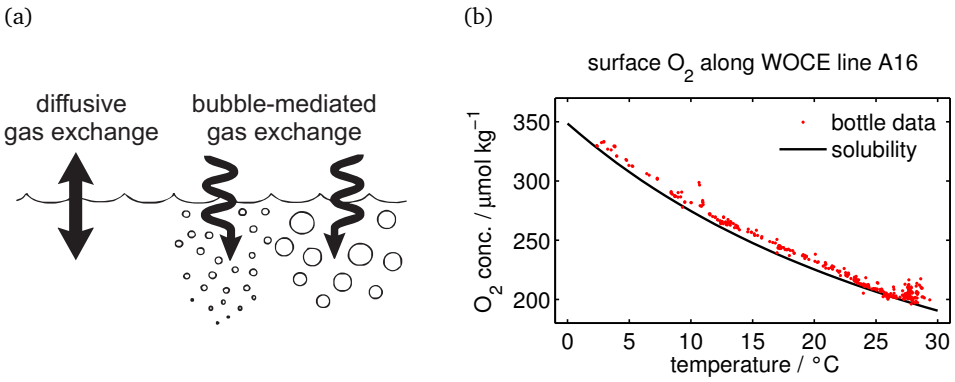

Figure 5.1: (a) Schematic representation of bubble-mediated (injection and exchange) and diffusive gas exchange fluxes (from Hamme and Emerson, 2006). (b) Observations of surface water O_2 supersaturation (red dots) along WOCE line A16 in the Atlantic ocean (see figure 5.3; data from eWOCE, http://www.ewoce.org) and O_2 solubility according to Garcia and Gordon (1992) (black line).

Ar) are therefore (physically) supersaturated to some degree in the oceans (Nicholson et al., 2011; figure 5.1b).

Strong super- or undersaturations of O_2 do not persist in the ocean and are quickly re-equilibrated on a timescale of 1 month (Broecker and Peng, 1974). The exact equilibration time, however, depends on the surface mixed layer depth, i.e., the volume to be equilibrated, and the wind speed history (see, e.g., Reuer et al., 2007).

Ventilation

Away from the surface, oxygen behaves physically like a passive ocean tracer, i.e., it is affected by mixing and advection. Deep water formation at high latitudes causes sinking of cold, i.e., oxygen-rich water, which is subsequently advected into the ocean interior through the thermohaline circulation. In this respect, O_2 behaves just the same as age tracers (e.g., tritium, CFCs) or anthropogenic CO_2. In principle, this is true for the shallow thermocline ventilation as well. However, O_2 is not biologically inert, so other processes (see below) are superimposed to ocean physics. Therefore, pelagic and epipelagic O_2 distributions differ significantly from age tracers.

5.3 Biological Processes

Oxygen is tightly coupled to biological processes through photosynthesis and respiration (Anderson, 1995).

$$106\,CO_2 + 16\,HNO_3 + H_3PO_4 + 78\,H_2O \underset{\text{respiration}}{\overset{\text{photosynthesis}}{\rightleftharpoons}} C_{106}H_{175}O_{42}N_{16}P + 150\,O_2 \tag{5.4}$$

It is involved in other biogeochemical conversions, too, but photosynthesis and respiration dominate. Because of this tight coupling, oxygen is frequently used to infer net community production (see chapter 8). Apparent oxygen utilization (*AOU*), defined as the difference between the measured oxygen c_{O_2} and the O_2 saturation concentration α_{O_2},

$$AOU = \alpha_{O_2} - c_{O_2} \,, \tag{5.5}$$

is used to decouple biological O_2 changes from physical effects: While oxygen concentrations in surface waters at saturation vary between 190 and 350 µmol kg^{-1} due to temperature effects (figure 5.1b), *AOU* is zero throughout. Its value decreases with photosynthesis, i.e., O_2 production, and increases with respiration, i.e., O_2 consumption. If there were no biology, *AOU* would be zero everywhere and O_2 would behave like an inert gas. Comparison of *AOU* with a truly inert gas (e.g., CFCs) as an age tracer can thus be used to derive the apparent oxygen utilization rate on specific density horizons (e.g., Karstensen et al., 2008).

5.4 Oxygen Distribution

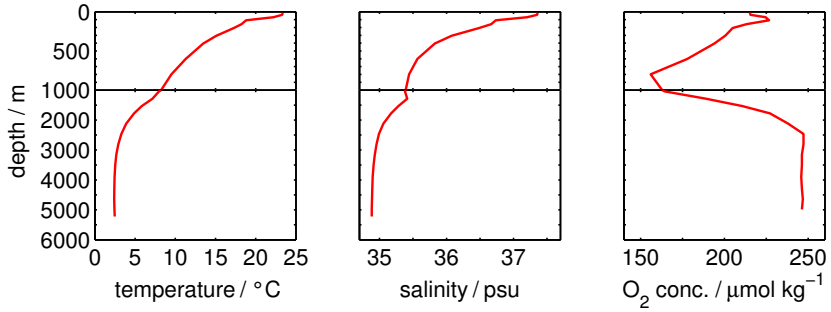

Figure 5.2: Typical temperature, salinity and oxygen water column profile in the open North Atlantic ocean (28.1° N 24.5° W; from eWOCE, http://www.ewoce.org). The surface is close to saturation (209 µmol kg^{-1}) whereas sub-surface waters have an increased O_2 level due to photosynthesis. Below the euphotic zone (ca. 110 m), O_2 is consumed due to respiration. Below ca. 1000 m, advective supply increases O_2 again and waters below 2500 m have a nearly homogeneous North Atlantic deep water (NADW) signature.

Physical and biological effects on O_2 are superimposed in the ocean but their relative contribution varies with depth and location. A typical water column profile from the Atlantic ocean is shown in figure 5.2. While air sea gas exchange restores near-equilibrium at the surface, the sun-lit upper ocean is supersaturated due to O_2 production from photosynthesis. Below the euphotic zone, strong respiration reduces oxygen concentrations. Deeper in the water column (>1000 m), little organic material is left that can be remineralized. Therefore, *AOU* changes only little at depth and deep waters keep their source region signature for prolonged periods.

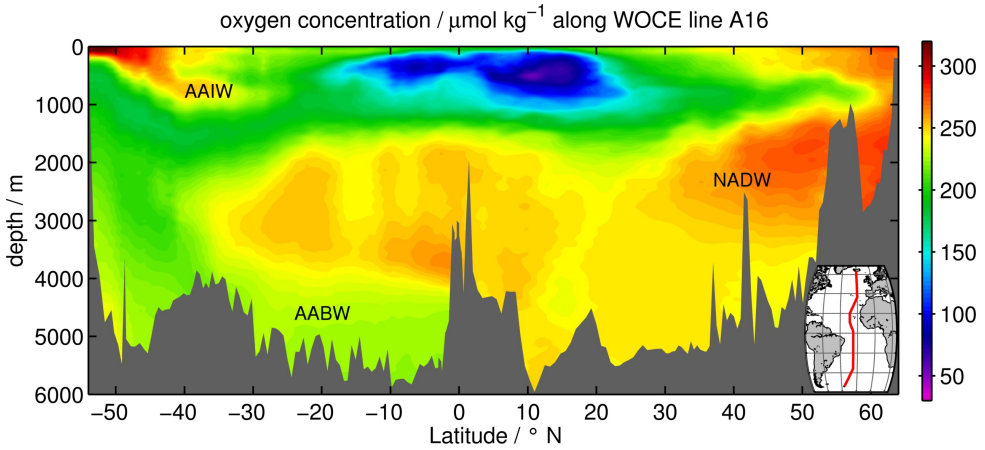

Figure 5.3: Meridional section of dissolved oxygen across the Atlantic ocean along WOCE line A16 (data from eWOCE, http://www.ewoce.org, with gridding through ODV). Labels indicate water masses of the thermohaline overturning circulation (NADW: North Atlantic deep water, AABW: Antarctic bottom water, AAIW: Antarctic intermediate water).

Therefore, physical processes tend to dominate the deep ocean's O_2 distribution, e.g., the ventilation pathway of cold North Atlantic deep water (NADW) can be clearly followed through its high O_2 content (see figure 5.3).

However, ventilation is also important for the O_2 distribution in shallower waters were biological processes have a large amplitude: The potential vorticity conservation constraint of the shallow thermocline ventilation (Luyten et al., 1983) causes sluggishly ventilated zones in the Eastern, equatorward parts of the subtropical gyres, so called "shadow zones". There, biological respiration below the euphotic zone reduces oxygen concentrations while there is only little physical supply from advection and turbulent mixing. The result are oxygen minimum zones in the Eastern tropical Atlantic (figure 5.4) and Pacific (Karstensen et al., 2008).

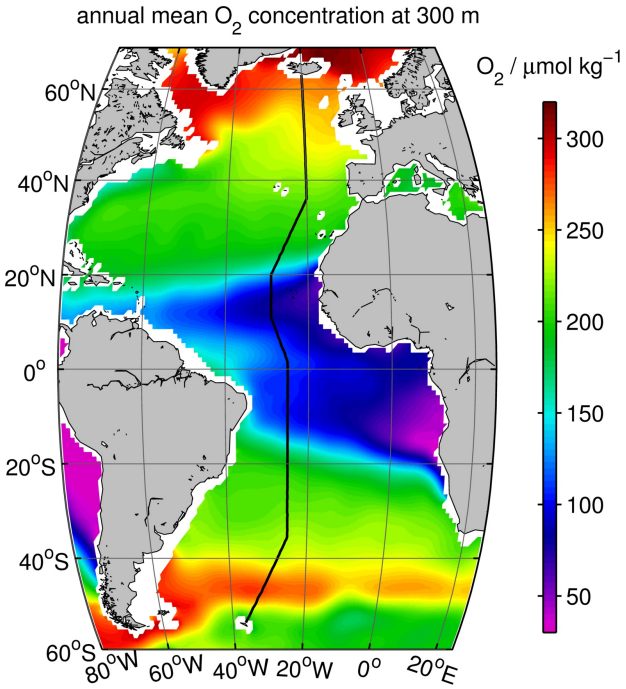

Figure 5.4: Horizontal section of the annual mean oxygen concentration across the Atlantic ocean at 300 m (data from World Ocean Atlas 2013, Garcia et al., 2013). The WOCE line A16 is indicated as thick black line. High-latitude deep and intermediate water formation regions where cold water is subducted are identified by high O_2 concentrations. Oxygen minimum zones are formed in the equatorward shadow zones of the anticyclonic subtropical gyres.

6 Surface Processes

submitted as:
Tortell, P. D., Bittig, H. C., Körtzinger, A., Jones, E., and Hoppema, M. 2014. Biological and physical controls on N_2, O_2 and CO_2 distributions in contrasting Southern Ocean surface waters. Global Biogeochem. Cycles.

Abstract

We present measurements of pCO_2, O_2 concentrations, biological oxygen saturation ($\Delta O_2/Ar$) and N_2 saturation (ΔN_2) in Southern Ocean surface waters during austral summer, 2010–2011. Phytoplankton biomass varied strongly across distinct hydrographic zones, with high chlorophyll *a* (Chl *a*) concentrations in regions of frontal mixing and sea-ice melt. pCO_2 and $\Delta O_2/Ar$ exhibited large spatial gradients (range 90 to 450 µatm and −10 to 60 %, respectively) and co-varied strongly with Chl *a*. However, the ratio of biological O_2 accumulation to dissolved inorganic carbon (DIC) drawdown was significantly lower than expected from photosynthetic stoichiometry, reflecting the differential time-scales of O_2 and CO_2 air-sea equilibration. We measured significant oceanic CO_2 uptake, with a mean air-sea flux (≈100 mmol m^{-2} d^{-1}) that significantly exceeded regional climatological values. N_2 was mostly supersaturated in surface waters (mean ΔN_2 of +2.5 %), while physical processes resulted in both super-saturation and under-saturation of mixed layer O_2 ($\Delta O_{2\,phys}$ ranging from −6 % to +15 %). Box model calculations were able to reproduce the spatial variability of ΔN_2 and $\Delta O_{2\,phys}$ along the cruise track, demonstrating significant effects of atmospheric processes and mixed layer entrainment on surface gas disequilibria. Net community production (NCP), derived from entrainment-corrected surface $\Delta O_2/Ar$ data, ranged from ≈ −100 to 200 mmol O_2 m^{-2} d^{-1} and showed good coherence with independent NCP estimates based on seasonal mixed layer DIC deficits. The highest NCP was observed in frontal mixing zones and regions of sea-ice melt with shallow mixed layer depths, reflecting the importance of physical controls on surface biological processes.

Acknowledgements

Data are freely available from the corresponding author upon request. Support for this work was provided from the Natural Sciences and Engineering Council of Canada (P. Tortell), the Von Humboldt Foundation (P. Tortell), the OCEANET project of the WGL Leibniz Association (A. Körtzinger and H. Bittig), the German Science Foundation's O_2-Floats project (grant KO 1717/3-1; H. Bittig), and from the EU project CARBOCHANGE (gant no. 264879; M. Hoppema). We acknowledge the tremendous leadership of Eberhard Fahrbach (AWI) as chief scientist for our cruise, and the efforts of Gerd Rohardt (AWI) in the compilation and quality control of all hydrographic data. Christopher Payne and Constance Couture (UBC) provided ship-board technical assistance with the mass spectrometer.

6.1 Introduction

The Southern Ocean plays a key role in global nutrient and carbon cycles (Schlitzer, 2002; Sarmiento et al., 2004). This vast region contributes significantly to oceanic CO_2 uptake through the vertical export of particulate organic carbon (Schlitzer, 2002; Trull et al., 2001; Honjo et al., 2008), and the subduction of CO_2-rich polar water masses into the ocean interior (Sarmiento and Toggweiler, 1984; Caldeira and Duffy, 2000). These biological and physical carbon pumps also transport oxygen and macro-nutrients into the low latitudes, where they influence biological productivity over large spatial scales (Sarmiento et al., 2004; Marinov et al., 2006). In the offshore pelagic realm, Southern Ocean primary production and biological CO_2 uptake appear to be controlled by a combination of light and iron limitation (Boyd, 2002). Large scale patterns of aeolian iron deposition have been linked to spatial gradients in surface water productivity (Cassar et al., 2007), while vertical mixing at frontal zones has been shown to drive mesoscale and sub-mesoscale biological gradients (Sokolov and Rintoul, 2007). Relative to the open ocean, field data are sparse over much of the Antarctic continental shelf and marginal ice zone (MIZ), where productivity is influenced by iron input from sediments (Coale et al., 2005; Planquette et al., 2013) and melting ice (Sedwick and DiTullio, 1997; Gerringa et al., 2012), and by large seasonal cycles in solar irradiance, mixed layer depth and sea ice cover (Arrigo and van Dijken, 2003). Although these high latitude regions contribute disproportionately (on an aerial basis) to Southern Ocean nutrient and carbon cycles (Arrigo et al., 2008), their biological and physical dynamics remain poorly described.

Here we present new results from a two month survey of surface hydrography and dissolved gas concentrations across the Atlantic sector of the Southern Ocean and the region west of the Antarctic Peninsula. We use our observations to characterize the spatial variability of surface gases in contrasting Southern Ocean regions (offshore pelagic, continental shelf and MIZ), and to examine the relative influence of physical vs. biological controls on biogeochemical processes. The interplay of physical and biological forcing is particularly important in determining surface water pCO_2 and O_2 distributions. Net community production (NCP, i.e. gross photosynthesis minus community respiration) leads to CO_2 drawdown (i.e. decreased pCO_2)

in the mixed layer, coupled with biologically-induced O_2 supersaturation (Carrillo et al., 2004). NCP is sensitive to physical factors such as wind speed, solar irradiance and ice cover that control nutrient supply and mixed layer light intensity. Physical processes also influence surface O_2 and CO_2 by modulating the strength of diffusive sea-air exchange, which acts to restore gas concentrations back to atmospheric equilibrium, and bubble processes, which lead to super-saturation of surface water gases (Keeling, 1993). Due to chemical buffering of the inorganic C system in seawater, the diffusive air-sea equilibration time scale is typically ≈10-fold faster for O_2 than for CO_2 (Sarmiento and Gruber, 2006), and gas exchange can thus overprint the biological production signal, shifting the $pCO_2 - O_2$ relationship away from photosynthetic stoichiometry (Körtzinger et al., 2008).

Changes in surface water temperature and salinity can also influence O_2 and CO_2 distributions through their effect on gas solubility. For O_2, these thermodynamic effects can be removed by normalization to Argon, a biologically inert gas with solubility properties that are virtually identical to O_2 (Craig and Hayward, 1987). The O_2/Ar ratio thus serves as a specific tracer for biological O_2 cycling, and recent field measurements of O_2/Ar disequilibrium (ΔO_2/Ar) have been used to map the large-scale spatial distribution of NCP in Southern Ocean surface waters (Tortell and Long, 2009; Cassar et al., 2011; Castro-Morales et al., 2013; Shadwick et al., 2014). NCP estimates derived from ΔO_2/Ar are based on a steady-state mixed layer model (Kaiser et al., 2005; Reuer et al., 2007), where vertical and lateral exchange of O_2 into the mixed layer is assumed to be negligible and NCP is then equated to the biologically induced sea-air flux of O_2 (O_2-bioflux). These assumptions are likely invalid over significant portion of the Southern Ocean, leading to significant uncertainty in derived NCP values (Jonsson et al., 2013). Better constraints on the physical contributions to mixed layer O_2 mass balance are thus needed to improve the use of ΔO_2/Ar as a productivity tracer.

Like Ar, N_2 is biologically inert in the Southern Ocean, where nitrogen fixation and denitrification are inhibited by high NO_3^- and O_2 concentrations, respectively. Given the high atmospheric concentrations of N_2 and its relatively low solubility in seawater, this gas provides a useful tracer for air-sea exchange processes, including bubble injection (Schudlich and Emerson, 1996). A number of studies have used surface ocean N_2 disequilibrium measurements (ΔN_2) to examine air-sea exchange (Emerson et al., 2002; Hamme and Emerson, 2006; Vagle et al., 2010), and a mechanistic framework has recently been developed to quantitatively interpret surface N_2 data (Emerson et al., 2008; Nicholson et al., 2011). At present, we are aware of only one published ΔN_2 data set from Southern Ocean waters (Weeding and Trull, 2014). Additional ΔN_2 measurements from this region are thus needed to validate the modelling approach of Nicholson et al. (2011) under conditions of high windspeeds, strong gradients in atmospheric pressure and significant bubble injection fluxes.

Using simultaneous measurements of N_2, O_2, Ar and CO_2, in combination with ancillary data and box model calculations, we examined the dominant controls on surface gas saturation states in contrasting Southern Ocean surface waters. Our results provide insight into the factors driving gas dynamics in various sub-regions of

the Southern Ocean, demonstrating clear regional differences in the relative importance of physical and biological forcing. Our observations reveal strong biological controls on surface CO_2 and O_2 distributions, with a significant imprint of air-sea exchange. We show that the box model formulation of Nicholson et al. (2011) is able to accurately represent physically-induced changes in O_2 and N_2 saturation states, and we derive NCP estimates that are corrected for entrainment of sub-surface O_2 into the mixed layer. Our work builds on the recent study of Shadwick et al. (2014) examining CO_2, O_2 and $\Delta O_2/Ar$ along a transect south of Australia, and of Weeding and Trull (2014) who present a mooring-based O_2 and N_2 time-series for the Subantarctic region south of Tasmania. To our knowledge, our work represents the first simultaneous measurements of pCO_2, ΔO_2, $\Delta O_2/Ar$ and ΔN_2 for the Southern Ocean, and we show how these combined observations can provide powerful insights into surface water biogeochemical processes across a range of hydrographic regimes.

6.2 Methods

Study Site and Hydrographic Measurements

We conducted a 10-week survey of Southern Ocean waters from Nov. 29, 2010 to Feb. 3, 2011 on board the research vessel Polarstern (cruise ANT-XXVII/2; Rohardt et al. (2011)). Our cruise track from Cape Town, South Africa, to Punta Arenas, Chile (Figure 6.1) encompassed a number of distinct hydrographic regimes. For the purposes of our analysis, we separate the cruise track into three sub-regions. We first sampled a N-S transect ≈40° S to 70° S, crossing a number of prominent hydrographic fronts (Orsi et al., 1995), including the Subtropical Front (STF), Subantarctic Front (SAF), Polar Front (PF), Southern Antarctic Circumpolar Current Front (SACCF) and Southern Boundary of the Antarctic Circumpolar Current (SBdy). We then followed an E-W transect along the outer edge of the Weddell Sea MIZ, and conducted an intensive survey of the West Antarctic Peninsula (WAP) along the Palmer Long Term Ecological Research (LTER) sampling grid (Waters and Smith, 1992).

Sea surface temperature (SST) and salinity (SSS) were measured continuously along the cruise track using an on-board thermosalinograph (TSG; Sea-Bird Electronics, model SBE-21) sampling from an uncontaminated seawater supply with a nominal intake depth of 11 m. Daily calibrations of the TSG salinity measurements were conducted using discrete samples analyzed on a salinometer (Optimare GmbH, Precision Salinometer). Sea surface Chl *a* fluorescence, used as a proxy for bulk phytoplankton biomass, was continuously measured by the ship's underway fluorometer (Wetlabs, model Eco). The fluorometer data were not calibrated to absolute Chl *a* concentrations and are thus used here only as a relative measure of total phytoplankton abundance. Some day-time quenching of Chl *a* fluorescence is expected, independent of changes in phytoplankton biomass.

Depth profiles of seawater potential temperature, salinity and Chl *a* fluorescence were obtained from CTD casts at 188 stations along the cruise track. Temperature and conductivity were measured with Sea-Bird SBE3plus and SBE4 sensors,

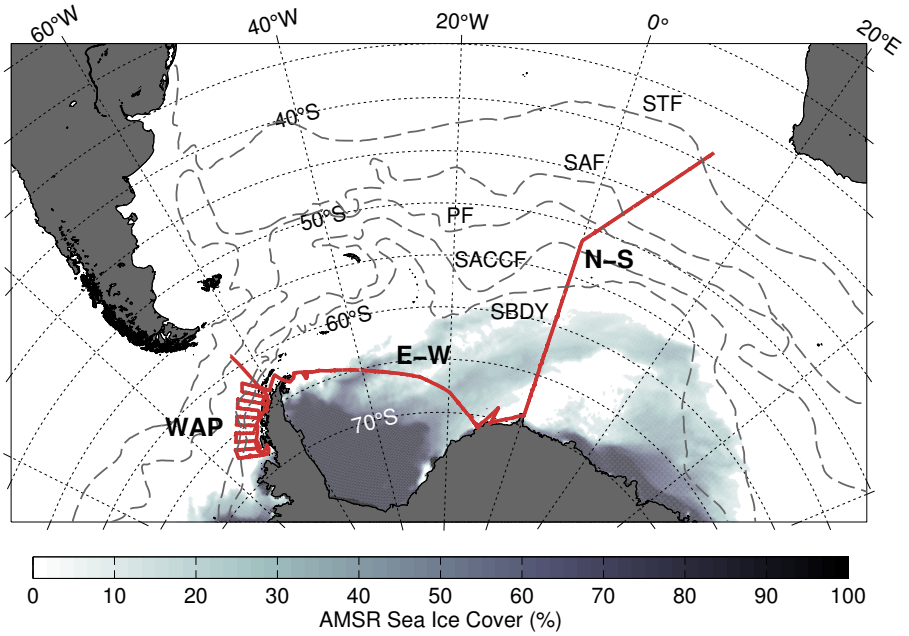

Figure 6.1: Map of the sampling area showing the cruise track (red line) and the position of various hydrographic fronts (dotted lines). From north to south, the fronts are: Subtropical Front (STF), Subantarctic Front (SAF), Polar Front (PF), Southern Antarctic Circumpolar Current Front (SACCF) and Southern Boundary of the Antarctic Circumpolar Current (SBdy). Location of mean frontal positions was derived from Orsi et al. (1995). N-S, E-W and WAP denote different portions of our sampling region, as described in the text. Grey / black shading around the Antarctic continent represents the mean sea ice cover during the period of our survey, derived from the AMSR-E satellite product.

respectively, while Chl *a* fluorescence was measured with a Wetlabs Eco fluorometer. Temperature and salinity profiles were used to define the mixed layer depth for each station based on the curvature of near surface layer density or temperature profiles as described by Lorbacher et al. (2006). Mixed layer temperature and salinity data derived from CTD casts showed very good agreement with surface TSG data (mean offset of −0.078 °C and −0.01, respectively). The concentration of O_2 in depth profiles was measured using a CTD-mounted Sea-Bird SBE43 sensor. The CTD O_2 sensor was calibrated using Winkler titrations of discrete samples, with visual end-point determination using a starch indicator (precision of 0.3 μmol L^{-1}) and KIO_3 standardization of the thiosulfate titration solutions (Dickson, 1994). All of the CTD sensors were sent to the manufacturer for calibration prior to and immediately after the cruise. Full quality-controlled hydrographic data from the cruise are available in the Pangaea database (www.pangaea.de).

Surface Water Gas Measurements

Surface pCO_2 and O_2/Ar ratios were measured every ≈ 30 s from the keel intake supply using membrane inlet mass spectrometry (MIMS), following the protocols described by Tortell et al. (2011). At typical cruising speeds of 8 – 10 knots, this sampling frequency translates into one measurement every ≈200 m along the cruise track. The pCO_2 measurements were calibrated using temperaturecontrolled seawater standards (Tortell et al., 2011), and the resulting pCO_2 data were corrected to in situ SST following Takahashi et al. (2002). Note that pCO_2 data are not available for much of the N-S transect due to instrument problems. O_2/Ar measurements in the flow-through seawater were normalized to air-equilibrated, temperature-controlled seawater standards (Tortell et al., 2011), analyzed every few hours, to derive a biological O_2 saturation term, ΔO_2/Ar, expressed in % deviation from equilibrium.

Additional surface O_2 concentration measurements were made using an Optode (Aanderaa Data Instruments, model 3830), while total gas pressure (mbar) was measured using a gas tension device (Pro-Oceanus, model HGTD). The gas tension device was not functional during the latter half of the cruise. Both the Optode and HGTD were submerged in a thermally insulated flow-through box connected to the keel seawater intake supply, and set to acquire data with a 1 min resolution. The Optode O_2 measurements were calibrated against CTD-O_2 data, and cross validated against discrete Winkler titrations. The O_2 saturation state (ΔO_2; % deviation from equilibrium) was derived from measured O_2 concentrations and an equilibrium O_2 concentration computed from surface water temperature, salinity and atmospheric pressure with the solubility function of Garcia and Gordon (1992). Using our Optode and MIMS data, we derived an estimate of the physical contribution to O_2 disequilibria in surface waters, $\Delta O_{2\,\mathrm{phys}}$.

$$\Delta O_{2\,\mathrm{phys}} = \Delta O_{2\,\mathrm{Optode}} - \Delta O_2/\mathrm{Ar}_{\mathrm{MIMS}} \tag{6.1}$$

This approach is based on the fact that Optode-based ΔO_2 is sensitive to both physical and biological influences, whereas MIMS-based ΔO_2/Ar reflects only the biological contribution to O_2 disequilibria (Craig and Hayward, 1987).

Following the approach of McNeil et al. (1995, 2005), we derived estimates of N_2 partial pressure from GTD total gas pressure by subtracting the partial pressures of O_2 (derived from Optode measurements), water vapour (calculated from SST and SSS) and Ar.

$$pN_2 \approx p\text{Total} - pO_2 - pH_2O - p\text{Ar} \tag{6.2}$$

In previous studies, seawater Ar concentrations have been assumed to be at atmospheric equilibrium values. This assumption contributes only a small uncertainty (< 0.1 %) to the calculation of N_2 concentrations (McNeil et al., 1995). Indeed, we observed a negligible difference between pN_2 calculated assuming 100 % Ar saturation vs. calculations which included a specific ΔAr term (derived from ΔO_2/Ar and ΔO_2). Similarly, the inclusion of pCO_2 into the calculation did not have a significant effect on the resulting pN_2. The N_2 saturation state (ΔN_2) was calculated from GTD-derived N_2 concentrations using the SST and salinity-dependent N_2 solubility constant of Hamme and Emerson (2004).

Ancillary Data

Ancillary meteorological and oceanographic data from a number of sources were used to provide a broader environmental context for our observations, and input data for model calculations (see below). Instantaneous measurements of sea level atmospheric pressure, wind speed (corrected to 10 m above sea level) and solar irradiance were obtained from weather station sensors on board the research vessel. Additional synoptic data on sea level atmospheric pressure and humidity were obtained from the NCEP reanalysis (http://www.esrl.noaa.gov/psd/data/reanalysis/reanalysis.shtml) at 2.5° and 6 h resolution, while regional SST information was derived from NOAA OISST (http://www.ncdc.noaa.gov/sst/) at 0.25° and 24 h resolution. Sea ice data (% cover) at 3 km and 24 h resolution were derived from AMSR-E satellite imagery using the ASI re-processing algorithm provided by the Institute of Environmental Physics at the University of Bremen, Germany (Spreen et al., 2008). Regional sea surface salinity was obtained from the Mercator global operational system PSY3V3 model at 0.25° and 24 h resolution. Surface Chl *a* concentrations were obtained from Level 3 AquaModis satellite data (http://oceancolor.gsfc.nasa.gov/cgi/l3). We used 9 km resolution imagery, with 8 day composite data linearly interpolated to daily values.

CO_2 Flux Calculations

Surface gas measurements and wind-speed data were used to derive sea-air flux estimates for CO_2. The CO_2 fluxes were calculated as:

$$F_{CO_2} = k_{CO_2} \cdot \alpha_{CO_2} \cdot (pCO_{2,sw} - pCO_{2,atm}) \cdot (1 - A)^{0.4}\,, \tag{6.3}$$

where k_{CO_2} is the gas transfer velocity (m d^{-1}), calculated from ship-based wind speed data and the temperature-dependent Schmidt number using the parameterization of Wanninkhof (1992) for instantaneous wind speed, α_{CO_2} is the temperature

and salinity-dependent solubility of CO_2 (Weiss, 1974) and A is the fraction of sea surface covered by ice. The exponential term used to scale gas exchange as a function of ice cover is derived from Loose et al. (2009). For these flux calculations, we used an atmospheric CO_2 mole fraction of 396 ppmv, derived from the GlobalView pCO_2 data (www.esrl.noaa.gov/gmd/ccgg/globalview/; 60° S to 70° S, Dec. 2010 – Feb. 2011), corrected to 100 % humidity at SST and SSS and the atmospheric pressure derived from ship-based sensors.

Carbonate System Measurements and Calculations

Discrete samples for carbonate system measurements were collected at selected stations along the cruise track using 12 L Niskin bottles mounted on the CTD rosette. Total alkalinity was measured using potentiometric gran titration (Brewer et al., 1986), calibrated against certified reference material (batches 100 and 105) supplied by Dr. Andrew Dickson, Scripps Institution of Oceanography (Dickson et al., 2007). The precision of the alkalinity measurements was 1.5 μmol kg^{-1}. Seawater (500 ml) for DIC analysis was collected in borosilicate glass bottles and analysed within 20 hours using a VINDTA 3C instrument (Versatile INstrument for the Determination of Total Alkalinity, Marianda, Kiel). The DIC concentration was determined by coulometric analysis (Johnson et al., 1987), with calibration against certified reference materials (CRM, batches 100 and 105) performed at the start and end of each measurement cycle. The precision of the DIC measurements was 1.0 μmol kg^{-1}, based on the average difference between all CRM in-bottle duplicate analyses ($n = 87$), and the accuracy was estimated as 2.0 μmol kg^{-1}.

Depth-integrated DIC deficits were calculated from vertical profiles relative to the concentration at the depth of the potential temperature minimum, representing the Winter Water. The depth of the potential temperature minimum was determined from the CTD profiles. Vertical integration to the potential temperature minimum was used to derive the chemical deficits in the summer surface layer. DIC data were normalised to average Winter Water salinity (34.2, $n = 105$) to account for dilution through addition of sea ice melt water. The chemical deficits, calculated in this way, represent the time-integrated change of the surface ocean since the end of the winter. This technique assumes that DIC concentrations at the potential temperature minimum represent the winter reference with no significant lateral or vertical exchange. This assumption has been used in prior studies (Hoppema et al., 2007; Jennings et al., 1984; Rubin et al., 1998) and appears to be reasonably robust for the Weddell Sea (Hoppema et al., 2000b).

In order to obtain high spatial resolution surface carbonate system data along the cruise track, we derived an empirical relationship between salinity and alkalinity along the E-W and WAP transects (n = 2098, $r^2 > 0.85$, root mean square error = 6.1 μmol kg^{-1}), and used this relationship to compute alkalinity from thermosalinograph salinity measurements. Total dissolved inorganic carbon (DIC) along the cruise track was then computed from measured pCO_2 and the derived alkalinity using CO2SYS (Pierrot et al., 2006), with the equilibrium constants of Mehrbach et al. (1973) refit by Dickson and Millero (1987). For the WAP and Weddell regions,

the root mean square error of the DIC estimates derived from this analysis was 7.1 and 3.8 μmol kg^{-1}, respectively. This error term was based on a comparison of DIC values obtained using measured vs. empirically-derived alkalinity.

Box Model Calculations

Following the work of Emerson et al. (2008) and Nicholson et al. (2011), we used a simple box model to assess the physical contributions to N_2 and O_2 disequilibria in the mixed layer. The 1-D model includes an air-sea gas exchange term, F_{as} and a sub-surface water entrainment term, F_{entr}, associated with mixed layer deepening events. Lateral advection was assumed to be negligible and no biological production / consumption term was included in order to isolate physical forcing. For a given gas, x, the physically-induced change in mixed layer concentrations, mld dc_x, was computed as:

$$\text{mld}\ \frac{dc_x}{dt} = F_{as,x} + F_{entr,x} \tag{6.4}$$

The air-sea flux term, F_{as}, was separated into several components: diffusional gas exchange, F_{dif}, injection of small bubbles, F_{inj}, and air-water interface exchange across larger bubble surfaces, F_{ex}. The diffusive component was scaled to the fraction of open water, A, following Loose et al. (2009). The total air-sea flux term (F_{as}) for gas x was thus computed as:

$$F_{as,x} = F_{dif,x} + F_{inj,x} + F_{ex,x} \tag{6.5}$$

$$F_{dif,x} = -k_x \cdot (c_x - \alpha_x \cdot p_x) \cdot (1-A)^{0.4} \tag{6.6}$$

$$F_{inj,x} = A_{inj} \cdot p_x \cdot (u_{10} - 2.27\ \text{m s}^{-1})^3 \tag{6.7}$$

$$F_{ex,x} = A_{ex} \cdot p_x \cdot \left(\frac{D_x}{1\ \text{m}^2\ \text{s}^{-1}}\right)^{0.5} \cdot \frac{\alpha_x}{1\ \text{mol m}^{-3}\ \text{atm}^{-1}} \cdot \left(u_{10} - 2.27\ \text{m s}^{-1}\right)^3 \tag{6.8}$$

where k_x is the gas transfer velocity (m s^{-1}), α_x the solubility (mol m^{-3} atm^{-1}), p_x the partial pressure calculated from the mole fraction in dry air and the dry atmospheric pressure ($p_x = \chi_x \cdot p_{atm,dry}$), and D_x the diffusion coefficient (m^2 s^{-1}). The injection and exchange rates A_{inj} and A_{ex} (mol s^2 m^{-5} atm^{-1}) given in Nicholson et al. (2011) were derived for average wind speeds. For our calculations based on instantaneous wind-speeds, we use a flux enhancement factor, R, of 1.5 as discussed in Nicholson et al. (2011). The bubble fluxes F_{inj} and F_{ex} scale with whitecap coverage (0 for $u_{10} < 2.27$ m s^{-1}), and are set to zero for regions with more than 25 % sea ice coverage.

The entrainment term is governed by the change in mixed layer depth (only deepening of the mixed layer impacts the surface water budget), and by difference between mixed layer concentration c_x and the concentration in the sub-surface layer $c_{x,sub}$:

$$F_{entr} = \left(c_{x,sub} - c_x\right) \frac{d\,\text{mld}}{dt} \tag{6.9}$$

For N_2, the choice of the sub-mixed layer concentration $c_{N_2,sub}$ has a minor influence on the calculation given the weak vertical gradients of this gas and its small deviations from saturation. We thus chose a uniform value of 100 % surface saturation for $c_{N_2,sub}$. In the case of O_2, however, strong vertical gradients and variable saturation levels have a significant influence on the entrainment term, and the choice of $c_{O_2,sub}$ values can thus exert a significant influence on the model calculations under conditions of mixed layer deepening. In our calculations, we used the average O_2 concentration 5 – 10 m below the mixed layer depth to define the end member concentration for entrained waters. The mean end member values calculated for each sampling station were then interpolated to the full resolution of our cruise track and used in the entrainment calculations. As discussed below, we found that this choice of $c_{O_2,sub}$ provided a good fit of model calculations to our observations. The changes in mixed layer depth used to quantify the physical entrainment term were obtained from temperature and salinity profiles of the Mercator global operational system PSY3V3.

The model mixed layer concentrations of O_2 and N_2 were initialized at 100 % saturation starting 30 d prior to the underway measurements. The ancillary data (e.g. wind speed, atmospheric pressure, mixed layer depth etc.) were interpolated to the cruise track position and time, and used to force the model calculations for 30 d with time-steps of 6 h.

Net Community Production

We used the approach of Reuer et al. (2007) to estimate net community production (NCP, i.e. gross photosynthesis minus community respiration) from our mixed layer $\Delta O_2/Ar$ measurements. The calculations presented by Reuer et al. (2007) are based on a steady-state model, where lateral advection and vertical entrainment are assumed to be negligible, and the mixed layer O_2 mass balance is influenced solely by NCP and gas exchange. Under these conditions, steady-state NCP is equivalent to the air-sea flux of biogenic O_2 (obtained from $\Delta O_2/Ar$ and the air-equilibrium O_2 concentration, $\alpha_{O_2} \cdot p_{atm}$). The gas exchange term, k, is derived using a weighting function to account for variability in wind speed history over the residence time of O_2 in the mixed layer (see Reuer et al. (2007) for details) .

$$NCP = \Delta O_2/Ar \cdot \alpha_{O_2} \cdot p_{atm} \cdot k \tag{6.10}$$

We recognize that the assumptions required for the $\Delta O_2/Ar$-based NCP calculations are unrealistic for at least some portions of our cruise track where entrainment of sub-surface waters into the mixed layer is likely non-negligible. To examine the influence of mixed layer entrainment on NCP, we used the output from our box model calculations (see above) to estimate the O_2 flux associated with changes in mixed layer depth. We derived a value of $\Delta O_2/Ar$ corrected for entrainment-derived O_2 fluxes, and used this value as input to equation 10. Given the physical complexity of our study region, and its high degree of temporal variability, we treat our NCP calculations as a first order estimate of biological O_2 production rates in the mixed layer, recognizing the quantitative limitations of this approach.

Additional NCP estimates were derived from an analysis of mixed layer DIC deficits as described above. To estimate the mean daily NCP rate, we normalized the seasonal DIC deficits to a period of two months for open water regions, and three weeks for recently ice-covered waters. We used a photosynthetic quotient of 1.4 mol O_2 : mol DIC (Laws, 1991) to convert DIC-based NCP to O_2 units for comparison with our ΔO_2/Ar-based NCP estimates.

6.3 Results and Discussion

Surface Water Hydrography and Chl *a*

Sea surface temperature (SST) exhibited a strong latitudinal gradient along the northern portion of the N-S transect, across the transition from sub-tropical to Antarctic waters (Figures 6.2a, 6.3d). In contrast, the ice covered waters south of the SBdy frontal zone were characterized by near homogeneous SST (±0.3 °C) close to the freezing point of seawater. Along the E-W and WAP transects, SST ranged from −1.8 to 3 °C, and exhibited significant spatial heterogeneity (Figures 6.2a, 6.3d). The relatively warm SST of the WAP region reflects the influence of surface warming in shallow near-shore waters, and/or the signature of modified circumpolar deep water (MCDW) flowing onto the continental shelf (Martinson and McKee, 2012). Salinity also showed significant spatial variability across the E-W and WAP regions. Relatively fresh waters (salinity ≈ 33.2), indicative of local sea ice melt, were observed along the Weddell Sea MIZ at ≈ 42° W and along the WAP in the near shore waters adjacent to Marguerite Bay (Figure 6.2b). Mixed layer depths, computed from CTD profile data, ranged from < 10 m to ≈ 100 m, with an overall mean of 26 m (±20 m std.). The shallowest mixed layer depths were observed in low salinity regions along the western portion of the Weddell Sea MIZ and in near shore waters of the WAP.

Strong gradients in surface hydrography were associated with significant variability in phytoplankton Chl *a* fluorescence. Pelagic waters of the N-S transect were generally characterized by relatively low Chl *a* fluorescence, although elevated values were observed along frontal zones of the SAF, PF, SACCF and SBdy (Fig. 6.2d). Increased Chl *a* concentrations along frontal zones is a well known feature of the Southern Ocean that has been attributed to the supply of nutrients through enhanced vertical mixing (Laubscher et al., 1993; Sokolov and Rintoul, 2007; Sokolov, 2008). The intensity of this mixing is particularly strong in the polar frontal region, where we observed the greatest enhancement of surface Chl *a* fluorescence. Relative to the N-S transect, waters of the Weddell Sea MIZ and near shore regions of the WAP showed extreme variability in Chl *a* fluorescence. Values ranged by more than two orders of magnitude, and exhibited sharp gradients over small spatial scales, often in regions of local sea-ice melt (Fig. 6.3c). Previous studies have demonstrated a strong influence of sea-ice processes on phytoplankton growth in surface waters (Smith and Nelson, 1985; Arrigo and van Dijken, 2004). Melting ice can stimulate phytoplankton growth through the release of Fe (Sedwick and DiTullio, 1997; Gerringa et al., 2012) and/or decreasing surface salinity, which acts to stabilize the

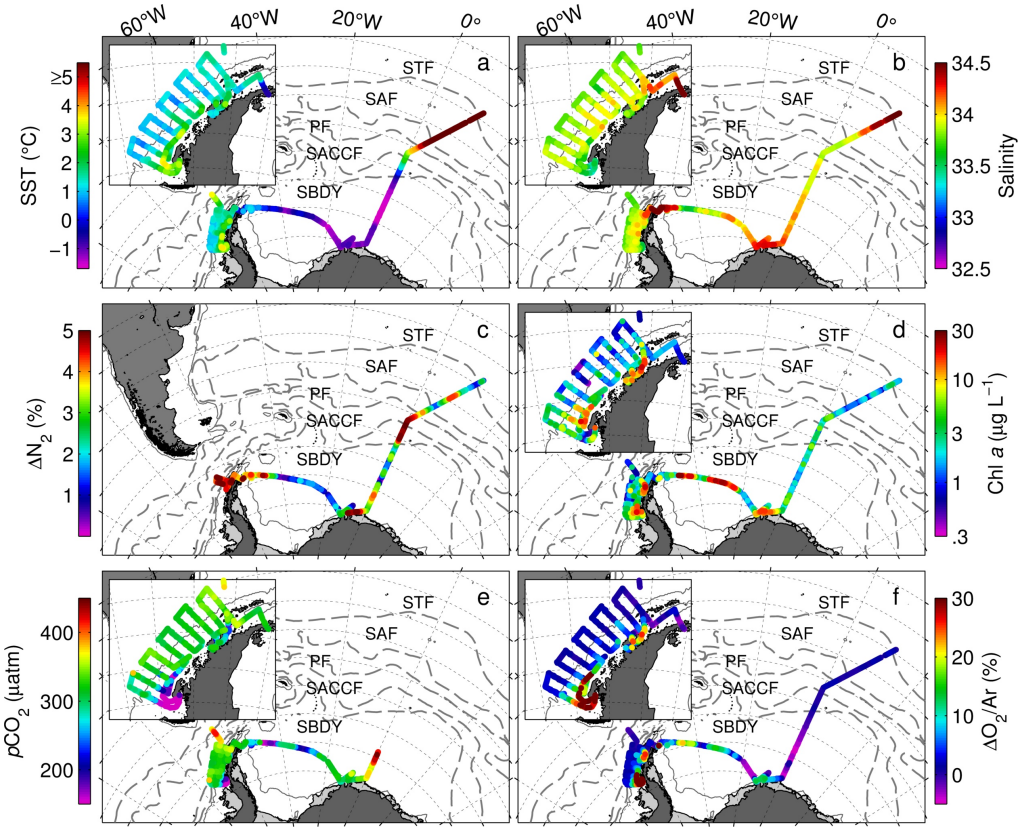

Figure 6.2: Spatial distribution of sea-surface temperature, SST (a), salinity (b), N_2 saturation, ΔN_2 (c), Chl *a* fluorescence (d), pCO_2 (e), and biological O_2 saturation, $\Delta O_2/Ar$ (f) along the cruise track. Inset figures show a detailed view of the property distributions along the WAP transect. Note that pCO_2 and ΔN_2 data are not available for the full cruise track due to instrument problems.

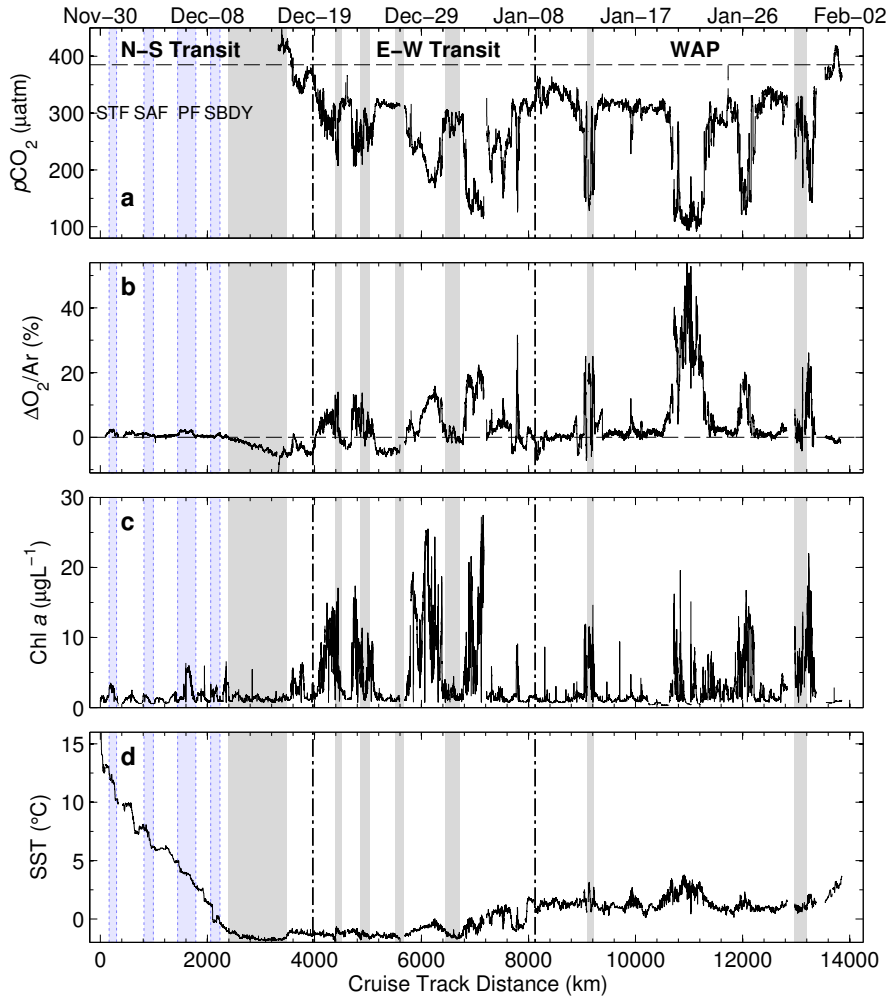

Figure 6.3: Line plots of pCO_2 (a), biological O_2 saturation, $\Delta O_2/Ar$ (b), Chl *a* fluorescence (c) and sea surface temperature (d) along the cruise track. Black vertical lines show the demarcation between the different portions of the cruise track, vertical grey shaded bars show regions with more than 50 % ice cover and blue shaded areas with dotted lines show the position of different frontal regions.

mixed layer. Indeed, we observed a negative relationship between Chl *a* fluorescence and salinity in the WAP ($r = -0.42$) and, to a lesser extent, along the E-W transit ($r = -0.17$). The relationship between biological productivity and mixed layer depth is addressed further below.

ΔO_2/Ar and pCO_2 Distributions

Along the N-S transect, ΔO_2/Ar was generally within a few percent of atmospheric equilibrium, with slightly positive values north of 55° S (< 2000 km along the cruise track) and negative values in ice-covered waters of the Weddell Sea MIZ (Figure 6.2f, 6.3b). Negative ΔO_2/Ar values are indicative of net heterotrophic conditions under the sea ice and/or the presence of deep mixed layers bearing a remnant heterotrophic signature. Although relatively few pCO_2 data are available for the N-S transect, we observed a sharp pCO_2 gradient (from 450 to 330 μatm) on the southern edge of the MIZ (Figure 6.2e, 6.3a). Surface water pCO_2 and ΔO_2/Ar showed high variability in the Weddell Sea MIZ (E-W transect) and WAP region. In these areas, pCO_2 reached minimum values of ≈ 100 μatm, while ΔO_2/Ar in excess of 50 % was observed (Figure 6.3a,b). The lowest pCO_2 and highest ΔO_2/Ar occurred in near shore waters of Marguerite Bay (WAP; Figure 6.2e,f) at ≈ 11000 km along our cruise track.

The pCO_2 and ΔO_2/Ar disequilibria we observed are substantially higher than values previously reported for the offshore pelagic Southern Ocean (Cassar et al., 2011; Shadwick et al., 2014), but they are consistent with recent observations from the highly productive waters of the Ross Sea and Amundsen Sea polynyas (Smith and Gordon, 1997; Tortell et al., 2011, 2012). The relative contributions of physical and biological processes to O_2 supersaturation are discussed further below. Here, we note only that ΔO_2/Ar was positively correlated with Chl *a* ($r = 0.66$ and 0.43 along the E-W and WAP transects, respectively), and showed enhancements in frontal zones along the N-S transect. Unlike ΔO_2/Ar, pCO_2 is sensitive to temperature-dependent solubility changes. During the 30 days prior to our sampling, the NOAA OISST data show an average surface water warming of ≈ 1 °C along our cruise track. This warming would lead to a 4 % (≈ 15 μatm) increase in pCO_2 (Takahashi et al., 2002), which is small compared to the observed pCO_2 variability along the cruise track. This result indicates that biological uptake exhibited a first order control on pCO_2 distributions.

As expected, pCO_2 exhibited a strong negative correlation with ΔO_2/Ar along our cruise track (Pearson's correlation coefficient, $r = -0.85$ and -0.91 for the E-W and WAP regions, respectively). Figure 6.4 shows the corresponding relationship between O_2 and total dissolved inorganic carbon (DIC) concentrations derived from pCO_2 and ΔO_2/Ar data. For both the WAP and E-W regions, the slope of the O_2 : DIC relationship was significantly lower than the expected photosynthetic stoichiometry (photosynthetic quotient, PQ, 1.0 – 1.4 mol O_2 : mol DIC; Laws, 1991). This discrepancy can be explained by the differential rate of sea-air O_2 and CO_2 exchange. Faster air-sea equilibration of O_2 results in a shorter residence time of this gas in the mixed layer, and a more rapid ventilation of photosynthetically-derived O_2. Dur-

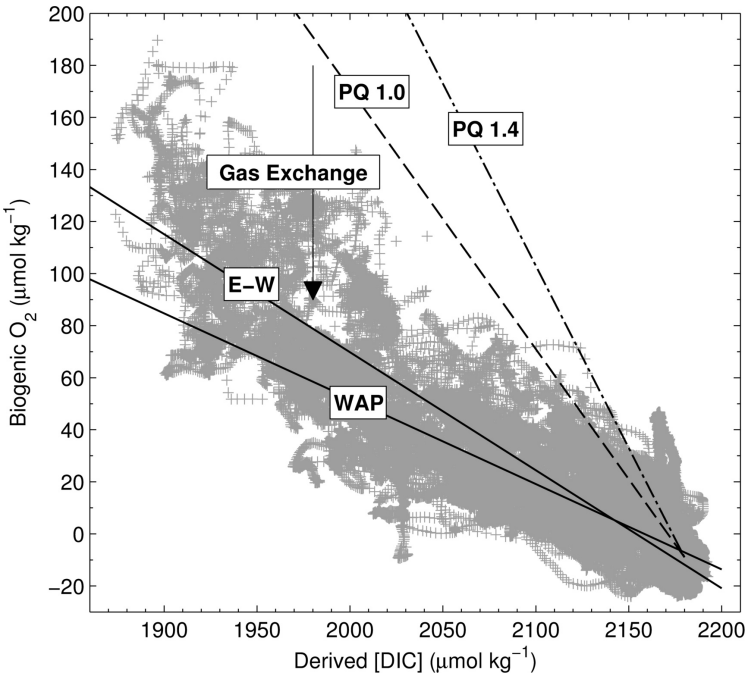

Figure 6.4: Relationship between dissolved inorganic carbon (DIC) concentrations and biogenic O_2. DIC values were obtained from MIMS pCO_2 data, using empirically-derived alkalinity values (based on surface salinity). Biogenic O_2 was derived from $\Delta O_2/Ar$ data using a temperature and salinity-dependent O_2 solubility function. Solid lines show the relationship for the E-W and WAP portions of the ship track derived from a Type II regression analysis, while dashed lines show the expected DIC – O_2 relationship for a photosynthetic quotient (PQ) of 1 or 1.4 mol O_2 produced per mol DIC consumed. The slope of the O_2 – DIC relationship is 0.45 and 0.33 for the E-W and WAP regions, respectively.

ing our cruise, the average residence time of O_2 in the mixed layer was < 1 week, given the mean wind speed (9.2 m s^{-1}) and MLD (26 m) observed across the survey region. In contrast, disequilibria in pCO_2, which is buffered by the seawater carbonate system, can persist for many weeks and even months in the surface mixed layer (Takahashi et al., 2009). The degree of uncoupling between CO_2 and O_2 in the mixed layer should thus provide insight into temporal evolution of biological productivity in surface waters. Regions where the biological production signal is 'older' should exhibit a higher degree of CO_2 – O_2 uncoupling. In our data set, we observed a difference in the O_2 – DIC slope between the WAP and E-W transects (0.32 and 0.45, respectively). The lower slope in the WAP region suggests that the production signal was integrated over a longer time interval. Indeed, remote sensing data show the presence of phytoplankton blooms in the WAP for over two months prior to our sampling (see further below). In contrast, much of the biological production along the E-W region occurred following recent ice retreat, with shorter time interval for gas exchange to uncouple O_2 and DIC. Similar observations on the time-dependent coupling of CO_2 and O_2 coupling have been recently reported by Shadwick et al. (2014) although these authors did not present their results in terms of derived O_2 and DIC concentrations.

Sea-Air CO_2 Fluxes

During the time of the survey, our sampling region served as a strong CO_2 sink. Along the E-W transit, CO_2 fluxes showed a distinct bimodal distribution (Fig. 6.5), with an overall mean of -97.5 ± 77.8 mmol m^{-2} d^{-1}, and a range of -343 to -1.98 mmol m^{-2} d^{-1} (negative fluxes signify oceanic uptake). For the WAP region, the mean CO_2 flux was -91.5 ± 91.8 mmol m^{-2} d^{-1} (range $-426 - 38.4$), with a long tail on the frequency distribution at high flux values (more than 20 % of the WAP observations showed oceanic uptake > 100 mmol m^{-2} d^{-1}). The highest oceanic CO_2 uptake along the entire cruise track (> 350 mmol m^{-2} d^{-1}) was observed near Marguerite Bay along the WAP, while a small net CO_2 efflux from surface waters was observed north of the WAP in pelagic waters of the Drake Passage.

Current estimates of regional air-sea CO_2 fluxes in the Southern Ocean are based on the climatology of Takahashi et al. (2009), compiled from many years of field measurements. This climatology indicates a weak to moderate Southern Ocean CO_2 sink between $\approx 40^\circ$ and 50° S (between the STF and PF), and suggests that waters south of the PF are either neutral or slight sources of CO_2 to the atmosphere. Actual data coverage is sparse, however, over much of the high latitude Southern Ocean, the MIZ and the continental shelf regions. Moreover, the resolution of the climatology grid cells (4° x 5°) is coarse relative to the observed length scales of variability. For these reasons, it is likely that significant features are not well represented in the climatological maps of Southern Ocean CO_2 fluxes.

In Fig. 6.5, we have plotted our cruise track over the gridded CO_2 fluxes of Takahashi et al. (2009). Our sampling region encompassed ≈ 25 grid cells, and we derived mean CO_2 fluxes and air-sea CO_2 gradients (ΔCO_2) for these areas. The results, shown in Table 1, highlight a significant difference between the CO_2 fluxes

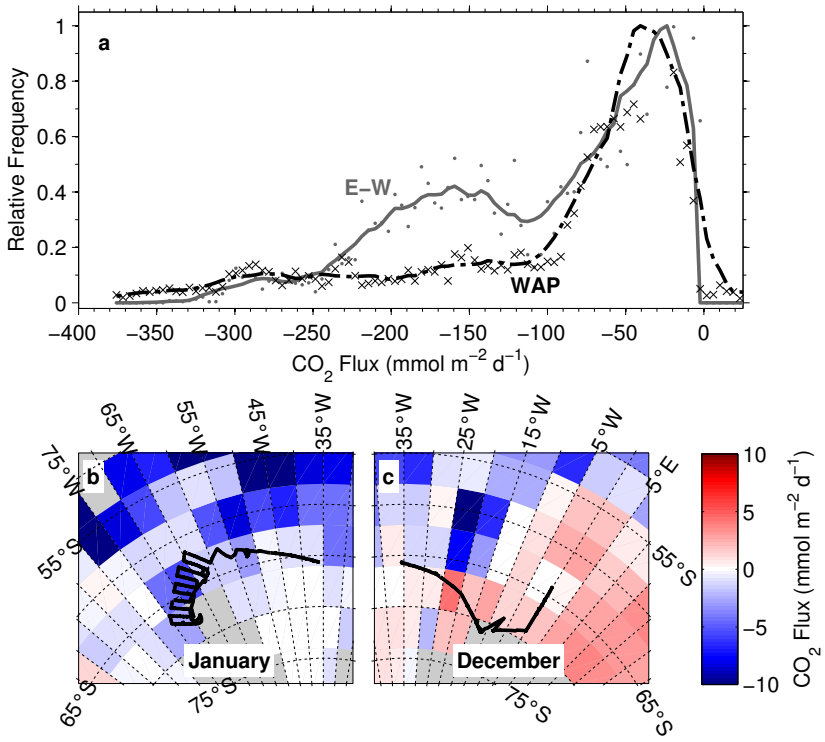

Figure 6.5: Frequency distribution of air-sea CO_2 fluxes along the E-W and WAP regions of our cruise track (a). Panels (b) and (c) show the ship-track plotted over the monthly climatological CO_2 flux derived from the global climatology of Takahashi et al. (2009). Negative fluxes imply oceanic uptake of CO_2.

derived from our MIMS data, and those from the climatology. In December, the climatology shows our sampling region to be neutral with respect to air-sea CO_2 fluxes (0.10 ± 1.1 mmol m^{-2} d^{-1}), whereas our measurements show mean oceanic uptake of 50 mmol m^{-2} d^{-1}. In January, the climatolgical CO_2 flux is close to -2 mmol m^{-2} d^{-1}, compared to the nearly -70 mmol m^{-2} d^{-1} we derived from our measurements. There are several likely reasons for the differences between MIMS-based and climatological CO_2 fluxes. The climatology represents a mean value averaged over many years of observations, and some inter-annual variability is expected. During our survey, we measured significantly higher air-sea CO_2 disequilibria than is present in the climatology: For December and January, respectively, we observed an average ΔCO_2 of ≈ -50 and -100 µatm, compared to the climatological values of $\approx +4$ and -20 µatm. These differences are likely too large to represent simple inter-annual variability, and likely reflect real differences in the underlying distribution of data. In addition to the larger air-sea CO_2 disequilibria we observed, mean wind speeds for our cruise were also $\approx$40 % higher than those used to compute fluxes in the climatology. Even neglecting the difference in wind-speeds (which results in an approx. two-fold difference in the gas exchange coefficient, k_{CO_2}), our results suggest significantly higher oceanic CO_2 uptake in high latitude Antarctic waters than is represented by the global climatology. Similar observations have been reported in previous studies (Hoppema et al., 2000a; Bellerby et al., 2004; Arrigo et al., 2008).

High latitude Antarctic waters, and the MIZ in particular, should be effective at sequestering CO_2 from the atmosphere due to the coupling of biological productivity with sea ice dynamics. As observed in our study and that of previous authors (Bakker et al., 2008; Jones et al., 2010), ice retreat leads to enhanced phytoplankton biomass and strong CO_2 uptake. Previous studies have shown that much of the CO_2 taken up by spring phytoplankton growth can effectively be sequestered into sub-surface layers during late summer cooling and the return of ice cover at the end of the growing season (Sweeney, 2003). Late season sea ice cover acts to limit out-gassing of high CO_2 during the net heterotrophic period of the annual growing season, enhancing the CO_2 sequestration efficiency of surface waters. For this reason, Antarctic continental shelf waters are likely to contribute disproportionately to Southern Ocean CO_2 uptake (Arrigo et al., 2008). Inclusion of more data from these regions into updated climatologies (with finer-scale grid cell resolution, and greater seasonal data coverage) could lead to revised estimates of Southern Ocean CO_2 uptake, with significant implications for the global C budget.

ΔN_2 Distribution

Across the majority of our sampling region, N_2 was supersaturated with respect to atmospheric equilibrium (i.e. $\Delta N_2 > 0$; Fig. 6.2c, 6.6a). The one exception occurred in an ice-covered region of the Weddell Sea ($\approx$ 6500 km), where we measured a ΔN_2 of ≈ -1 %. This feature may reflect the recent release of cold and fresh melt water that is under-saturated in N_2. The average ΔN_2 along the full cruise track was $\approx$ 2.5 %, with maximum values of $\approx$ 6 % observed in regions of high wind speed (> 20 m s^{-1}) and/or strong decreases in atmospheric pressure along the northern

portion of the N-S transect (in the SACCF region), the Weddell Sea continental margin and the northern WAP (Figure 6.6). The maximum ΔN_2 values we observed are significantly higher than those reported previously for mid-latitude oceanic regions (McNeil et al., 2005; Emerson et al., 2008; Vagle et al., 2010), including recent observations from the Subantarctic zone of the Southern Ocean (Weeding and Trull, 2014), where ΔN_2 did not exceed $\approx$3 % during an observation period of 7 months.

Box model calculations of ΔN_2, based on gas exchange processes and mixed layer entrainment (Nicholson et al., 2011), were used to examine the various processes contributing to the high ΔN_2 across our survey region. In general, the calculated ΔN_2 values were in good agreement with our observations, and the model was able to reproduce both the absolute magnitude of ΔN_2 and its spatial variability along much of our cruise track (Figure 6.6a). In a number of instances, however, modelled ΔN_2 was significantly lower than the observed values, particularly at the beginning and end of the HGTD data record. While it is possible that offsets between observations and model output at the end of the data reflect instrument problems with the HGTD, several sources of uncertainty are also present in our calculations. The 1-D model we used for our calculations does not account for advection of water masses with possibly different pre-formed gas concentrations. The dynamic system of frontal zones between Cape Town and the Polar Front may thus explain part of the discrepancy between observations and model output during the northern portion of the N-S transect. The remainder of our survey region is less prone to advection, owing to a (zonally) more homogeneous water mass structure. In the MIZ, uncertainty in the model calculations may result from sea-ice dependent processes. The sea ice history used in the model was derived from reprocessed satellite data with a relatively coarse spatial resolution. Sea ice cover exerts a significant influence on the strength of air-sea exchange, and errors in the representation of sea ice cover or in the parameterization of ice effects on gas exchange coefficients (Loose et al., 2009) would lead to uncertainty in the ΔN_2 calculation. Notwithstanding these sources of uncertainty, we conclude that our observations provide validation of the Nicholson et al. (2011) model in various Southern Ocean regions with high wind speeds and strong temporal changes in atmospheric pressure.

To examine the relative importance of atmospheric processes (diffusive air sea gas exchange, bubble injection, bubble exchange, and atmospheric pressure variations) and entrainment fluxes on ΔN_2, we ran model calculations with and without an explicit entrainment term. Results from this analysis (Fig. 6.6a) show that the effect of entrainment is small (mean entrainment effect of ≈ -1 %), with the majority of N_2 disequilibrium along the cruise track attributable to atmospheric exchange processes (mostly bubble injection). Whereas bubble injection leads to N_2 supersaturation, entrainment fluxes reduce ΔN_2 in the mixed layer if sub-surface values are at air equilibrium (i.e. $\Delta N_2 = 0$). Under this assumption, we calculated a mean entrainment effect of ≈ -1 % on ΔN_2, with a range between ≈ 0 and -3 %. Using this calculated entrainment term, we then derived the contribution of air-sea exchange processes to the mixed layer ΔN_2 signature (i.e. full model ΔN_2 – entrainment effect). Results from this calculation show that air-sea exchange processes resulted in a mean ΔN_2 of 2.4 % with a maximum value of $\approx$7 % under conditions of high

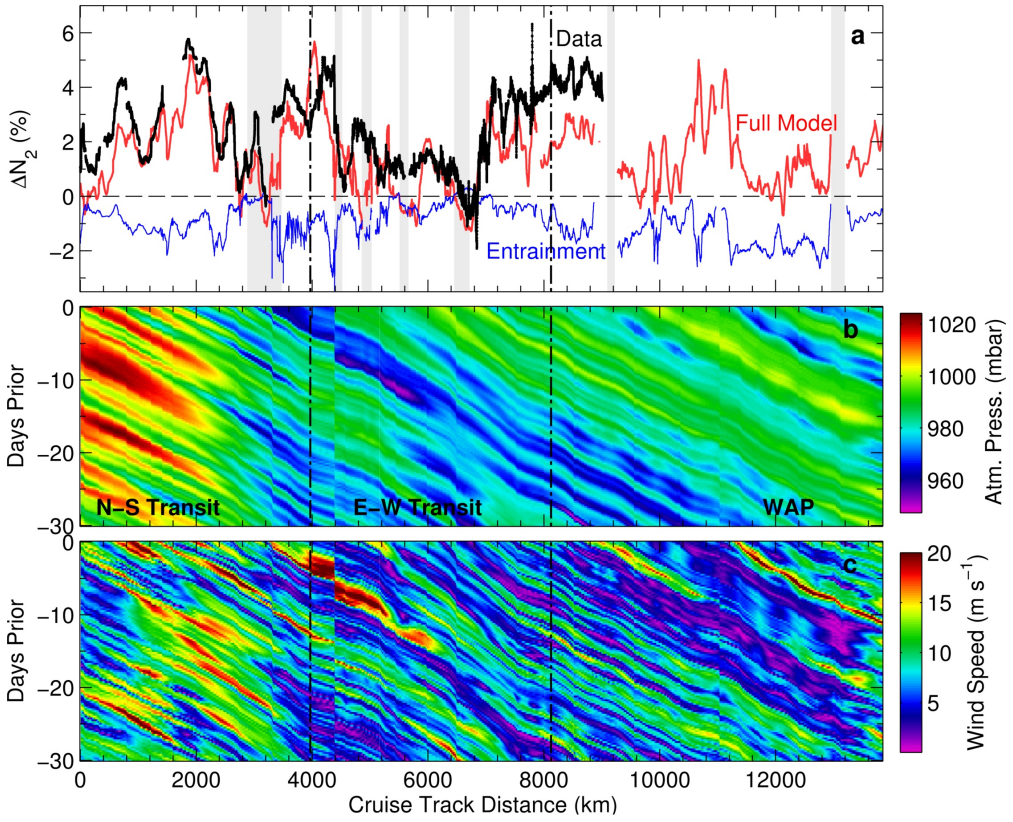

Figure 6.6: Nitrogen saturation, ΔN_2 (a), atmospheric pressure history (b) and wind speed history (c) along the cruise track. The black line in panel (a) shows the ΔN_2 value derived from GTD measurements, while the red line shows the results of box model calculations (see text for a full description). The blue line in panel (a) shows the effect of mixed layer entrainment fluxes on surface ΔN_2, while grey vertical patches in panel (a) show regions with greater than 50 % ice cover. Atmospheric pressure and wind speed data shown in panels (b) and (c) were derived from NCEP re-analysis. The y axis in panels (b) and (c) represents the number of days prior to the ship's sampling at any particular location along the cruise track.

wind speeds and high atmospheric pressure gradients. Our observations may be indicative of a persistently high ΔN_2 signal across large areas of the S. Ocean, driven by high regional wind speeds and strong changes in atmospheric pressure. Additional GTD data and higher resolution physical models will be needed to further examine the distribution of ΔN_2 across various Southern Ocean regions. Inclusion of GTD sensors on new biogeochemical ocean floats and gliders (Emerson et al., 2002; Nicholson et al., 2008) would be particularly useful in this respect.

Physical Controls on O_2 Saturation States

Unlike N_2, oxygen saturation states are strongly influenced by both physical and biological processes. We quantified the physical effects on O_2 saturation state ($\Delta O_{2\,\mathrm{phys}}$), using simultaneous MIMS and Optode measurements (see methods). Given the very similar thermodynamic properties of O_2 and Ar, the use of $\Delta O_2/Ar$ is preferable to N_2-normalization to separate the physical and biological effects on surface O_2. While $\Delta O_2/Ar$ is now increasingly being measured in various ship-based field studies, there are no current methods available for in situ Ar measurements.

$\Delta O_{2\,\mathrm{phys}}$ showed significant variability along our cruise track (Fig. 6.7), with values ranging from ≈ -6 % (undersaturation) to $> +15$ % (supersaturation). This range of values is significantly larger than that reported recently by Shadwick et al. (2014), who measured ± 3 % $\Delta O_{2\,\mathrm{phys}}$ along a transect from Australia to the Antarctic MIZ. In our study, maximum O_2 supersaturation was observed in the WAP region ($\approx$11000 km cruise track), whereas undersaturation was largely confined to several regions of local sea-ice cover (Fig. 6.7a). Box model calculations of $\Delta O_{2\,\mathrm{phys}}$ showed good agreement with observations, and were able to reproduce the magnitude and spatial pattern of $\Delta O_{2\,\mathrm{phys}}$ along much of the cruise track (Fig. 6.7a). In particular, the model captured the very high $\Delta O_{2\,\mathrm{phys}}$ along the WAP, and the physically induced O_2 under-saturation in ice covered regions. The largest discrepancy between the model and observations occurred along the N-S transect, possibly resulting from the lateral advection of heterogeneous waters masses, as described above, or an inappropriate choice of the sub-mixed layer O_2 end-member ($c_{O_2,\mathrm{sub}}$).

As with ΔN_2, we ran the box model calculations with and without an entrainment term to isolate the influence of atmospheric processes on $\Delta O_{2\,\mathrm{phys}}$. Based on our calculations, we estimate that atmospheric processes (primarily bubble injection) led to a physical supersaturation of O_2 of up to 5 %, whereas entrainment fluxes led to both supersaturation and undersaturation of O_2 (range -5 % to > 10 %) along different portions of the cruise track (Fig. 6.7b). The variable effect of entrainment on the surface O_2 budget results from differences in O_2 depth profiles and mixed layer depth history along the cruise track. When entrainment occurs in response to a deepening of the mixed layer, the depth profile of O_2 determines the extent to which surface water O_2 is either increased or decreased. Typically, sub-surface O_2 is lower than mixed layer values due to net heterotrophy in the sub-euphotic zone. Under these conditions, entrainment of sub-surface waters decreases $\Delta O_{2\,\mathrm{phys}}$. However, we observed a number of regions with high sub-surface O_2 levels, likely reflecting a remnant productivity signal prior to mixed layer shoaling. The entrainment of these

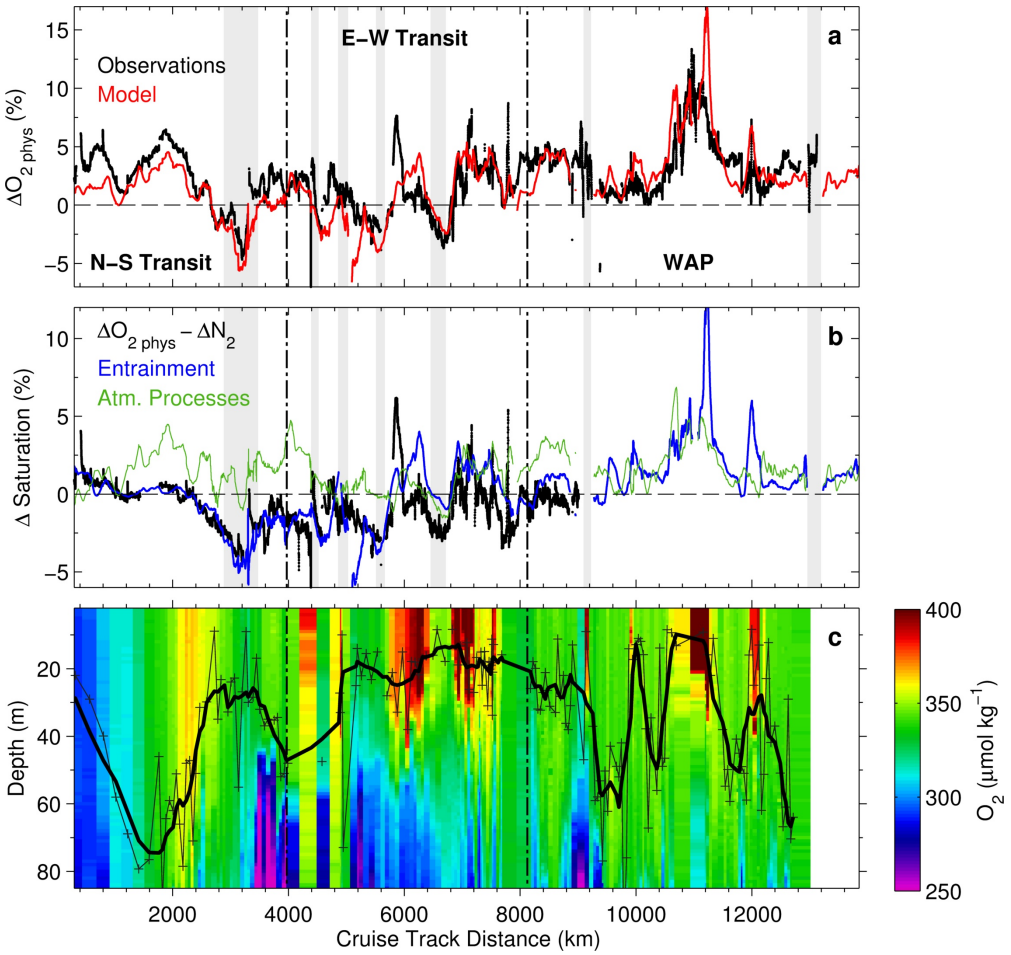

Figure 6.7: Effects of physical processes on mixed layer O_2 saturation state, $\Delta O_{2\,\mathrm{phys}}$. The black line in panel (a) shows observed values of $\Delta O_{2\,\mathrm{phys}}$, derived from MIMS ΔO_2/Ar and Optode ΔO_2, while the red line shows the results of box model calculations. Panel (b) shows the calculated effects of entrainment and atmospheric processes (air-sea diffusive flux and bubble injection) derived from the box model. The black line in panel (b) shows the difference between $\Delta O_{2\,\mathrm{phys}}$ and ΔN_2. This derived value provides a measure of entrainment fluxes (see text). Panel (c) shows O_2 depth profiles along the cruise track (derived from CTD observations) with the black line representing the computed mixed layer depth.

O_2-enriched sub-surface waters into the mixed layer results in a positive $\Delta O_{2\,phys}$ signature. This process was particularly evident in the WAP region where $\Delta O_{2\,phys}$ in excess of 10 % was observed. Jonsson et al. (2013) have also noted the importance of entrainment as a potential source of O_2 into the mixed layer.

The effects of entrainment on $\Delta O_{2\,phys}$ can be further examined using combined ΔO_2 and ΔN_2 observations. Whereas $\Delta O_{2\,phys}$ incorporates significant contributions from both air-sea exchange processes and entrainment, entrainment fluxes are significantly smaller for ΔN_2 as a result of the relatively weak vertical N_2 gradients. The difference between $\Delta O_{2\,phys}$ and ΔN_2 should thus reflect the entrainment effect on ΔO_2. Indeed, we observed a good correspondence between $\Delta O_{2\,phys} - \Delta N_2$ and the modeled entrainment contribution to $\Delta O_{2\,phys}$. This result suggests that our observations and model are able to provide reasonable constraints on the physical processes influencing the mixed layer O_2 budget. As described in the following section, this information can be used to refine NCP estimates derived from surface ΔO_2/Ar.

Net Community Production

In recent years, a number of studies have examined Southern Ocean NCP using mixed layer ΔO_2/Ar measurements, both from discrete samples and continuous underway analysis. This work has been largely based on the approach developed by Kaiser et al. (2005) and Reuer et al. (2007), where the mixed layer O_2 budget is assumed to be in a steady-state, with negligible vertical or lateral fluxes. Under these conditions, the biologically-induced flux of O_2 to the atmosphere (O_2-bioflux) provides a measure of NCP. The assumptions used in these calculations are problematic in weakly stratified and highly dynamic waters encountered over large portions of the Southern Ocean. Jonsson et al. (2013) have shown that O_2-bioflux provides good regional estimates of Southern Ocean NCP ($\pm \approx 25$ %), but significant offsets can exist at smaller scales due to an uncoupling between O_2 production and air-sea exchange, and to vertical O_2 fluxes across the base of the mixed layer. Using our box model results (section above), we can estimate the contribution of entrainment fluxes to the surface O_2 budget, and use this information to correct NCP estimates derived from surface ΔO_2/Ar data. However, our calculations do not include other physical processes such as upwelling and diapycnal mixing that can also influence NCP derived from ΔO_2/Ar measurements (Jonsson et al., 2013).

Figure 6.8 presents NCP estimates along our cruise track derived from ΔO_2/Ar, with and without a correction for entrainment. The figure also shows satellite-derived Chl *a* data, which provide information on the temporal evolution of phytoplankton biomass prior to our sampling. Across the full survey region, O_2/Ar-derived NCP ranged from ≈ -100 to 200 mmol O_2 m^{-2} d^{-1}. As discussed in previous studies (Stanley et al., 2010; Castro-Morales et al., 2013; Jonsson et al., 2013), an O_2 deficit in the mixed layer (i.e. negative ΔO_2/Ar) does not necessarily imply net heterotrophic conditions. The uptake of O_2 into the surface mixed layer can mask the in situ production signal, while physical mixing may be responsible for at least part of the negative ΔO_2/Ar signature. Indeed, our analysis suggests that vertical

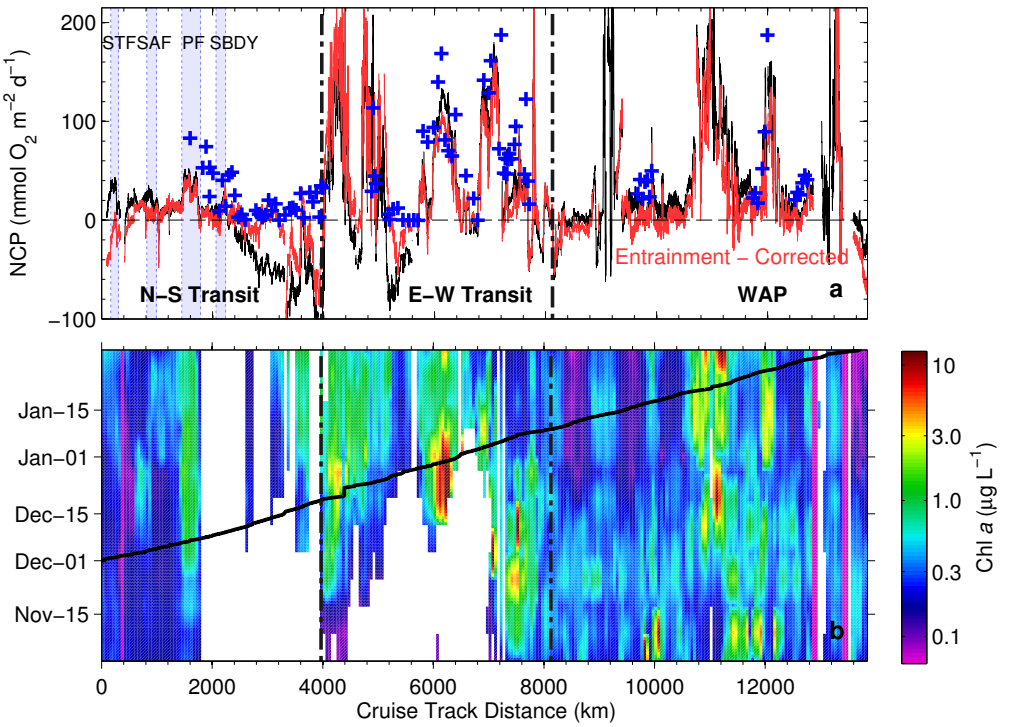

Figure 6.8: Distribution of net community production (NCP) along the cruise track (a), and time-history of Chl *a* concentrations derived from the Aqua-Modis remote sensing product (b). Black and red lines in (a) represent NCP estimates derived from $\Delta O_2/Ar$ data, with and without a correction for O_2 entrainment fluxes. The blue crosses in (a) represent NCP estimated from seasonal DIC deficits in the mixed layer. Vertical blue patches in (a) show frontal regions. The black line in (b) shows the location of the research vessel in space and time. Note the logarithmic scaling of the Chl *a* axis.

entrainment of low O_2 waters into the mixed layer was at least partially responsible for the negative NCP values we encountered along the cruise track, similar to the recent observations of Castro-Morales et al. (2013). For example, the strong negative NCP encountered between the SBdy frontal zone and the Weddell Sea MIZ (e.g. ≈3000 – 4000 km cruise track distance) was largely eliminated by the entrainment correction. In contrast, when NCP was large, the entrainment correction term was generally small compared to the biological production term. Even in the WAP region, where $\Delta O_{2\,\mathrm{phys}} > 10$ % was observed, the entrainment effect accounted for only ≈ 20 % of the total ΔO_2/Ar signal. In several other regions along the cruise track (e.g. in the STF zone), the entrainment-corrected NCP was lower than the uncorrected value, suggesting a signature of sub-MLD O_2 accumulation. This result depends on our choice of mixed layer depth and sub-surface O_2 end-member, and does not necessarily imply net heterotrophy in surface waters.

The variability of our ΔO_2/Ar-derived NCP values is somewhat higher than previous observations for the Southern Ocean, but the mean values for each of the survey regions is comparable to recently published values. Excluding negative values, the average NCP for the N-S, E-W and WAP transects was 12, 63 and 28 mmol O_2 m^{-2} d^{-1}, respectively. Based on discrete sampling of surface ΔO_2/Ar, Reuer et al. (2007) reported mean NCP estimates ranging from 20 – 36 mmol O_2 m^{-2} d^{-1} for the Subantarctic Zone, Polar Frontal Zone and Antarctic Zone. More recently, Shadwick et al. (2014) have reported a range of NCP estimates from 15 – 75 mmol O_2 m^{-2} d^{-1} (assuming a photosynthetic quotient of 1.4) along a transect from Australia to the Antarctic continent, while Cassar et al. (2011) report NCP of approx. up to 150 mmol O_2 m^{-2} d^{-1} for Subantarctic waters south of Australia. The maximum NCP values measured along our cruise track (≈200 mmol O_2 m^{-2} d^{-1}) are among the highest reported for the Southern Ocean, yet these values are not without precedent. Recent time-series work at the Palmer Station LTER site along the WAP (Tortell et al., 2014), show NCP values similar or higher to those we observed along the WAP region of our cruise track.

Independent NCP estimates, based on calculated seasonal DIC deficits at discrete sampling stations, showed good coherence with our ΔO_2/Ar-derived values. Both the spatial distribution and range of NCP values was similar between the two methods. Notably, the deficit calculations suggested NCP values close to 200 mmol O_2 m^{-2} d^{-1} at a number of stations, providing support for the very high NCP we derived from ΔO_2/Ar data. The major uncertainty in the derivation of daily NCP values from deficit calculations relates to the time-period over which DIC uptake is normalized. In regions subject to ice cover, it is typically assumed that DIC deficits accumulate once ice retreat begins, even though significant productivity has been shown to occur under sea ice (Arrigo et al., 2012). In the perennially ice-free open ocean, the initiation of net DIC consumption should be tied to mixed layer stratification in the spring time. In our analysis, we used the simplifying assumption that DIC consumption occurred over a two month period in the pelagic realm and three weeks in recently ice-covered waters. In principle, one could employ a more sophisticated approach, using satellite Chl *a* data, sea ice cover and mixed layer depth estimates, to infer the timing of NCP initiation. Although our approach is simplistic,

we are encouraged by the good correspondence between DIC deficit-derived and ΔO_2/Ar-derived NCP estimates.

Beyond the absolute value of our derived NCP estimates, the spatial distribution of biological productivity across our survey region is of interest. Over much of our cruise track, we observed a strong coherence between NCP and phytoplankton biomass detected by remote sensing (Fig. 6.8). Elevated NCP and Chl *a* were present in several frontal regions along the N-S transect, most notably in the PF zone where vertical mixing can supply Fe to iron-limited surface waters (de Baar et al., 1995). South of the SBdy frontal zone and along the E-W transect, sea ice processes appeared to be an important determinant of NCP distributions. As discussed above, the negative NCP observed in the ice-covered waters of the MIZ (i.e. between $\approx$2000 and 4000 km along the cruise track), may have resulted, in part, from deep water entrainment into the mixed layer. However, even after correcting for O_2 entrainment fluxes, a residual negative NCP signal remained. This may reflect the importance of other physical processes not accounted for in our simple box model, or it could be indicative of a true net heterotrophic signature in ice-covered waters. Net heterotrophy is expected under sea ice, if mixed layer irradiance falls below the photosynthetic compensation depth. Conversely, melting sea ice acts to decrease surface water salinity, leading to a stratification of the mixed layer and an enhancement of NCP.

Since macro-nutrients were plentiful across our entire survey region (minimum $NO_3^- > 8$ μM), light and/or iron availability are the most likely bottom-up controls on phytoplankton productivity. Although no iron data are available for our cruise, we assume, based on previous studies, that Fe availability was highest in regions of sea ice melt along the continental shelf (Klunder et al., 2011; Gerringa et al., 2012), where maximum NCP was observed. To examine the influence of light availability on surface water productivity, we derived NCP estimates for the regions surrounding each of our hydrographic stations (within 5 km), and correlated these values to the mixed layer depths derived from CTD data. As shown in Fig. 6.9, we observed a weak negative trend between NCP and MLD, particularly for stations with mixed layer depths less than 40 m. This relationship provides some evidence for light-dependent productivity, as suggested previously (Cassar et al., 2011; Huang et al., 2012; Shadwick et al., 2014). We note, however, that instantaneous MLD estimates do not necessarily provide a good indication of light availability over time scales relevant to our NCP calculations. A more refined analysis could be used, taking into account the time-dependent history of MLD, surface irradiance and water column light extinction (based on Chl *a* concentrations). Even without this added complexity, our derived NCP estimates likely reflect the dominant influence of light, micro-nutrient supply and sea ice cover on biological productivity across strongly contrasting regions of the Southern Ocean. Our results suggest that surface ΔO_2/Ar measurements have the capacity to provide meaningful NCP estimates with high spatial resolution.

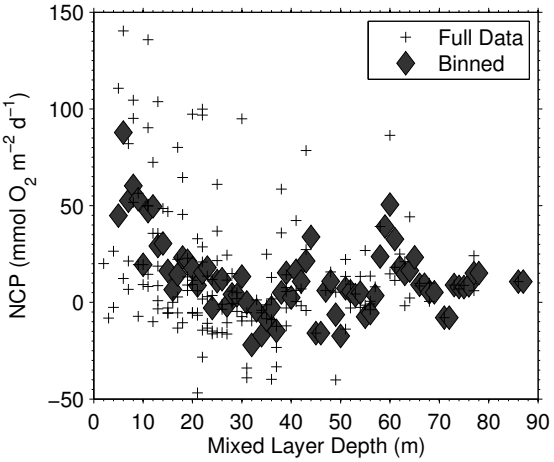

Figure 6.9: Relationship between $\Delta O_2/Ar$-derived NCP and mixed layer depth at the hydrographic stations along the cruise track.

6.4 Conclusions and Future Directions

Our results provide new information on the distribution of pCO_2, O_2, and N_2 in contrasting Southern Ocean regions, and insight into the underlying factors driving these distributions. Across our survey region, strong hydrographic variability led to large gradients in phytoplankton biomass, which, in turn, exerted a significant influence on surface water pCO_2 and $\Delta O_2/Ar$ distributions. This biological signature was modified by physical processes including sea-air exchange, and mixed layer entrainment. Using our observations and box model calculations, we were able to quantify the physical contributions to surface water O_2 and N_2 disequilibria, and we used this information to refine our estimates of NCP from surface $\Delta O_2/Ar$ observations. The NCP rates derived in this manner were consistent with independent measurements based on surface DIC deficits, providing a high spatial resolution description of biological productivity across distinct Southern Ocean regions. Our surface water pCO_2 observations suggest that the high latitude Southern Ocean may be a much stronger sink for atmospheric CO_2 than is currently represented in the global climatology (Takahashi et al., 2009). To the extent that our results are applicable on a broad regional scale, there may thus be a need to critically re-evaluate current estimates of Southern Ocean CO_2 uptake.

The increasing availability of autonomous ship-board instruments for surface gas measurements (e.g. Optodes, GTDs and sea-going mass spectrometers) has significantly expanded the spatial and temporal coverage of oceanic dissolved gas observations. In the future, continued deployments of these autonomous instruments, along with instrumented floats, gliders and moorings (Emerson et al., 2008; Nicholson et al., 2008), will allow us to assemble more robust databases of ΔN_2, ΔO_2, $\Delta O_2/Ar$ to help constrain NCP and air-sea exchange processes. Moreover, additional pCO_2 measurements in poorly sampled regions will help to refine mean climatological CO_2 fluxes for the Southern Ocean. In conjunction with increased

data coverage, more sophisticated modelling approaches could be used to interpret surface gas distributions, taking into account smaller-scale physical processes that act to perturb the mixed layer mass balance. Improved datasets and models will facilitate more robust NCP and CO_2 flux estimates, and increase our understanding of the Southern Ocean's role in global biogeochemical cycles.

7 A Conceptual View of Sub-Surface Processes in the Atlantic Subtropical Gyres

Abstract

Five biogeochemical floats featuring CTD, biooptical, oxygen, and/or nitrate sensors have been deployed in the North and South Atlantic subtropical gyres as part of the RemOcean project. Their first 2 years of data are presented with a focus on O_2, NO_3^- and the relation to biooptical proxies. The depth horizons of the deep chlorophyll *a* maximum (DCM) and the nitracline are in close proximity and follow a seasonal cycle determined by light and density variations, respectively. The summer time shallow sub-surface O_2 maximum is consistently displaced by approx. 50 m relative to the DCM and the nitracline. Three distinct biogeochemical layers can be identified based on ther biogeochemical signature: First, a net productive surface layer (layer I) with excess O_2 and depleted NO_3^-, second, a net heterotrophic layer II where NO_3^- is in stoichiometric deficit compared to O_2, and third, a net heterotrophic layer III where O_2 and NO_3^- are stoichiometrically balanced. This pattern is found in all subtropical gyres. Boundaries between the layers are set by the node of $AOU = 0$ around 100 – 120 m (ca. 25 $\mu mol\, s^{-1}\, m^{-2}$ noon-time PAR) and by the advective supply of surface NO_3^- through subtropical mode water around 200 m.

Acknowledgements

Float planning, operations and decoding is performed by the Oceanographic Autonomous Observations (OAO) group at the Laboratoire d'Ocanographie de Villefranche (LOV) and is a cornerstone of this work. Special thanks go to Hervé Claustre, Antoine Poteau, and Catherine Schmechtig of the OAO-LOV team. We want to thank the captain, crew and scientists of RSS James Cook cruise AMT22 for the float deployments and reference data. Data of the cruise are provided by the British Oceanographic Data Centre. Financial support by the RemOcean project (EU ERC grant agreement 246777) for the floats and float infrastructure as well as the O2-Floats project (KO 1717/3-1) of the German Science Foundation (DFG) (optodes & H.B.) is gratefully acknowledged.

7.1 Introduction

This chapter deals with surface and sub-surface observations from five floats deployed in the North and South Atlantic subtropical gyres and gives a qualitative picture of the dominant biogeochemical processes. The first section describes the platform configuration and the floats' drift, whereas the following ones address their upper 400 m record of almost 2 years of data acquired until October 15, 2014. The data interpretation starts with a semi-quantitative characterization of horizontal (spatial and temporal) variability and the discussion of seasonal patterns. Emphasis is put on prefomed nitrate as tracer for production, respiration, and their stoichiometric balance and biogeochemical depth horizons in the subtropical gyres are discussed. This lays the conceptual foundation for the quantitative estimation of net community production (NCP) in the next chapter.

lovbio Float Platform

The float platform termed "lovbio" is based on the Provor CTS4 float (nke Instrumentation, Hennebont/France) and was developed in cooperation between nke and the OAO-LOV team. Apart from the Argo-CTD (model SBE41CP, Sea-Bird, Bellevue/USA), the lovbio float can accomodate a suite of additional sensors: an oxygen optode model 4330 (Aanderaa Data Instruments, Bergen/Norway), a SUNA nitrate sensor (Satlantic, Halifax/Canada), an ECO Triplet sensor (WET Labs, Philomath/USA) for chlorophyll *a* and CDOM fluorescence as well as particle backscatter at 700 nm, a transmissiometer (model C-Rover, WET Labs, Philomath/USA) for beam attenuation at 660 nm, or an OCR504 radiometer (Satlantic, Halifax/Canada) for photosynthetically available radiation (PAR) and downwelling irradiance at 380 nm, 412 nm, and 490 nm. The latter sensor is powered in the upper 250 m only. Details of the float sensor configurations are summarized in table 7.1.

The lovbio floats can operate in two profiling modes termed "single" and "multi". The single profile mode is a typical one-profile & park cycle (see figure 1.5b) except that the surfacing time is adjusted to local noon. The multi profile mode consists of a sequence of four profiles, surfacing at local sunrise, noon, sunset, and

float	WMO ID	region	O_2	NO_3^-	mode	interval	cycles
lovbio003	6901437	SAG	x	x	single	10 d	68
lovbio005	6901439	SAG	x		single	1 d	455
lovbio006	6901474	NAG	x	x	multi	10 d	75
lovbio009	6901472	NAG	x	x	single	10 d	77
lovbio010	6901473	NAG	x		multi	10 d	76

Table 7.1: Float specifications for the five lovbio floats discussed here: Identifiers, sensor configuration, operation mode, and number of cycles as of October 15, 2014. While lovbio005 went out of operation in early 2014 (), the other four floats are still active. In addition to O_2 and NO_3^-, all floats featured sensors for PAR, chlorophyll *a* fluorescence, particle backscatter, and CDOM fluorescence. The profile and park depth is set to 1000 dbar.

sunrise of the next day, before parking again. The first profile of each sequence is always to full profile depth, i.e., 1000 dbar, whereas the depth for consecutive profiles in multi profile mode varies between 350 dbar and 500 dbar. The parking depth for all floats is 1000 dbar.

Float Positions in the Atlantic Subtropical Gyres

Initially, seven lovbio floats with oxygen optodes were deployed in October and November 2012 in the North and South Atlantic subtropical gyre, respectively, but two of them failed immediately at or shortly after deployment. The profile locations for the remaining five floats are mapped in figure 7.1. Streamlines indicate the direction whereas the shading gives the mean velocity of currents in the upper 500 m between 1992 and 2012 (Data from the ECCO2 project, Wunsch et al., 2009).

All floats stayed close to their deployment location (within $\approx$ 250 km) and only float lovbio010 shows a systematic drift to the West starting in 2014. Lovbio005 was set to a 1 day cycle and finished its service after 455 cycles on February 7, 2014. All other floats were set to a 10 day cycle and continue to transmit data (as of October 2014).

7.2 Methods

Sensor Calibrations

All oxygen optodes were multipoint laboratory calibrated (Bittig et al., 2012) against triplicate Winkler samples with an average root mean square error of 1.2 µmol L^{-1}. As their calibration response drifted in the months between laboratory calibration and deployment, the laboratory calibration was in-situ adjusted to a concurrent deployment CTD-O_2 cast (R/V James Cook, AMT 22 cruise, data provided by the British Oceanographic Data Centre) by matching the profiles as described in section 3.2.

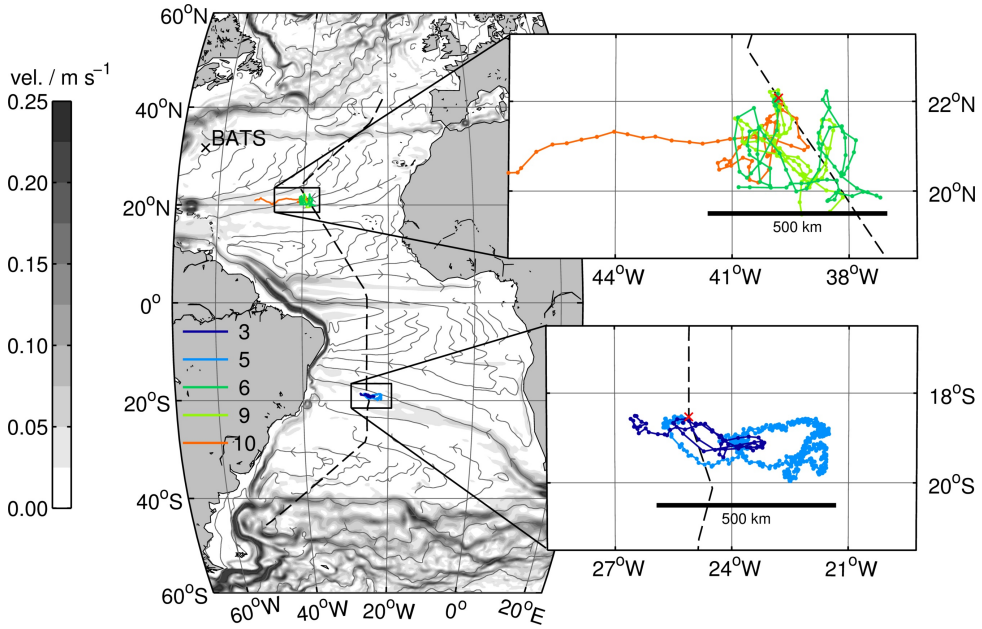

Figure 7.1: Map of the profile locations for all five North and South Atlantic subtropical gyre floats. The floats are colour-coded by their serial number and their deployment location is marked with a red cross. The AMT22 cruise track is shown as dashed line and the Bermuda Atlantic Time-series Study (BATS) site as black cross. Streamlines indicate the direction of the mean circulation (1992 – 2012) in the upper 500 m based on data from the ECCO2 project. The shading indicates the current velocity.

All other parameters except oxygen are handled by the OAO team, including sensor calibration and data processing. They process nitrate data using the temperature compensated, salinity subtracted (TCSS) algorithm of Sakamoto et al. (2009) and fine-tune the sensor's wavelengths used for the calculation to avoid artifically increasing nitrate concentrations towards the surface (de Fommervault, 2014). Since surface nitrate concentrations should be effectively zero, we applied a drift correction to the nitrate data on top. It was implemented as a piecewise linear fit of the upper 60 dbar (with one variable breakpoint per 30 cycles) and corrections are below 1 μmol kg^{-1} throughout, i.e., on the order of the sensor's detection limit.

Mixed Layer and Nitracline Depth

Mixed layer depth is based on the Lorbacher et al. (2006) curvature criterion using density. To adapt to their temperature-based algorithm, density profiles where multiplied with a factor between 0.2 and 60 to adjust the magnitude of the profiles' standard deviation, i.e., to adjust the curvature algorithm's sensitivity. The factor was iteratively increased until their mixed layer stratification quality index was above 0.75.

The nitracline depth uses a Δ criterion and is defined as the depth where nitrate concentrations reach a difference of 0.5 μmol L^{-1} above the surface concentration.

Preformed Chemical Tracers

To study the distribution of chemical tracers free of biological processes, the approach of preformed concentrations c° has been established. The working hypothesis for a preformed tracer is that the observed concentration can be separated into a preformed and a remineralized part.

$$c = c^\circ + c_{\text{remin.}} \tag{7.1}$$

The preformed part c° has properties similar to a conservative tracer and the remineralized part $c_{\text{remin.}}$ is estimated using a second parameter to which an assumed stoichiometric ratio can be applied (e.g., equation 5.4, Anderson, 1995). Commonly, apparent oxygen utilization AOU (equation 5.5) is used to quantify the remineralized part and definitions for preformed phosphate (Anderson, 1995), preformed nitrate (Emerson and Hayward, 1995), and dissolved inorganic carbon (DIC) (Johnson and Riser, 2014) are given below.

$$c^\circ_{PO_4^{3-}} = c_{PO_4^{3-}} - \frac{1}{150} \cdot AOU \tag{7.2}$$

$$c^\circ_{NO_3^-} = c_{NO_3^-} - \frac{1}{10} \cdot AOU \tag{7.3}$$

$$c^\circ_{DIC} = c_{DIC} - \frac{106}{150} \cdot AOU - 2070 \text{ μmol kg}^{-1} \tag{7.4}$$

Variability Analysis

Spatial and temporal patterns are inherently linked and this section aims to provide a semi-quantitative description using a statistical approach. The main tool is the spatial correlation R between float observations Z_{x_i,t_i} as a function of distance d and time lag Δt

$$R_{d,\Delta t} = \frac{\sum_{i=1}^{N_{d,\Delta t}} \left(Z_{x_i,t_i} - \overline{Z}\right) \cdot \left(Z_{x_i+d,t_i+\Delta t} - \overline{Z}\right)}{\sqrt{\sum_{i=1}^{N_{d,\Delta t}} \left(Z_{x_i,t_i} - \overline{Z}\right)^2} \cdot \sqrt{\sum_{i=1}^{N_{d,\Delta t}} \left(Z_{x_i+d,t_i+\Delta t} - \overline{Z}\right)^2}}\,, \tag{7.5}$$

where $\overline{Z}$ is the mean of all observations. Observations with a small separation are expected to be more strongly correlated than observations with a large separation.

All pairs of observations in a given depth interval are thus binned in d and Δt and a metric is generated according to equation 7.5. Other approaches use, e.g., the spatial covariance (the numerator in equation 7.5) or semivariance (see Glover et al., 2011). In principle, this metric can be used to estimate separate spatial and temporal decorrelation scales. Commonly one would use the contour level at which the experimental correlation $R_{d,\Delta t}$ drops to $1/e$ of the experimental zero-lag correlation $R_{d=0,\Delta t=0}$ (a measure for the variability within the depth bin). However, we refrained from doing this quantification for reasons discussed below.

7.3 Spatial and Temporal Variability

Two special cases for the variability analysis in the NAG are shown in figure 7.2, one for the depth interval 7 – 15 dbar near the surface (top) and one for the depth interval 245 – 265 dbar (bottom). The correlograms are given for temperature (left), salinity (middle), and oxygen (right), respectively.

These two depths deviate from the expected decay of the correlation with increasing separation. Instead, systematic patterns are observed. They are shown here to illustrate the importance of large scale processes on small scale dynamics.

Near the surface, radiative forcing is nearly homogeneous on scales of 100 km and there is thus a strong correlation of surface temperature data on spatial scales. On temporal scales, however, seasonality causes a correlation-anticorrelation pattern with a period of 1 year (top left). The seasonal imprint is also visible in oxygen caused by solubility changes due to heating and cooling (top, right). Surface waters are spatially homogeneous in O_2 with almost no attenuation of R on a scale of 300 km. Salinity, in contrast is dominated by episodic rain events and less by seasonality. Its correlation attenuates with time and distance separation as expected from a set of independent observations.

Comparison with the deep bin (bottom) shows two differences: First, data seem to be correlated less strongly. However, the smaller magnitude of R simply arises from the larger size of the pressure bin (to cover a similar number of data points) and stronger depth gradients, i.e., a higher variability within each bin. Second, there

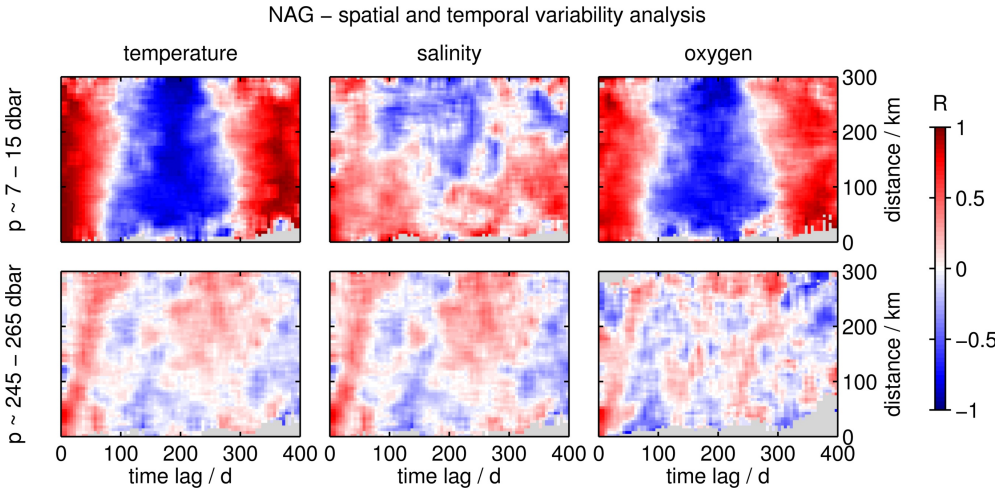

Figure 7.2: Correlation between observations against distance and time lag for two depth intervals, 7 – 15 dbar near the surface (top) and 245 – 265 dbar (bottom) for temperature, salinit, and oxygen (left to right). Generally, the higher the separation, the lower the correlation. However, patterns may arise due to, e.g., the seasonal cycle (top left and right) or propagating Rossby waves (bottom, local maximum at ca. 4 km d^{-1} inclination).

is a local maximum in R at an inclination of ca. 4 km per day. This local maximum is present in temperature, salinity, and oxygen and indicates data along this space – time path to be more strongly correlated than data at the same space/time but different time/space separation. This suggests a recurring, propagating feature to determine variability of the whole water mass at that pressure. This local maximum is visible in deeper pressure bins as well, but it nearly vanishes if the analysis is done on isopycnals. This is strong evidence for propagating Rossby waves being the main cause of variability in the permanent pycnocline of the gyre. In fact, a speed of 4 km d^{-1} is in the typical range for Rossby waves at 20° N (Tomczak and Godfrey, 1994).

The Rossby waves cause a consistent distortion of the correlogram invalidating the assumption of an independent space and time component, i.e.,

$$R_{d,\Delta t} \neq R_d \cdot R_{\Delta t} \ . \tag{7.6}$$

Since quantification of space and time decorrelation scales are based on this separation, we did not derive them for our float data.

7.4 Float Observations

The dominant cause of temporal surface variability in the subtropical gyres is the seasonal cycle. For the two deployment regions, an operational definition of the seasons is used: spring starts with an increase in sea surface temperature and a shoaling of the mixed layer. Consequently, the onset of spring is considered as March 15 in the

Northern hemisphere region and November 15 in the Southern hemisphere region. The other seasons follow accordingly with 3-month separation.

Physical Parameters

Figure 7.3 illustrates the physical setting in the North Atlantic subtropical gyre: It shows the lovbio009 measurements of temperature, salinity, derived potential density, and PAR in the upper 400 dbar of the water column as well as mixed layer depth (grey dashed line) based on the curvature of potential density (Lorbacher et al., 2006). Figures for the other four floats can be found in the appendix (figures A.7.1 – A.7.5).

Light penetration follows a clear seasonal cycle and is deepest during northern hemisphere spring and summer (March 15 – Sept. 15), following the solar elevation. Consequently, sea surface temperatures lag by a quarter year and rise during spring and summer and decrease during autumn and winter.

The temperature cycle determines the surface stratification and thus mixed layer depth. With the onset of spring, a seasonal surface thermocline is formed which intensifies during summer, leading to strong density stratification. With surface cooling in autumn, surface density is increased and deeper waters are entrained as the mixed layer deepens until the end of winter. Thus, the mixed layer gradually deepens from 10 – 20 m in spring to about 50 m during summer reaching up to 140 m in late winter.

The summer stratification is stabilized by episodical rain events, which freshen the surface mixed layer thus making the water even less dense. With a deeper mixed layer in winter, the same amount of freshwater is distributed over a larger volume and thus causes a smaller effect. While the subtropical gyres are regions of net evaporation, the shallow overturning circulation balances the freshwater budget and determines the salinity distribution (Talley, 2008), e.g., the shallow salinity maximum layer (Subtropical Underwater) in the NAG (figure 7.3). Below around 200 m (i.e., the permanent pycnocline), variability is dominated by mesoscale features (see, e.g., March/April 2013 in figure 7.3 and 7.4; section 7.3 above).

Biogeochemical and Biooptical Parameters

Biogeochemical parameters from NAG float lovbio009 are summarized in figure 7.4 (see appendix figures A.7.1 – A.7.5 for the other floats). While surface O_2 is slightly supersaturated year-round, a shallow sub-surface oxygen maximum (SOM) forms below the thermocline between spring and autumn, caused both by physics and biology: Surface warming of the mixed layer reduces oxygen solubility, i.e., mixed layer O_2 concentrations decline throughout spring and summer because of outgassing of excess O_2 to the atmosphere. High winter-time O_2 levels, however, persist below due to limited exchange in stratified, sub-mixed layer waters. Moreover, net biological production leads to an increase in oxygen at depths around 70 – 80 m, further strengthening the SOM (see figure 7.4). At the same time, excess oxygen produced in the mixed layer is quickly lost to the atmosphere due to gas exchange.

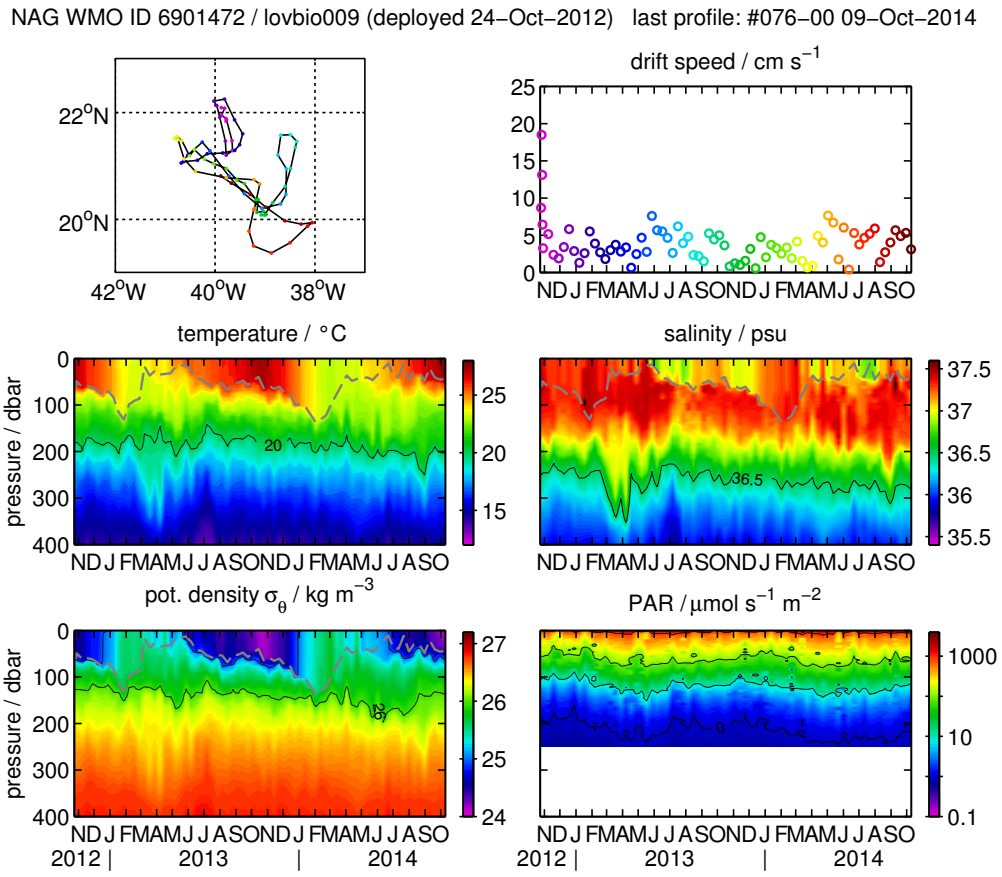

Figure 7.3: Float track, drift speed, and physical data (temperature, salinity, density, and PAR) for NAG float lovbio009. Only the upper 400 dbar portion is shown. The grey dashed line in the lower panels indicates the mixed layer depth.

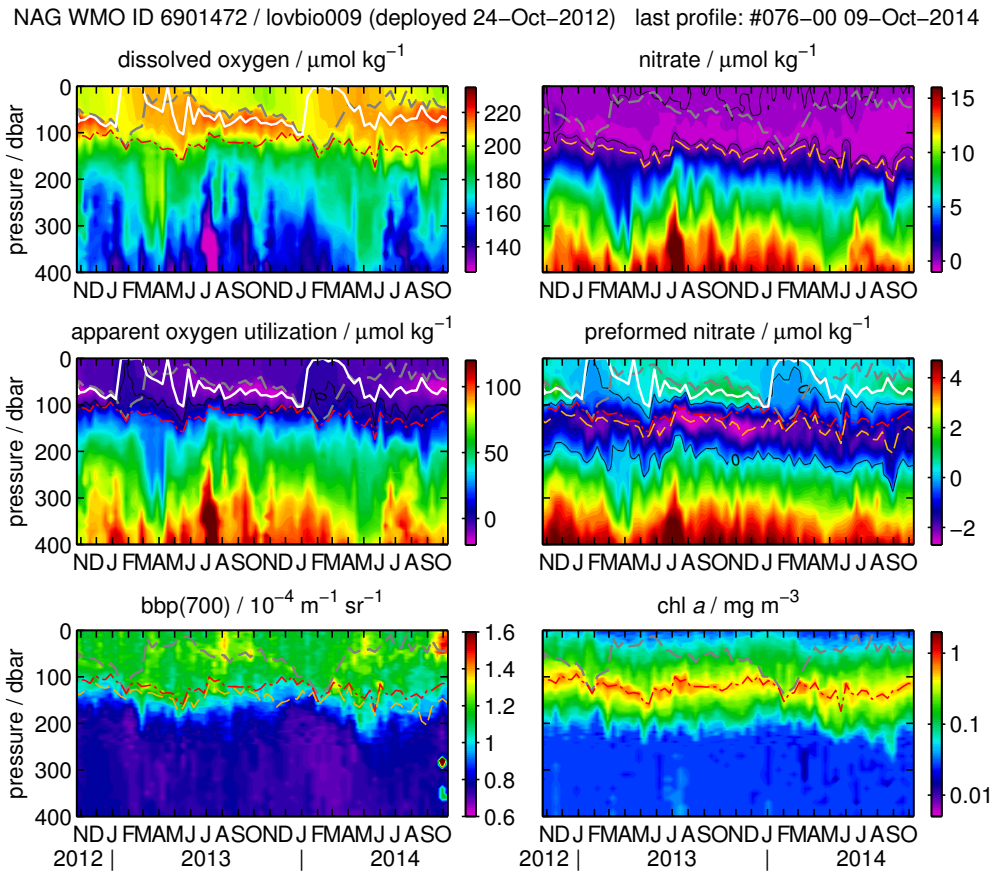

Figure 7.4: Oxygen, nitrate, apparent oxygen utilization *AOU*, preformed nitrate concentration, backscatter b_{bp} at 700 nm, and chlorophyll *a* fluorescence in the upper 400 dbar for NAG float lovbio009. The grey dashed line indicates the mixed layer depth, whereas the white line marks the O_2 maximum, the red dash-dot line the deep chlorophyll *a* maximum, and the orange dashed line the nitracline.

With deepening of the mixed layer in autumn, the shallow sub-surface oxygen maximum is eroded from above until surface waters are near-homogeneous in dissolved oxygen in early winter. At the same time, surface cooling causes undersaturation of the mixed layer and thus ingassing of O_2, which continues throughout winter. Therefore, the O_2 maximum is found at the surface for the second half of winter after complete erosion of the SOM (see white line in figure 7.4). With rising surface temperatures with the onset of spring, the mixed layer is shoaling, surface O_2 solubility decreases and the cycle starts again.

Surface waters are depleted of nitrate year-round and the nitracline (defined with a $\Delta 0.5$ µmol L^{-1} criterion) is found at ca. 140 m in the NAG and around 160 m in the SAG region. Approx. 15 m to 20 m above this layer, a deep chlorophyll *a* maximum (DCM) with values around 0.8 mg m^{-3} is located.

While chlorophyll *a* is a valid proxy for phytoplankton, its quantitative value is severely biased by the light adaptation of phytoplankton with depth and thus increased chlorophyll *a* to biomass ratios. The DCM is thus not necessarily the depth with the highest biomass. In fact, particle backscatter b_{bp} (figure 7.4) or beam attenuation c_p (not shown), both better proxies for (standing stock) biomass, show a relatively homogeneous distribution above the nitracline with some depletion towards the surface. We need to emphasize, however, that c_p observations are questionable due to possible issues with the C-Rover instrument.

Because of the O_2 surface supersaturation, apparent oxygen utilization is slightly negative at the surface. Its lowest values are observed at the shallow oxygen maximum, whereas it is steadily increasing below (figure 7.4).

Surface values of preformed NO_3^- are slightly positive due to O_2 supersaturation, i.e., negative *AOU*. Based on the assumption that the stoichiometric ratio (equation 7.3) is representative of the regional organic matter production and respiration, the effects of photosynthesis and respiration should cancel below the surface and yield a homogeneous distribution of $c^\circ_{NO_3^-}$. In contrast, preformed NO_3^- shows a clear pattern: a shallow maximum near the SOM and a minimum with *negative* values near the nitracline (dashed orange) below. This unexpected observation will be addressed in detail in section 7.5.

Seasonal Patterns and Productivity

As discussed above, the surface waters of the subtropical gyres follow a clear seasonal cycle. A summary of the seasonal depth variations of the mixed layer depth (MLD), the oxygen maximum (OM), the deep chlorophyll *a* maximum (DCM), the 5 µmol s^{-1} m^{-2} noon time isolume (PAR = 5), and the nitracline (NCL) is given in figure 7.5, binning all available profiles of the NAG and SAG region, respectively. In addition, the sub-surface node of *AOU* (*AOU* = 0) is given as dashed blue line. The node of *AOU* is at the same time the shallow node of preformed nitrate ($c^\circ_{NO_3^-} = 0$, since no measureable nitrate is present) and the nitracline coincides with the minimum of preformed nitrate.

Except for periods with deep mixing, i.e., the winter season, the highest oxygen concentrations are found below the mixed layer around 70 – 80 m due to sub-

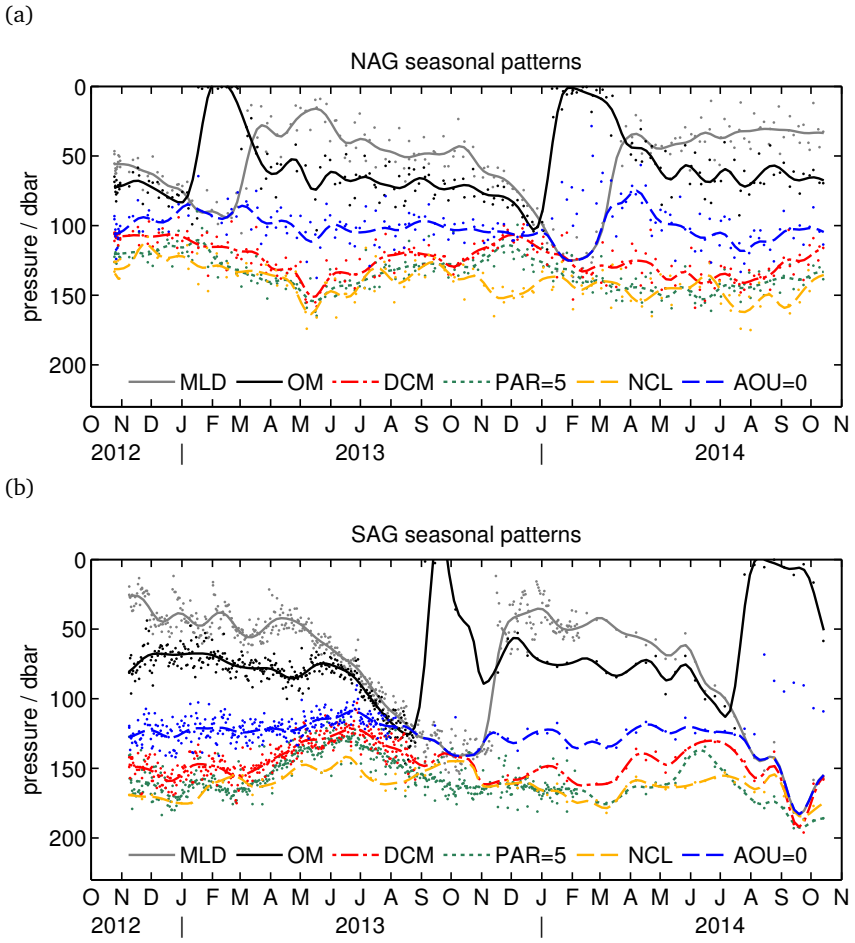

Figure 7.5: Seasonal patterns in the depth of the mixed layer (MLD), the oxygen maximum (OM), the deep chlorophyll *a* maximum (DCM), the 5 μmol s^{-1} m^{-2} noon time isolume (PAR = 5), the nitracline (NCL), and the sub-surface node of *AOU* (*AOU* = 0) obtained from all floats (a) in the North and (b) South Atlantic subtropical gyre region (see figure 7.1).

surface O_2 production. The occurence of this SOM, however, does not imply that productivity is highest at that depth, since mixed layer excess O_2 is quickly lost to the atmosphere and O_2 thus can only accumulate in the stratified waters below. Instead, backscatter as a proxy of particulate organic matter is quite homogeneous down to the depth of the DCM which suggests a similar level of primary productivity at the SOM and above.

The node of *AOU* at ca. 100 m in the NAG and ca. 120 m in the SAG separates between the domain of net autotrophy (above) and net heterotrophy (below). With low light intensities at depth, primary producers need to increase their chlorophyll *a* to biomass ratio to maintain photosynthesis. This light adaptation comes at the cost of a reduced productivity (e.g., Sakshaug et al., 2009; Sarmiento and Gruber, 2006) and eventually respiration becomes dominant over primary production.

In turn, the DCM (120 – 140 m in the NAG and 140 – 150 m in the SAG) can be seen as proxy for the deep limit of production. It closely follows the isolume at that depth and is located just above the edge of measureable nitrate (i.e., the nitracline). Controlled by the physical supply from below (see below & table 7.2), nitrate gets depleted within a few meters below the DCM. This tight control suggests nitrate to be taken up at the edge of the phytoplankton-inhabited zone where productivity is constrained by a combination of light and nitrate availability.

Preformed nitrate indicates that the surface water column is not in a Redfield-balance throughout. Instead, there is a nitrate excess/oxygen excess above the node of *AOU* and a nitrate deficit/oxygen deficit below.

Light vs. Density Control

Seasonal displacements of both the nitracline and the DCM are highly coherent with density and PAR levels, i.e., the DCM is always close to the same isolume (8 ± 4 μmol s^{-1} m^{-2} noon time PAR). For a detailed analysis, the depth variations of the DCM, the nitracline as well as the depth variations of a nearby isolume and isopycnal were decomposed into a seasonal component and a short timescale residual using a low-pass filter with a 90 d cutoff frequency. Correlation coefficients R^2 are summarized in table 7.2.

On seasonal scales, the depth of the DCM is determined by the light intensity (light limitation) rather than density (mean R^2 of 0.78 for PAR vs. 0.39 for σ_θ), whereas on shorter time scales density fluctuations and light intensity show now strong correlation with the DCM depth (mean R^2 of 0.21 for PAR vs. 0.27 for σ_θ). Nitracline depth variations, however, are dominated by density fluctuations on both seasonal (0.37 for PAR vs. 0.71 for σ_θ) and shorter time scales (0.09 for PAR vs. 0.52 for σ_θ), i.e., the physical supply through advection and diffusion dominates nitrate. However, nitrate is quickly consumed if it is accessible to organisms and the nitracline is thus always a few meters below the DCM (and thus somewhat correlated to PAR on seasonal scales).

$R^2(\downarrow, \rightarrow)$	region	float SN	isolume (PAR) seasonal	isolume (PAR) residual	isopycnal (σ_θ) seasonal	isopycnal (σ_θ) residual
DCM	SAG	3	0.77	0.03	0.42	0.56
	NAG	6	0.64	0.33	0.13	0.15
	NAG	9	0.87	0.01	0.51	0.28
	NAG	10	0.82	0.47	0.50	0.10
nitracline	SAG	3	0.41	0.02	0.78	0.69
	NAG	6	0.30	0.17	0.73	0.50
	NAG	9	0.39	0.08	0.63	0.38

Table 7.2: Correlation coefficient R^2 between the depth of the chlorophyll *a* maximum (DCM) or nitracline and the depth of a nearby isolume (PAR) or isopycnal (σ_θ), respectively. The depth timeseries were separated into a seasonal and a residual component using a low-pass filter with a 90 d cutoff frequency. Float lovbio005 was excluded because of its incomplete seasonal cycle for chlorophyll *a*.

7.5 Negative Preformed Nitrate and Biogeochemical Depth Horizons

Implications from Float Observations

The clear imbalance in $c^\circ_{NO_3^-}$ with depth (figure 7.4) indicates a vertical stoichiometric decoupling. The biogeochemically linked processes of nitrate uptake and oxygen production appear to take place at different depth horizons:

- Oxygen production – and likely DIC drawdown – occurs throughout the euphotic zone (the upper $\approx$100 m) where there is no measureable nitrate present.
- Towards the DCM, net production rates as evidenced by smaller oxygen accumulation decline gradually due to reduced light levels.
- Decoupled from O_2 production, nitrate uptake ocurs near the nitracline about 10 – 15 m below the DCM.

These different horizons cause an inhomogeneous preformed nitrate distribution (figure 7.4): Oxygen production without stoichiometric nitrate consumption (because of depleted NO_3^-) yields a shallow maximum in preformed nitrate, while nitrate uptake, i.e., depletion of nitrate without stoichiometric oxygen production, gives negative preformed nitrate concentrations near the nitracline.

Such a non-Redfieldian stoichiometry (not following equation 5.4), i.e., production without nitrate, has been observed before both for DIC (e.g., at BATS, Michaels et al., 1994) and oxygen (e.g., at HOT, Johnson et al., 2010). Our observations thus add to the production controversy and nitrate puzzle (see below).

The Bigger Picture: Time Series and Global Observations

The mean annual cycle of preformed nitrate and preformed DIC based on 25 years of bottle data from BATS is shown in figure 7.6 (after Johnson and Riser, 2014): From spring to autumn, a shallow preformed nitrate maximum builds up near the seasonal mixed layer around 50 m while negative preformed nitrate concentrations develop at approx. 130 m. With winter convection, the system is reset and preformed nitrate equalized in the deep mixed layer.

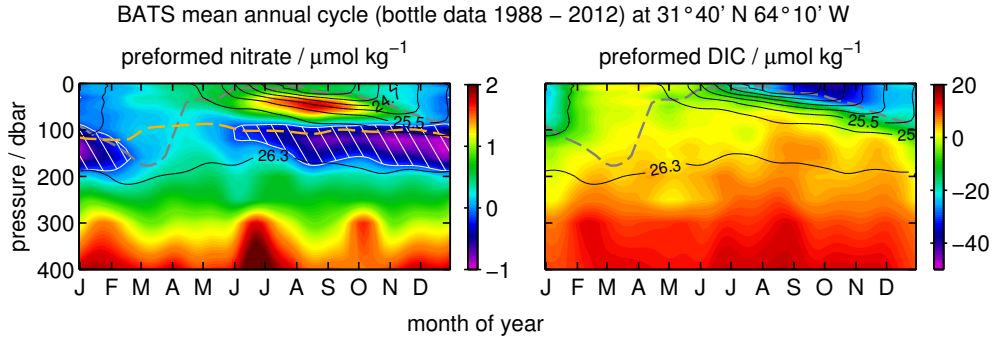

Figure 7.6: Mean annual cycle of preformed nitrate (left) and preformed DIC (right) from BATS bottle data (obtained from http://bats.bios.edu). Potential density is given as black contours and the mixed layer depth as grey dashed line. In addition, the white hatching gives the domain of negative preformed nitrate concentrations and the orange dashed line denotes the nitracline.

This pattern is similar to our observations, but it differs in a few important details:

- The shallow node of preformed nitrate/*AOU* is only ≈ 10 m shallower than the nitracline.
- The minimum of preformed nitrate is not co-located but about 20 – 30 m deeper than the nitracline.
- The domain of negative preformed nitrate is a seasonal phenomenon and gets eroded with deep winter mixing.

While preformed phosphate has a similar mean annual cycle as preformed nitrate (not shown), no concurrent pattern is visible in preformed DIC (after equation 7.4), indicating that O_2 and DIC behave Redfieldian. The negative preformed DIC that develops in the mixed layer is an artifact of the slower gas equilibration of CO_2 compared to O_2 (figure 7.6).

Similarly, negative preformed nitrate concentrations occur on a broader scale, e.g., in the North Pacific subtropical gyre (figure 7.7, after Emerson and Hayward, 1995) as well as in the North and South Atlantic subtropical gyres (figure 7.8, AMT22 cruise, RSS James Cook, data provided by the British Oceanographic Data Centre). The patterns discussed here are thus representative for vast stretches of all subtropical gyres. During the AMT22 cruise, the NAG was observed during boreal

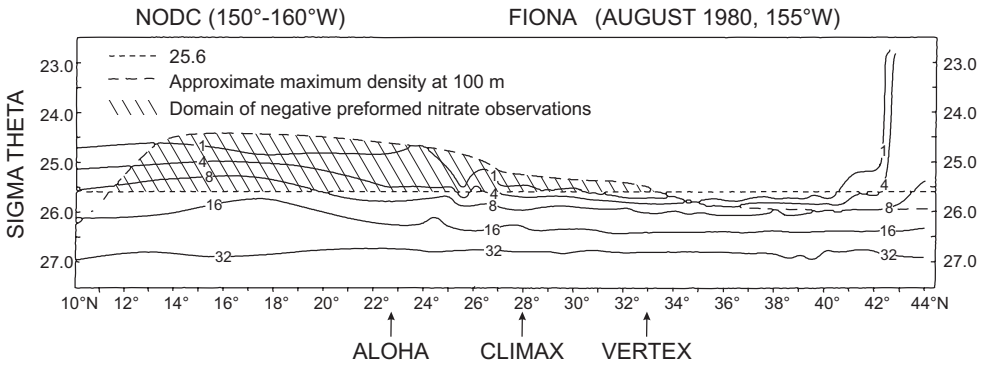

Figure 7.7: A North-South section of nitrate (solid contours) versus density along 155° W in the Eastern North Pacific. The light-dashed line is the density of the top of the positive preformed nitrate horizon ($\sigma_\theta = 25.6$). The heavy-dashed line is the maximum density observed at 100 m, the approximate depth of the 1 % light level. The domain of the negative preformed nitrate observations is the hatched region between the two lines (reproduced after Emerson and Hayward, 1995).

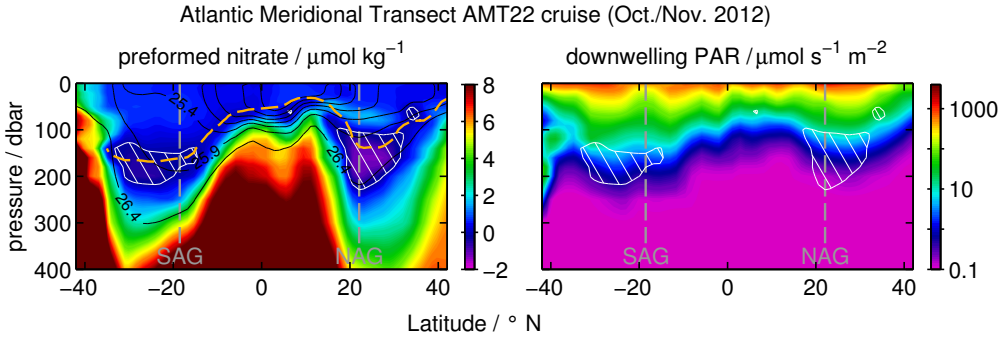

Figure 7.8: A North-South section of preformed nitrate with contours (black) of potential density (left) and of PAR (right) along the Atlantic Meridional Transect (AMT22 cruise). The white hatched region gives the domain of negative preformed nitrate observations and the nitracline is shown as orange dashed line.

autumn while the SAG was in austral spring. The negative preformed nitrate domain therefore appears to have a considerable larger extent in the NAG than in the SAG (compare the temporal evolution at BATS, figure 7.6).

The upper boundary of the negative preformed nitrate domain is determined by the light level through photosynthesis (see, e.g., figure 7.8 right) and found around 25 $\mu mol\, s^{-1}\, m^{-2}$ in our observations. Since nitrate is depleted in surface waters, it coincides with the node of *AOU*, i.e., the transition between net production and net respiration.

The lower boundary is below the nitracline, i.e., there is a domain in between where measureable nitrate is present but it is in deficit compared to the remineralization's O_2 deficit. At the lower node, nitrate and the oxygen deficit are in stoichiometric balance, i.e., $c^\circ_{NO_3^-} = 0$, while there is excess nitrate in the layers below due to advective supply of non-remineralized surface nutrients. The lower boundary is therefore set by the thermocline ventilation. For the North Pacific subtropical gyre, Emerson and Hayward (1995) come to a similar conclusion and determine the $\sigma_\theta = 25.6$ density level as lower boundary. Based on the data in figure 7.6 and 7.8, the lower boundary would follow $\sigma_\theta = 26.3$ at BATS and $\sigma_\theta = 26.4$ in the NAG. In fact, this density layer corresponds to subtropical mode water (STMW) with a characterisic signature of 18 °C and 36.5 psu (Worthington, 1976) subducted from the base of the mixed layer in late winter in the Northern part of the gyre (Qiu and Huang, 1995) and then following the gyre's ventilation pathways (Sarmiento et al., 1982) which is illustrated in figure 7.9.

Figure 7.9a reproduces a schematic cross section of the subtropical North Pacific (Emerson and Hayward, 1995; compare figure 7.7) and shows its isopycnal and diapycnal ventilation paths, which are comparable to the NAG situation. Figure 7.9b gives the density at the base of the winter mixed layer (reproduced from Qiu and Huang, 1995) and 7.9c one-year long particle trajectories along the $\sigma_\theta = 26.5$ isopycnal (Sarmiento et al., 1982, reproduced from Sarmiento and Gruber, 2006), while 7.9d gives the nitrate at the base of the February mixed layer using the de Boyer Montégut et al. (2004) mixed layer climatology and the World Ocean Atlas 2013 (Garcia et al., 2013). The edge of surface nitrate between 30° N and 35° N (figure 7.9d) corresponds to the winter outcrops $\sigma_\theta = 26.3$ in the West near the boundary of the North Atlantic current and the Sargasso Sea and to $\sigma_\theta = 26.4$ in the East near the Canary islands (figure 7.9b). After shoaling of the mixed layer in spring, this surface nitrate is subducted and ventilated into the gyre's interior (figure 7.9c) This supply pathway is also visible in the AMT22 observations (figure 7.8, left): The lower boundary closely follows the $\sigma_\theta = 26.4$ isopycnal with a shape as expected from the Luyten et al. (1983) theory of the ventilated thermocline.

The SAG floats observe the lower boundary at $\sigma_\theta = 26.0$ which corresponds to the lightest portion of South Atlantic subtropical mode water (SASTMW, Provost et al., 1999; Sato and Polito, 2014). This water originates in the Brazil current recirculation while the heavier portions of SASTMW are mainly formed in the Brazil-Malvinas confluence region (Provost et al., 1999; Karstensen and Quadfasel, 2002). Another fraction of light subtropical mode water, however, may also come from the Indian Ocean through the Agulhas retroflection as Agulhas ring water advected by

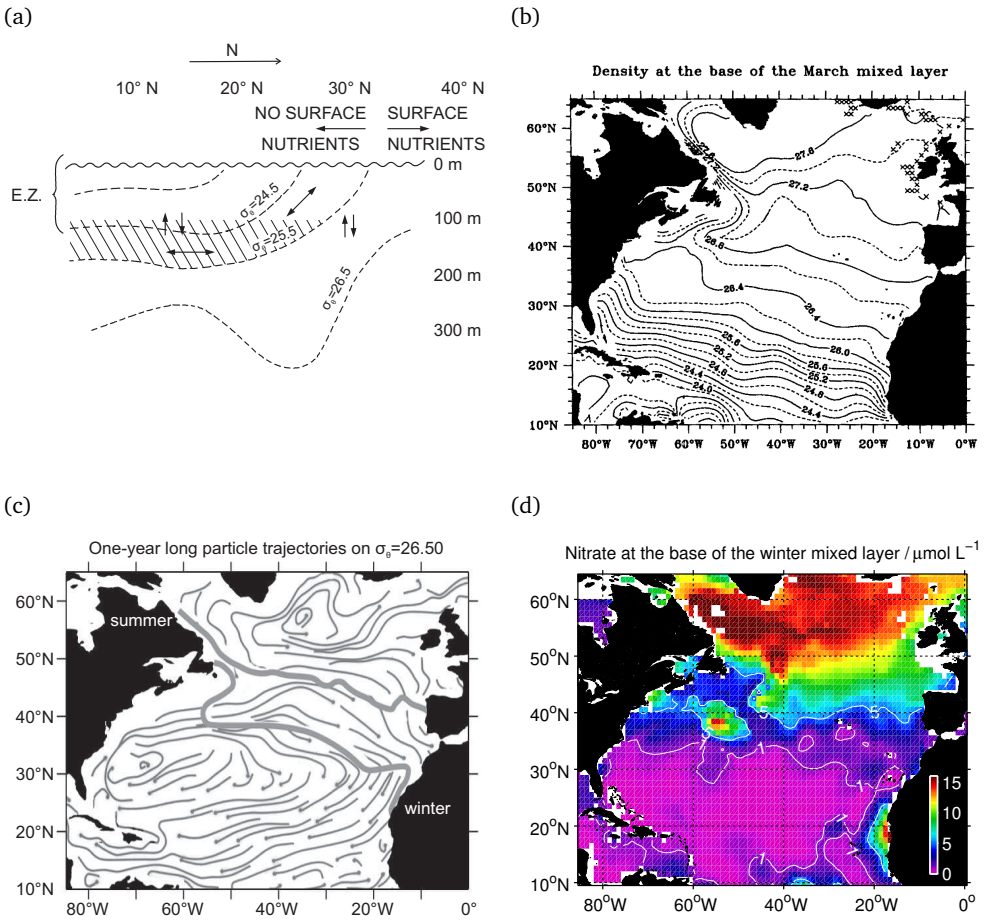

Figure 7.9: Correspondence between the negative preformed nitrate domain and the ventilation of the subtropical gyres: (a) Schematic from Emerson and Hayward (1995) showing the isopycnal and diapycnal ventilation pathways of the North Pacific subtropical gyre. (b) Density level at the base of the late winter mixed layer (Qiu and Huang, 1995). (c) One-year long modeled particle trajectories on the $\sigma_\theta = 26.5$ isopycnal surface (Sarmiento et al., 1982). The dot marks the end of the trajectory and the grey lines the summer and winter time surface outcrops. (d) Nitrate concentration (World ocean atlas 2013, Garcia et al., 2013) at the base of the mixed layer (de Boyer Montégut et al., 2004) in February.

the Benguela current (Provost et al., 1999), which is likely the case for our SAG float location at 20° S. The heterogeneity in SASTMWs is a plausible cause for the wider range of density levels of the negative preformed nitrate domain's lower boundary in the AMT22 section compared to the near-isopycnal behaviour in the NAG (figure 7.8, left).

Productive vs. Respiratory Depth Horizons

The vertical extent of productive and respiratory layers can be analyzed using the preformed nitrate distribution. For the seasonal production (spring – autumn) at BATS, Johnson and Riser (2014) propose a three layer model based on data obtained from floats at/near BATS (compare figure 7.6). They identify three layers as follows:

I. A net productive layer between the surface and 60 m, i.e., most part of the mixed layer, where oxygen is produced without concurrent consumption of nitrate (since it is fully depleted).

II. An intermediate remineralization layer between 60 m and 170 m where oxygen is consumed but nitrate is below the expected stoichiometric ratio and does not increase with the season's progression.

III. A Redfieldian remineralization layer below 170 m where oxygen is consumed and nitrate increases concurrently, closely following the expected stoichiometric ratio (equation 5.4).

We can extend that model and generalize the layer boundaries using our NAG and SAG data.

Layer I extends from the surface down to the node of *AOU*, i.e., the depth where in-situ production and respiration are balanced. This depth is determined by the light availability and found at ca. 25 $\mu mol\, s^{-1}\, m^{-2}$ PAR in our observations. Layer I is characterized by net production and thus a seasonal excess of O_2, depleted nitrate, and as consequence a positive $c^\circ_{NO_3^-}$ signature.

Layer II is net heterotrophic and can be separated into two domains: The upper one, layer IIa, extends from the node of *AOU* to the nitracline. While undersaturated O_2 levels (positive *AOU*) indicate respiration, nitrate is still depleted and the nitrate deficit causes a negative $c^\circ_{NO_3^-}$. The lower one, layer IIb, extends from the nitracline down to the ventilation boundary of the gyre's permanent thermocline. Here, measureable nitrate is present from remineralization. However, it is below the stoichiometric amount expected from the oxygen deficit-respiration signature and $c^\circ_{NO_3^-}$ is thus still negative.

In layer III below, the amount of nitrate exceeds the amount expected from remineralization through the additional advective supply of subducted and ventilated surface nutrients via subtropical mode waters. Oxygen and nitrate appear to be in stoichiometric balance (Johnson and Riser, 2014) and $c^\circ_{NO_3^-}$ and $c_{NO_3^-}$ increase concurrently with depth. Figure 7.10 gives the biogeochemical depth horizons for our NAG and SAG float regions according to this definition.

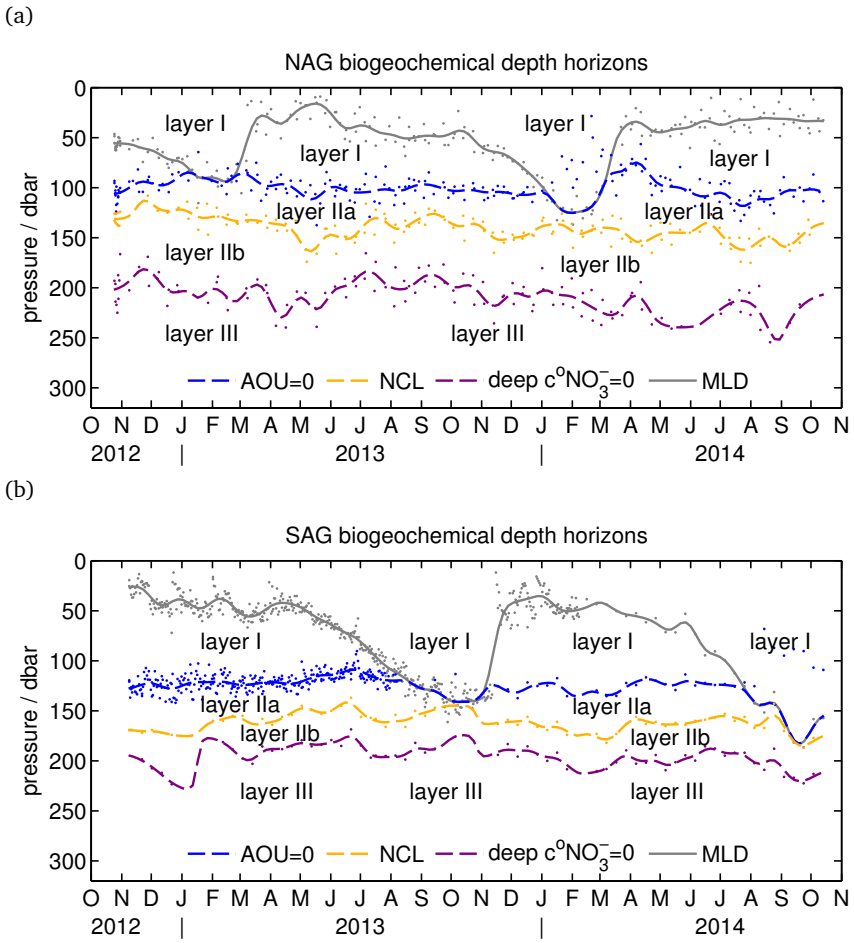

Figure 7.10: Biogeochemical depth horizons obtained from all floats (a) in the North and (b) South Atlantic subtropical gyre region. The layers are separated by the dashed lines of $AOU = 0$ (blue), the nitracline (orange), and the deep node of preformed nitrate (purple), respectively. Layer I is net productive with $AOU < 0$, $c_{NO_3^-} = 0$, and $c^\circ{}_{NO_3^-} > 0$. Layer IIa is net respiratory with $AOU > 0$, $c_{NO_3^-} = 0$, and $c^\circ{}_{NO_3^-} < 0$. layer IIb is net respiratory with $AOU > 0$, $AOU/r > c_{NO_3^-} > 0$ (r being the stoichiometric ratio, equation 7.3), and $c^\circ{}_{NO_3^-} < 0$. Layer III is net respiratory and stoichiometrically balanced with $AOU > 0$, $c_{NO_3^-} > AOU/r$, and $c^\circ{}_{NO_3^-} > 0$.

While the negative preformed nitrate domain (layer II) is a seasonal phenomenon at BATS, we observe its presence year-round in the NAG and SAG. The difference in the temporal extent is related to the depth of the winter mixed layer and the nitracline depth.

In our setting in the NAG and SAG, winter mixing never reaches the nitracline at ca. 140 m/$\sigma_\theta = 26.0$ and 160 m/$\sigma_\theta = 25.7$, respectively, and no nitrate is supplied to the surface through convection. Only the excess O_2 in layer I (SOM/shallow maximum of $c^\circ_{NO_3^-}$) is eroded each winter (and some of the excess O_2 deficit in layer IIa if mixing goes deeper than the node of AOU), but the NO_3^- deficit/negative $c^\circ_{NO_3^-}$ in layer IIb below persists in a quasi "steady-state" (figure 7.4 and 7.10).

At BATS, winter mixing reaches below the nitracline well into the negative $c^\circ_{NO_3^-}$ domain, thus homogenizing the imbalance (figure 7.6). Without such a seasonal "reset", the evolution of O_2 or NO_3^- is governed by the near-balance of biological processes (e.g., remineralization) and ocean physics (diffusion & mesoscale activity) and no seasonal signature arises.

In fact, Johnson and Riser (2014) take advantage of exceptionally cold and stormy winters at BATS and thus deep winter mixing down to 200 m in 2010 and 2011. Thus, formerly "steady-state" O_2 and NO_3^- concentrations are perturbed throughout the water column down to layer III and they can follow the seasonal pattern in these parameters, i.e., O_2 production and NO_3^- consumption in layer I, an O_2 decline due to respiration in layer II, and a near-stoichiometric O_2 consumption and NO_3^- production due to remineralization in layer III. Below the winter mixing depth, waters in Layer III are unperturbed and follow the near-balanced, "steady-state" regime, i.e., no seasonal signature is discernible.

In the net heterotrophic respiration layer II, NO_3^- would be expected to increase with the season. Instead, all nitrate mixed into layer IIa gets depleted and NO_3^- in layer IIb approaches pre-convection levels, i.e., in deficit to the O_2 respiration signature.

There is an ongoing speculation on how nitrate is supported to layer I and what maintains the imbalance between layer I and II.

Johnson and Riser (2014) argue that the nitrate expected to appear in layer II (due to remineralization) is immediately taken up and somehow transported to the surface layer I. While yet unproven, active biological transport via vertically migrating organisms is the most likely candidate. Diatom mats in the North Pacific subtropical gyre have been shown to transport nitrate from depth to the surface thus potentially contributing to the negative preformed nitrate domain's formation (Villareal et al., 1999). This vertical migration with feeding at depth/excretion in the surface may also be accessible to other organisms through "hitchhiking" on migrating zooplankton (Grossart et al., 2010).

Emerson and Hayward (1995) suggest nitrogen-poor DOM from the oligotropic surface to cause the negative $c^\circ_{NO_3^-}$ domain in layer II: With a high C/N-ratio, the $c^\circ_{NO_3^-}$ stoichiometric assumption (equation 7.3) would be violated and the O_2 respiratory requirement exceed the amount of nitrate. However, this cannot explain the nitrate supply to layer I that causes the O_2 excess. At the same time, N_2 fixation (Singh et al., 2013) may be an additional input of nitrogen to the surface (layer I),

however, without the capability to support the bulk of the O_2 production/DIC drawdown (Johnson and Riser, 2014).

Episodic mesoscale eddies are thought to play an important role for the vertical entrainment of nitrate through uplifting of isopycnals, a process badly resolved on timescales of non-autonomous observations (Johnson et al., 2010). However, the total effect of such an "eddy-pumping" mechanism may have been overestimated previously (Oschlies, 2002). As an alternative to diapycnal and isopycnal mixing, both too small to support the surface nitrate reguirement, Jenkins and Doney (2003) suggest the "subtropical nutrient spiral" as three-dimensional pathway to return remineralized nutrients from the permanent thermocline to the productive surface layers via strong mixing in the Western boundary current. However, the authors also recognize that stoichiometric ratios would be unaffected by such a physical process while observations show substantial deviations from Redfield stoichiometry.

In fact, solely physical nitrate supply pathways can be dismissed due to the absence of a concurrent O_2 deficit transport. For such a preferential displacement of nitrate over other ocean tracers biology is the most likely cause.

8 Productivity Estimates for the Atlantic Subtropical Gyres

Abstract

The aim of this work is to yield quantitative estimates of biological productivity from 2 years of float data in the North and South Atlantic subtropical gyres (NAG and SAG, respectively). To overcome temporal and spatial limitations of a mixed layer mass balance or sub-mixed layer O_2 accumulation approach, we developed a simple model that reproduces physical effects on O_2. Use of this model in combination with a 1D turbulence model (GOTM) provides a realistic, abiotic background distribution of O_2. Comparison of float observations with this abiotic background gives the biological contribution which was used to derive net community production (NCP). Oxygen Optodes on the floats drifted significantly and a conservative in-situ correction (-0.3 to -5.5 μmol kg^{-1} yr^{-1}) was applied. Due to this correction, our estimates probably represent a lower bound to NCP. We obtain a O_2-based NCP of 1.2 ± 1.1 mol C m^{-2} yr^{-1} for the NAG and 1.6 ± 0.8 mol C m^{-2} yr^{-1} for the SAG. Between 20 – 35 % of this is lost to the atmosphere through gas exchange. Turbulent vertical nitrate fluxes alone are insufficient to sustain this production. Accordingly, preformed nitrate-based rates show a stoichiometric imbalance in the upper ca. 150 m but are not significantly different from zero below, indicating stoichiometrically-balanced waters at depth.

Acknowledgements

Float planning, operations and decoding is performed by the Oceanographic Autonomous Observations (OAO) group at the Laboratoire d'Ocanographie de Villefranche (LOV) and is a cornerstone of this work. Special thanks go to Hervé Claustre, Antoine Poteau, and Catherine Schmechtig of the OAO-LOV team. The developers' time and effort put into the freely available GOTM and FABM software is gratefully acknowledged. We want to thank the captain, crew and scientists of RSS James Cook cruise AMT22 for the float deployments and reference data. Data of the cruise are provided by the British Oceanographic Data Centre. Financial support by the RemOcean project (EU ERC grant agreement 246777) for the floats and float infrastructure as well as the O2-Floats project (KO 1717/3-1) of the German Science Foundation (DFG) (optodes & H.B.) is gratefully acknowledged.

8.1 Quantitative Approaches for O_2-based NCP Estimates

In the literature, two complementing approaches are common to quantify the seasonal net community production (NCP) based on oxygen measurements: One employs the air sea exchange flux of O_2 to estimate mixed layer production while the other uses the accumulation of O_2 in sub-mixed layer waters. Both are not applicable to the winter season and have a limited depth scope. Here we present a third approach that is applicable to the whole water column and is not limited by the seasons.

Mixed-Layer O_2 Mass Balance

Mixed layer waters are always in contact with the atmosphere, i.e., the air sea O_2 flux is an important term of the mixed layer mass balance. If other boundary fluxes like isopycnal and diapycnal mixing, lateral advection, or entrainment are negligible or can be quantified, a residual air sea O_2 flux must be caused by internal sources or sinks, i.e., production or respiration within the mixed layer (figure 8.1) (Emerson and Hedges, 2008; Hamme and Emerson, 2006).

The steady state assumption is commonly valid in spring and summer months with a shoaling or steady mixed layer depth and strong (thermal) stratification. This approach is extensively used if only surface data, e.g., from underway measurements, are available (see, e.g., chapter 6, Shadwick et al., 2014). Especially with $\Delta O_2/Ar$ surface measurements (e.g., Kaiser et al., 2005), the term "O_2-bioflux" was coined since physical side effects of gas exchange (bubble fluxes) are largely eliminated (Craig and Hayward, 1987). This approach works best where the mixed layer comprises most part of the euphotic zone, i.e., with deep seasonal mixed layer depths.

Seasonal Sub-Mixed Layer O_2 Accumulation

Waters below the mixed layer are decoupled from the atmosphere and thus gas exchange. Therefore, oxygen accumulation in sub-surface waters can easily be at-

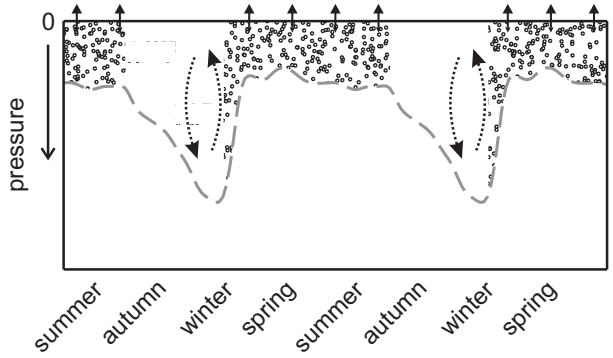

Figure 8.1: The mixed layer mass balance approach is only sensitive to (biological) O_2 changes above the MLD (grey dashed line) if there are no other dominant boundary fluxes except gas exchange (stippled area). Periods with deepening MLD and convective periods (dotted double arrows) have a considerable and usually not well constrained entrainment flux and need to be excluded.

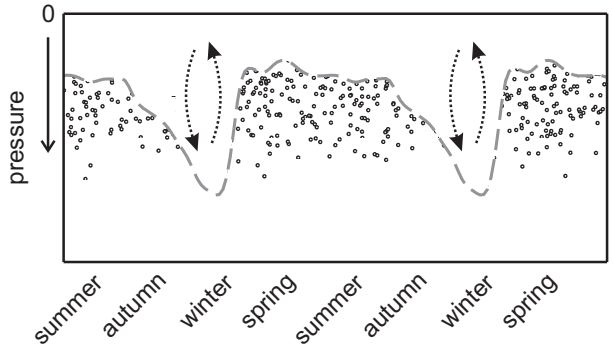

Figure 8.2: The sub-mixed layer approach is only sensitive to (biological) O_2 changes below the MLD (stippled area and grey dashed line). It can not assess productivity within the mixed layer or during winter convection (dotted double arrows).

tributed to net production (Craig and Hayward, 1987) if concurrent physical processes (mixing, advection) are quantifiable or negligible (figure 8.2). Since only sub-mixed layer production can be derived from this approach, it is typically applied in regions with a shallow seasonal mixed layer where a significant portion of the euphotic zone is below the MLD (see, e.g., Riser and Johnson, 2008).

Abiotic Model

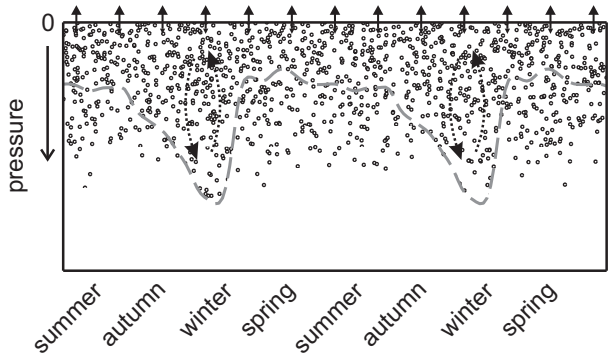

Figure 8.3: Use of a physical model removes temporal and spatial limitations and productivity can be assessed on the full domain (stippled area). Air sea gas exchange remains as important boundary flux.

The previous two approaches lack completeness: Because of their simplifying assumptions, either neglecting interior ocean physics or gas exchange, they are only sensitive to the surface layer or the ocean interior. A complete picture of both surface and sub-surface production is in principle accessible through the use of a model that accounts both for ocean physics within the water column (e.g., diapycnal mixing) and gas exchange (diffusive and bubble fluxes) at the surface (figure 8.3). In this way, the above approaches can be unified if boundary conditions of the simple model are met (e.g., negligible horizontal advection for a 1D model). The biological contribution can thus be derived as difference between observations and the abiotic model. This approach is applied here to data from the NAG and SAG region.

8.2 Methods

Model Structure

The model is separated into a hydrodynamical and a biogeochemical part. Both parts are coupled and the model structure is sketched in figure 8.4 (after Bruggeman and Bolding, 2014). The hydrodynamical part consists of the General Ocean Turbulence Model (GOTM) as physical driver (Burchard et al., 2006; http://gotm.net) whereas the biogeochemical part consists of an abiotic dissolved oxygen and a nitrate model. They are interfaced through the Framework for Aquatic Biogeochemical Models (FABM) as coupler (Bruggeman and Bolding, 2014; http://fabm.net).

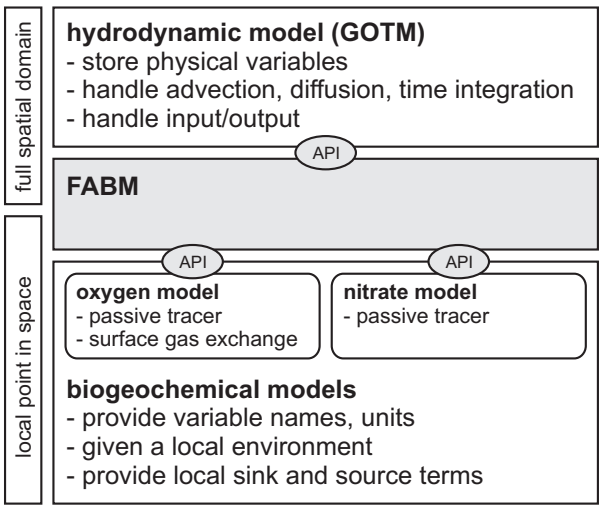

Figure 8.4: Model structure and task division between hydrodynamic and biogeochemical models and FABM (after Bruggeman and Bolding, 2014). FABM provides the application programming interface (API) between the different models.

GOTM is a 1D water column model with turbulent mixing parameterizations (see, e.g., Umlauf and Burchard, 2005). Through FABM, GOTM handles input, storage, and output as well as advection, diffusion, and time integration of all variables and provides the main interface to the entire simulation.

FABM provides a common set of rules and interfaces for the interaction of a generic hydrodynamic model as "physical driver", GOTM in our case, with biogeochemical models that conform to these rules. The biogeochemical models provide local sink and source terms for the biogeochemical variables defined in the model, while they are unaware of the spatial domain they act on, e.g., a 1D water column or a 3D world ocean. FABM provides the interface to supply the local conditions (e.g., temperature, oxygen concentration, etc.) to the biogeochemical models and to transfer the local biogeochemical sink and source terms back to the hydrodynamic model (and thus the spatial context). Therefore, arbitrary combinations of hydrodynamic and biogeochemical models are possible without changing the source code. FABM allows multiple biogeochemical models to be combined and allows coupling between them and common use of variables (e.g., several plankton groups with common nutrients and/or grazing, see Bruggeman and Bolding, 2014).

In our case, two biogeochemical models are used: an abiotic dissolved oxygen and an abiotic nitrate model. Both are meant to solely reproduce physical effects on O_2 and NO_3^-, respectively, and do not provide any biological fluxes. The nitrate component uses a simple passive tracer module that is included in the FABM source code (bb_passive). The oxygen component builds on the passive tracer model for the interior but adds surface O_2 gas exchange following common parameterizations (see below). With the abiotic model providing the physical background, comparison between the model and observations gives the biological signature to the observed O_2 and NO_3^- distributions.

Abiotic O_2 Model

The abiotic O_2 module has been programmed in Fortran following the rules of FABM to interact with a generic physical host. The passive tracer module bb_passive was expanded to include surface gas exchange fluxes, both diffusive and bubble fluxes. The dissolved gas is otherwise treated as passive tracer, i.e., any biological sources or sinks are intentionally neglected. For testing purposes, however, a bulk production rate can be given to the model through an optional input. In its current state, the module is designed for dissolved oxygen only but it may handle other gases by adjusting the respective constants.

The air sea gas exchange flux (F_{as}) is the sum of diffusive gas exchange (F_{dif}), bubble injection (F_{inj}), and bubble exchange (F_{ex}) fluxes,

$$F_{\mathrm{as}} = F_{\mathrm{dif}} + F_{\mathrm{inj}} + F_{\mathrm{ex}}\,, \tag{8.1}$$

where the bubble fluxes can be switched off by an optional module parameter. Diffusive gas exchange follows

$$F_{\mathrm{dif}} = -k_{\mathrm{O_2}} \cdot \left(c_{\mathrm{O_2}} - \alpha_{\mathrm{O_2}} \cdot p\mathrm{O_2}\right)\,, \tag{8.2}$$

$$p\mathrm{O_2} = \chi_{\mathrm{O_2}} \cdot (p_{\mathrm{atm}} - p\mathrm{H_2O}) \tag{8.3}$$

with $k_{\mathrm{O_2}}$ being the gas transfer velocity, $\alpha_{\mathrm{O_2}}$ the solubility, and $p\mathrm{O_2}$ the partial pressure of oxygen calculated from the mole fraction in dry air ($\chi_{\mathrm{O_2}}$) and the dry atmospheric pressure (equation 8.3). The bubble fluxes follow

$$F_{\mathrm{inj}} = A_{\mathrm{inj}} \cdot p\mathrm{O_2} \cdot (u_{10} - 2.27\ \mathrm{m\ s^{-1}})^3 \tag{8.4}$$

$$F_{\mathrm{ex}} = A_{\mathrm{ex}} \cdot p\mathrm{O_2} \cdot \left(\frac{D_{\mathrm{O_2}}}{1\ \mathrm{m^2\ s^{-1}}}\right)^{0.5} \cdot \frac{\alpha_{\mathrm{O_2}}}{1\ \mathrm{mol\ m^{-3}\ atm^{-1}}} \cdot \left(u_{10} - 2.27\ \mathrm{m\ s^{-1}}\right)^3 \tag{8.5}$$

where u_{10} is the wind speed, $D_{\mathrm{O_2}}$ the diffusion coefficient, and A_{inj} and A_{ex} are the injection and exchange rates from Nicholson et al. (2011). The bubble fluxes F_{inj} and F_{ex} scale with the whitecap coverage, i.e., they are 0 for $u_{10} < 2.27\ \mathrm{m\ s^{-1}}$.

Different transfer velocity – wind speed parameterizations (Liss and Merlivat, 1986; Wanninkhof, 1992; Nightingale et al., 2000; Ho et al., 2006; Sweeney et al., 2007) can be chosen by the user. We used the equations of Nightingale et al. (2000) for our simulations. The oxygen solubility from Garcia and Gordon (1992) given at 1 atm was scaled to atmospheric pressure according to

$$\alpha_{\mathrm{O_2}} = \alpha_{\mathrm{O_2}}^{1\,\mathrm{atm}} \cdot \frac{p_{\mathrm{atm}} - p\mathrm{H_2O}}{1\,\mathrm{atm} - p\mathrm{H_2O}}\,. \tag{8.6}$$

The diffusivity was derived by dividing the kinematic viscosity of water ν (Pilson, 1998) with the Schmidt number Sc for oxygen from Wanninkhof (1992).

Atmospheric pressure, air temperature and humidity are obtained from the physical host as part of the FABM standard variables.

Simulation Setup

The simulations used GOTM version 4.1.0 and the FABM API version 0.93 obtained on 19 August 2014. Standard parameterizations were used for the hydrodynamic model: It applies a second order turbulence closure model (Canuto et al., 2001) together with a dynamic k-ϵ style equation for the turbulent kinetic energy (TKE, k) and a dynamic dissipation rate equation as model for the dissipative length scale l (see the GOTM documentation for full details: Umlauf et al., 2014). In addition, the option to have TKE injection at the surface (breaking waves) was enabled. Simulations were done for the full 1000 m profile depth with a timestep of 5 minutes, a total of 200 layers, and a surface zooming factor of 2. Thus, the layer thickness gradually increases from 0.7 m at the surface to 10.4 m at depth.

Each run was initialized with observations (i.e., profiles of temperature, salinity, O_2, and NO_3^-) and was run freely, i.e., without data assimilation or nudging. The only exception was the upper 1 m of salinity which was relaxed towards observations with a 0.5 h relaxation time constant. This was done to match the surface layer freshwater budget (see below).

Meteorological data for wind speed, air temperature, pressure, humidity, cloud cover, short wave radiation, and precipitation were fed to GOTM to derive surface fluxes of momentum and energy. They were obtained by interpolating MERRA data (Rienecker et al., 2011) at 1 h time and 1/2° x 2/3° spatial resolution to the float track. This was found to yield more realistic results than using coarser NCEP data (6 h and 2.5° x 2.5° resolution) (Kalnay et al., 1996). MERRA data were accessed from the Goddard Earth Sciences Data and Information Services Center (GES DISC). They are distributed monthly with a time lag of 5-8 weeks. Therefore, our simulation period ends on 1 Sept. 2014.

A GOTM simulation for the entire deployment period of lovbio009 is shown in figure 8.5: It illustrates the generally remarkable match between model and float observations, but also shows its limitations, e.g., the simple model can not mimic internal waves (see figure 8.5, below 150 m). While the temperature pattern is nearly identical, the surface salinity shows some discrepancy. Episodic surface freshening events in the float data are generally not mirrored in the precipitation data, i.e., they can by necessity not be reproduced in the model (not shown). For this reason, the surface salinity relaxation in the upper 1 m was included in the model setup. With this adjustment, mixed layer salinity lags somewhat behind the observations (since it only reacts to observed salinity changes), but generally follows the trend of surface freshening or saltening (see figure 8.5, middle). Using this setup, the performance of the free-running model is very good, considering its 1D nature. The most challenging part is the late autumn/early winter period with mixed layer deepening, entrainment of subsurface waters, and deep convection. During this period, the model is especially sensitive to the entrained water properties and thus the depth profiles used for initialization. If these properties are biased, e.g., by mesoscale activity, the model may easily deviate from the observations. However, even the mixed layer depth is quite well reproduced during this nearly 2 years of free-running 1D simulation (see figure 8.5).

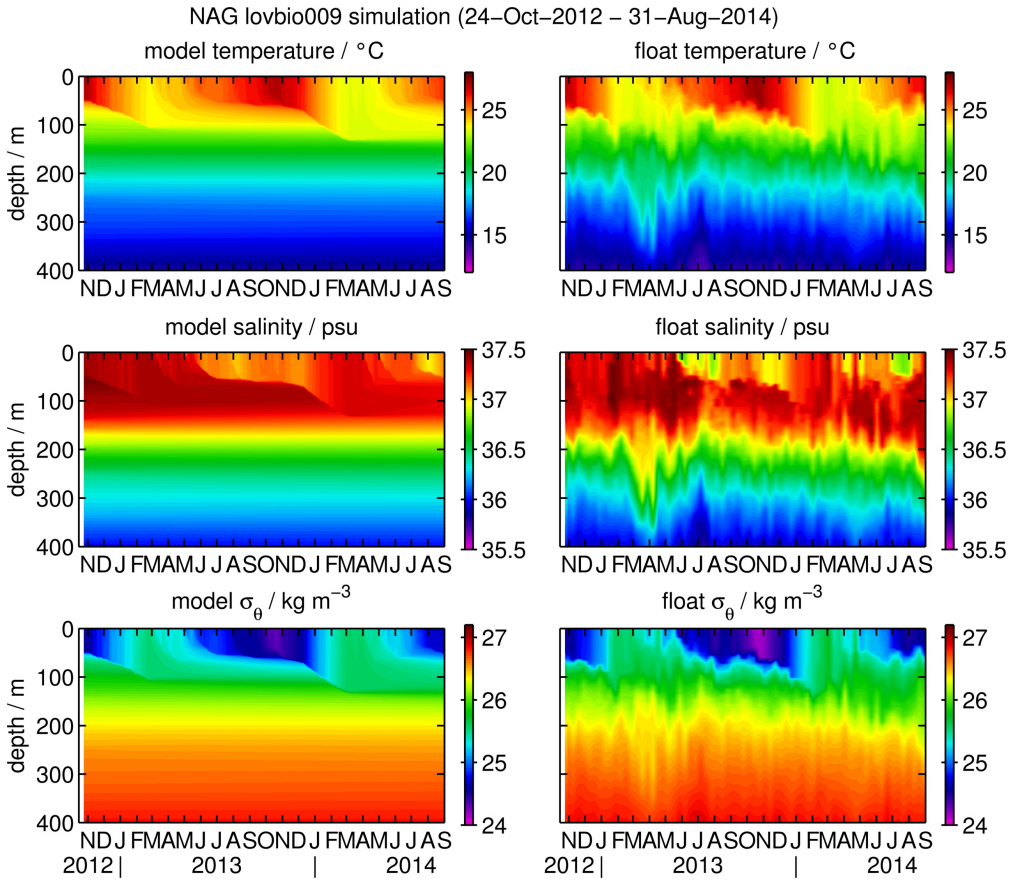

Figure 8.5: GOTM simulation run of lovbio009 in the NAG. The simulation was initialized with observed profiles and free-running for nearly 2 years except for a surface layer salinity relaxation in the upper 1 m. Panels show the temperature (top), salinity (middle), and potential density (bottom) in the upper 400 m for the model run (left) and the float observations (right).

To exclude any significant excursions of the model hydrodynamics from observations and the bias by the resulting modeling artifacts, our simulations were limited to subsets of 6 weeks duration (see below).

Gas Exchange Flux from Observations

The air sea gas exchange flux is an important component of the oxygen mass balance. While it is directly available for the abiotic case from the simulation itself, it needs to be derived for the real-world case from observations. By using a specialty of GOTM/ FABM, we can use the same model machinery in both cases. By relaxing all variables toward observations with a time constant equal to the simulation's time step, data of the simulation equal the observations for the entire run since any hydrodynamic changes or oxygen fluxes are simply "overwritten" by observations in the next time step. Thus, air sea gas exchange always uses the observed surface disequilibrium and fluxes are calculated with the same method and forcing as in the abiotic case. In fact, a difference between observed and abiotic case exists only in the diffusive component since the bubble fluxes are treated identically.

Observation – Model Comparison

The analysis depends on a proper match of abiotic model output and observations. The most important difference is the lack of internal waves in the model (see figure 8.5) since the 1D model is a simplified representation of the real world. To account for internal wave-driven vertical displacements present in the observations but not in the model, we use the mixed axis match described in chapter 3. It is a combination of an isopycnal match below the mixed layer depth (to catch isopycnal vertical displacements) and an isobaric match above the mixed layer depth (to catch diel density variations of the surface layer). An example of this mixed axis match is given in figure 8.6 for a simulation run of the entire lovbio009 deployment: The modeled abiotic O_2 distribution is intrinsically smooth below the mixed layer (upper panel), while the observations show regular fluctuations (lower panel), which are reproduced to a high degree using the mixed axis match (middle panel). The different intensity, e.g., of the SOM (middle vs. lower panel) is due to in-situ production.

NCP Quantification

The analysis approach is depicted conceptually in figure 8.7 with a simulated test case. The observational record (8.7a) is split into subsets which are simulated independently. The depiction shows subsets of 4 months duration with a separation of 3 months. Model simulation of each subset follows two parallel tracks, a completely nudged observation run (8.7b) and an abiotic model run (8.7c). The nudged run is used to estimate the gas exchange O_2 flux from observations (8.7b, upper panel) using the model parameterizations and meteorological forcing (see above). In contrast, the abiotic run is used to fully reproduce physical mixing and gas exchange without a biological contribution. It yields an abiotic air sea O_2 flux and an abiotic

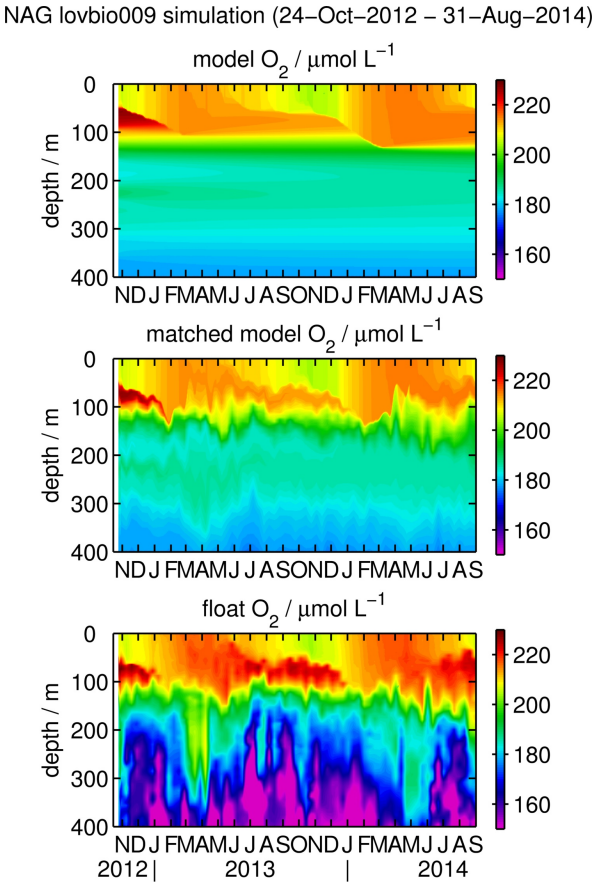

Figure 8.6: Result of the mixed axis match for the full simulation of float lovbio009 in the NAG. The abiotic model was initialized with observed profiles but has no biological component, i.e., it shows only the thermally-caused SOM in 2013 and 2014. The 1D model shows no sub-surface vertical oscillations due to simplified ocean physics and the lack of internal wave activity (top). The observations show both internal waves and a biological accumulation of O_2 in the SOM (bottom). To account for internal waves, both were matched on a mixed density/pressure axis and the displaced model result is shown in the middle panel.

water column O_2 distribution, i.e., the physical background (8.7c). The abiotic water column O_2 is matched on the mixed axis with the observations (8.7d) to account for vertical displacements due to internal waves (see figure 8.6).

The biological air sea O_2 flux (8.7e, upper panel) is obtained as the difference between abiotic and observed air sea O_2 flux (8.7c and 8.7b, upper panel), while the biological signature of O_2 in the water column (8.7e, lower panel) arises from the difference in matched abiotic and observed water column O_2 concentrations (8.7d and 8.7b, lower panel). To get a combined biological signature, the biological air sea O_2 flux is translated to a mixed layer O_2 change by distributing the surface flux evenly over the mixed layer depth (8.7f). For each subset, this combined biological O_2 is then converted to a water column O_2 production rate with a single time stamp at the middle of the simulation period (8.7g).

The depiction so far used 4 month subsets with a separation of 3 months for clarity. The actual subsets used for float data are of 6 weeks duration and separated by the float cycle interval (1 d for lovbio005 and 10 d for the other floats), i.e., the overlap between subsets is significantly higher and the simulation period is much shorter. The spacing of the O_2 production rate profiles is therefore as dense as the float cycle interval (8.7h) and can be interpolated to give a pseudo-continuous timeseries of production rates (8.7i). Integration over the net productive layer I, i.e., down to the depth of $AOU = 0$ based on observations (black line in 8.7i), yields the integrated net community production (8.7j). The integrated NCP (continuous line) includes both the water column O_2 accumulation and the biological air sea O_2 flux (dashed line).

The approach for nitrate is analogous except for the missing gas exchange term. Both O_2 and nitrate were converted to carbon units using a fixed stoichiometry of O_2:C $= -1.4$:1 and of N:C = 16:106 (Anderson, 1995).

Simulation and Analysis Sensitivity

There are a few sensitive parameters both for the simulation and the analysis. The most important one for the simulation is the absolute level of surface O_2, i.e., its accuracy. A low/high bias in the observations leads to a too weak/too strong diffusive outgassing flux, and mixed layer production is consistently under/overestimated. Moreover, the water column comparison is affected, too: A low/high bias in the initial profile (from observations) is quickly re-equilibrated within the abiotic model, leading to an increase/decrease in water column O_2 solely due to physical gas exchange. When comparing the model with observations, the increase/decrease is only present in the model while the observations read consistently low/high. This apparent excess/deficit causes, again, an under/overestimation of the biological contribution, thus exaggerating the surface flux error.

The simulated test case depicted in figure 8.7 used a prescribed production profile with a productive zone in the upper 120 m (integrated NCP of 1.9 mol C m^{-2} yr^{-1}; red dotted line in figure 8.7j) and a slightly net heterotrophic zone below. The analysis has a recovery of 97 % for this set of simulations, i.e., the approach is capable of extracting the biological effects on oxygen. With the same test case,

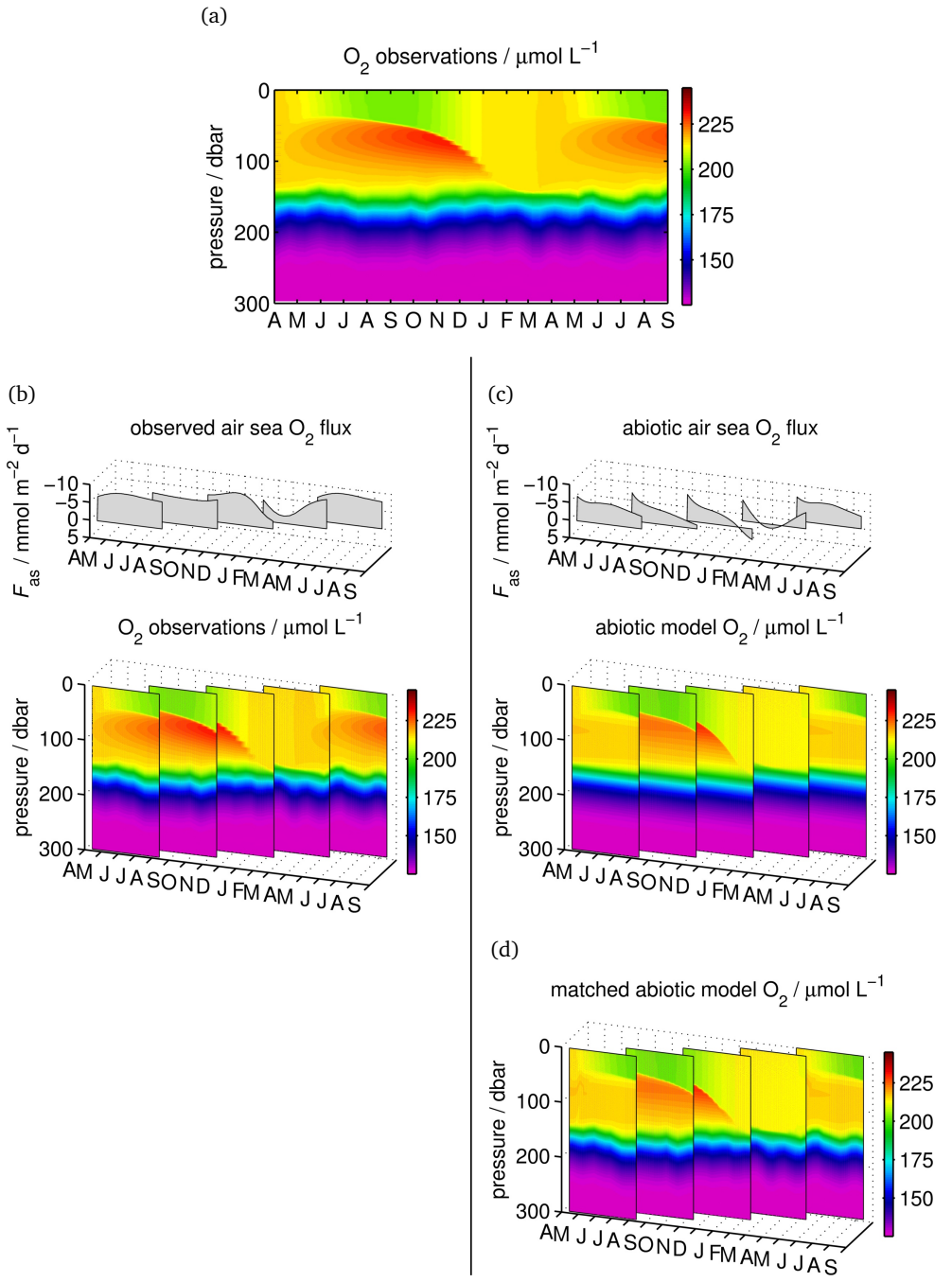

Figure 8.7: Schematic depiction of the NCP analysis (part 1) using a simulated test case. The observations (a) are split into subsets (4 months with 1 month overlap in the schematic) and model simulation of each subset follows two tracks: A completely nudged observation model run (b) to obtain the observed air sea O_2 flux (upper panel), and an abiotic model run (c) to get the abiotic air sea O_2 flux and abiotic water column O_2 distribution as physical background. To account for internal wave-driven vertical displacements inherent in the observations, the abiotic model O_2 is matched on a mixed axis with the observations (d).

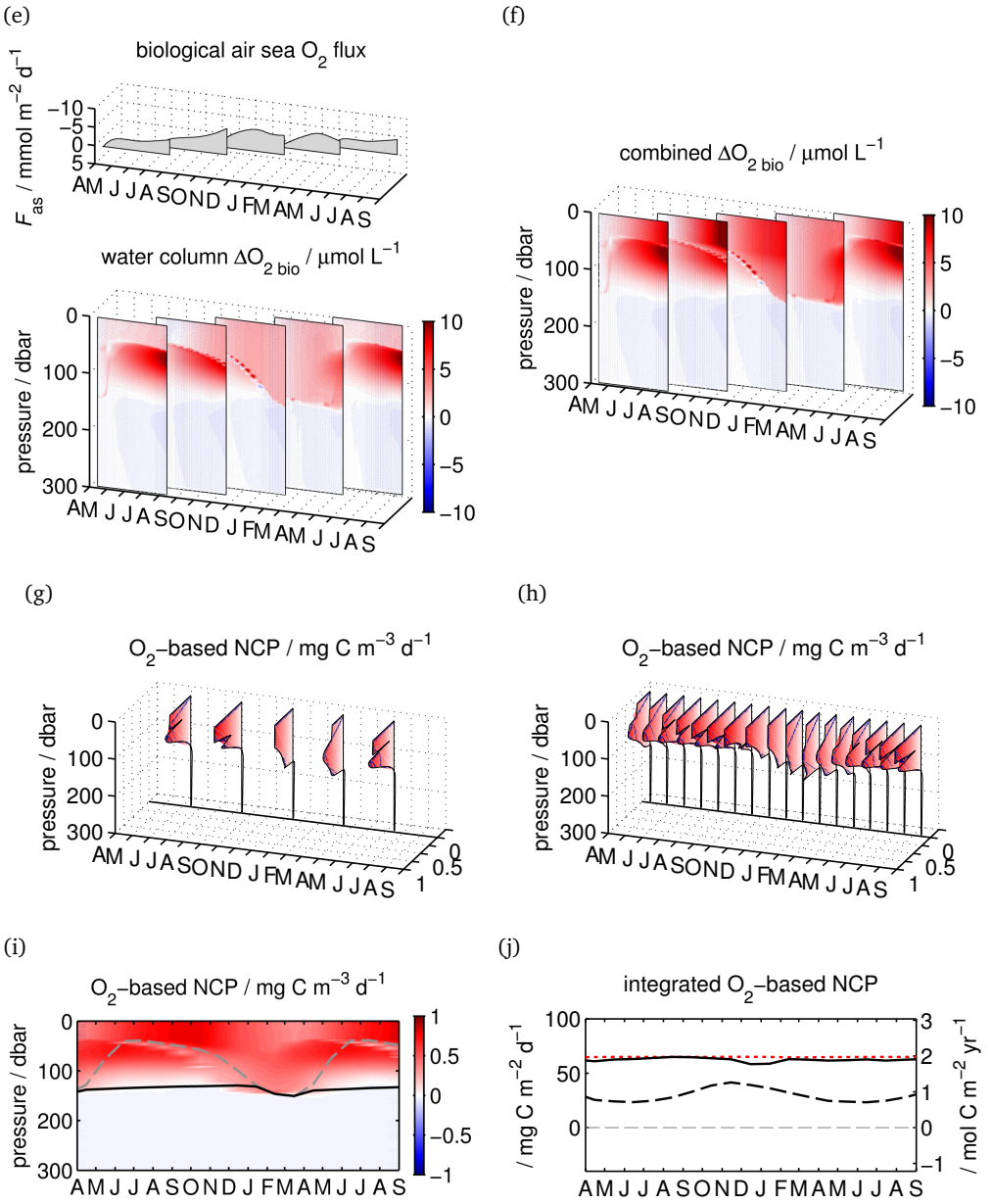

Figure 8.7: Schematic depiction of the NCP analysis (part 2): The biological air sea O_2 flux and water column O_2 change (e) is obtained as difference between observations (b) and abiotic model (c, upper panel, and d). Both biological parts are combined by translating the air sea O_2 flux to a mixed layer O_2 accumulation added to the water column ΔO_2 (f). For each subset, the combined biological ΔO_2 yields a O_2 production rate profile (g). For float simulations, the separation of subsets equals the float cycle time, i.e., the O_2 production profiles are spaced densely (h) so that a quasi-continuous time series of the O_2 production rate is obtained (i). The black line gives the integration depth ($AOU = 0$) (MLD as grey dashed line) and integration yields NCP (j, black line). The dashed line gives the biological air sea O_2 flux.

a ±1 μmol kg^{-1} uncertainty translates to a 0.7 mol C m^{-2} yr^{-1} (35 %) error in integrated NCP. Since this effect depends on the actual O_2 surface saturation, all float simulations are repeated with a ±1 μmol kg^{-1} offset to quantify the uncertainty caused by the confidence level of the O_2 accuracy.

In addition, the analysis is sensitive to the integration depth and to the way in which model and observations are matched. Based on the experience with previous (see, e.g., chapter 3) and current work (e.g., figure 8.6), we have high confidence in the mixed axis match. The node of *AOU* is the boundary between net O_2 production and net O_2 consumption (see chapter 7) and thus the proper depth of integration. It has an uncertainty of ca. 10 m when comparing individual profiles with the seasonal pattern (see figure 7.5). The impact of this uncertainty depends on the depth gradient of the analyzed production rate. If the production is constant with depth, the uncertainty of the integration depth is a simple depth scaling (±10 m). If there are significant gradients, a shallower or deeper integration depth can significantly affect the integrated rate. To get a realistic estimate of the introduced uncertainty, we repeated the integration for the depth of $AOU = 0$ ±10 m and added the mean bias to the ±1 μmol kg^{-1} offset uncertainty from above.

8.3 Optode Stability: A Note on in-situ Corrections

We observe two strong indications for an in-situ drift of the optodes, which has rarely been described before for sub-surface, ocean-deployed optodes (Körtzinger et al., 2005; Tengberg et al., 2006; Tengberg and Hovdenes, 2014).

First, summer surface and mixed layer O_2 levels become undersaturated for most floats after ca. 1.5 years while there is a clear build-up of a shallow oxygen maximum (SOM) just below (see figure 8.8 (right) for lovbio006 and appendix figure A.8.1 for the other floats). This undersaturation would lead to diffusive ingassing in the presence of spring and summer surface warming and a positive diffusive supply from sub-mixed layer waters while both thermal forcing and mixing would suggest supersaturation and a diffusive outgassing flux. This contradiction could only be consolidated by net heterotrophy in the surface mixed layer, while there is clearly production dominating over respiration, i.e., autotrophy, directly below. This does not seem to be a reasonable explanation (e.g., Riser and Johnson, 2008).

Second, isopycnal O_2 concentration at depth (950 – 1000 m) decrease significantly and uniformly for each float (figure 8.8 (left) for lovbio006 and appendix figure A.8.1 for the other floats). While the maximum profile depth of 1000 m is not guaranteed to have a stable O_2 level on a timescale of a year, the changes seen are very unlikely to represent environmental conditions and are thus indicative of a typical optode drift pattern.

While there is clear evidence for an optode drift, the options for in-situ correction are plentiful and badly constrained at the same time. As mentioned above, accuracy is key to get a proper and unbiased productivity estimate, so the correction method needs to be chosen carefully.

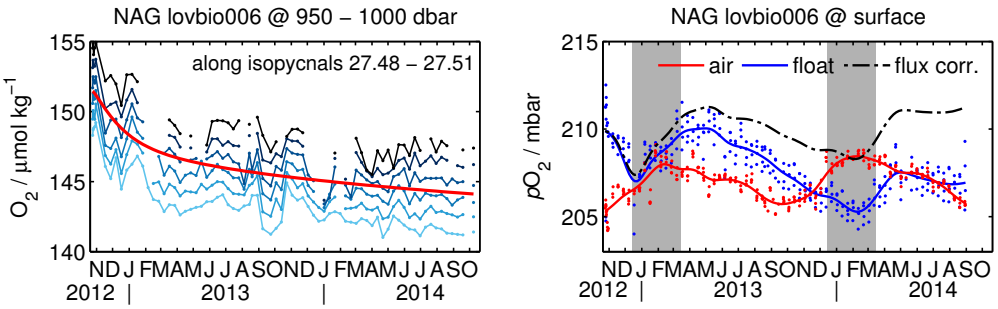

Figure 8.8: Indicators of an in-situ optode drift for float lovbio006 in the NAG: Deep optode readings drift towards lower values (left) and surface waters become apparently undersaturated (right), both of which are unrealistic and optode artifacts. Isopycnals are color coded (light to dark/deep) and a best fit (equation 8.7) is shown in red (left). Uncorrected optode data in the surface 1 m are shown in blue, atmospheric equilibrium pO_2 based on MERRA data are shown in red, and grey shading marks the winter period where the SOM is eroded and undersaturated waters may have been entrained. The black dash-dot line gives the drift-corrected surface pO_2 using a seasonal boundary on the biological air sea O_2 flux (see text).

It may seem obvious and straightforward to employ the deep observations and a steady-state assumption for this depth to characterize and quantify the drift. In fact, the shape of the drift (i.e., strong at the beginning and steadying later on) is similar to the time evolution seen in laboratory studies (D'Asaro and McNeil, 2013; Tengberg and Hovdenes, 2014). However, we do not believe the deep correction to be a viable option: It is unclear which portion of the observations comes from an optode drift itself since there may be other effects in parallel: Is the pressure effect of the optode constant or changing, too? Has the O_2 level at 1000 m been truly constant over the region covered by the float trajectory? Can there be additional artifacts on the isopycnal level from a (small) drift in the conductivity cell? These effects may be small in magnitude (and do not affect the conclusion that there *is* a drift), but they may be large enough to cause a significant bias in the surface saturation which must be avoided (see accuracy effect on NCP above).

An alternative would be the analysis of chance-crossovers with other cruises to repeat the in-situ calibration done at the deployment. However, even Winkler-based data may be biased by several µmol kg^{-1}, as has been nicely shown by Stendardo et al. (2009). The authors compared crossovers between 98 cruises in the Atlantic Ocean and had to apply a mean adjustment of 2 % to 23 of these cruises to reach an internal consistency of 2 µmol kg^{-1}. While this is a rather favourable case with a large number of crossovers, it still exceeds our desired level of accuracy. Comparison with a few chance-crossovers therefore is not a viable option for a full in-situ correction either.

In absence of a better reference, we decided to use the presence of the SOM and the seasons as a boundary on the gas exchange flux: During spring and summer, the observed O_2 flux must be equal or higher than the abiotic flux, i.e., there must be

an outgassing biological O_2 flux component. The buildup of the SOM in spring and summer is a clear sign of net production so the biological O_2 gas exchange needs to be outgassing as well. Moreover, any mixing (or entrainment) effect that brings waters of the SOM into the mixed layer can only increase the mixed layer O_2. This can only increase the biological O_2 flux in our analysis since the SOM is stronger in the observations than in the abiotic model. This way, we obtain a valid lower bound on the optode correction for the spring and summer part of the year.

In autumn, (intense) surface cooling might lead to surface undersaturation. However, this would be the case for the abiotic model, too, so the effect should be picked up by using the model as a reference as we do. The mixed layer deepens concurrently and erodes the accumulated SOM. While we believe this entrainment, i.e., erosion of the SOM, is of similar magnitude in the observations and the model, we can not exclude that the observations are biased high due to simplified physics of the model causing an incorrect mixed layer deepening. Therefore, we limited our boundary condition to the spring and summer period. A similar argument applies for winter where surface cooling and deep mixing reduces the confidence into the model. In addition, deep waters with lower O_2 content may be entrained. Our boundary condition may thus be invalid for the rest of the year and it is only applied to spring and summer.

While we expect a stronger drift in the beginning of the deployment and some weakening later on (see deep values in figure 8.8 or D'Asaro and McNeil, 2013), this way of surface referencing provides not sufficient information to asses the time constant and amplitude. While we used a drift model of the form

$$c_{O_2}\big|_t \; - \; c_{O_2}\big|_{t_0} = a \cdot (t - t_0)^b \cdot \left(1 - e^{\frac{t-t_0}{c}}\right) , \qquad 0 < b < 1 \tag{8.7}$$

for the deep data (red line in figure 8.8, left), we have to resort to a simple linear trend with the seasonal surface boundary. Thus derived annual drift rates are shown in table 8.1.

This is a "minimum correction" to the data, both that it potentially underestimates the drift early in the timeseries (compare figure 8.8, left, vs. a linear trend; table 8.1) and that it uses a lower boundary on the biological O_2 flux: It is required to be at least zero, but may be higher in reality. Given the argument of the model sensitivity on the accuracy of the surface saturation state (see above), this correction gives a lower bound on the net community production.

The in-situ correction is least constrained for SAG float lovbio005 where quality O_2 data is only available for the first 10 months of the deployment. Moreover, months 7 – 10 are in the autumn season and thus not included for the surface flux boundary condition. Therefore, the significance of the drift correction is reduced for lovbio005 and its magnitude is only a first order approximation.

Uncertainties associated with this correction can be easily overcome if a proper in-situ reference during the float's lifetime were available. In air and near surface measurements at the end of each profile (see chapter 3) can provide this kind of reference. Such a reference is crucial for the accuracy with which the surface disequilibrium can be determined which, in turn, is essential to get an accurate productivity estimate using the methods shown here.

float	region	method	drift / μmol kg^{-1} after n months			
			$n=6$	$n=12$	$n=18$	$n=24$
lovbio003	SAG	surf.	−1.11	−2.22	−3.33	−4.44
		deep	−2.67	−3.40	−3.91	−4.32
lovbio005	SAG	surf.	−2.74	−5.47	–	–
		deep	−3.17	−4.41	–	–
lovbio006	NAG	surf.	−1.17	−2.33	−3.50	−4.67
		deep	−4.99	−6.10	−6.82	−7.38
lovbio009	NAG	surf.	−0.14	−0.27	−0.41	−0.55
		deep	−3.48	−4.50	−5.13	−5.64
lovbio010	NAG	surf.	−1.14	−2.28	−3.42	−4.56
		deep	−4.58	−4.71	−4.79	−4.84

Table 8.1: Drift rates derived from deep optode measurements (deep) and from a seasonal boundary condition on the surface flux (surf.) for all floats after 6, 12, 18, and 24 months. The surface variant uses a linear trend and is the in-situ correction we applied to the data.

8.4 Results and Discussion

The logic and steps of the analysis have been shown in detail in section 8.2 and figure 8.7. In the following, we present results starting with the depth-dependent production rates (compare figure 8.7i) to illustrate the correspondance between float data and analysis results. This is done in detail for NAG float lovbio009 (figure 8.9). The argumentation is analogous for the other floats and their production rates are shown in figure 8.10 for the O_2-only floats and in figure 8.11 for the O_2 and NO_3^- floats. The mean depth profiles of O_2-based production are given in figure 8.12 while figure 8.13 summarizes the time evolution of both depth-integrated NCP and biological O_2 gas exchange.

Correspondance between Observations and Simulation Results

Starting the discussion of lovbio009 with O_2 at the surface, the model shows a consistent productivity around 0.5 mg C m^{-3} d^{-1} for a major part of the year (8.9b). This mixed layer production is not as such obvious from the O_2 observations alone (8.9a) due to the outgassing of O_2 (while some production can be expected from the presence of the SOM below). In fact, mixed layer productivity and production rates just below the MLD (dashed grey line) are of similar magnitude from the analysis of lovbio009. The sub-MLD production corresponds to the O_2 accumulation seen at the SOM during spring, summer, and early autum. Below the $AOU = 0$ node, temporal variability increases significantly, both in frequency and intensity. Vertical variability, however, is relatively low. This corresponds to mesoscale activity that advects water with slightly different characteristics into and out of the float path. A clear example is the high oxygen, low nitrate filament seen in April 2013 between 150 – 350 m

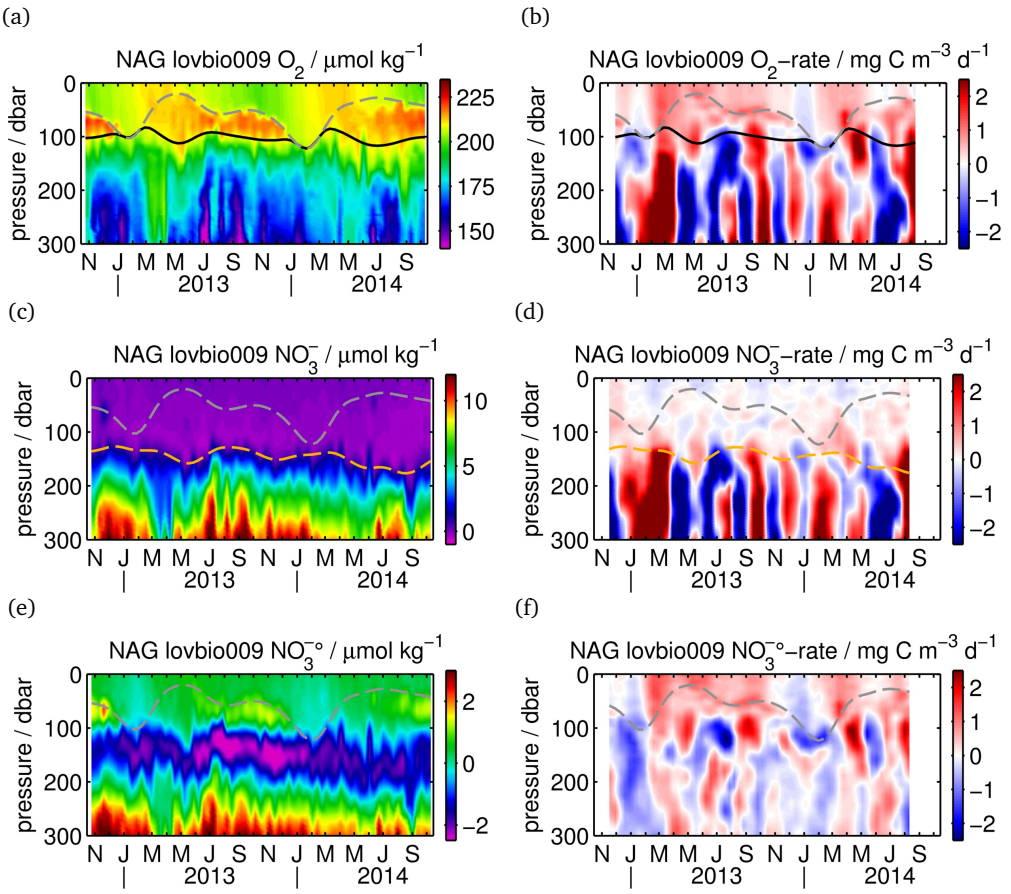

Figure 8.9: Correspondance between observations (left) and simulation results (right) for NAG float lovbio009. Panels b, d, and f give the production rates (converted to carbon units) based on oxygen, nitrate, and preformed nitrate (a, c, and e), respectively. The mixed layer depth is shown as grey dashed line, the integration depth for O_2-based NCP, i.e., the node of apparent oxygen utilization ($AOU = 0$), in black and the nitracline as orange dashed line.

(8.9a and 8.9c). The increase in oxygen leads to apparent high production rates at this depth in February and March. The return to pre-filament concentrations yields an apparent strong respiration signal in April and May (8.9b). These high rates and frequent oscillations at this intermediate depth are thus an artifact of ocean physics unresolved by the model and need to be viewed as artifact of the method used here. Some of these mesoscale features reach close to or into the depth of integration (black line) and thus may affect the NCP estimate (see below).

Finally, the model suggests the mixed layer of lovbio009 to be nearly balanced or net heterotrophic in early winter. This could be caused by strong mixed layer deepening reaching well into the net respiratory layers so that the mixed layer balance is turned net O_2 consuming. However, the MLD barely touches the node of *AOU*, i.e., the boundary between net production and net respiration (see previous chapter; figure 7.10), so a major respiratory signal from entrained waters seems unlikely. As discussed before, mixed layer deepening in late autumn and early winter is a challenging period for the model. Moreover, surface cooling may cause undersaturation and the O_2 accuracy is thus of prime importance for the sign (and magnitude) of the air sea flux. While it is therefore feasible, that the net respiration signal is an artifact of the model, it may as well arise from reality with a low production rate to start with. Since this dip in early winter O_2-based productivity is seen for all floats (both NAG and SAG, see figures 8.10 and 8.11), we can not exclude either interpretation with our present data. Still, it is encouraging that this feature is consistent, so a generally-applicable explanation is likely.

Nitrate is depleted in the upper 140 m of the NAG water column (8.9c), so it is not surprising that nitrate-based production rates are near zero above the nitracline (8.9d). Below the nitracline, nitrate-based production rates show a similar variability as O_2-based estimates and patterns are mirrored (8.9d and 8.9b). This underlines mesoscale activity and the advection of different water masses as the main cause of this strong variability. When using changes in preformed nitrate, these mid-depth oscillations vanish almost completely (8.9f) and two conclusions can be drawn: First, oxygen and nitrate co-vary within the mesoscale features and second, they closely follow the assumed stoichiometry (equation 7.3). This is the desired behaviour of a preformed tracer (i.e., eliminating the production/respiration effect on the quantity) and it confirms the findings of Johnson and Riser (2014) that layer III is stoichiometrically balanced (see chapter 7).

In the shallower layers, however, this stoichiometric balance is violated. With no nitrate and no changes in nitrate above the nitracline (i.e., no nitrate-based production), changes in preformed nitrate are determined by changes in *AOU*. The preformed nitrate-based rates mirror the oxygen-based rates, i.e., there is O_2 production without concurrent NO_3^- uptake (layer I). Layer I is "net productive" in respect to preformed nitrate, causing a shallow maximum to build up in parallel to the SOM (8.9e & f and 8.12a). There is also an imbalance in layer II indicated by transient oscillations when a mesoscale feature passes by (e.g., August 2013 or May 2014, figure 8.9f). In total, a "net heterotrophic" signature tends to dominate this layer (see 8.12) thus closing the imbalance between excess O_2 and NO_3^- deficit in layer I and II.

Regional Coherence and Mean Depth Profile

The other four floats follow similar patterns and their model-derived production rates show great similarity. Figure 8.10 gives the result for SAG float lovbio005 (left) and NAG float lovbio010 (right), both only equipped with an O_2 optode, while figure 8.11 shows the data for SAG float lovbio003 (left) and NAG float lovbio006 (right), both equipped with an O_2 optode and a nitrate sensor. Lovbio003 has no transmitted profiles for cycles 36 – 38 (15 October – 04 November 2013) and we therefore excluded that portion of the timeseries (8.11 (left) and 8.13b).

All floats show net O_2-production in the mixed layer and sub-mixed layer down to about 100 m. The analysis suggests a local maximum in productivity just below the base of the mixed layer (see, e.g., 8.10a, 8.10b, 8.11a, or 8.11b). If there exists a mechanism to access nutrients from depth, the strong stratification at the base of the mixed layer would certainly still be a border difficult to cross. The highest light level accessible to sub-MLD organisms is thus just below the mixed layer base which might cause this local maximum. This surface net O_2-production is also evident from the average depth profiles shown for each float in figure 8.12. The thick line gives the median O_2-production rate while the thin lines give their 25- and 75-percentiles, respectively. Except for SAG float lovbio005, O_2 rates suggest a slightly respiratory zone below ca. 150 m. However, this is not significant given the natural variability.

At greater depths, production rates are consistently dominated by oscillations due to unresolved ocean physics with a net effect approaching zero (8.12). However, the amplitude is significantly smaller in the SAG than in the NAG (compare left panels in 8.10 and 8.11 vs. right panels in 8.9, 8.10, and 8.11). The depth O_2 gradient is weaker in the SAG and mesoscale activity thus causes a smaller pertubation. In fact, rates at intermediate depths are therefore in principle better constrained in the SAG (8.12b vs. 8.12a) and the uncertainty of the integration depth is less important for the integrated NCP estimate (8.13b vs. 8.13a).

There is a residual calibration bias on the nitrate sensor of NAG floats lovbio006 and lovbio009 that causes nitrate concentrations to increase by about 0.2 μmol kg^{-1} between 100 m and the surface (e.g., 8.9c). This level is below the sensor's detection limit and probably a temperature compensation issue. However, this small imbalance of nitrate is quickly redistributed in the model's mixed layer. Comparison with the observations, where this gradient persists, thus causes an apparent excess of NO_3^- in the surface and an apparent deficit at the base of the mixed layer, i.e., an apparent remineralization and production signal, respectively. While the mixed layer depth varies with the season and the apparent production signal is thus blurred, the apparent NO_3^- excess can be found at the surface year-round, thus causing a small but continuous, data-driven bias towards remineralization (8.9d). This is well visible in the mean production depth profiles where NO_3^--based production rates of lovbio006 and lovbio009 show a distinct inclination (8.12a, middle). This is a measurement artifact and mixed layer rates are likely to be zero in reality. The nitrate sensor on SAG float lovbio003 does not show this residual calibration bias and NO_3^--based rates are not significantly different from zero (8.12b, middle). A small positive peak in production rates would have been expected at the depth of the nitra-

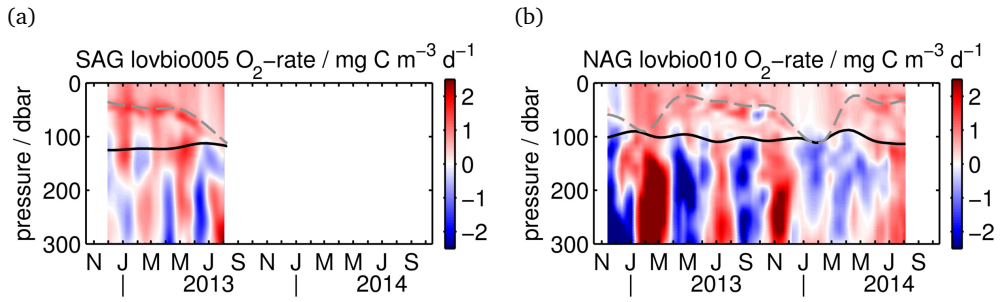

Figure 8.10: Production rates for the O_2-only floats lovbio005 in the SAG (a) and lovbio010 in the NAG (b). The mixed layer depth is shown as grey dashed line, the integration depth for NCP as black line, and the nitracline as orange dashed line.

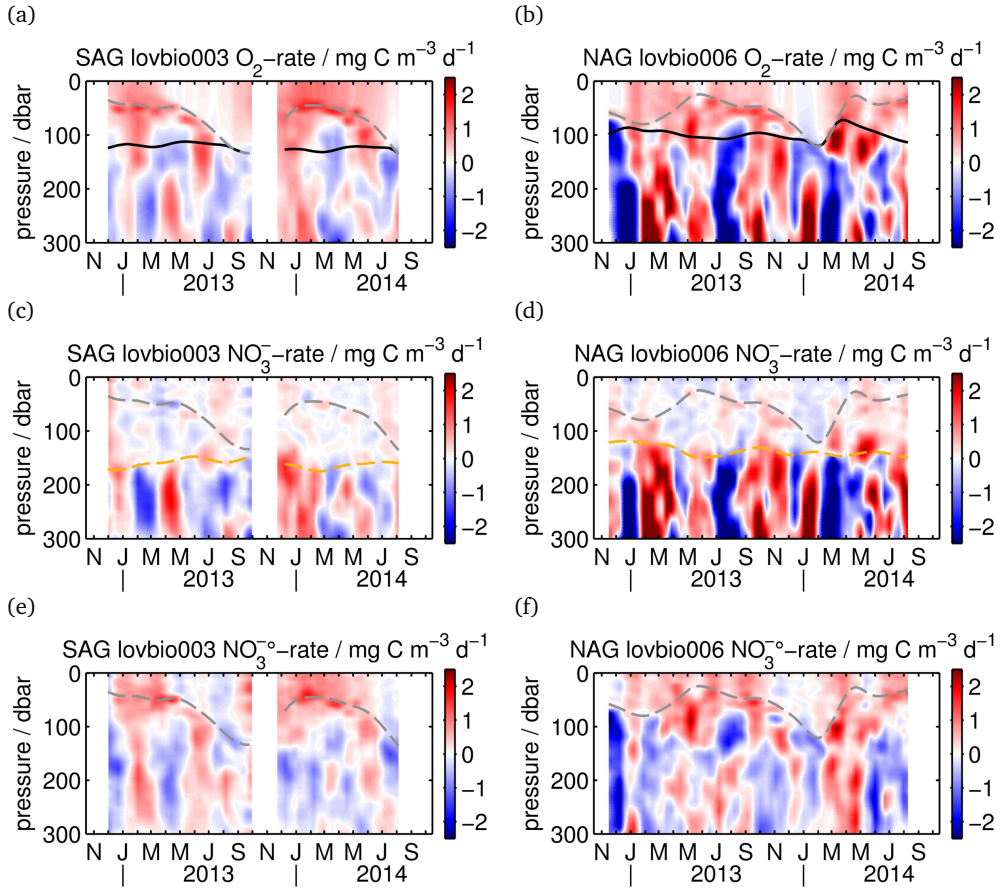

Figure 8.11: Production rates for SAG float lovbio003 (left) and NAG float lovbio006 (right) based on oxygen (top), nitrate (middle), and preformed nitrate (bottom), respectively. The mixed layer depth is shown as grey dashed line, the integration depth for O_2-based NCP as black line, and the nitracline as orange dashed line.

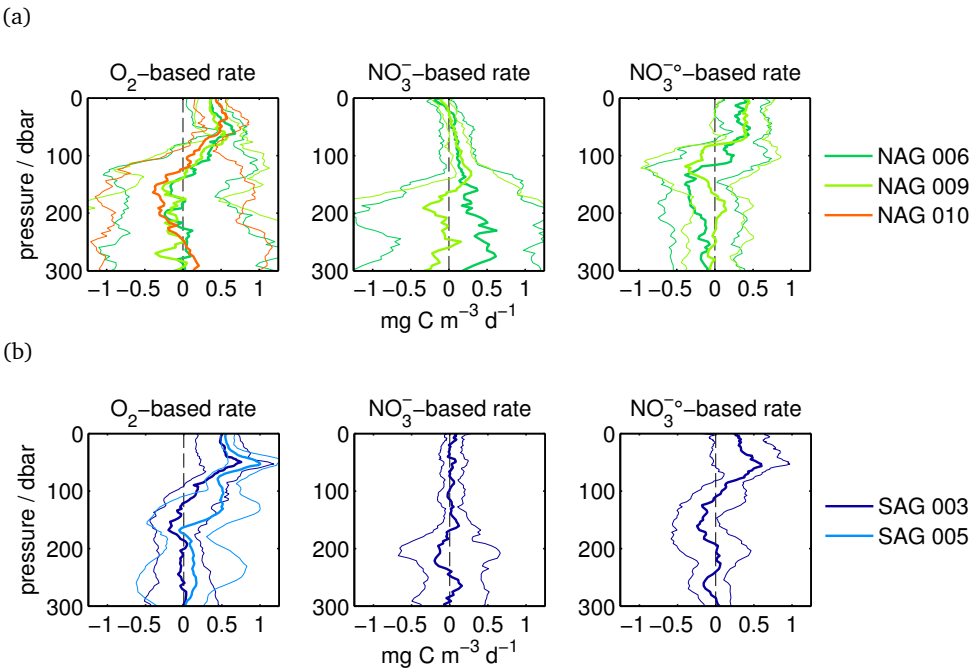

Figure 8.12: Average production rate depth profiles based on oxygen (left), nitrate (middle), and preformed nitrate (right) in the NAG (a) and SAG (b). The thick line gives the median and the thin lines the 25- and 75-percentiles.

cline. However, this is hardly visible in the analysis due to the increased variability at depth. In any case, NO_3^--based production is well below O_2-based production, confirming that turbulent mixing alone is not capable to support the nutrient requirement from O_2 production as has been found in many previous studies (e.g., Michaels et al., 1994).

The depth profiles of preformed nitrate give the well-constrained pattern: There is an imbalance at shallow depths with an O_2 excess in layer I and a nitrate deficit in layer II. At depth, changes in preformed nitrate approach zero implying a stoichiometrically balanced system.

The data of SAG lovbio005 shows a higher uncertainty than the other floats (see, e.g., 8.13b) due to the float's limited lifetime. While it performed more profiles than any other float to date (see table 7.1), it covered a shorter time period and therefore a fewer number of eddies. The physical imprint on sub-MLD production rates is thus stronger compared to the other floats which have a longer averaging period over a higher number of mesoscale structures. Moreover, its sampling is seasonally biased: Lovbio005 covered the spring, summer, and autumn season but not the winter period. While winter has been low in productivity for all other floats, this time of year is missing for lovbio005 and its mean production rates are therefore higher compared to the other floats (8.12b).

Temporal Evolution

The temporal evolution of the depth-integrated net community production and of the biological O_2 surface flux is given in figure 8.13a and 8.13b for all floats of the North and South Atlantic subtropical gyre, respectively. The thick line shows the model result with application of an in-situ drift correction based on a seasonal boundary on the O_2 surface flux. Thin lines represent the uncertainty range which includes a ± 1 µmol kg^{-1} O_2 offset to account for the calibration accuracy and a ± 10 m offset on the integration depth.

The magnitude of the temporal variability is on the order of the mean signal. However, temporal patterns within the regions are surprisingly coherent. This is especially evident for the NAG region with three floats providing *independent* observations. The strong coherence relates to the floats' close proximity (see NAG inset in figure 7.1) in relation to the basin-scale size of distinct biogeochemical provinces (see Longhurst et al., 1995). It also indicates that the observations are typical for a region larger than the area covered by the floats' trajectories.

In addition, the time series show a consistent dip in NCP and biological O_2 flux in late autumn and early winter while the rest of the year is at a higher level. This has been discussed earlier for the water column production rates and we can not clearly distinguish between a limitation of the model (and the O_2 in-situ correction) or a real reduction in integrated NCP.

In both NAG and SAG, the biological air sea exchange flux represents less than half to the total NCP. Its portion is between 20 – 35 % and water column processes dominate (e.g., the SOM intensification). However, it contributes significantly and should not be neglected (see seasonal sub-mixed layer approach, section 8.1).

The uncertainty on the integrated NCP comes to about 80 % from the O_2 accuracy and to 20 % from the integration depth. The total uncertainty of NCP is somewhat lower in the SAG than in the NAG (8.13), which might be related to the weaker O_2 depth gradient and thus reduced variability caused by mesoscale activity.

Annual Net Community Production

The averaged O_2-based NCP and the mean biological O_2 flux is given in table 8.2, with their respective uncertainty range in parentheses. Both the NAG and the SAG are net productive from our analysis with a mean annual NCP of 1.2 ± 1.1 and 1.6 ± 0.8 mol C m^{-2} yr^{-1}, respectively. However, the uncertainty is of a similar range as the net productive signal for two reasons. First, the O_2 accuracy has a large effect on the O_2 mixed layer balance where most of the productivity is found (figures 8.9, 8.10, and 8.11). This needs to be improved for a more accurate estimate, e.g., by proper referencing (e.g., chapter 3). Second, our NCP signal is small to start with. Since we did this analysis in the subtropical gyres, considered as "ocean deserts", a low NCP was to be expected from the beginning. However, because of the optode drift and the lack of a proper reference for in-situ correction, we can only provide a lower bound and are thus at the low end of possible NCPs. If there were good reasons to correct the optode more strongly, the ratio between signal and uncertainty would be more favourable, too.

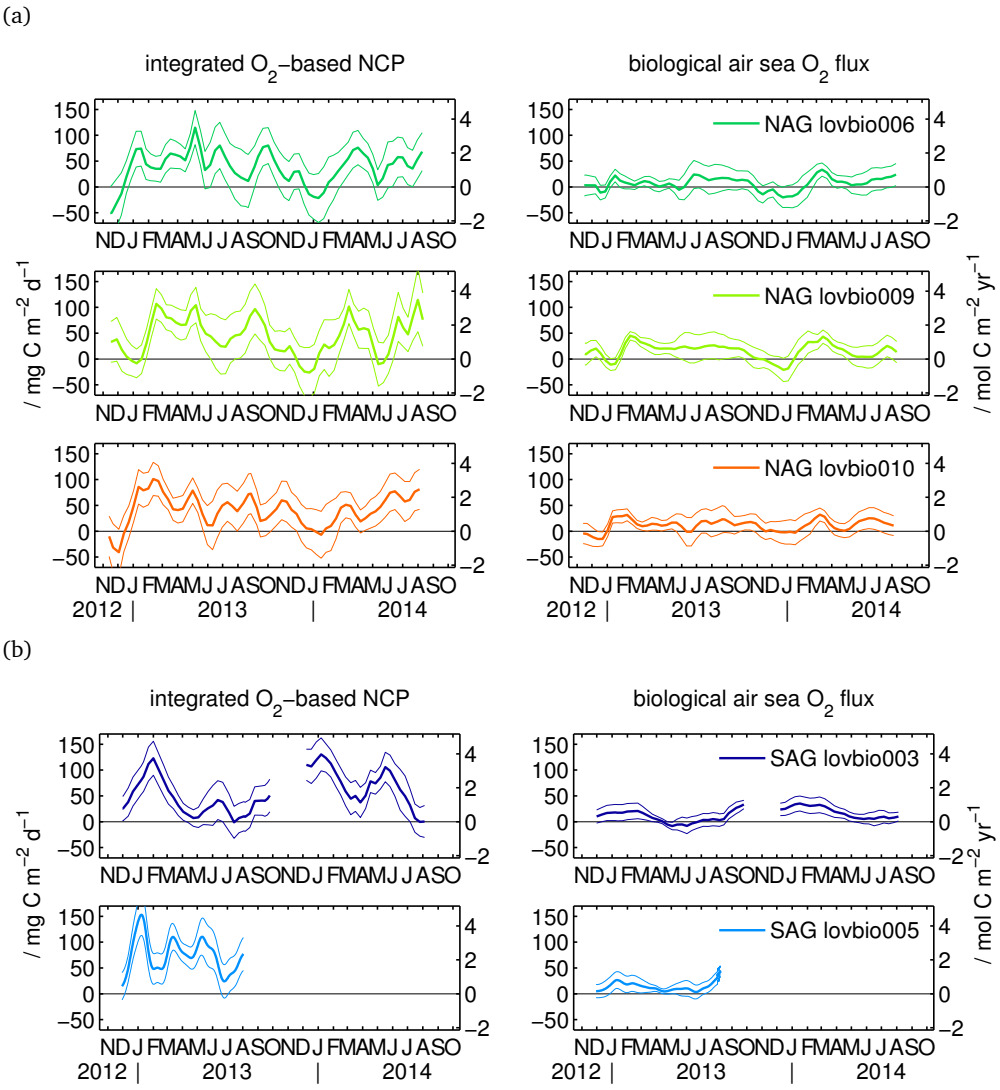

Figure 8.13: Time series of O_2-based, depth-integrated NCP for all floats in the North (a) and South Atlantic subtropical gyre (b). The left axis has units of mg C m^{-2} d^{-1} while the right axis gives data in mol C m^{-2} yr^{-1}.

float	region	integrated NCP / mol C m^{-2} yr^{-1}		surface flux / mol C m^{-2} yr^{-1}	
lovbio003	SAG	1.6	(0.8;2.5)	0.4	(0.1;0.8)
lovbio005	SAG	2.3	(1.4;3.2)	0.4	(0.0;0.8)
lovbio006	NAG	1.0	(−0.1;2.2)	0.2	(−0.3;0.8)
lovbio009	NAG	1.3	(0.1;2.5)	0.5	(−0.1;1.0)
lovbio010	NAG	1.2	(0.2;2.2)	0.3	(−0.2;0.9)

Table 8.2: Mean NCP in the NAG and SAG and mean biological surface flux, i.e., loss of O_2 to the atmosphere. The uncertainty range is given in parentheses.

An exception is lovbio005 which gives a significantly higher NCP estimate than the other floats. This is predominantly caused by the seasonal bias where lovbio005 lacks the winter observations. This raises the question wether extrapolation to an annual NCP is justified and consequently only lovbio003 is used for the mean annual SAG estimate given above.

Comparison with other geochemical NCP estimates shows that our NCP is within the range of previously reported values, albeit at the low end. The Sargasso Sea and BATS is one of the most intensively studied region of the Atlantic subtropical gyres and a number of techniques have been applied there. From ^{13}C isotopic constraints and four years of data, Gruber et al. (1998) estimated a NCP of 2.3 ± 0.9 mol C m^{-2} yr^{-1} for the mixed layer and extrapolated this to 3.8 mol C m^{-2} yr^{-1} in the euphotic zone. More recently, they expanded their analysis using a diagnostic model and 18 years of the time series to obtain a mean NCP of 3.4 ± 0.8 mol C m^{-2} yr^{-1} (Gruber et al., 2002). A slightly smaller value (2.2 ± 0.4 mol C m^{-2} yr^{-1}) is reported by Stanley et al. (2012) for the (regionally-averaged) export production based on apparent oxygen utilization rates derived from tritium and ^{3}He tracer data. However, Cianca et al. (2013) argue that a focus on BATS, i.e., on the Western boundary of the gyre, is not necessarily representative of the NAG and complement this with time series observations from ESTOC at the Eastern boundary. Using different methods to analyze the annual O_2 cycle, they arrive at a production equivalent to 1.6 ± 0.3 mol C m^{-2} yr^{-1} at ESTOC and 2.8 mol C m^{-2} yr^{-1} at BATS. In fact, the injection of nutrients from deep winter mixing and an associated peak in primary production at BATS as well as BATS' location in a region of high eddy energetics (Steinberg et al., 2001) may explain that difference between Eastern and Western basin, with our NAG deployment region being more closely related to ESTOC. The South Atlantic subtropical gyre is studied less intensively and independent in-situ NCP estimates are not abundant.

8.5 Summary

Our method using an abiotic model is well suited to extract the biological effect on the oxygen distribution year-round and without depth limitations. However, we currently lack highest quality data to fully use its potential. Current oxygen sensors do not appear to exhibit the long term stability and thus accuracy required for air sea interface calculations when deployed in surface waters. Biogeochemical floats themselves, however, are an ideal platform for long term deployments in remote regions of the open ocean where other observational approaches are limited. Future deployments, though, should be complemented by a proper referencing method during the float's lifetime (such as repeated optode in-air measurements, chapter 3) to obtain the correct magnitude of NCP. In this regard it is no surprise that previous work from autonomous floats was concentrated around time series stations like HOT or BATS (e.g., Riser and Johnson, 2008; Johnson and Riser, 2014) where regular and high quality reference data are available. We expanded this approach to the open Atlantic ocean and were still able to obtain significant and consistent results.

Our NCP estimates of 1.2 ± 1.1 mol C m^{-2} yr^{-1} for the NAG and 1.6 ± 0.8 mol C m^{-2} yr^{-1} for the SAG are at the lower end of NCPs from similar studies but in a realistic range. This is to be expected given our "minimum-correction" approach of the optode drift, i.e., to limit our correction to a level that is easily justified. Between 20 – 35 % of our NCP is lost to the atmosphere through gas exchange. While our unifying model approach is sensitive to O_2 at all depth horizons, both the O_2 mass balance approach and the sub-MLD O_2 accumulation approach would each miss a significant portion of the production (and could not be applied to some parts of year). Our estimate is thus methodologically more robust (but only a lower limit due to data limitations).

Finally, turbulent nitrate mixing can not sustain the observed O_2 productivity and other processes need to be invoked. Consequently, preformed nitrate–based rates show a non-stoichiometric behaviour in layer I and layer II, but are nearly balanced below (analogous to Johnson and Riser, 2014), which is remarkable considering the variability in O_2- and NO_3^--based rates in layer III.

Physical effects unresolved in our simple 1D model have a strong impact on the NCP's uncertainty. For the sub-MLD approach, this has been solved by using the *seasonal* O_2 accumulation (Riser and Johnson, 2008), i.e., averaging over the entire season vs. 6 weeks in our case. This gives a longer averaging period thus amplifying the biological signal. However, time resolution is lost and the approach itself is blind for the surface parts of the water column. Moreover, a too long simulation time in our approach might create additional biases by divergence between the 1D model and observations. In a more comprehensive approach, our abiotic O_2 model could be used with a more complex 3D ocean model as physical host, which can be easily accomplished using FABM.

Concluding Remarks

Oxygen optodes have been introduced to marine science almost two decades ago (Klimant et al., 1995). Profiling floats evolved in the same decade (Davis et al., 1992), and the combination of both, an Argo-O_2 float, has been first deployed about a decade ago (Körtzinger et al., 2004). In contrast to the still growing Argo core mission, however, Argo-O_2 stayed at a rather constant level since the beginning of this thesis (using the number of active O_2 floats registered at the Argo Information Centre as proxy, see figure 9.1).

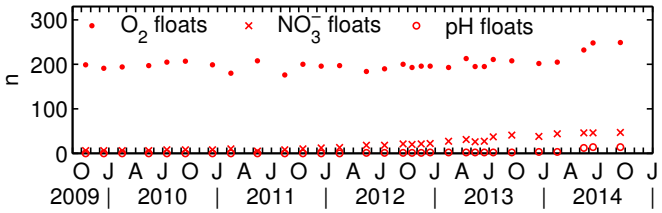

Figure 9.1: Number of Argo floats equipped with oxygen sensors (dots) and other biogeochemical sensors (nitrate and pH, crosses and circles, respectively) according to data from the Argo Information Centre (http://argo.jcommops.org).

This can be clearly attributed to shortcomings that existed in the characterization and accuracy of O_2 sensors. In the meantime, however, these have been largely addressed as described in part I and by work in parallel to this thesis (e.g., Takeshita et al., 2013). The last missing piece of the characterization puzzle is a proper analysis of the hydrostatic pressure dependence, which will follow in the near future. With solutions for a drift detection and correction at hand (chapter 3), routine high accuracy O_2 measurements are possible. At the same time, pre- and post-deployment quality control procedures for oxygen are being established (see SCOR working group 142) which will further improve the quality and reliability of autonomous O_2 data.

There is thus good prospect that the abundance of Argo-O_2 floats (see figure 9.2) will eventually follow the rising and successful trajectory cast by the core Argo program. An early sign is the recent shift of Argo-O_2 float deployments from a PI-based approach to a community-based approach: Examples are multidisciplinary projects like RemOcean (see chapter 7) or the Southern Ocean Carbon and Climate

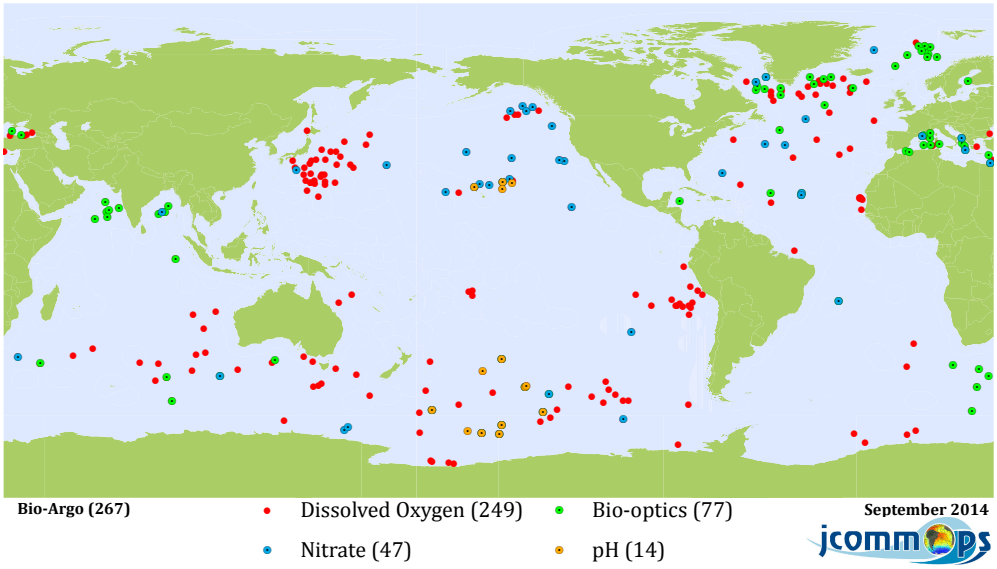

Figure 9.2: Recent map of Bio-Argo floats provided by the Argo Information Centre (http://argo.jcommops.org). Floats with nitrate and pH as well as a large portion of biooptical floats tend to have O_2 sensors as well. Some float clusters can be associated with specific projects, e.g., RemOcean in the subpolar North Atlantic, pre-SOCCOM in the Pacific sector of the Southern Ocean, and a number of projects in the Kuroshio extension.

Observations and Modeling (SOCCOM) project, where nearly 200 Bio-Argo floats are to be deployed in the Southern Ocean and are accompanied with concurrent modelling efforts.

As shown in part II of this thesis, high quality O_2 data are of great value. The gas exchange in the mixed layer can be described comprehensively (chapter 6). With adequate methods, water column physical effects on O_2 can be replicated as well, which ultimately gives access to O_2-based net production estimates from autonomous floats. The approach's feasibility has been demonstrated in the permanently stratified, oligotrophic subtropical gyres (chapter 8). In other, more productive ocean regions, it is likely even more sensitive (if O_2 data show the required accuracy).

But the scope of Bio-Argo floats goes beyond just oxygen. Floats have become multidisciplinary research platforms (see chapter 7) and thus provide an unprecedent level of detail via direct chemical and indirect biooptical proxy measurements. This complementary combination of autonomous technology produces not only a larger, more detailed, and more informative data set than ever before, but also leads to new or improved theories and concepts (chapter 7).

A word of caution at the end: Float technology and autonomous deployments are not without peril. Once deployed, floats are often "gone for good" and there is commonly no simple way to access the platform again. Floats either work as in-

tended – and there is extensive testing done to new firmware and hardware to ensure this – or they don't and there is little that can be fixed remotely. However, if they perform as anticipated, they do their work with high endurance. Floats can operate where research vessels can't (anymore), e.g., they are not impaired by bad weather or the season. It is thus not surprising that an early adoption to float technology has been ice detection algorithms and under ice location to provide year-round observations in polar seas including the winter months (Klatt et al., 2007).

This flexibility and the relative low cost per profile is a great advantage of autonomous observations. They will help to reduce spatial and temporal observation gaps but only if the sensors possess a sufficient characterization and reliability.

Appendix

Additional Figures

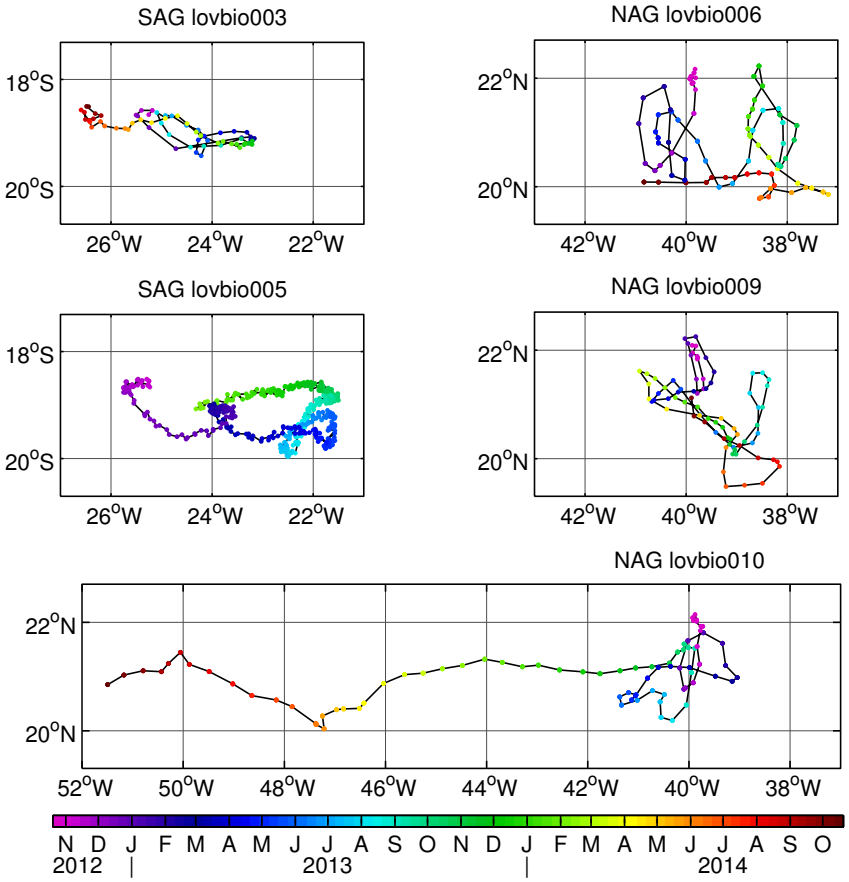

Figure A.7.1: Close-up of the lovbio float tracks in the SAG (left) and NAG (right). The colour coding gives the date of the respective profile.

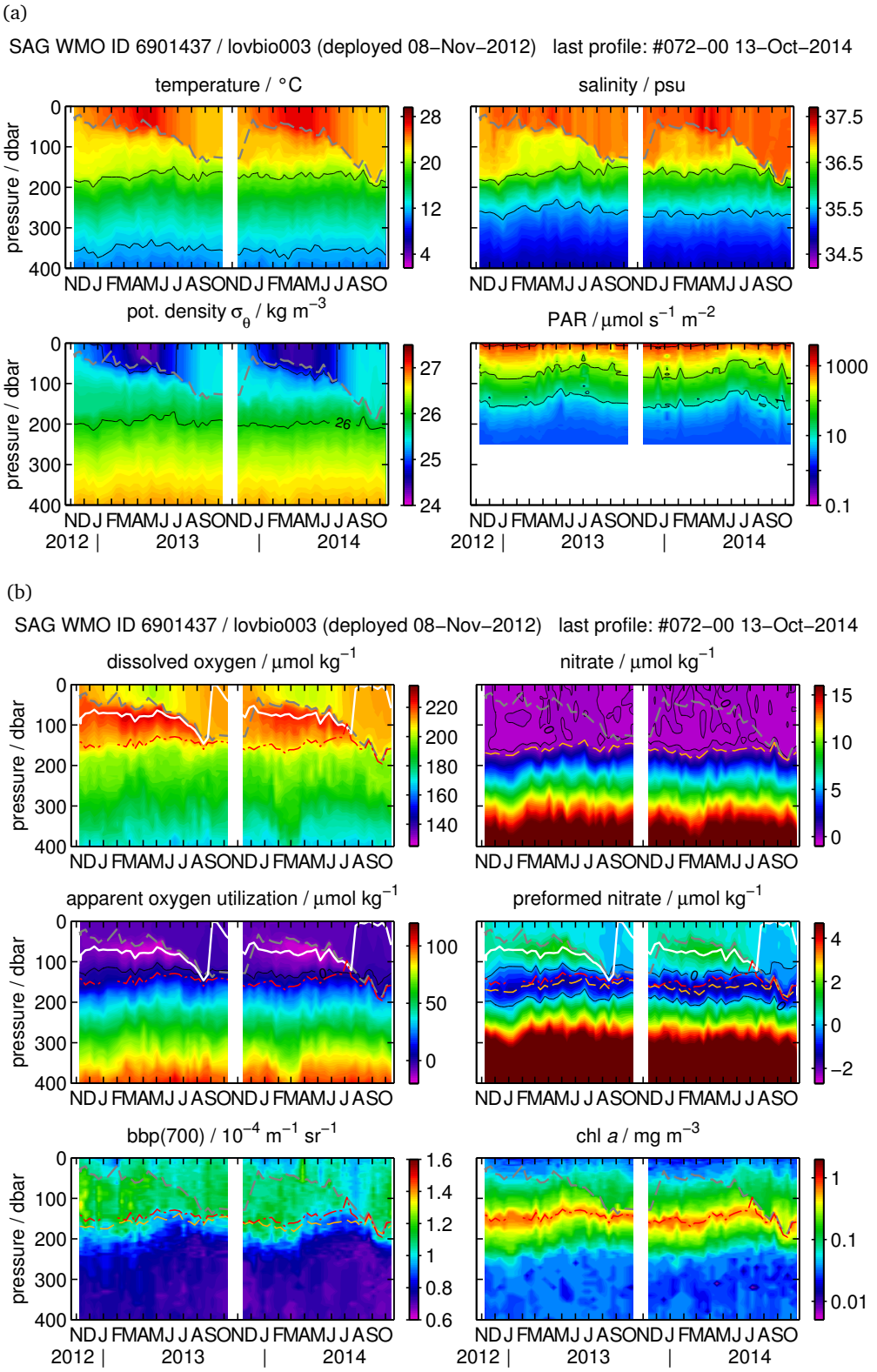

Figure A.7.2: Physical and biogeochemical data of SAG float lovbio003. O_2 data includes an in-situ drift correction (see table 8.1).

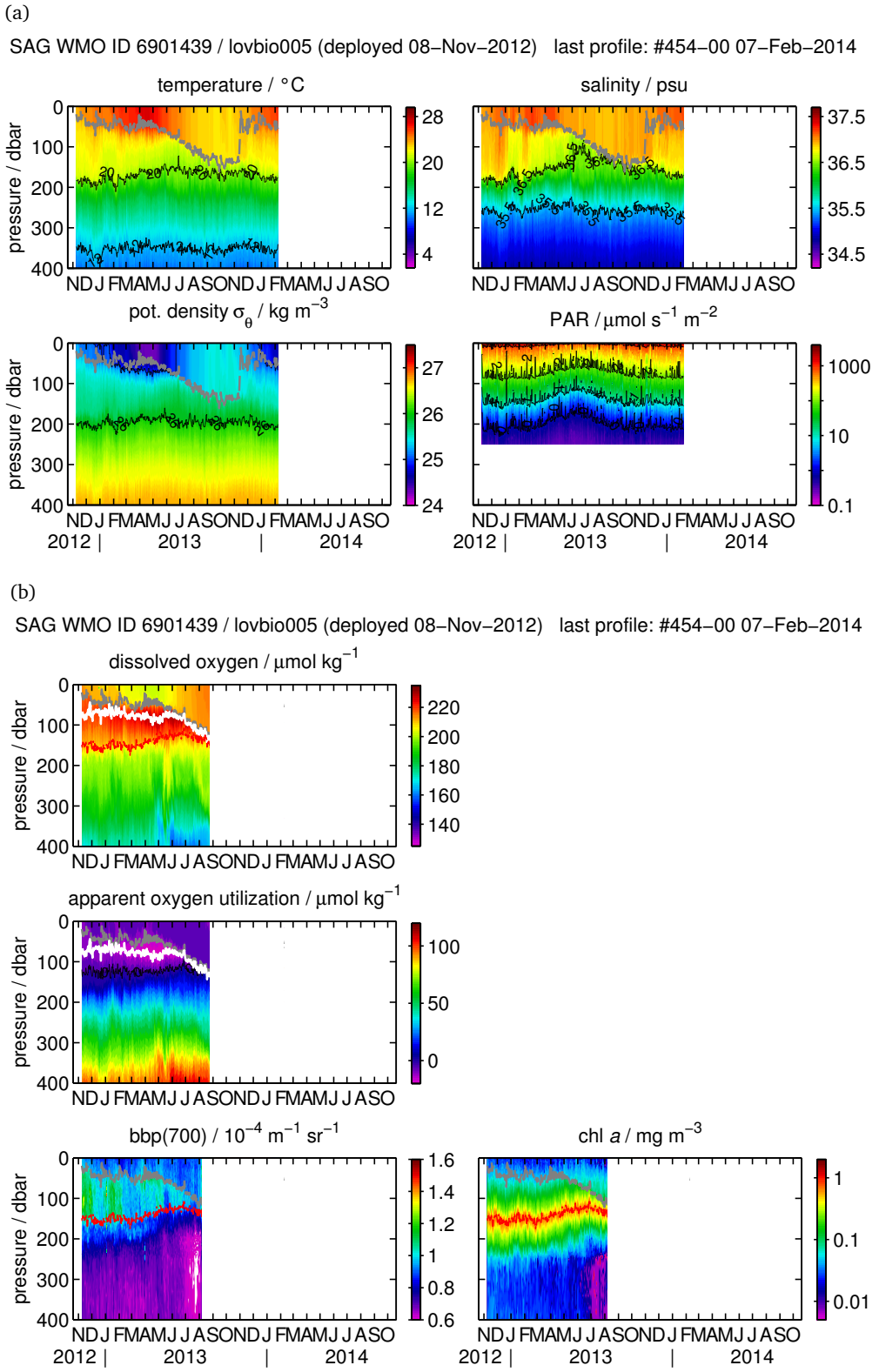

Figure A.7.3: Physical and biogeochemical data of SAG float lovbio005. O_2 data includes an in-situ drift correction (see table 8.1).

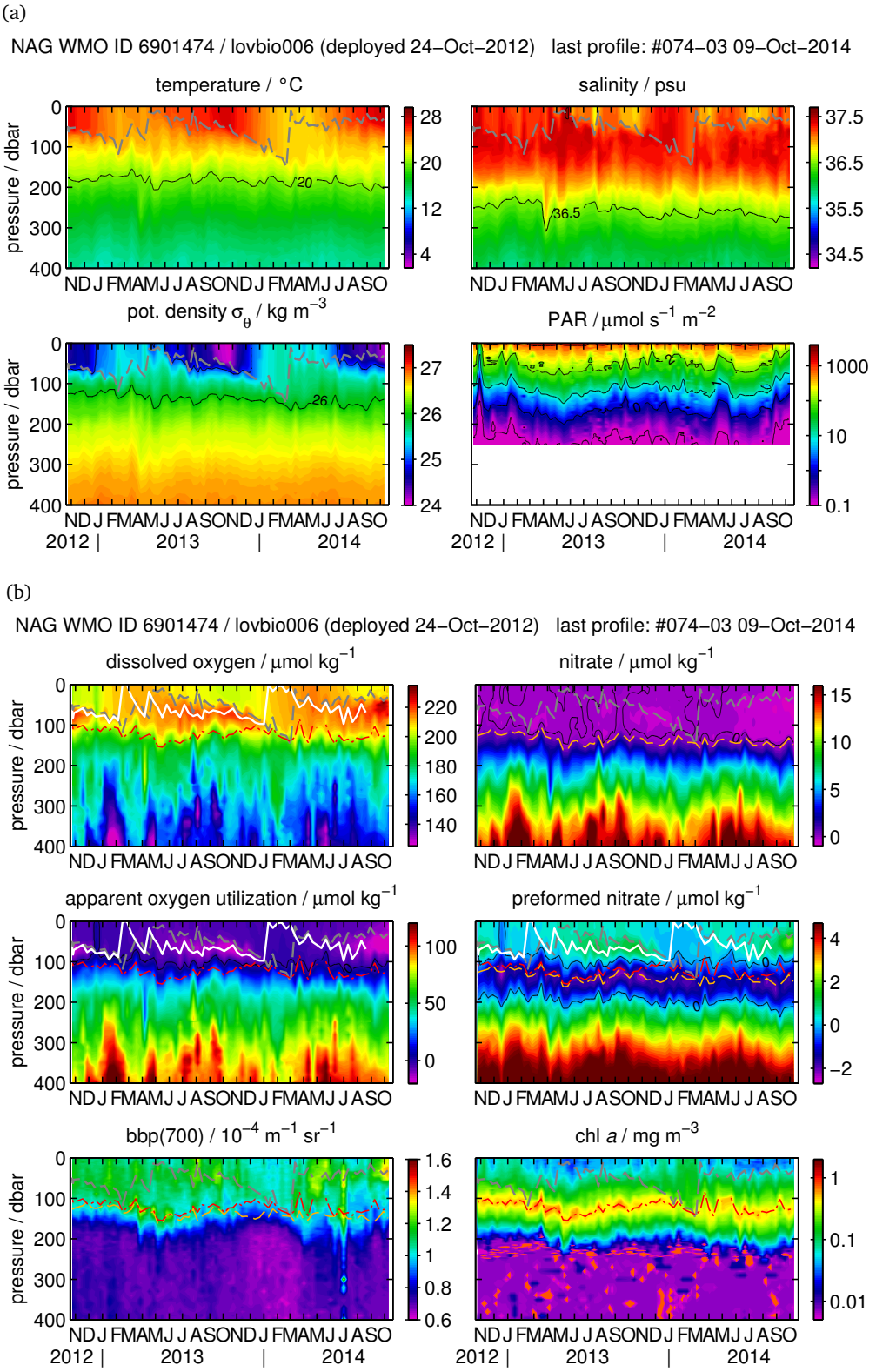

Figure A.7.4: Physical and biogeochemical data of NAG float lovbio006. O_2 data includes an in-situ drift correction (see table 8.1).

(a)

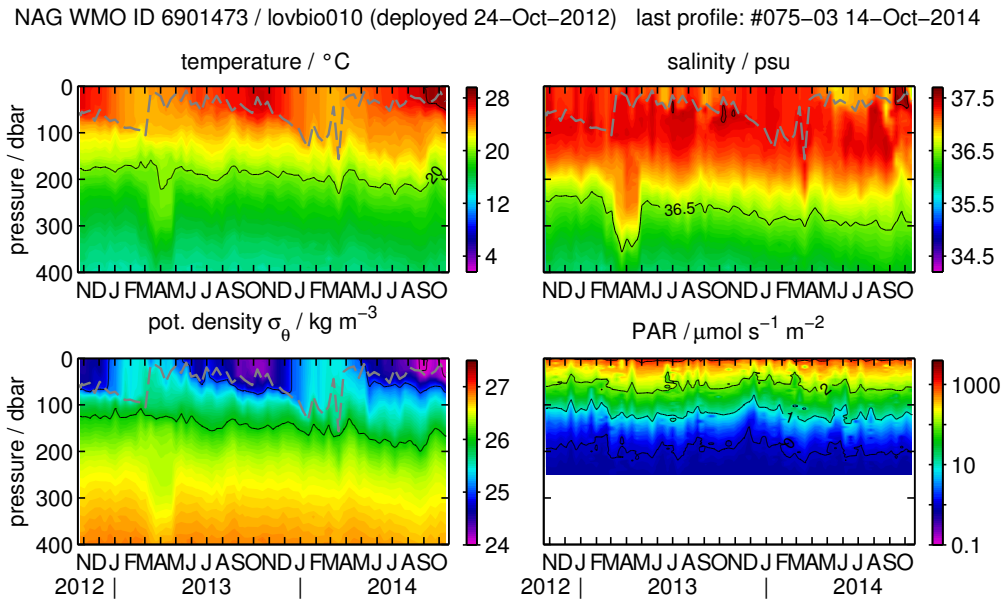

(b)

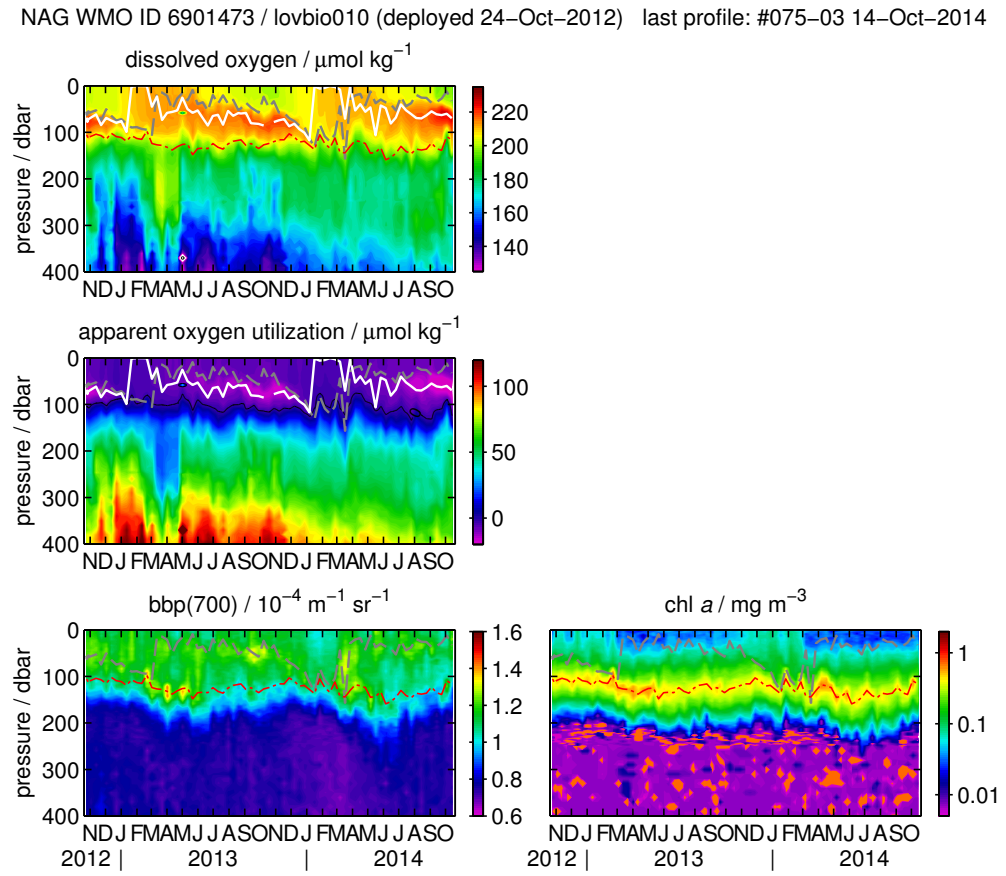

Figure A.7.5: Physical and biogeochemical data of NAG float lovbio010. O_2 data includes an in-situ drift correction (see table 8.1).

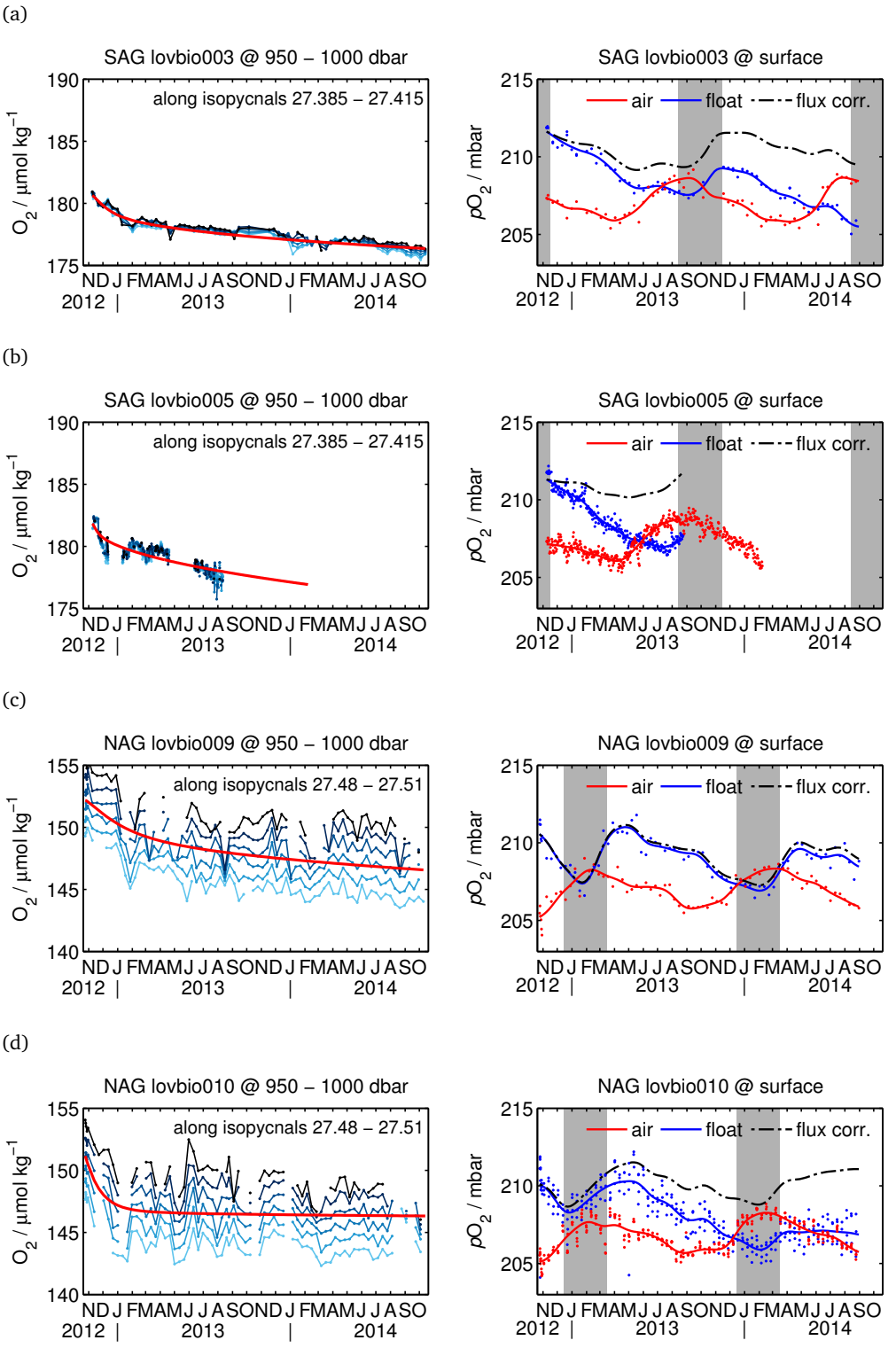

Figure A.8.1: Indicators of an in-situ optode drift shown for all floats in the SAG and NAG but lovbio006 (see figure 8.8).

Bibliography

Aanderaa Data Instruments AS. 2012. Oxygen optode 4330/4330F data sheet. Bergen, Norway. Feb. 2012.

Anderson, L. A. 1995. On the hydrogen and oxygen content of marine phytoplankton. Deep Sea Res. Part I Oceanogr. Res. Pap. **42**: 1675–1680. [doi:10.1016/0967-0637(95)00072-E].

Argo Science Team. 1998. On the design and implementation of Argo: An initial plan for a global array of profiling floats. *In* International CLIVAR Project Office Report 21. GODAE International Project Office, Melbourne, Australia. GODAE Report 5. p. 32.

Arrigo, K. R., van Dijken, G., and Long, M. 2008. Coastal Southern Ocean: A strong anthropogenic CO_2 sink. Geophys. Res. Lett. **35**: L21602. [doi:10.1029/2008GL035624].

Arrigo, K. R. and van Dijken, G. L. 2003. Phytoplankton dynamics within 37 Antarctic coastal polynya systems. J. Geophys. Res.-Oceans **108**: 3271. [doi:10.1029/2002JC001739].

Arrigo, K. R. and van Dijken, G. L. 2004. Annual changes in sea-ice, chlorophyll a, and primary production in the Ross Sea, Antarctica. Deep Sea Res. Part II Top. Stud. Oceanogr. **51**: 117–138. [doi:10.1016/j.dsr2.2003.04.003].

Arrigo, K. R., Perovich, D. K., Pickart, R. S., Brown, Z. W., Dijken, G. L. v., Lowry, K. E., Mills, M. M., Palmer, M. A., Balch, W. M., Bahr, F., Bates, N. R., Benitez-Nelson, C., Bowler, B., Brownlee, E., Ehn, J. K., Frey, K. E., Garley, R., Laney, S. R., Lubelczyk, L., Mathis, J., Matsuoka, A., Mitchell, B. G., Moore, G. W. K., Ortega-Retuerta, E., Pal, S., Polashenski, C. M., Reynolds, R. A., Schieber, B., Sosik, H. M., Stephens, M., and Swift, J. H. 2012. Massive Phytoplankton Blooms Under Arctic Sea Ice. Science **336**: 1408. [doi:10.1126/science.1215065].

de Baar, H. J. W., de Jong, J. T. M., Bakker, D. C. E., Löscher, B. M., Veth, C., Bathmann, U., and Smetacek, V. 1995. Importance of iron for plankton blooms and carbon dioxide drawdown in the Southern Ocean. Nature **373**: 412–415. [doi:10.1038/373412a0].

Bakker, D. C. E., Hoppema, M., Schröder, M., Geibert, W., and de Baar, H. J. W. 2008. A rapid transition from ice covered CO_2-rich waters to a biologically mediated CO_2 sink in the eastern Weddell Gyre. Biogeosciences **5**: 1373–1386. [doi:10.5194/bg-5-1373-2008].

Bellerby, R. G. J., Hoppema, M., Fahrbach, E., de Baar, H. J. W., and Stoll, M. H. C. 2004. Interannual controls on Weddell Sea surface water fCO_2 during the autumn-winter transition phase. Deep Sea Res. Part I Oceanogr. Res. Pap. **51**: 793–808. [doi:10.1016/j.dsr.2004.01.002].

van den Besselaar, E. J. M., Haylock, M. R., van der Schrier, G., and Klein Tank, A. M. G. 2011. A European daily high-resolution observational gridded data set of sea level pressure. J. Geophys. Res.-Atmos. **116**: D11110. [doi:10.1029/2010JD015468].

Bittig, H. C., Fiedler, B., Steinhoff, T., and Körtzinger, A. 2012. A novel electrochemical calibration setup for oxygen sensors and its use for the stability assessment of Aanderaa optodes. Limnol. Oceanogr.: Methods **10**: 921–933. [doi:10.4319/lom.2012.10.921].

Boyd, P. W. 2002. Environmental Factors Controlling Phytoplankton Processes in the Southern Ocean1. J. Phycol. **38**: 844–861. [doi:10.1046/j.1529-8817.2002.t01-1-01203.x].

de Boyer Montégut, C., Madec, G., Fischer, A. S., Lazar, A., and Iudicone, D. 2004. Mixed layer depth over the global ocean: An examination of profile data and a profile-based climatology. J. Geophys. Res.-Oceans **109**: C12003. [doi:10.1029/2004JC002378].

Brewer, P. G., Bradshaw, A. L., and Williams, R. T. 1986. Measurements of Total Carbon Dioxide and Alkalinity in the North Atlantic Ocean in 1981. *In* J. R. Trabalka and D. E. Reichle [eds.] The Changing Carbon Cycle. Springer, New York. pp. 348–370.

Broecker, W. S. and Peng, T.-H. 1974. Gas exchange rates between air and sea1. Tellus **26**: 21–35. [doi:10.1111/j.2153-3490.1974.tb01948.x].

Bruggeman, J. and Bolding, K. 2014. A general framework for aquatic biogeochemical models. Environ. Model. & Software **61**: 249–265. [doi:10.1016/j.envsoft.2014.04.002].

Burchard, H., Bolding, K., Kühn, W., Meister, A., Neumann, T., and Umlauf, L. 2006. Description of a flexible and extendable physical-biogeochemical model system for the water column. J. Marine Syst. **61**: 180–211. [doi:10.1016/j.jmarsys.2005.04.011].

Bushinsky, S., Emerson, S., Riser, S. C., and Swift, D. 2014. Accurate oxygen on Argo floats using on-going in-situ air calibrations. In prep.

Caldeira, K. and Duffy, P. B. 2000. The Role of the Southern Ocean in Uptake and Storage of Anthropogenic Carbon Dioxide. Science **287**: 620–622. [doi:10.1126/science.287.5453.620].

Canuto, V. M., Howard, A., Cheng, Y., and Dubovikov, M. S. 2001. Ocean turbulence. Part I: One-point closure model – Momentum and heat vertical diffusivities. J. Phys. Oceanogr. **31**: 1413–1426. [doi:10.1175/1520-0485(2001)031<1413:OTPIOP>2.0.CO;2].

Carpenter, J. H. 1965. The accuracy of the Winkler method for dissolved oxygen analysis. Limnol. Oceanogr. **10**: 135–140. [doi:10.4319/lo.1965.10.1.0135].

Carraway, E. R., Demas, J. N., DeGraff, B. A., and Bacon, J. R. 1991. Photophysics and photochemistry of oxygen sensors based on luminescent transition-metal complexes. Anal. Chem. **63**: 337–342. [doi:10.1021/ac00004a007].

Carrillo, C. J., Smith, R. C., and Karl, D. M. 2004. Processes regulating oxygen and carbon dioxide in surface waters west of the Antarctic Peninsula. Mar. Chem. **84**: 161–179.

Carslaw, H. S. and Jaeger, J. C. 1976. Conduction of heat in solids. Clarendon Press, Oxford. 2. edition.

Cassar, N., Bender, M. L., Barnett, B. A., Fan, S., Moxim, W. J., Levy, H., and Tilbrook, B. 2007. The Southern Ocean Biological Response to Aeolian Iron Deposition. Science **317**: 1067–1070. [doi:10.1126/science.1144602].

Cassar, N., DiFiore, P. J., Barnett, B. A., Bender, M. L., Bowie, A. R., Tilbrook, B., Petrou, K., Westwood, K. J., Wright, S. W., and Lefevre, D. 2011. The influence of iron and light on net community production in the Subantarctic and Polar Frontal Zones. Biogeosciences **8**: 227–237. [doi:10.5194/bg-8-227-2011].

Castro-Morales, K., Cassar, N., Shoosmith, D. R., and Kaiser, J. 2013. Biological production in the Bellingshausen Sea from oxygen-to-argon ratios and oxygen triple isotopes. Biogeosciences **10**: 2273–2291. [doi:10.5194/bg-10-2273-2013].

Cianca, A., Santana, R., Hartman, S. E., Martín-González, J. M., González-Dávila, M., Rueda, M. J., Llinás, O., and Neuer, S. 2013. Oxygen dynamics in the North Atlantic subtropical gyre. Deep Sea Res. Part II Top. Stud. Oceanogr. **93**: 135–147. [doi:10.1016/j.dsr2.2013.01.004].

Clark, L. C., Jr., Wolf, R., Granger, D., and Taylor, Z. 1953. Continuous recording of blood oxygen tensions by polarography. J. Appl. Physiol. **6**: 189–193.

Clegg, S. L. and Brimblecombe, P. 1990. The solubility and activity coefficient of oxygen in salt solutions and brines. Geochim. Cosmichim. Ac. **54**: 3315–3328. [doi:10.1016/0016-7037(90)90287-U].

Clissold, P. 2008. Candidate Earth Explorer Core Missions: A-SCOPE – Advanced Space Carbon and Climate Observation of Planet Earth. Reports for Assessment ESA SP-1313/1.

Coale, K. H., Michael Gordon, R., and Wang, X. 2005. The distribution and behavior of dissolved and particulate iron and zinc in the Ross Sea and Antarctic circumpolar current along 170Â°W. Deep Sea Res. Part I Oceanogr. Res. Pap. **52**: 295–318. [doi:10.1016/j.dsr.2004.09.008].

Cox, M. E. and Dunn, B. 1986. Oxygen diffusion in poly(dimethyl siloxane) using fluorescence quenching. I. Measurement technique and analysis. J. Polym. Sci., Part A: Polym. Chem. **24**: 621–636. [doi:10.1002/pola.1986.080240405].

Craig, H. and Hayward, T. 1987. Oxygen Supersaturation in the Ocean: Biological Versus Physical Contributions. Science **235**: 199–202. [doi:10.1126/science.235.4785.199].

Crank, J. 1975. The mathematics of diffusion. Clarendon Press, Oxford. 2. edition.

Culberson, C. H., Knapp, G., Stalcup, M. C., Williams, R. T., and Zemlyak, F. 1991. A comparison of methods for the determination of dissolved oxygen in seawater. WHP office report WHPO 91-2. WOCE report 73/91.

Danneel, H. L. 1897. Über den durch diffundierende Gase hervorgerufenen Reststrom. Z. Elektrochem. **4**: 227–232. [doi:10.1002/bbpc.18970040903].

D'Asaro, E. A. and McNeil, C. 2013. Calibration and stability of oxygen sensors on autonomous floats. J. Atmos. Oceanic Technol. **30**: 1896–1906. [doi:10.1175/JTECH-D-12-00222.1].

Davis, R. E., Regier, L. A., Dufour, J., and Webb, D. C. 1992. The autonomous Lagrangian circulation explorer (ALACE). J. Atmos. Oceanic Technol. **9**: 264–285. [doi:10.1175/1520-0426(1992)009<0264:TALCE>2.0.CO;2].

Dee, D. P., Uppala, S. M., Simmons, A. J., Berrisford, P., Poli, P., Kobayashi, S., Andrae, U., Balmaseda, M. A., Balsamo, G., Bauer, P., Bechtold, P., Beljaars, A. C. M., van de Berg, L., Bidlot, J., Bormann, N., Delsol, C., Dragani, R., Fuentes, M., Geer, A. J., Haimberger, L., Healy, S. B., Hersbach, H., Hólm, E. V., Isaksen, L., Kållberg, P., Köhler, M., Matricardi, M., McNally, A. P., Monge-Sanz, B. M., Morcrette, J.-J., Park, B.-K., Peubey, C., de Rosnay, P., Tavolato, C., Thépaut, J.-N., and Vitart, F. 2011. The ERA-Interim reanalysis: configuration and performance of the data assimilation system. Q. J. R. Meteorol. Soc. **137**: 553–597. [doi:10.1002/qj.828].

Demas, J. N., DeGraff, B. A., and Coleman, P. B. 1999. Oxygen sensors based on luminescence quenching. Anal. Chem. **71**: 793A–800A. [doi:10.1021/ac9908546].

Demas, J. N., DeGraff, B. A., and Xu, W. 1995. Modeling of luminescence quenching-based sensors: Comparison of multisite and nonlinear gas solubility models. Anal. Chem. **67**: 1377–1380. [doi:10.1021/ac00104a012].

Dickson, A. G. 1994. Determination of dissolved oxygen in sea water by Winkler titration. *In* WOCE operations manual. Part 3.1.3 Operations & methods. WHP office report WHPO 91-1.

Dickson, A. G. and Millero, F. J. 1987. A comparison of the equilibrium constants for the dissociation of carbonic acid in seawater media. Deep Sea Res. Part I Oceanogr. Res. Pap. **34**: 1733–1743. [doi:10.1016/0198-0149(87)90021-5].

Dickson, A. G., Sabine, C. L., and Christian, J. R. 2007. Guide to Best Practices for Ocean CO2 Measurements. PICES Special Publication 3.

Draxler, S. and Lippitsch, M. E. 1996. Lifetime-based sensing: Influence of the microenvironment. Anal. Chem. **68**: 753–757. [doi:10.1021/ac9507092].

Duursma, E. and Boisson, M. 1994. Global oceanic and atmospheric oxygen stability considered in relation to the carbon-cycle and to different time scales. Oceanol. Acta **17**: 117–141.

Edwards, B., Murphy, D., Janzen, C., and Larson, N. 2010. Calibration, response, and hysteresis in deep-sea dissolved oxygen measurements. J. Atmos. Oceanic Technol. **27**: 920–931. [doi:10.1175/2009JTECHO693.1].

Emerson, S. and Bushinsky, S. 2014. Oxygen Concentrations and Biological Fluxes in the Open Ocean. Oceanography **27**: 168–171. [doi:10.5670/oceanog.2014.20].

Emerson, S. and Hayward, T. L. 1995. Chemical tracers of biological processes in shallow waters of North Pacific: Preformed nitrate distributions. J. Mar. Res. **53**: 499–513. [doi:10.1357/0022240953213179].

Emerson, S., Stump, C., Johnson, B., and Karl, D. M. 2002. In situ determination of oxygen and nitrogen dynamics in the upper ocean. Deep Sea Res. Part I Oceanogr. Res. Pap. **49**: 941–952. [doi:10.1016/S0967-0637(02)00004-3].

Emerson, S., Stump, C., and Nicholson, D. 2008. Net biological oxygen production in the ocean: Remote in situ measurements of O_2 and N_2 in surface waters. Global Biogeochem. Cycles **22**: GB3023. [doi:10.1029/2007GB003095].

Emerson, S. R. and Hedges, J. I. 2008. Chemical oceanography and the marine carbon cycle. Cambridge University Press, Cambridge.

Fiedler, B., Fietzek, P., Vieira, N., Silva, P., Bittig, H. C., and Körtzinger, A. 2013. In situ CO_2 and O_2 measurements on a profiling float. J. Atmos. Oceanic Technol. **30**: 112–126. [doi:10.1175/JTECH-D-12-00043.1].

de Fommervault, O. P. 2014. Nitrate's data treatment. *In* RemOcean project meeting. Villefranche, France. 23 Jan. 2014.

Garcia, H. E. and Gordon, L. I. 1992. Oxygen solubility in seawater: Better fitting equations. Limnol. Oceanogr. **37**: 1307–1312. [doi:10.4319/lo.1992.37.6.1307].

Garcia, H. E., Locarnini, R. A., Boyer, T. P., Antonov, J. I., Baranova, O. K., Zweng, M. M., Reagan, J. R., and Johnson, D. R. 2013. Dissolved inorganic nutrients (phosphate, nitrate, silicate). *In* S. Levitus and A. Mishonov [eds.] World ocean atlas 2013, vol. 4. NOAA Atlas NESDIS 76. p. 25.

Gerringa, L. J. A., Alderkamp, A.-C., Laan, P., Thuróczy, C.-E., De Baar, H. J. W., Mills, M. M., van Dijken, G. L., van Haren, H., and Arrigo, K. R. 2012. Iron from melting glaciers fuels the phytoplankton blooms in Amundsen Sea (Southern Ocean): Iron biogeochemistry. Deep Sea Res. Part II Top. Stud. Oceanogr. **71–76**: 16–31. [doi: 10.1016/j.dsr2.2012.03.007].

Glover, D. M., Jenkins, W. J., and Doney, S. C. 2011. Modeling Methods for Marine Science. Cambridge University Press, Cambridge, UK.

Glueckauf, E. 1951. The composition of atmospheric air. *In* T. F. Malone [ed.] Compendium of Meteorology. Am. Met. Soc., Boston, MA. pp. 3–12.

Gould, J., Roemmich, D., Wijffels, S., Freeland, H., Ignaszewsky, M., Jianping, X., Pouliquen, S., Desaubies, Y., Send, U., Radhakrishnan, K., Takeuchi, K., Kim, K., Danchenkov, M., Sutton, P., King, B., Owens, B., and Riser, S. 2004. Argo profiling floats bring new era of in situ ocean observations. EOS T. Am. Geophys. Un. **85**: 185–191. [doi:10.1029/2004EO190002].

Grossart, H.-P., Dziallas, C., Leunert, F., and Tang, K. W. 2010. Bacteria dispersal by hitchhiking on zooplankton. P. Nat. Acad. Sci. USA **107**: 11959–11964. [doi: 10.1073/pnas.1000668107].

Gruber, N., Doney, S. C., Emerson, S. R., Gilbert, D., Kobayashi, T., Körtzinger, A., Johnson, G. C., Johnson, K. S., Riser, S. C., and Ulloa, O. 2010. Adding oxygen to Argo: Developing a global in-situ observatory for ocean deoxygenation and biogeochemistry. *In* J. Hall, D. E. Harrison, and D. Stammer [eds.] Proceedings of OceanObs'09: Sustained Ocean Observations and Information for Society. ESA Publication WPP-306, Venice, Italy, 21-25 September 2009. volume 2. [doi: 10.5270/OceanObs09.cwp.39].

Gruber, N., Keeling, C. D., and Bates, N. R. 2002. Interannual variability in the North Atlantic ocean carbon sink. Science **298**: 2374–2378. [doi:10.1126/ science.1077077].

Gruber, N., Keeling, C. D., and Stocker, T. F. 1998. Carbon-13 constraints on the seasonal inorganic carbon budget at the BATS site in the Northwestern Sargasso Sea. Deep Sea Res. Part I Oceanogr. Res. Pap. **45**: 673–717. [doi:10.1016/S0967-0637(97)00098-8].

Hahn, J. 2013. Oxygen variability and eddy-driven meridional oxygen supply in the tropical North East Atlantic oxygen minimum zone. Ph.D. thesis. Universität Kiel.

Hamme, R. C. and Emerson, S. R. 2004. The solubility of neon, nitrogen and argon in distilled water and seawater. Deep Sea Res. Part I Oceanogr. Res. Pap. **51**: 1517–1528. [doi:10.1016/j.dsr.2004.06.009].

Hamme, R. C. and Emerson, S. R. 2006. Constraining bubble dynamics and mixing with dissolved gases: Implications for productivity measurements by oxygen mass balance. J. Mar. Res. **64**: 73–95. [doi:10.1357/002224006776412322].

Hartmann, P., Leiner, M. J. P., and Lippitsch, M. E. 1995. Response characteristics of luminescent oxygen sensors. Sensors and Actuat. B: Chem. **29**: 251–257. [doi: 10.1016/0925-4005(95)01691-0].

Ho, D. T., Law, C. S., Smith, M. J., Schlosser, P., Harvey, M., and Hill, P. 2006. Measurements of air-sea gas exchange at high wind speeds in the Southern Ocean: Implications for global parameterizations. Geophys. Res. Lett. **33**: L16611. [doi: 10.1029/2006GL026817].

Holmén, K. and Liss, P. 1984. Models for air-water gas transfer: an experimental investigation. Tellus **36B**: 92–100. [doi:10.1111/j.1600-0889.1984.tb00231.x].

Honjo, S., Manganini, S. J., Krishfield, R. A., and Francois, R. 2008. Particulate organic carbon fluxes to the ocean interior and factors controlling the biological pump: A synthesis of global sediment trap programs since 1983. Progr. Oceanogr. **76**: 217–285. [doi:10.1016/j.pocean.2007.11.003].

Hoppema, M., Goeyens, L., and Fahrbach, E. 2000a. Intense nutrient removal in the remote area off Larsen Ice Shelf (Weddell Sea). Polar Biol. **23**: 85–94. [doi: 10.1007/s003000050012].

Hoppema, M., Middag, R., De Baar, H. J. W., Fahrbach, E., van Weerlee, E. M., and Thomas, H. 2007. Whole season net community production in the Weddell Sea. Polar Biol. **31**: 101–111. [doi:10.1007/s00300-007-0336-5].

Hoppema, M., Stoll, M. H. C., and de Baar, H. J. W. 2000b. CO_2 in the Weddell Gyre and Antarctic Circumpolar Current: austral autumn and early winter. Mar. Chem. **72**: 203–220. [doi:10.1016/S0304-4203(00)00082-7].

Huang, K., Ducklow, H., Vernet, M., Cassar, N., and Bender, M. L. 2012. Export production and its regulating factors in the West Antarctica Peninsula region of the Southern Ocean. Global Biogeochem. Cycles **26**: GB2005. [doi:10.1029/ 2010GB004028].

Huber, C. 2010. personal communication.

Jähne, B. and Haußecker, H. 1998. Air-water gas exchange. Annu. Rev. Fluid Mech. **30**: 443–468. [doi:10.1146/annurev.fluid.30.1.443].

James, D. R. and Ware, W. R. 1985. A fallacy in the interpretation of fluorescence decay parameters. Chem. Phys. Lett. **120**: 455–459. [doi:10.1016/0009-2614(85)85640-2].

Jenkins, W. J. and Doney, S. C. 2003. The subtropical nutrient spiral. Global Biogeochemical Cycles **17**: 1110. [doi:10.1029/2003GB002085].

Jennings, J. C., Gordon, L. I., and Nelson, D. M. 1984. Nutrient depletion indicates high primary productivity in the Weddell Sea. Nature **309**: 51–54. [doi:10.1038/309051a0].

JFE Alec Co., Ltd. 2009. RINKO fast-optical oxygen sensor data sheet. Kobe, Japan. Rev. Oct. 6, 2009.

Johnson, K. M., Sieburth, J. M., Williams, P. J. l., and Brändström, L. 1987. Coulometric total carbon dioxide analysis for marine studies: Automation and calibration. Mar. Chem. **21**: 117–133. [doi:10.1016/0304-4203(87)90033-8].

Johnson, K. S., Needoba, J. A., Riser, S. C., and Showers, W. J. 2007. Chemical sensor networks for the aquatic environment. Chem. Rev. **107**: 623–640. [doi:10.1021/cr050354e].

Johnson, K. S. and Riser, S. C. 2014. Carbon export drives nitrate supply in the North Atlantic Ocean. Nature. *submitted*.

Johnson, K. S., Riser, S. C., and Karl, D. M. 2010. Nitrate supply from deep to near-surface waters of the North Pacific subtropical gyre. Nature **465**: 1062–1065. [doi:10.1038/nature09170].

Jones, E. M., Bakker, D. C. E., Venables, H. J., Whitehouse, M. J., Korb, R. E., and Watson, A. J. 2010. Rapid changes in surface water carbonate chemistry during Antarctic sea ice melt. Tellus B **62**: 621–635. [doi:10.1111/j.1600-0889.2010.00496.x].

Jonsson, B. F., Doney, S. C., Dunne, J., and Bender, M. 2013. Evaluation of the Southern Ocean O_2/Ar-based NCP estimates in a model framework. J. Geophys. Res. Biogeosci. **118**: 385–399. [doi:10.1002/jgrg.20032].

Juranek, L. W., Hamme, R. C., Kaiser, J., Wanninkhof, R., and Quay, P. D. 2010. Evidence of O_2 consumption in underway seawater lines: Implications for air-sea O_2 and CO_2 fluxes. Geophys. Res. Lett. **37**: L01601. [doi:201010.1029/2009GL040423].

Kaiser, J., Reuer, M. K., Barnett, B., and Bender, M. L. 2005. Marine productivity estimates from continuous O_2/Ar ratio measurements by membrane inlet mass spectrometry. Geophys. Res. Lett. **32**: L19605. [doi:10.1029/2005GL023459].

Kalnay, E., Kanamitsu, M., Kistler, R., Collins, W., Deaven, D., Gandin, L., Iredell, M., Saha, S., White, G., Woollen, J., Zhu, Y., Leetmaa, A., Reynolds, R., Chelliah, M., Ebisuzaki, W., Higgins, W., Janowiak, J., Mo, K. C., Ropelewski, C., Wang, J., Jenne, R., and Joseph, D. 1996. The NCEP/NCAR 40-year reanalysis project. Bull. Amer. Meteor. Soc. **77**: 437–471. [doi:10.1175/1520-0477(1996)077<0437:TNYRP>2.0.CO;2].

Karl, D. M. and Lukas, R. 1996. The Hawaii Ocean Time-series (HOT) program: Background, rationale and field implementation. Deep Sea Res. Part II Top. Stud. Oceanogr. **43**: 129–156. [doi:10.1016/0967-0645(96)00005-7].

Karstensen, J. and Quadfasel, D. 2002. Formation of Southern Hemisphere Thermocline Waters: Water Mass Conversion and Subduction. J. Phys. Oceanogr. **32**: 3020–3038. [doi:10.1175/1520-0485(2002)032<3020:FOSHTW>2.0.CO;2].

Karstensen, J., Stramma, L., and Visbeck, M. 2008. Oxygen minimum zones in the eastern tropical Atlantic and Pacific oceans. Prog. Oceanogr. **77**: 331–350. [doi:10.1016/j.pocean.2007.05.009].

Kautsky, H. 1939. Quenching of luminescence by oxygen. Trans. Faraday Soc. **35**: 216–219. [doi:10.1039/TF9393500216].

Keeling, R. F. 1993. On the role of large bubbles in air-sea gas exchange and supersaturation in the ocean. J. Mar. Res. **51**: 237–271. [doi:10.1357/0022240933223800].

Keeling, R. F., Körtzinger, A., and Gruber, N. 2010. Ocean deoxygenation in a warming world. Annu. Rev. Mar. Sci. **2**: 199–229. [doi:10.1146/annurev.marine.010908.163855].

Klatt, O., Boebel, O., and Fahrbach, E. 2007. A profiling float's sense of ice. J. Atmos. Oceanic Technol. **24**: 1301–1308. [doi:10.1175/JTECH2026.1].

Klimant, I., Meyer, V., and Kühl, M. 1995. Fiber-optic oxygen microsensors, a new tool in aquatic biology. Limnol. Oceanogr. **40**: 1159–1165. [doi:10.4319/lo.1995.40.6.1159].

Klunder, M. B., Laan, P., Middag, R., De Baar, H. J. W., and van Ooijen, J. C. 2011. Dissolved iron in the Southern Ocean (Atlantic sector). Deep Sea Res. Part II Top. Stud. Oceanogr. **58**: 2678–2694. [doi:10.1016/j.dsr2.2010.10.042].

Körtzinger, A., Schimanski, J., and Send, U. 2005. High quality oxygen measurements from profiling floats: A promising new technique. J. Atmos. Oceanic Technol. **22**: 302–308. [doi:10.1175/JTECH1701.1].

Körtzinger, A., Schimanski, J., Send, U., and Wallace, D. 2004. The ocean takes a deep breath. Science **306**: 1337. [doi:10.1126/science.1102557].

Körtzinger, A., Send, U., Wallace, D. W. R., Karstensen, J., and DeGrandpre, M. 2008. Seasonal cycle of O_2 and pCO_2 in the central Labrador Sea: Atmospheric, biological, and physical implications. Global Biogeochem. Cycles **22**: GB1014. [doi:10.1029/2007GB003029].

Krahmann, G. and Fischer, T. 2012. Physical oceanography during Maria S. Merian cruise MSM18/3. IFM-GEOMAR Leibniz-Institute of Marine Sciences, Kiel University [doi:10.1594/PANGAEA.783445].

Lakowicz, J. R. [ed.] 2006. Principles of fluorescence spectroscopy. Springer, Boston, MA. [doi:10.1007/978-0-387-46312-4].

Langdon, C. 2010. Determination of dissolved oxygen in seawater by Winkler titration using the amperometric technique. *In* E. M. Hood, C. L. Sabine, and B. M. Sloyan [eds.] The GO-SHIP repeat hydrography manual: A collection of expert reports and guidelines. IOCCP report number 14. ICPO publication series number 134.

Laubscher, R. K., Perissinotto, R., and McQuaid, C. D. 1993. Phytoplankton production and biomass at frontal zones in the Atlantic sector of the Southern Ocean. Polar Biol. **13**: 471–481. [doi:10.1007/BF00233138].

Laws, E. A. 1991. Photosynthetic quotients, new production and net community production in the open ocean. Deep Sea Res. **38**: 143–167. [doi:10.1016/0198-0149(91)90059-O].

Linek, V., Moucha, T., Kordac, M., Dubcová, M., Hovorka, F., and Rejl, J. 2009. Liquid film effect on dynamics of optical oxygen probe. Comparison with polarographic oxygen probes. Diffusion coefficients measuring technique. Chem. Eng. Sci. **64**: 4005–4015. [doi:10.1016/j.ces.2009.06.015].

Liss, P. S. and Merlivat, L. 1986. Air-sea gas exchange rates: Introduction and synthesis. *In* P. Buat-Ménard [ed.] The Role of Air-Sea Exchange in Geochemical Cycling. Springer Netherlands. number 185 in NATO ASI Series. pp. 113–127. [doi:10.1007/978-94-009-4738-2_5].

Longhurst, A., Sathyendranath, S., Platt, T., and Caverhill, C. 1995. An estimate of global primary production in the ocean from satellite radiometer data. J. Plankton Res. **17**: 1245–1271. [doi:10.1093/plankt/17.6.1245].

Loose, B., McGillis, W. R., Schlosser, P., Perovich, D., and Takahashi, T. 2009. Effects of freezing, growth, and ice cover on gas transport processes in laboratory seawater experiments. Geophys. Res. Lett. **36**: L05603. [doi:200910.1029/2008GL036318].

Lorbacher, K., Dommenget, D., Niiler, P. P., and Köhl, A. 2006. Ocean mixed layer depth: A subsurface proxy of ocean-atmosphere variability. J. Geophys. Res. **111**: C07010. [doi:10.1029/2003JC002157].

Ludwig, H. and Macdonald, A. G. 2005. The significance of the activity of dissolved oxygen, and other gases, enhanced by high hydrostatic pressure. Comp. Biochem. Phys. A **140**: 387–395. [doi:10.1016/j.cbpb.2005.02.001].

Luyten, J. R., Pedlosky, J., and Stommel, H. 1983. The ventilated thermocline. J. Phys. Oceanogr. **13**: 292–309. [doi:10.1175/1520-0485(1983)013<0292:TVT>2.0.CO;2].

Marinov, I., Gnanadesikan, A., Toggweiler, J. R., and Sarmiento, J. L. 2006. The Southern Ocean biogeochemical divide. Nature **441**: 964–967. [doi:10.1038/nature04883].

Martinson, D. G. and McKee, D. C. 2012. Transport of warm Upper Circumpolar Deep Water onto the western Antarctic Peninsula continental shelf. Ocean Sci. **8**: 433–442. [doi:10.5194/os-8-433-2012].

McNeil, C., Katz, D., Wanninkhof, R., and Johnson, B. 2005. Continuous shipboard sampling of gas tension, oxygen and nitrogen. Deep Sea Res. Part I Oceanogr. Res. Pap. **52**: 1767–1785. [doi:10.1016/j.dsr.2005.04.003].

McNeil, C. L. and D'Asaro, E. A. 2014. A calibration equation for oxygen optodes based on physical properties of the sensing foil. Limnol. Oceanogr.: Methods **12**: 139–154. [doi:10.4319/lom.2014.12.139].

McNeil, C. L., Johnson, B. D., and Farmer, D. M. 1995. In-situ measurement of dissolved nitrogen and oxygen in the ocean. Deep Sea Res. Part I Oceanogr. Res. Pap. **42**: 819–826. [doi:10.1016/0967-0637(95)97829-W].

Mehrbach, C., Culberson, C. H., Hawley, J. E., and Pytkowicz, R. M. 1973. Measurement of the apparent dissociation constants of carbonic acid in seawater at atmospheric pressure. Limnol. Oceanogr. **18**: 897–907. [doi:10.4319/lo.1973.18.6.0897].

Michaels, A. F., Bates, N. R., Buesseler, K. O., Carlson, C. A., and Knap, A. H. 1994. Carbon-cycle imbalances in the Sargasso Sea. Nature **372**: 537–540. [doi:10.1038/372537a0].

Miloshevich, L. M., Paukkunen, A., Vömel, H., and Oltmans, S. J. 2004. Development and validation of a time-lag correction for Vaisala radiosonde humidity measurements. J. Atmos. Oceanic Technol. **21**: 1305–1327. [doi:10.1175/1520-0426(2004)021<1305:DAVOAT>2.0.CO;2].

Neill, C. 2011. personal communication.

Nicholson, D., Emerson, S., and Eriksen, C. C. 2008. Net community production in the deep euphotic zone of the subtropical North Pacific gyre from glider surveys. Limnol. Oceanogr. **53**: 2226–2236. [doi:10.4319/lo.2008.53.5_part_2.2226].

Nicholson, D., Emerson, S. R., Khatiwala, S., and Hamme, R. C. 2011. An inverse approach to estimate bubble-mediated air-sea gas flux from inert gas measurements. *In* S. Komori, W. R. McGillis, and R. Kurose [eds.] Proceedings of the 6th International Symposium on Gas Transfer at Water Surfaces. Kyoto University Press, Kyoto. pp. 223–237.

Nightingale, P. D., Malin, G., Law, C. S., Watson, A. J., Liss, P. S., Liddicoat, M. I., Boutin, J., and Upstill-Goddard, R. C. 2000. In situ evaluation of air-sea gas exchange parameterizations using novel conservative and volatile tracers. Global Biogeochem. Cycles **14**: 373–387. [doi:10.1029/1999GB900091].

Okura, I. and Kamachi, T. 2011. Application of porphyrins and related compounds as optical oxygen sensors. *In* K. M. Kadish, K. M. Smith, and R. Guilard [eds.] Applications. World Scientific, Singapore. volume 12 of *Handbook of porphyrin science*

with applications to chemistry, physics, materials science, engineering, biology and medicine. pp. 297–348.

Orsi, A. H., Whitworth III, T., and Nowlin Jr., W. D. 1995. On the meridional extent and fronts of the Antarctic Circumpolar Current. Deep Sea Res. Part I Oceanogr. Res. Pap. **42**: 641–673. [doi:10.1016/0967-0637(95)00021-W].

Oschlies, A. 2002. Can eddies make ocean deserts bloom? Global Biogeochem. Cycles **16**: 1106. [doi:10.1029/2001GB001830].

Pierrot, D., Wallace, D., and Lewis, E. 2006. MS Excel program developed for CO_2 system calculations. ORNL/CDIAC-105a. Carbon Dioxide Information Analysis Center, Oak Ridge National Laboratory, US Department of Energy, Oak Ridge, Tennessee [doi:10.3334/CDIAC/otg.CO2SYS_XLS_CDIAC105a].

Pilson, M. E. Q. 1998. An introduction to the chemistry of the sea. Prentice Hall, Upper Saddle River, NJ.

Planquette, H., Sherrell, R. M., Stammerjohn, S., and Field, M. P. 2013. Particulate iron delivery to the water column of the Amundsen Sea, Antarctica. Mar. Chem. **153**: 15–30. [doi:10.1016/j.marchem.2013.04.006].

Provost, C., Escoffier, C., Maamaatuaiahutapu, K., Kartavtseff, A., and Garçon, V. 1999. Subtropical mode waters in the South Atlantic Ocean. J. Geophys. Res.-Oceans **104**: 21033–21049. [doi:10.1029/1999JC900049].

Qiu, B. and Huang, R. X. 1995. Ventilation of the North Atlantic and North Pacific: Subduction versus obduction. J. Phys. Oceanogr. **25**: 2374–2390. [doi:10.1175/1520-0485(1995)025<2374:VOTNAA>2.0.CO;2].

Quaranta, M., Borisov, S. M., and Klimant, I. 2012. Indicators for optical oxygen sensors. Bioanal. Rev. **4**: 115–157. [doi:10.1007/s12566-012-0032-y].

Reuer, M. K., Barnett, B. A., Bender, M. L., Falkowski, P. G., and Hendricks, M. B. 2007. New estimates of Southern Ocean biological production rates from O_2/Ar ratios and the triple isotope composition of O_2. Deep Sea Res. Part I Oceanogr. Res. Pap. **54**: 951–974. [doi:10.1016/j.dsr.2007.02.007].

Rienecker, M. M., Suarez, M. J., Gelaro, R., Todling, R., Bacmeister, J., Liu, E., Bosilovich, M. G., Schubert, S. D., Takacs, L., Kim, G.-K., Bloom, S., Chen, J., Collins, D., Conaty, A., da Silva, A., Gu, W., Joiner, J., Koster, R. D., Lucchesi, R., Molod, A., Owens, T., Pawson, S., Pegion, P., Redder, C. R., Reichle, R., Robertson, F. R., Ruddick, A. G., Sienkiewicz, M., and Woollen, J. 2011. MERRA: NASA's Modern-Era Retrospective Analysis for Research and Applications. J. Climate **24**: 3624–3648. [doi:10.1175/JCLI-D-11-00015.1].

Riser, S. C. and Johnson, K. S. 2008. Net production of oxygen in the subtropical ocean. Nature **451**: 323–325. [doi:10.1038/nature06441].

Robb, W. L. 1968. Thin silicone membranes – Their permeation properties and some applications. Ann. N.Y. Acad. Sci. **146**: 119–137. [doi:10.1111/j.1749-6632.1968.tb20277.x].

Robinson, C. and Williams, P. J. l. B. 2005. Respiration and its measurement in surface marine waters. *In* P. del Giorgio and P. J. l. B. Williams [eds.] Respiration in Aquatic Ecosystems. Oxford University Press, Oxford. pp. 147–180. [doi:10.1093/acprof:oso/9780198527084.003.0009].

Rohardt, G., Fahrbach, E., and Wisotzki, A. 2011. Physical oceanography during POLARSTERN cruise ANT-XXVII/2. Alfred Wegener Institute, Helmholtz Center for Polar and Marine Research, Bremerhaven [doi:10.1594/PANGAEA.772244].

Rosner, B. 1983. Percentage points for a generalized ESD many-outlier procedure. Technometrics **25**: 165–172. [doi:10.2307/1268549].

Rubin, S. I., Takahashi, T., Chipman, D. W., and Goddard, J. G. 1998. Primary productivity and nutrient utilization ratios in the Pacific sector of the Southern Ocean based on seasonal changes in seawater chemistry. Deep Sea Res. Part I Oceanogr. Res. Pap. **45**: 1211–1234. [doi:10.1016/S0967-0637(98)00021-1].

Sakamoto, C. M., Johnson, K. S., and Coletti, L. J. 2009. Improved algorithm for the computation of nitrate concentrations in seawater using an in situ ultraviolet spectrophotometer. Limnol. Oceanogr.: Methods **7**: 132–143. [doi:10.4319/lom.2009.7.132].

Sakshaug, E., Johnsen, G., Kristiansen, S., von Quillfeldt, C., Rey, F., Slagstad, D., and Thingstad, F. 2009. Phytoplankton and primary production. *In* E. Sakshaug, G. Johnsen, and K. Kovacs [eds.] Ecosystem Barents Sea. Tapir Academic Press, Trondheim, Norway. pp. 167–208.

Sarmiento, J. L. and Gruber, N. 2006. Ocean biogeochemical dynamics. Princeton University Press, Princeton.

Sarmiento, J. L., Gruber, N., Brzezinski, M. A., and Dunne, J. P. 2004. High-latitude controls of thermocline nutrients and low latitude biological productivity. Nature **427**: 56–60. [doi:10.1038/nature02127].

Sarmiento, J. L., Rooth, C. G. H., and Roether, W. 1982. The North Atlantic tritium distribution in 1972. J. Geophys. Res.-Oceans **87**: 8047–8056. [doi:10.1029/JC087iC10p08047].

Sarmiento, J. L. and Toggweiler, J. R. 1984. A new model for the role of the oceans in determining atmospheric pCO_2. Nature **308**: 621–624. [doi:10.1038/308621a0].

Sato, O. T. and Polito, P. S. 2014. Observation of South Atlantic subtropical mode waters with Argo profiling float data. J. Geophys. Res.-Oceans **119**: 2860–2881. [doi:10.1002/2013JC009438].

Schlichting, H. and Gersten, K. 1997. Grenzschicht-Theorie. Springer, Berlin. 9. edition.

Schlitzer, R. 2002. Carbon export fluxes in the Southern Ocean: results from inverse modeling and comparison with satellite-based estimates. Deep Sea Res. Part II Top. Stud. Oceanogr. **49**: 1623–1644. [doi:10.1016/S0967-0645(02)00004-8].

Schudlich, R. and Emerson, S. 1996. Gas supersaturation in the surface ocean: The roles of heat flux, gas exchange, and bubbles. Deep Sea Res. Part II Top. Stud. Oceanogr. **43**: 569–589. [doi:10.1016/0967-0645(95)00098-4].

Sea-Bird Electronics, Inc.. 2010. Application note 64: SBE43 dissolved oxygen sensor – background information, deployment recommendations, and cleaning and storage. Feb. 2010.

Sea-Bird Electronics, Inc.. 2012. SBE63 optical dissolved oxygen sensor brochure. Bellevue, WA, USA. Mar. 2012.

Sedwick, P. N. and DiTullio, G. R. 1997. Regulation of algal blooms in Antarctic Shelf Waters by the release of iron from melting sea ice. Geophys. Res. Lett. **24**: 2515–2518. [doi:10.1029/97GL02596].

Severinghaus, D. J. W. and Astrup, P. B. 1986. History of blood gas analysis. IV. Leland Clark's oxygen electrode. J. Clin. Monit. **2**: 125–139. [doi:10.1007/BF01637680].

Shadwick, E. H., Tilbrook, B., Cassar, N., Trull, T. W., and Rintoul, S. R. 2014. Summertime physical and biological controls on O_2 and CO_2 in the Australian Sector of the Southern Ocean. Journal of Marine Systems [doi:10.1016/j.jmarsys.2013.12.008].

Singh, A., Lomas, M. W., and Bates, N. R. 2013. Revisiting N_2 fixation in the North Atlantic Ocean: Significance of deviations from the Redfield ratio, atmospheric deposition and climate variability. Deep Sea Res. Part II Top. Stud. Oceanogr. **93**: 148–158. [doi:10.1016/j.dsr2.2013.04.008].

Smith, S. R., Legler, D. M., and Verzone, K. V. 2001. Quantifying Uncertainties in NCEP Reanalyses Using High-Quality Research Vessel Observations. J. Climate **14**: 4062–4072. [doi:10.1175/1520-0442(2001)014<4062:QUINRU>2.0.CO;2].

Smith, W. O. and Gordon, L. I. 1997. Hyperproductivity of the Ross Sea (Antarctica) polynya during austral spring. Geophys. Res. Lett. **24**: 233–236. [doi:10.1029/96GL03926].

Smith, W. O. and Nelson, D. M. 1985. Phytoplankton Bloom Produced by a Receding Ice Edge in the Ross Sea: Spatial Coherence with the Density Field. Science **227**: 163–166. [doi:10.1126/science.227.4683.163].

Sokolov, S. 2008. Chlorophyll blooms in the Antarctic Zone south of Australia and New Zealand in reference to the Antarctic Circumpolar Current fronts and sea ice forcing. J. Geophys. Res.-Oceans **113**: C03022. [doi:10.1029/2007JC004329].

Sokolov, S. and Rintoul, S. R. 2007. On the relationship between fronts of the Antarctic Circumpolar Current and surface chlorophyll concentrations in the Southern Ocean. J. Geophys. Res.-Oceans **112**: C07030. [doi:10.1029/2006JC004072].

Spreen, G., Kaleschke, L., and Heygster, G. 2008. Sea ice remote sensing using AMSR-E 89-GHz channels. J. Geophys. Res.-Oceans **113**: C02S03. [doi:10.1029/2005JC003384].

Stanley, R. H. R., Doney, S. C., Jenkins, W. J., and Lott III, D. E. 2012. Apparent oxygen utilization rates calculated from tritium and helium-3 profiles at the Bermuda Atlantic Time-series Study site. Biogeosciences **9**: 1969–1983. [doi:10.5194/bg-9-1969-2012].

Stanley, R. H. R., Kirkpatrick, J. B., Cassar, N., Barnett, B. A., and Bender, M. L. 2010. Net community production and gross primary production rates in the western equatorial Pacific. Global Biogeochem. Cycles **24**: GB4001. [doi:10.1029/2009GB003651].

Steinberg, D. K., Carlson, C. A., Bates, N. R., Johnson, R. J., Michaels, A. F., and Knap, A. H. 2001. Overview of the US JGOFS Bermuda Atlantic Time-Series study (BATS): A decade-scale look at ocean biology and biogeochemistry. Deep Sea Res. Part II Top. Stud. Oceanogr. **48**: 1405–1447. [doi:10.1016/S0967-0645(00)00148-X].

Stendardo, I., Gruber, N., and Körtzinger, A. 2009. CARINA oxygen data in the Atlantic Ocean. Earth Syst. Sci. Data **1**: 87–100. [doi:10.5194/essd-1-87-2009].

Sweeney, C. 2003. The annual cycle of surface water CO_2 and O_2 in the Ross Sea: A model for gas exchange on the continental shelves of Antarctica. *In* G. R. DiTullio and R. B. Dunbar [eds.] Antarctic Res. Ser. Am. Geophys. Union, Washington, D.C. volume 78. pp. 295–312.

Sweeney, C., Gloor, E., Jacobson, A. R., Key, R. M., McKinley, G., Sarmiento, J. L., and Wanninkhof, R. 2007. Constraining global air-sea gas exchange for CO_2 with recent bomb ^{14}C measurements. Global Biogeochem. Cycles **21**: GB2015. [doi:10.1029/2006GB002784].

Takahashi, T., Sutherland, S. C., Sweeney, C., Poisson, A., Metzl, N., Tilbrook, B., Bates, N., Wanninkhof, R., Feely, R. A., Sabine, C., Olafsson, J., and Nojiri, Y. 2002. Global sea-air CO_2 flux based on climatological surface ocean pCO_2, and seasonal biological and temperature effects. Deep Sea Res. Part II Top. Stud. Oceanogr. **49**: 1601–1622. [doi:10.1016/S0967-0645(02)00003-6].

Takahashi, T., Sutherland, S. C., Wanninkhof, R., Sweeney, C., Feely, R. A., Chipman, D. W., Hales, B., Friederich, G., Chavez, F., Sabine, C., Watson, A., Bakker, D. C. E.,

Schuster, U., Metzl, N., Yoshikawa-Inoue, H., Ishii, M., Midorikawa, T., Nojiri, Y., Körtzinger, A., Steinhoff, T., Hoppema, M., Olafsson, J., Arnarson, T. S., Tilbrook, B., Johannessen, T., Olsen, A., Bellerby, R., Wong, C. S., Delille, B., Bates, N. R., and de Baar, H. J. W. 2009. Climatological mean and decadal change in surface ocean pCO_2, and net sea-air CO_2 flux over the global oceans. Deep Sea Res. Part II Top. Stud. Oceanogr. **56**: 554–577. [doi:10.1016/j.dsr2.2008.12.009].

Takeshita, Y., Martz, T. R., Johnson, K. S., Plant, J., Riser, S., and Gilbert, D. 2010. Quality control and application of oxygen data from profiling floats. AGU Fall Meeting Abstracts p. D1496.

Takeshita, Y., Martz, T. R., Johnson, K. S., Plant, J. N., Gilbert, D., Riser, S. C., Neill, C., and Tilbrook, B. 2013. A climatology-based quality control procedure for profiling float oxygen data. J. Geophys. Res.-Oceans **118**: 5640–5650. [doi: 10.1002/jgrc.20399].

Talley, L. D. 2008. Freshwater transport estimates and the global overturning circulation: Shallow, deep and throughflow components. Prog. Oceanogr. **78**: 257–303. [doi:10.1016/j.pocean.2008.05.001].

Tengberg, A. and Hovdenes, J. 2014. Information on long-term stability and accuracy of Aanderaa oxygen optodes and Information about multipoint calibration system and sensor option overview. Technical note. Aanderaa Data Instruments AS.

Tengberg, A., Hovdenes, J., Andersson, H. J., Brocandel, O., Diaz, R., Hebert, D., Arnerich, T., Huber, C., Körtzinger, A., Khripounoff, A., Rey, F., Ronning, C., Schimanski, J., Sommer, S., and Stangelmayer, A. 2006. Evaluation of a lifetime-based optode to measure oxygen in aquatic systems. Limnol. Oceanogr.: Methods **4**: 7–17. [doi:10.4319/lom.2006.4.7].

Tomczak, M. and Godfrey, J. S. 1994. Regional Oceanography: An Introduction. Pergamon.

Tortell, P. D., Asher, E. C., Ducklow, H. W., Goldman, J. A., Dacey, J. W., Grzymski, J. J., Young, J. N., Kranz, S. A., Bernard, K. S., and Morel, F. M. 2014. Metabolic balance of coastal Antarctic waters revealed by autonomous pCO_2 and $\Delta O_2/Ar$ measurements. Geophys. Res. Lett. p. 2014GL061266. [doi:10.1002/2014GL061266].

Tortell, P. D., Guéguen, C., Long, M. C., Payne, C. D., Lee, P., and DiTullio, G. R. 2011. Spatial variability and temporal dynamics of surface water pCO_2, $\Delta O_2/Ar$ and dimethylsulfide in the Ross Sea, Antarctica. Deep Sea Res. Part I Oceanogr. Res. Pap. **58**: 241–259. [doi:10.1016/j.dsr.2010.12.006].

Tortell, P. D. and Long, M. C. 2009. Spatial and temporal variability of biogenic gases during the Southern Ocean spring bloom. Geophys. Res. Lett. **36**: L01603. [doi:10.1029/2008GL035819].

Tortell, P. D., Long, M. C., Payne, C. D., Alderkamp, A.-C., Dutrieux, P., and Arrigo, K. R. 2012. Spatial distribution of pCO_2, $\Delta O_2/Ar$ and dimethylsulfide (DMS) in polynya waters and the sea ice zone of the Amundsen Sea, Antarctica. Deep Sea Res. Part II Top. Stud. Oceanogr. **71–76**: 77–93. [doi:10.1016/j.dsr2.2012.03.010].

Trull, T. W., Bray, S. G., Manganini, S. J., Honjo, S., and François, R. 2001. Moored sediment trap measurements of carbon export in the Subantarctic and Polar Frontal zones of the Southern Ocean, south of Australia. J. Geophys. Res.-Oceans **106**: 31489–31509. [doi:10.1029/2000JC000308].

Uchida, H. 2010. High-quality oxygen measurements by using fast-responding optode sensors. *In* Aoyama, M., Hydes, D., Daniel, A., Bakker, K., Murata, A., Tanhua, T., and Woodward, E. M. S. [eds.] IOC Reports of Meetings of Experts and Equivalent Bodies, 223. UNESCO. Paris, 24 Mar. 2010.

Uchida, H., Johnson, G. C., and McTaggart, K. E. 2010. CTD oxygen sensor calibration procedures. *In* E. M. Hood, C. L. Sabine, and B. M. Sloyan [eds.] The GO-SHIP repeat hydrography manual: A collection of expert reports and guidelines. IOCCP report number 14. ICPO publication series number 134.

Uchida, H., Kawano, T., Kaneko, I., and Fukasawa, M. 2008. In-situ calibration of optode-based oxygen sensors. J. Atmos. Oceanic Technol. **25**: 2271–2281. [doi:10.1175/2008JTECHO549.1].

Umlauf, L. and Burchard, H. 2005. Second-order turbulence closure models for geophysical boundary layers. A review of recent work. Cont. Shelf Res. **25**: 795–827. [doi:10.1016/j.csr.2004.08.004].

Umlauf, L., Burchard, H., and Bolding, K. 2014. GOTM – Scientific documentation. Version 4.2. `http://gotm.net`.

Vagle, S., McNeil, C., and Steiner, N. 2010. Upper ocean bubble measurements from the NE Pacific and estimates of their role in air-sea gas transfer of the weakly soluble gases nitrogen and oxygen. J. Geophys. Res.-Oceans **115**: C12054. [doi:10.1029/2009JC005990].

Villareal, T. A., Pilskaln, C., Brzezinski, M., Lipschultz, F., Dennett, M., and Gardner, G. B. 1999. Upward transport of oceanic nitrate by migrating diatom mats. Nature **397**: 423–425. [doi:10.1038/17103].

Wanninkhof, R. 1992. Relationship between wind speed and gas exchange over the ocean. J. Geophys. Res. **97**: 7373–7382. [doi:199210.1029/92JC00188].

Wanninkhof, R., Asher, W. E., Ho, D. T., Sweeney, C., and McGillis, W. R. 2009. Advances in quantifying air-sea gas exchange and environmental forcing. Annu. Rev. Mar. Sci. **1**: 213–244. [doi:10.1146/annurev.marine.010908.163742].

Waters, K. J. and Smith, R. C. 1992. Palmer LTER: A sampling grid for thePalmer LTER program. Antarct. J. U.S. **27**: 236–239.

Wattenberg, H. 1939. Die Verteilung des Sauerstoffs und des Phosphats im Atlantischen Ozean. *In* A. Defant [ed.] Wissenschaftliche Ergebnisse der deutschen atlantischen Expedition auf dem Forschungs- und Vermessungsschiff „Meteor“ 1925 – 1927. de Gruyter, Berlin. Bd. 9.

Wedler, G. 1985. Lehrbuch der physikalischen Chemie. VCH, Weinheim. 2. edition.

Weeding, B. and Trull, T. W. 2014. Hourly oxygen and total gas tension measurements at the Southern Ocean Time Series site reveal winter ventilation and spring net community production. J. Geophys. Res.-Oceans **119**: 348–358. [doi: 10.1002/2013JC009302].

Weiss, R. F. 1974. Carbon dioxide in water and seawater: the solubility of a non-ideal gas. Mar. Chem. **2**: 203–215. [doi:10.1016/0304-4203(74)90015-2].

Weiss, R. F. and Price, B. A. 1980. Nitrous-oxide solubility in water and seawater. Mar. Chem. **8**: 347–359. [doi:10.1016/0304-4203(80)90024-9].

Winkler, L. W. 1888. Die Bestimmung des im Wasser gelösten Sauerstoffes. Ber. Dtsch. Chem. Ges. **21**: 2843–2854. [doi:10.1002/cber.188802102122].

Worthington, L. V. 1976. On the North Atlantic circulation. Number 6 in The Johns Hopkins oceanographic studies. Johns Hopkins University Press, Baltimore.

Wunsch, C., Heimbach, P., Ponte, R., and Fukumori, I. 2009. The global general circulation of the ocean estimated by the ECCO-Consortium. Oceanography **22**: 88–103. [doi:10.5670/oceanog.2009.41].

List of Manuscripts

This thesis contains manuscripts that have been prepared in collaboration with other authors. The contribution of Henry Bittig for each paper is listed below.

- Bittig, H. C., Fiedler, B., Steinhoff, T., and Körtzinger, A. 2012. A novel electrochemical calibration setup for oxygen sensors and its use for the stability assessment of Aanderaa optodes. Limnol. Oceanogr.: Methods **10**: 921–933. [doi:10.4319/lom.2012.10.921].

  - Development and building of the calibration setup
  - Devising the calibration procedure
  - Laboratory evaluation and field evaluation including Winkler titrations
  - Full data analysis and interpretation
  - Writing of the manuscript

- Bittig, H. C. and Körtzinger, A. 2014. Near-surface and in-air oxygen optode measurements on a float provide an accurate in-situ calibration reference. J. Atmos. Oceanic Techn. Submitted.

  - Laboratory calibrations of the oxygen sensors
  - Participation in the deployment cruise (including a reference profile)
  - Full data analysis and interpretation
  - Writing of the manuscript

- Bittig, H. C., Fiedler, B., Scholz, R., Krahmann, G., and Körtzinger, A. 2014. Time response of oxygen optodes on profiling platforms and its dependence on flow speed and temperature. Limnol. Oceanogr.: Methods **12**: 617–636. [doi:10.4319/lom.2014.12.617].

  - Design of and conducting the laboratory experiments
  - Field experiments onboard R/V Polarstern including Winkler titrations and deployment of polar floats
  - Full data analysis and interpretation
  - Writing of the manuscript

- Tortell, P. D., Bittig, H. C., Körtzinger, A., Jones, E., and Hoppema, M. 2014. Biological and physical controls on N_2, O_2 and CO_2 distributions in contrasting Southern Ocean surface waters. Global Biogeochem. Cycles. Submitted.

  - Field experiments onboard R/V Polarstern and Winkler titrations
  - Processing and analysis of the O_2 and N_2 data
  - Implementation of the box model and performing the simulations
  - Contributing to the writing and review of the manuscript

Acknowledgements

It required a second try to arrive in Kiel and get the “Chapter Chemical Oceanography” started – the first e-mail to Arne (and Doug) remained unanswered. But it eventually worked out and the choice could not have been better. Arne has been one of the greatest supervisors I know. Thank you for the always open door and ear, the advise on work, life, the universe, and everything, the joy to discuss small technical practicalities while in the midst of proposal writing or institute administration, the encouragement when needed and the promotion when appropriate, and the freedom to stop and smell the roses.

I had the pleasure to join a number of projects, cruises, and meetings that gave me the opportunity to do things I otherwise never would have done, to see places I never would have gone, to meet people I never would have met. I am grateful for every single one, but I need to point out a few (not even including non-work related ones). A special warm memory belongs to R/V Oceania cruise AREX10 and the lovely people onboard. It may have been one of the smaller and more rustic ships I have been on, but you made up for it plentiful! Thank you to UNIS course AB-323, team “Blue Ice”, and Heidi, one of the most inspiring persons I met. The same warm memory is linked to R/V Polarstern cruise ANT-XXVII/2 with its marvelous group of people. Thank you Eberhard for an extraordinary leadership and cruise I will remember!

A special thanks belongs of course to the inspiring office community, Martina and the “Sabbelheinis” (self-protrayal), who ensured that I get my regular share of sweets, cookies, and entertainment. This work would not have been possible and not been half as fun without the (C)O_2-AG, so thank you Meike, Björn, Tobi, Tobi, Peer, Sebastian, Steffen, and Robin! This extends to the entire chemistry department and quite a few more people at GEOMAR, too many to name.

Finally, I want to mention the German National Academic Foundation with their pleasant summer distractions and the way too little used postgraduate forums as well as the ten NEMO floats that quickly disappeared and the two optodes that were flooded during the course of this thesis.

And while I’m at it: Actually, the preface to this chapter was already written in Bergen, Norway, in 2008 by great people like Tor Gammelsrød, Christoph Heinze, Craig Neill and the marine biology group. Thanks guys, you made a good start!

Eidesstattliche Versicherung

Hiermit erkläre ich, dass ich die vorliegende Arbeit – abgesehen von der Beratung durch meine Betreuer – selbstständig und ohne Zuhilfenahme unerlaubter Hilfsmittel erstellt habe. Alle benutzten Quellen habe ich vollständig angegeben. Die Zusammenarbeit mit Dritten habe ich detailliert und vollständig beschrieben. Weder diese noch eine ähnliche Arbeit wurden einer anderen Abteilung oder Hochschule im Rahmen eines Prüfungsverfahrens vorgelegt, veröffentlicht oder zur Veröffentlichung vorgelegt. Ferner versichere ich, dass die Arbeit unter Einhaltung guter wissenschaftlicher Praxis der Deutschen Forschungsgemeinschaft entstanden ist.

Kiel, den 4. November 2014